APPLICATIONS OF ADDITIVE MANUFACTURING FOR AMBIENT RF ENERGY HARVESTING AND WIRELESS POWER TRANSFER SYSTEMS

A Dissertation
Presented to
The Academic Faculty

By

Jo Bito

In Partial Fulfillment
of the Requirements for the Degree
Doctor of Philosophy in the
School of Electrical and Computer and Engineering

Georgia Institute of Technology

August 2017

APPLICATIONS OF ADDITIVE MANUFACTURING FOR AMBIENT RF ENERGY HARVESTING AND WIRELESS POWER TRANSFER SYSTEMS

Approved by:

Dr. Manos M. Tentzeris, Advisor
Professor, School of Electrical and Computer Engineering
Georgia Institute of Technology

Dr. Gregory D. Durgin
Professor, School of Electrical and Computer Engineering
Georgia Institute of Technology

Dr. Andrew F. Peterson
Professor, School of Electrical and Computer Engineering
Georgia Institute of Technology

Dr. Yoshihiro Kawahara
Associate Professor, Department of Information and Communication Engineering
University of Tokyo

Dr. Yang Wang
Associate Professor, Civil and Environmental Engineering
Georgia Institute of Technology

Date Approved: July 25, 2017

The important thing is not to stop questioning.

Curiosity has its own reason for existing.

Albert Einstein

ACKNOWLEDGEMENTS

First, I would like to acknowledge the support and advice from my research advisor, Dr. Manos M. Tentzeris. Dr. Tetzeris has provided me an environment and suggestions to grow as a researcher. His encouragement and ever-enthusiastic support for trying novel things is what has made this doctorate degree possible, and for which I shall remain grateful.

I would like to thank Dr. Apostolos Georgiadis and Dr. Yoshihiro Kawahara for being collaborators and giving insight on research. Also, I would like to acknowledge Dr. Kenji Tsuruta, Dr. Kazuhiro Fujimori, Dr. Shigeji Nogi, and Dr. Erhan Kudeki for inspiring me to pursue a career in research and invited in the field RF engineering.

I would also like to thank the members of ATHENA group and friends for their support and suggestion.

Finally, I would like to thank my family, Sadamu, Yumi, Shun, and Kai Bito for being always the best supporters of me and encouraged me to do my best in life and research. This work could not be completed without their support.

TABLE OF CONTENTS

Acknowledgments iv

List of Tables xi

List of Figures xiii

List of Acronyms xxii

Summary xxvi

Chapter 1: Introduction 1

1.1 Overview of wireless sensor architectures 1

1.1.1 Wireless sensor node/ active RFID with primary or secondary battery 1

1.1.2 Backscatter radio/passive RFID 2

1.1.3 Chipless RFID 2

1.2 Research Objective and Thesis Outline 5

Chapter 2: Review of Wireless Power Transfer/energy Harvesting Technologies 7

2.1 Fundamental Operation of Rectennas 8

2.2 Losses in RF Rectification 12

2.2.1 Junction and Breakdown Voltage Effects 13

2.2.2 Harmonics Effects 14

2.2.3 Impedance Mismatch 15
2.2.4 Other Losses in RF Circuits 16
2.3 Rectifier Topologies 18
2.3.1 Series and Shunt Rectifiers 18
2.3.2 Full-wave Rectifier 20
2.3.3 Voltage Multipliers 20
2.4 Other Rectenna Design Aspects for Ambient RF Energy Harvesting/wireless Power Transfer 21
2.4.1 Wide-Band and High Gain Antennas for High RF Input Power . . . 21
2.4.2 Wave-form Optimization to Improve Power Conversion Efficiency . 22
2.5 Friis Transmission Equation and Available Ambient RF Power 22
2.6 Power Management Circuit 24
2.6.1 Duty Cycling 24
2.6.2 DC-DC Boost Converter 25
2.6.3 Maximum Power Tracking and Battery Charging 27

Chapter 3: Review of Additive Manufacturing Technologies 29

3.1 Inkjet-printing Technology 30
3.1.1 Operation of Piezoelectric DOD 30
3.1.2 Surface Tension and Viscosity for Droplet Formulating and Wetting 31
3.1.3 Droplet Size and Resolution 35
3.1.4 Printable Materials 35
3.1.5 Inkjet Printing for Masking 36
3.2 3D-printing Technology 38

3.2.1 FDM Printing . . . 39
3.3 Printed Material Electrical Property Characterization . . . 40
3.3.1 Sheet Resistance of Conductive Material . . . 40
3.3.2 Dielectric Constant . . . 41
3.3.3 Loss Tangent . . . 44
3.4 Additive Manufacturing for Energy Harvester Fabrication . . . 45
3.4.1 Solar . . . 48
3.4.2 Heat . . . 48
3.4.3 Vibration . . . 48
3.5 Additive Manufacturing Technologies for Energy Storage Devices in Autonomous Systems . . . 49
3.5.1 Dielectric Capacitors . . . 49
3.5.2 Electrochemical Capacitor . . . 50
3.5.3 Battery . . . 50

Chapter 4: Wearable Flexible Near-field RF Energy Harvester . . . 51

4.1 Wearable Flexible RF Energy Harvester Design . . . 51
4.1.1 Near-field Power Distribution Simulations and Measurements . . . 51
4.1.2 E- and H-field Receiver Design . . . 53
4.1.3 Input Power Estimation and RF-DC Conversion Circuit Design . . . 54
4.2 Wearable Energy Harvester DC and Communication Characterization . . . 58
4.2.1 RF-DC Conversion Efficiency Measurements . . . 58
4.2.2 System-Level Operation Test Utilizing Micro-controller Module . . . 60
4.2.3 Effect of Harvester on the Two-Way Radio Communication Quality 64

4.3 Real-time Active Matching Circuit for Wearable Flexible RF Energy Harvester 65

4.3.1 Real-time Active Matching System for Near-field RF Harvester . . 66

4.3.2 Characterization of Effect of Human Movement for Tx-Rx Network 68

4.3.3 Matching Circuit Design using GA and Clustering 69

4.4 Backscattering-based On-body Sensor Network 73

4.4.1 Energy Harvester Design and Measurement 75

4.4.2 Backscattering Sensor Tag Design 80

4.4.3 DC and RF Performance Evaluation 82

4.4.4 Operation Range Extension Using an RF Amplifier 83

4.4.5 Multiple Backscattering Tags 88

4.4.6 Ammonia Sensor 89

4.5 Discussion for Further Applications 90

Chapter 5: Hybrid RF/solar Energy Harvesting 93

5.1 Energy Harvesting from Ambient Energy Sources 93

5.2 Hybrid RF Solar Energy Harvesting System 94

5.2.1 Antenna Design and Measurement 95

5.2.2 RF-DC Conversion Circuit Design and Measurement 99

5.2.3 Module-level Operation Test 107

5.3 Hybrid RF Photovoltaic Energy Harvesting System 109

5.3.1 Selection of Rectifier Topology and Charge Tank Capacitor Value . 111

5.3.2 DC-DC Conversion Circuit Design and Characterization 114

5.3.3 Selection of PV cell and Operation Test 116

5.4 Power Management System for Overnight Operation of Long-range Active Van-Atta RFID Sensor 118

5.4.1 System Overview 119

5.4.2 Operation Test with a DC-DC converter 121

5.4.3 Field test in the office environment 123

5.5 Inkjet Printed Organic Solar Cell 123

5.5.1 Operation Principle of Organic Solar Cell 124

5.5.2 Characterization of P3HT:PCBM material 125

5.5.3 Work Function Characterization of Top and Bottom Electrodes . . . 127

5.5.4 Fully Inkjet Printed Solar Cells 130

5.6 Discussion for Future Extensions 133

Chapter 6: Real-time Active Matching for Near-field Wireless Power Transfer . 135

6.1 Operation Principle of Magnetic Resonant Coupling Wireless Power Transfer 136

6.1.1 Wireless Power Transfer Efficiency and Horn Effect 136

6.1.2 Numerical Analysis of an Open-helical Coil 141

6.2 Active Matching Circuit Design utilizing a Genetic Algorithm 143

6.2.1 Fundamentals of an Active Matching Circuit and a Genetic Algorithm 143

6.2.2 Real-time Matching Circuit System 147

6.2.3 Operation Test of the Automated Real-Time Matching System . . . 152

6.2.4 Operation Tests under Rugged Conditions 155

6.3 Active matching circuit for moving object 158

6.3.1 Characterization of Tx-Rx Coil Impedance under Moving Condition 159

6.3.2 Matching Circuit Design using Genetic Algorithm 160

6.3.3 K-means Clustering 165

6.3.4 Matching Circuit Design using Non-ideal Lumped Component Models 168

6.3.5 DC Bias Circuit Design 168

6.3.6 Measurement Results and Discussion 171

6.4 Discussion for Practical Applications 174

Chapter 7: Contribution and Conclusion 177

7.1 Conclusion 177

7.2 Contributions 178

7.3 Future Work 181

7.4 Author's Publications 183

7.4.1 Journals 183

7.4.2 Conferences 183

7.4.3 Book Chapters 183

7.4.4 Patents 183

References 198

Vita 199

LIST OF TABLES

1.1 Summary of different WPT and EH technologies 6

2.1 Summary of major diode parameters 10

3.1 Typical drop diameters and equivalent drop volumes 35

3.2 COMPARISON OF AVAILABLE AMBIENT ENERGY SOURCES 47

4.1 PARAMETERS OF RF-DC CONVERSION CKT COMPONENTS 67

4.2 FIGURE OF MERIT OF GA AND CLUSTERING 74

4.3 The performance comparison between the energy harvesters with and without an RF amplifier 88

5.1 PRELIMINARY DIMENSIONS OF THE DUAL-FED RECTANGULAR SHORTED ANTENNA. 98

5.2 DIMENSION OF THE RECTANGULAR SHORTED ANTENNA FOR THE FINAL PROTOTYPE. 99

5.3 RECTIFIER PERFORMANCE COMPARISON 113

5.4 COMPONENTS OF DC-DC CONVERTER 117

5.5 WORK FUNCTION OF PRINTED SILVER AND PEDOT:PSS 129

6.1 PARAMETERS OF THE OPTIMIZED OPEN HELICAL COIL FOR THE PROPOSED WPT SYSTEM 142

6.2 CIRCUIT COMPONENT VALUES FOR OPTIMIZED FIXED π MATCHING CIRCUIT TOPOLOGIES USING IDEAL LUMPED COMPONENT MODELS 162

6.3 CIRCUIT COMPONENT VALUES FOR OPTIMIZED ACTIVE MATCHING CIRCUITS WITH DIFFERENT NUMBER OF CELLS USING IDEAL LUMPED COMPONENT MODELS 164

6.4 FIGURE OF MERIT OF EACH MATCHING CIRCUIT TOPOLOGY 164

6.5 POWER TRANSFER EFFICIENCY COMPARISON USING MEASURED S-PARAMETERS FOR TRIALS 1-4 165

6.6 POWER TRANSFER EFFICIENCY COMPARISON BETWEEN ALL 100 MEASURED DATA VS 4, 8 AND 16 CLUSTER REPRESENTATIVE IMPEDANCE VALUES 168

6.7 CIRCUIT COMPONENT VALUES FOR OPTIMIZED FIXED π MATCHING CIRCUIT TOPOLOGIES USING NON-IDEAL LUMPED COMPONENT S-PARAMETERS MODELS 169

6.8 CIRCUIT COMPONENT VALUES FOR OPTIMIZED ACTIVE MATCHING CIRCUITS WITH DIFFERENT NUMBER OF CELLS USING NON-IDEAL LUMPED COMPONENT S-PARAMETERS MODELS 169

6.9 PARAMETERS OF ACTIVE MATCHING CIRCUIT UNIT CELL DC BIAS COMPONENTS 172

6.10 POWER TRANSFER EFFICIENCY COMPARISON WITH EACH MATCHING CIRCUIT WITH IDEAL LUMPED COMPONENTS, NON-IDEAL S-PARAMETERS MODELS AND MEASURED S-PARAMETERS 175

LIST OF FIGURES

2.1 Block diagram of rectenna with DC load. 8

2.2 IV curve of a typical diode model. 10

2.3 Ideal and non-ideal diode equivalent circuit model. 11

2.4 General relationship between RF-DC conversion efficiency and input power with the loss factors. 13

2.5 (a) Series rectifier. and (b) Shunt rectifier. 18

2.6 (a) Full-wave rectifier, (b) Cockcroft-Walton, (c) Modified Cockcroft-Walton, and (d) Dickson voltage multiplier. 19

2.7 General relationship between distance and path loss in VHF an UHF band. 23

2.8 DC-DC converter circuit while a switch is (a) on and (b) off state. 26

3.1 Phase of piezoelectric actuator movement while jetting a droplet. 31

3.2 Schematic of stable inkjet droplet formulation in terms of Reynolds and Ohnesorge numbers. 34

3.3 Fabrication process of flexible circuit traces utilizing inkjet printing masking. 37

3.4 Circuit traces for a TDFN8 IC package fabricated with inkjet printing masking. 38

3.5 FDM 3D printing process. 40

3.6 Model of sheet resistance. 41

3.7 Fully printed T-resonator structure. 43

3.8 Measured S_{11} of fully printed T-resonator. 44

3.9 Dielectric constant of printed thick SU-8 substrate. 44

4.1 RF input power of near- and far-field RF energy harvesting with respect to time. 52

4.2 E-field distribution of (a) Back side. (b) Palm side. H-field distribution of (c) Back side. (d) Palm side. 54

4.3 (a) Near-field probe measurement configuration. (b) Measured E- and H-field power levels at different relative angles and distances. 55

4.4 Additively manufactured receiver prototypes for (a) E-field, (b) H-field. . . 56

4.5 System configuration with equivalent S-parameters matrix. 58

4.6 Measured S-parameters for E- and H-field receivers. 58

4.7 RF-DC conversion circuit topology for the wearable (a) E-filed energy harvester. (b) H-filed energy harvester. 59

4.8 (a) Open voltage measurement of E-field harvester with an on-bottle setup. (b) Operation verification of the E-field harvester on the wrist. 61

4.9 (a) Open voltage measurement of H-field harvester with an on-bottle setup. (b) Operation verification of the H-field harvester on the hand. 62

4.10 Simulated and estimated RF-DC conversion efficiency values from S-parameters measurements and the measured output DC power from E-field harvester prototype with respect to load resistance. 62

4.11 Simulated and estimated RF-DC conversion efficiency values from S-parameters measurements and the measured output DC power from H-field harvester prototype with respect to load resistance. 63

4.12 Setup for the operation test of H-field harvester using a micro-controller module. 64

4.13 Measured micro-controller module (ED) current flow in the initial operation state and in the normal operation state. 64

4.14 Received power measurement in an anechoic chamber. 65

4.15 Effect of harvester prototype on received communication power. 66

4.16 Generalized near-field wearable energy harvester system with real-time active matching circuit model. 67

4.17 (a) Tx-Rx network characterization measurement with an on-bottle setup. (b) Optimal load impedance value for each of the 100 sampled S-parameters with an on-bottle setup. 69

4.18 Available DC power with ideal RF-DC conversion, typical RF-DC-DC conversion and GA optimized capacitor combinations. 71

4.19 Delivered DC power increase with GA optimized capacitor combinations compared to one fixed capacitor combination. 72

4.20 Distribution of available DC power increase for RF-DC-DC converter case and fixed matching circuit case, and their arithmetic mean values. 72

4.21 Capacitor value combinations with and without clustering. 73

4.22 Proposed wearable energy autonomous on-body wireless sensor network system. 74

4.23 Block diagram of energy autonomous on-body wireless sensor network system. 76

4.24 Prototype of proposed full-wave rectifier. 76

4.25 Simulated and measured output DC and RF power from the proposed rectifier with respect to the input power. 77

4.26 Prototype of the energy harvesting circuit for carrier emission. 77

4.27 (a) Side view of the wearable 928 MHz antenna (b) prototype of the FSS. . 78

4.28 Prototype of the (a) unfolded and (b) folded 928 MHz antenna. 79

4.29 Measured S_{11} of the folded and unfolded 928 MHz wearable antenna. . . . 79

4.30 Prototype of the custom RFID tag for on-body sensing. 81

4.31 Measured S-parameters of $464\,\mathrm{MHz}$ and $928\,\mathrm{MHz}$ with each expected input power and MOSFET bias voltage. 82

4.32 Measured S-parameters of 928MHz with each expected input power and MOSFET bias voltage. 83

4.33 Measured output voltage from the voltage regulator connected with the voltage doubler with $464\,\mathrm{MHz}$ RF input signal at each input power and MOSFET bias voltage. 83

4.34 Prototype of the custom backscattering RFID tag with a printed ammonia sensor. 84

4.35 Measurement setup for the wearable RF energy harvester powered on-body backscattering sensing system. 84

4.36 Block diagram of the proposed energy harvester with enhanced RF output by driving an RF amplifier using DC output power. 85

4.37 RF amplifier's supply voltage vs. supply current. 86

4.38 RF amplifier's supply voltage vs. equivalent load resistance. 86

4.39 RF amplifier's supply voltage vs. power consumption. 87

4.40 Amplifier gain vs. RF input power with supply voltage of $2\,\mathrm{V}$ and $3\,\mathrm{V}$. . . . 87

4.41 Proof-of-concept prototype of the proposed rectifier/frequency doubler including a DC power enabled amplifier. 88

4.42 Comparison of the 928 MHz output power between the harvesters with and without an RF amplifier. 89

4.43 Long-range operation test of the wearable RF energy harvester powered on-body backscatter sensing system with an integrated RF amplifier. 90

4.44 Measurement setup for the multiple sensors test. 91

4.45 Measured result for multiple sensors test. 91

4.46 Measured result for the ammonia sensor tag before exposure to ammonia. . 91

4.47 Measured result for the ammonia sensor tag after exposure to ammonia. . . 92

5.1 Block diagram of a typical multi-form-energy harvesting enabled autonomous sensor device. 94

5.2 Block diagram of a hybrid RF solar powered autonomous mote. 95

5.3 (a) Side and (b) top view of the prototype of the rectangular shorted antenna. 97

5.4 Prototype of the dual-feed rectangular shorted slot solar antenna with a filexible film solar cell (a) top and (b) inside. 97

5.5 Simulted S_{21} with respect to frequency with varied ground size. 98

5.6 Measured and simulated (design and post fabrication) (a) S_{11}, S_{22}, and (b) S_{21} of the dual-feed rectangular shorted slot antenna. 99

5.7 Simulated axial ratio of the rectangular shorted antenna with and without the solar cell with respect to (a) frequency and (b) θ direction rotation angle. 100

5.8 Simulated total realized gain of the rectangular shorted antenna with and without the solar cell. 100

5.9 Measured and simulated normalized radiation patten of the rectangular shorted antenna with and without the solar cell (a)ϕ = 0° and (b)ϕ = 90°. 101

5.10 (a) Side and (b) top view of the rectangular shorted antenna for the final prototype. 102

5.11 Simulated S-parameters of the final antenna design with respect to frequency. 102

5.12 (a) Circuit diagram of the hybrid RF solar harvester and (b) picture of the complete harvester prototype. 103

5.13 Measured and simulated (a) RF-DC conversion efficiency and (b) DC output voltage with respect to frequency with optimal load resistance at -17 dBm RF input power. 104

5.14 Measured and simulated (a) RF-DC conversion efficiency and (b) DC output voltage with respect to input power with optimal load resistance at $2.45\,\mathrm{GHz}$. 105

5.15 Measured (a) output DC power and (b) DC current (I_0) from the soalr cell with respect to the light intensity for the load resistance of $3.8\,\mathrm{k\Omega}$. 106

5.16 Simulated output DC power with respect to the output DC current from the solar cell (I_0) for RF input power of -17 dBm and -10 dBm. 106

5.17 Simulated and measured S_{11} with respect to output current from the solar cell (I_0). 107

5.18 Voltage in the $100\,\mu\mathrm{F}$ capacitor that is integrated in the bq25504 PMU during charging under different RF and solar conditions: (1) -12.6 dBm RF input power, (2) solar under room light condition, (3)-12.6 dBm RF input power + solar under room light condition, and (4) -15.6 dBm RF input power + solar under room light condition until cold start mode is over. . . . 108

5.19 (a) PCBs for the final prototype. (b) Prototype of integrated hybrid energy harvesting system. 110

5.20 Simulated current and voltage output of a single solar cell under varying light levels. 111

5.21 Block diagram of the proposed hybrid RF/PV powered energy harvesting system. 112

5.22 Comparison of average RF-DC conversion efficiency with respect to the charge tank capacitance values and different timer operation periods with a series rectifier, a one-, and a two-stage voltage multiplier. 114

5.23 Picture of series rectifier prototype optimized for $-20\,\mathrm{dBm}$ input power at $2.45\,\mathrm{GHz}$. 115

5.24 (a) Measured, simulated, and curve fitted output voltage of the recfier with a varied load resistance. (b) Measured and estimated $2\,\mathrm{mF}$ capacitor voltage while charging with respect to time. 116

5.25 Circuit schematic of a DC-DC boost converter. 117

5.26 (a) Operation test of the DC-DC converter prototype in a darkroom. (b) Measured output voltage from the DC-DC converter, the rectifier, the timer, and the PV during operation test. 118

5.27 Circuit schematic of a DC-DC boost converter. 120

5.28 (a) Measured VLF oscillator output voltage while power saving mode. (b)Close-up view of VLF oscillator output voltage (red line in (a)). 122

5.29 Picture of the fabricated prototypes of the power management circuit, VLF oscillator, DC-DC boost converter, and the off-the-shelf solar cells (AM-5610CAR). 122

5.30 Operation of the DC-DC converter circuit and the VLF oscillator while the power management circuit is in the normal operation mode and the low power mode. 123

5.31 (a) Operation test of the power management system with the RF energy harvester powered by a RF transmitter at $8\,\mathrm{m}$ away from the receiver. The VLF oscillator output voltage at (b) daytime, (c) midnight, and (d) sunrise. 124

5.32 Printed organic solar cell samples with (a) Two layer P3HT without UV ozone treatment. (b) Two layer P3HT with UV ozone treatment, (c) Three layer P3HT without UV ozone treatment. and (d) Three layer P3HT withUV ozone treatment. 127

5.33 Printed solar cell structure. 128

5.34 Printed PEDOT:PSS ink after curing and work function measurement points. 129

5.35 Printed solar cell structure with polymetric work function modification. . . 130

5.36 Fabricated fully inkjet printed solar cells. 131

5.37 Open voltage measurement of printed 131

5.38 Current density of a printed solar cell with respect to bias voltage at dark, medium ($6\,\mu\mathrm{W/cm^2}$), and strong ($68.75\,\mu\mathrm{W/cm^2}$) light irradiation. 132

5.39 Printed silver with and without the coating of PEI polymer. 133

6.1 Block diagram of a dual-transmitting-coil wireless power transmission system with on-transmitter real-time matching circuits. 137

6.2 Equivalent circuit of open-helical type coil 138

6.3 (a) Equivalent circuit of Tx-Rx coil network. and (b) T-shaped equivalent circuit of Tx-Rx coil network. 139

6.4 Open-helical-coil wireless power transfer system prototype. 141

6.5 Measured and simulated S_{11} of the single open helical coil prototype. 141

6.6 Measured S_{21} of the open-helical-coil wireless power transfer coil network at different separation distances. 142

6.7 Flow chart of the GA optimization for the matching circuit design. 146

6.8 Simulated input impedance values on a Smith chart generated by MATLAB's GA algorithm. 147

6.9 (a) Tunable 6-stage matching circuit schematic derived using the GA and ADS. (b) Prototype of the tunable matching circuit with modified components value. 148

6.10 Measured and simulated input impedance values of tunable matching circuit prototype on a Smith chart. 149

6.11 Block diagram of a matching circuit quality assessment system utilizing a directional coupler and an RF detector IC. 150

6.12 (a) Measured output voltage from the RF detector IC with respect to the input power. (b) Measured impedance of the RF detector with respect to the input power 151

6.13 (a) S_{21} of the directional coupler for different terminal impedance values of port2. (b) S_{32} of the directional coupler for different terminal impedance values of port2. 151

6.14 Flow chart of the automated real-time matching procedure utilizing a microcontroller. 153

6.15 Complete setup of the automated real-time matching system for operation testing purposes. 154

6.16 Measured received power with and without the automated matching circuit at different coil separation distances. 154

6.17 Measured S_{11} of coil with and without the matching circuit at the optimal power transfer state that is automatically chosen by the microcontroller at different coil separation distances. 155

6.18 Measured received power from the receiver coil and the output voltage from the RF detector IC at each p-i-n diode on/off state with coil separation distance of (a)$10\,\mathrm{cm}$. (b) $12\,\mathrm{cm}$. (c)$14.5\,\mathrm{cm}$. (d) $16\,\mathrm{cm}$. 156

6.19 Tx-Rx coil network under misaligned conditions caused by relative elevation. (b)Measured received power as a function of the coil separation distance for different Rx coil elevation levels. 157

6.20 (a) Non-symmetrical WPT coil system with a large Tx coil and a small Rx coil. (b) Measured received power of the non-symmetrical Tx-Rx coil network with respect to the coil separation distance. 157

6.21 Block diagram of the wireless power transfer (WPT) system with the optimized matching circuit in the transmitter (Tx) side. 159

6.22 Measured input impedances of Tx-Rx coil topology under random coil movements in 4 trials of 100 measurements each. 160

6.23 Distribution and arithmetic mean of the measured power transfer efficiency values for 4 trials with 100 measurements each (total of 400 counts). 161

6.24 π matching circuit topologies with a series inductor (left) and a series capacitor (right). 162

6.25 N-stage active matching circuit schematic. 163

6.26 N-stage active matching circuit schematic. 166

6.27 Measured 100 input impedance values of Tx-Rx coils configurations under random movements in Trial1 and representative impedance values selected by using K-means clustering. 167

6.28 Circuit topology of the active matching circuit unit cell including the switch-controlled DC bias circuit. 170

6.29 (a) S_{11} of the original and of the optimized bias circuits. (b) S_{21} of the original and of the optimized bias circuits. (c) Transient of the diode anode voltage after switching. (d) Steady state bias current at on/off states for the original and the optimized bias circuit. 171

6.30 Prototype of an 1-cell active matching circuit. 172

6.31 Measured and simulated input impedances of 1-cell active matching circuit at on and off conditions. 173

6.32 Measured input impedance of the 1-cell active matching circuit for different input power levels at (a) “on” and (b) “off” switch conditions. 174

6.33 Measured input impedance of (a) L- and (b) C- series passive (c) 1-cell (d) 2-cell (e) 3-cell (f) 4-cell matching circuit. 176

List of Acronyms

ABC Ambient Backscatter Communication

ABS Acrylonitrile Butadiene Styrene

AC Alternating Current

ADC Analog to Digital Converter

ADS Advanced Design System

AMC Artificial Magnetic Conductor

AR Augmented Reality

CTCSS Continuous Tone-Coded Squelch System

CPW Coplanar Waveguide

CVD Chemical Vapor Deposition

CW Continuous Wave

DC Direct Current

DOD Drop On Demand

EH Energy Harvesting

EM Electromagnetic

EV Electrical Vehicle

FCC Federal Communications Commission

FDM Fused Deposition Modeling

GA Genetic Algorithm

HOMO Highest Occupied Molecular Orbital

IoTs Internet of Things

ISM Industrial, Scientific, and Medical

ITO Indium Tin Oxide

LCP Liquid Crystal Polymer

LPM Low Power Mode

LUMO Lowest Occupied Molecular Orbital

MRC Magnetic Resonant Coupling

MC Matching Circuit

MCU Micro-Controller Unit

OPV Organic Photovoltaics

PCB Printed Circuit Board

PCE Power Conversion Efficiency

PEDOT:PSS poly(3,4-ethylenedioxythiophene):poly(styrenesulfonate)

PEI Polyethylenimine

PLA Polylactic Acid

PMU Power Management Unit

PV Photovoltaic

PVD Physical Vapor Deposition

RF Radio Frequency

RFID Radio Frequency IDentification

rGO reduced Graphene Oxide

Rx Receiver

SLA Stereolithography

SLS Selective Laser Sintering

SLM Selective Laser Melting)

SNR Signal-to-Noise Ratio

SPDT Single Pole Double Throw

SS Smart Skin

SSPS Space Solar Power System

Tx Transmitter

UAV Unmanned Aerial Vehicle

UHF Ultra High Frequency

VCO Voltage Controlled Oscillator

VHF Very High Frequency

VLF Very Low Frequency

VNA Vecor Network Analyzer

VR Virtual Reality

WISP Wireless Identification Sensing Platform

WARP Wireless Ambient Radio Power

WSNs Wireless Sensor Networks

SUMMARY

Power cables are the last wires that prevent us from realizing truly "wireless" electronic devices, and wireless power transfer and ambient RF energy harvesting technologies are the key enablers to achieve the energy autonomous operation of these devices for wearable, mobile, and IoT applications. However, a low output voltage and a low power conversion efficiency associated with a low ambient RF energy density, and the degradation of wireless power transfer efficiency hinder the use of these technologies in practical situations. In the meanwhile, additive manufacturing technologies, especially inkjet and 3D printing technologies, which has been exploited to fabricate RF circuits, have drastically improved over the past few decades. The on-demand deposition of multidisciplinary inks enables low-cost flexible coils, wearable RF energy harvesters as well as other type of ambient energy transducers with the same platform. These unique characteristics of additive manufacturing techniques can be utilized to overcome the challenges in RF energy harvesting and wireless power transfer. This work first reviews the challenges in wireless power transfer/RF energy harvesting, and capability and limitation of additive manufacturing technologies, then shows the application of additive manufacturing technologies in the field of near-field wearable RF energy harvesting and ultra low power far-field RF/solar hybrid energy harvesting. Also, an active matching circuit design and operation for near-field wireless power, which is caused in wearable and flexible electronics is discussed.

In this research, there are three major contributions. First, flexible wearable energy harvesters for off-the-shelf UHF ($464\,\mathrm{MHz}$) two-way talk radio which can generate $147\,\mathrm{mW}$ of output DC power and $24\,\mathrm{V}$ of open voltage was developed to power a conventional MSP430 MCU without the issue of cold start operation. The MCU and trimmable capacitor ICs, which are also powered by the wearable harvester, were utilized to improve the power transfer efficiency during human movement. By introducing novel hybrid GA and clustering matching circuit selection method, the power transfer loss was reduced by the

maximum of $45.6\,\mathrm{mW}$. The harvester was also used to realize a fully autonomous on-body sensor network by utilizing DC and second harmonic signal from the harvester for backscattering communication. The DC power was utilized to power an RF amplifier IC and it enabled a sensing and a data transmission more than $75\,\mathrm{m}$.

Second, a hybrid RF/solar energy harvester module for $2.45\,\mathrm{GHz}$ with an integrated MCU, DCDC boost converter, and transceiver was developed for wireless indoor sensing. The DCDC converter was further improved and realized a power management circuit which has RF sensitivity of $-25\,\mathrm{dBm}$ and can be powered by a solar cell with minimum of $3\,\mathrm{lx}$ light irradiation that is as dark as night was realized. The HF oscillator signal for DC-DC boost conversion can be simultaneously utilized for backscattering modulation realizing a continuous autonomous operation of backscattering tag. Also, a fully inkjet printed organic solar cell, which exhibits 0.2 to $0.25\,\mathrm{V}$ single cell open voltage under the room light condition, was developed.

Finally, a real-time active matching system for near-field power transfer were designed utilizing a genetic algorithm for wearable and in-vivo electronic devices. The active matching system can improve the power transfer efficiency by more than $3.2\,\mathrm{dB}$ with the coil separation distance in the range of $60\,\%$ of coil diameter. The matching circuit design was optimized for a fast moving object by introducing a K-means clustering and the time to select the optimal matching circuit condition was reduced by 16 times from $64\,\mathrm{ms}$ in the previous design.

CHAPTER 1

INTRODUCTION

These days, the desire for a "smart" society that utilizes technologies such as large-scale sensor networks, the Internet of Things (IoT), and smart skins is strengthening. In the coming decades, the number of devices connected to the existing network is expected to grow exponentially. From one estimation, the number of interconnected devices is expected to reach 24 billion by 2020 [1]. However, conventional device architectures have some challenges to support this massive growth of device population in terms of power, cost, communication, and security. In this chapter, existing wireless sensor architectures are briefly discussed to reveal the objective of this research. Following is the summary of existing wireless sensor device architectures based on the complexity of the sensor device.

1.1 Overview of wireless sensor architectures

1.1.1 Wireless sensor node/ active RFID with primary or secondary battery

This conventional approach has the most complex structure in terms device architecture. The device has a transceiver with RF amplifiers, a micro-controller unit (MCU), a power management unit (PMU), an analog to digital converter (ADC), and a direct current (DC) power source. This is a typical device architecture for conventional active radio frequency identifications (RFIDs) and smart sensor devices. Since it has an RF oscillator and amplifiers, the peak power consumption of this type of device is typically high. Although, the average power consumption can be reduced by utilizing duty cycling. The conventional solution of the DC power source is a primary battery. Also, relatively high required voltage for this digital circuit approach causes an issue of "cold-start" of integrated circuits (ICs), which is the high required voltage/power to kick start the operation of the device.

1.1.2 Backscatter radio/passive RFID

Backscatter radios, which only requires low-cost and low-power RF front-ends, communicate with reflection of RF signals instead of radiation without the need of power-hungry RF oscillators, MCU and an ADC in sensing devices. This is a commonly used architecture in passive RFIDs. An integrated oscillator in each tag can change its oscillation frequency depending on the electric characteristics, for example resistance, of a sensing element to change the modulation, which enables the sensing [2]. This approach reduces the cost of each sensing device drastically compared to conventional autonomous sensing devices. However, its use in WSNs has traditionally been limited, since commercial RFID technology only offers ranges of a few tens of meters. Recently, it has been demonstrated that the reading range of RFID tags/backscatter sensors can be extended with additional carrier emitters illuminating sensors with continuous wave (CW) RF signals [3].

1.1.3 Chipless RFID

Chipless technologies provide the most minimalist and lowest cost node paradigm, as their passive operation does not require the use of a power source, nor that of complex and costly active electronics. Nevertheless, the main trade-off-in addition to the limited variety of features that can be integrated in a passive manner lies in their strictly linear response to the impinging interrogation signal, which has traditionally greatly limited their detectability, and bounded their interrogation range under $2\,\mathrm{m}$. Novel approaches have, however, created a wide scope of new possibilities, enabled by the use of high-frequency Van-Atta reflectarray structures. Such a system was first reported in [4], which proposed the fully-printed humidity-sensing tag. The cross-polarizing, Van-Atta, and high frequency properties of the device were demonstrated to provide a reading range in excess of $30\,\mathrm{m}$–more than an order of magnitude improvement compared to the previous state of the art–and multi-device localization and sensing-detection.

Since most wireless sensors utilize active devices, one of the most pressing issues is

the lack of a sustainable power supply that could enable the autonomous operation of these sensors and devices. Conventional autonomous devices heavily rely on primary batteries, which can power the devices for only a certain amount of time. Once the sensor devices use up the stored available energy in their batteries, the batteries need replacement, and the cost of replacing batteries increases significantly as the number of sensor devices in the system increases. To avoid the maintenance cost issue and achieve completely self-sustainable low-cost ubiquitous systems for the IoT, smart cities and wearable devices, research communities have devoted a considerable interest in ambient energy harvesting (EH) and wireless power transfer (WPT) technologies. To maintain operation of the truly autonomous systems, this technology set harnesses energy from ambient power sources such as solar, heat, vibration, and electromagnetic waves using transducers and stores it in energy storage components such as secondary batteries and capacitors [5]–[7]. Among the ambient energy sources, RF energy is a highly attractive energy source because of its almost ubiquitous availability, especially in urban areas, and the low cost and size of transducers [8], [9]. However, compared to the energy density of other energy sources, that of RF energy is typically very low, so RF energy harvesters cannot directly drive devices that require relatively high power and voltage such as micro-controllers, especially from a cold-start condition. Since low energy density also causes low RF-DC conversion efficiency, RF energy harvesting is even more challenging to be practically exploited.

Similarly, emerging technologies such as augmented reality (AR)/ virtual reality (VR) devices and electrical vehicles (EVs)/unmanned aerial vehicles (UAVs), which require relatively high power and repeated battery charging, desperately need an alternative powering method which can eliminate the physical connection with wires to overcome their short operation time and inconvenience of wired charging. To overcome this pressing issue, one of the solution is WPT utilizing electromagnetic coupling technology, which can wirelessly charge these devices. The medical field is one of the most important application areas of this technology. For hygienic purposes, the unique capability of HF waves and microwaves

to transfer power to sealed devices in a contactless/cable-less way is a major advantage. Furthermore, WPT could have a significant impact in health and biomonitoring applications, virtually eliminating the need for painful and infection-prone surgical procedures, which are currently necessary for periodical battery replacement, by wirelessly charging in-vivo implanted electronics. One of the fundamental challenges appears when the Tx-Rx separation is not constant and a receiver is keep moving. The variable charging distance degrades the WPT efficiency and this can be highly problematic when more and more wearable mobile devices, which are expected to be charged wirelessly, are used in the real world.

To overcome the low-energy-density problem in RF energy harvesting and degradation of WPT efficiency for moving objects, researchers have striven in the last several decades to improve the performance of RF energy harvesters and WPT technology. In the process, additive manufacturing technology has emerged as an alternative to conventional fabrication techniques such as etching and milling. Additive manufacturing technology, including inkjet printing, 3D printing, and screen printing, has proven to be a very efficient solution for low-cost RF circuit patterning associated with a high 2D/3D resolution and a variety of available printable materials [10]. In particular, one of the most common methods of printing for both personal and commercial purposes is inkjet-printing technology. On the other hand, in the field of electrical engineering, the inkjet-printing technology enables the easy realization of high-resolution conductive traces that can support the operation of circuits up to the sub-terahertz range on a variety of substrates including flexible materials such as paper, plastic, and liquid crystal polymer (LCP) [11], [12]. In addition to conductive materials, various dielectric materials and semi-conductive materials can be printed using inkjet-printing technology, which allows us to fully print most of the basic circuit components such as capacitors, inductors, antennas, diodes, and so on [13]–[15]. The wide variety of printable materials also allows us to create both transducers and energy storage components for ambient harvesting from most energy sources. Also, the capability of printing of

flexible substrate with arbitrary design enables the fabrication of wearable coils for WPT.

By taking advantage of the fundamental features in additive manufacturing, this study proposes two solutions to the problems of RF energy harvesting. The first solution is to create a wearable RF energy harvester that can be mounted on the human body and that is exposed to relatively high RF energy levels from handheld communication devices. This research suggests a novel concept based on additive manufacturing techniques for a near-field wearable energy harvester along with a printed hybrid energy harvester in integrated sensor platforms. Also, the active matching circuit design technique utilizing heuristic approach, which is a key technology for the efficient charging of wearable electronics, is discussed. Another solution is to combine multiple ambient energy transducers that compensate for the shortcomings of each energy source. In particular, this research proposes the hybridization of RF and solar energy harvesters that both can be fabricated utilizing additive manufacturing technology.

1.2 Research Objective and Thesis Outline

The main objective of this research is to explore the possibility of implementing RF energy harvesting and WPT in real-world systems by utilizing the unique characteristics of additive manufacturing techniques. Nowadays, there are several commercially standardized WPT techniques, but most of them are still in the stage of research and development. Table 1.1 categorizes WPT/EH technologies that can be found in the literature and consumer market based on the operation distance. One of the biggest differences between WPT and ambient RF energy harvesting is the transmitter (Tx) of RF signals. An intentional RF signal source is set for WPT applications and usually there is the freedom of the selection of Tx in terms of operation frequency, gain of Tx antenna and so on within the range of FCC regulation. Unlike WPT, EH utilizes ambient RF signals originally used for mobile communication and broadcasting. Currently, there is no limitations regarding operation frequency of RF energy harvester, so it is possible to utilize broad-band signals

for RF EH. However, the circuit design is usually limited for Rx side of the system.

TABLE 1.1SUMMARY OF DIFFERENT WPT AND EH TECHNOLOGIES

	Near-field	Far-field
Intentional (WPT)	Magnetic Resonant Coupling (MRC) [16], [17] Qi [18] **Chap. 6**	Wireless Identification and Sensing Platform (WISP) [19] Space Solar Power System (SSPS) [20], [21]
Ambient (EH)	**Chap. 4**	Wireless Ambient Radio Power (WARP) [7], [8] Ambient Backscattering Communication (ABC) [22] **Chap. 5**

From the brief analysis above, there is no significant efforts found in literature regarding flexible/wearable near-field RF energy harvester and WPT circuit. This is partially because most of conventional RF energy circuits are fabricated on solid substrates such as FR-4, but additive manufacturing technologies allow easy circuit fabrication on flexible substrates, which are the key enablers of upcoming flexible and wearable electronics, with multi-discipline inks. Therefore, this research reviews the basic of RF EH and WPT in Chap. 2 and that of additive manufacturing in Chap. 3. By taking the advantage of flexibility, the wearable near-field RF energy harvester design, which has numerous unique advantages, is throughly studied in Chap. 4. In addition, this research addresses the cold-start voltage of ICs, which is one of the fundamental difficulties of far-field ambient RF energy harvesting, by introducing a hybrid RF/solar energy harvesting concept, which is discussed in Chap. 5. Finally, this research addresses the design of a real-time active matching circuit to compensate the degradation of WPT efficiency in wearable near-field WPT in Chap. 6, and Chap. 7 concludes.

CHAPTER 2

REVIEW OF WIRELESS POWER TRANSFER/ENERGY HARVESTING TECHNOLOGIES

In this chapter, current efforts in wireless power transfer and energy harvesting technologies from the perspectives of fundamental RF rectifier operation, antenna and matching circuit design, and power/voltage requirements of ICs are reviewed. The idea of wireless power transfer has been around since the emergence of modern electrical technologies. In the 19^{th} century, Nikola Tesla announced the idea of a "World Wireless System" claiming that this system would allow for "the transmission of electric energy without wires" on a global scale as well as point-to-point wireless telecommunications and broadcasting [23]. Tesla first attempted to transmit power without wires at Colorado Springs, CO, USA, in 1899. He built the huge "Tesla coil" under a $30,000 grant provided by Colonel John Jacob Astor. The Tesla coil resonated $300\,\mathrm{kW}$ of energy at $150\,\mathrm{kHz}$ to propagate electromagnetic waves in the surrounding field. According to Tesla, when the RF output of the Tesla coil was unleashed into the mast, $100\,\mathrm{MV}$ of RF potential was produced on the sphere in the Tesla coil. Although, there is no documentation he ever transmitted power beyond relatively short distances, the idea of wireless power transfer has motivated research communities to realize a truly wireless device which not only allows the obvious freedom of movement, but also enables devices to be more compact by removing the necessity of a large battery in a device. Historically speaking, Tesla was decades ahead of his time, but after the late 1950s, a number of developments occurred which revealed that WPT technologies can be realized with a reasonable power transfer efficiency. In the modern research, two major communities, the space solar power system (SSPS) and the RFID, have made significant contributions to realize the wireless powered society that Tesla dreamed of. SSPS is the project to launch solar power in space and deliver the generated power via microwaves over the sky. Researchers in the SSPS community have managed to wirelessly transfer $10\,\mathrm{kW}$ of RF energy over $500\,\mathrm{m}$ away and they plan to launch the first solar satel-

lite in the next 20 years [21]. Also, RFIDs have been already commonly used in our society as public transportation tickets, ID cards, and so on. The importance of this technology is increasing because of the upcoming era of IoTs and WSNs. Associated with the expansion of the use of EM signals for cellular communication and digital TV broadcasting, more and more EM energy is wasted, especially in urban areas. RF energy waste is expected to increase as the number of devices used increases for communication and wireless power transfer. Therefore, ambient RF EH is also getting attention from research community. Similarly, wireless power transfer technologies utilizing near-field coupling are increasing their importance in this society because of people's demands for more comfortable wireless usability of mobile electronics and EVs. After the research of near-field magnetic resonance coupling by Soljacics team at the Massachusetts Institute of Technology in 2007 [16], this area of research is getting more and more attention.

2.1 Fundamental Operation of Rectennas

Throughout the history of RF engineering, energy conversion from RF waves to DC has been a focus of study. The 1960s witnessed the invention of a special type of antenna called the "rectenna," which can convert RF energy to DC. The invention of the rectenna enabled long-distance wireless power transmission. In this section, the fundamental operation of rectenna is reviewed to clarify the challenges in the design of rectennas. The rectenna topology is based on the far-field radiation of EM waves, which is different from EM coupling based near-field WPT, and near-field WPT is more detailedly discussed in Chap. 6.

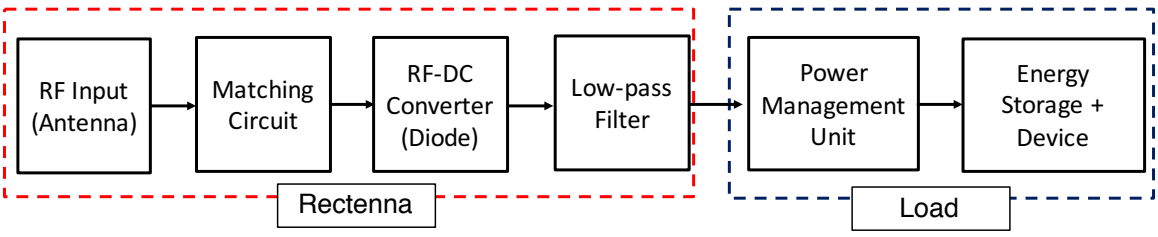

Figure 2.1. Block diagram of rectenna with DC load.

Typically, the rectenna consists of an antenna, a matching circuit, and a diode as depicted in Fig. 2.1. This basic circuit topology can also be applied to ambient RF energy harvesting. The classic PN junction diode commonly used at low frequencies has a relatively large junction capacitance that prevents a PN junction diode from following the fast transition of voltage in RF signals. However, the Schottky barrier, which consists of a metal-semiconductor junction, has much lower junction capacitance that associated with the fast switching speed and low threshold voltage. Since one of the three main components in the rectenna is the diode, the selection of the diode is critical to achieve high RF-DC conversion efficiency. In this section, the fundamental operation of a Schottky diode while rectifying RF signals is discussed.

The Schottky diode can be modeled as a non-linear resistor, with a small-signal I-V relationship expressed as Eq. (2.1), where $\alpha = \frac{q}{nKT}$ and q is the charge of an electron, k is Boltzmann's constant, T is temperature, n is the idealty factor, and I_S is the saturation current. Typically, I_S is between 10^{-6} to 10^{-5} A, and $\alpha = \frac{q}{nKT}$ is approximately $\frac{1}{25\ (mV)}$ for $T = 290\,\mathrm{K}$ (room temperatures). Another important parameter to express the characteristics of a diode is the reverse breakdown voltage (V_r), which represents the voltage when the diode becomes highly conductive while applying negative voltage. Therefore, the I-V curve of a diode can be classified into three regions; breakdown, reverse, and forward as depicted in Fig. 2.2. The reverse voltage region has a very low leakage current in the negative direction of a diode. This very slowly increases as the applied negative voltage goes up, and there is a very sharp hike at the breakdown voltage. On the other hand, when a positive voltage is applied to a diode, forward direction current starts exponentially increasing after the threshold voltage of V_{th}. Table 2.1 summarizes major parameters of commonly used diodes for WPT and EH applications.

$$I(V) = I_S(e^{\alpha V} - 1) \tag{2.1}$$

The rectification process can be explained in following manner. For a simplification,

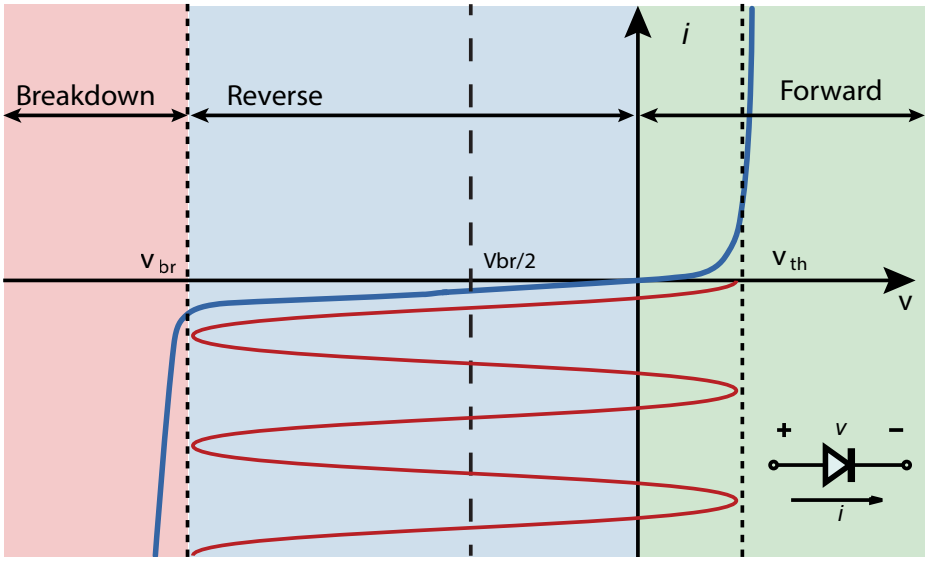

Figure 2.2. IV curve of a typical diode model.

TABLE 2.1SUMMARY OF MAJOR DIODE PARAMETERS

Diode	V_{th} (V)	V_{br} (V)	I_s (µA)	N	R_s (Ω)	C_j (pF)
SMS7630	0.18	1	5	1.05	20	0.14
HSMS-282	0.34	15	0.022	1.08	6.0	0.7
HSMS-285	0.25	3.8	3	1.06	25	0.18
HSMS-286	0.35	7.0	0.05	1.08	6.0	0.18

harmonics generated during the rectification process are smoothed with a capacitor. Assume a CW signal (Eq. (2.2)), where $V_a > V_{th}$), is applied to a diode which is connected to a load as depicted in Fig. 2.3. When the positive voltage of CW signal exceeds the threshold voltage of a diode, a positive DC potential (V_{DC}) is generated and charges a capacitor. While $V_t + V_{DC} > V_{th}$, the DC potential keeps increasing and self-biases a diode until V_t reaches its maximum value. If $0 < V_{DC} < \frac{V_{br}}{2}$, the circuit reaches steady state. However, if the amplitude of the applied CW signal is too high making $V_{DC} > \frac{V_{br}}{2}$, the DC potential can no longer increase because a voltage above V_{br} causes high negative current flow and some of charges flow directly to the ground.

$$V_t = V_a \, cos(\omega_0 t) \tag{2.2}$$

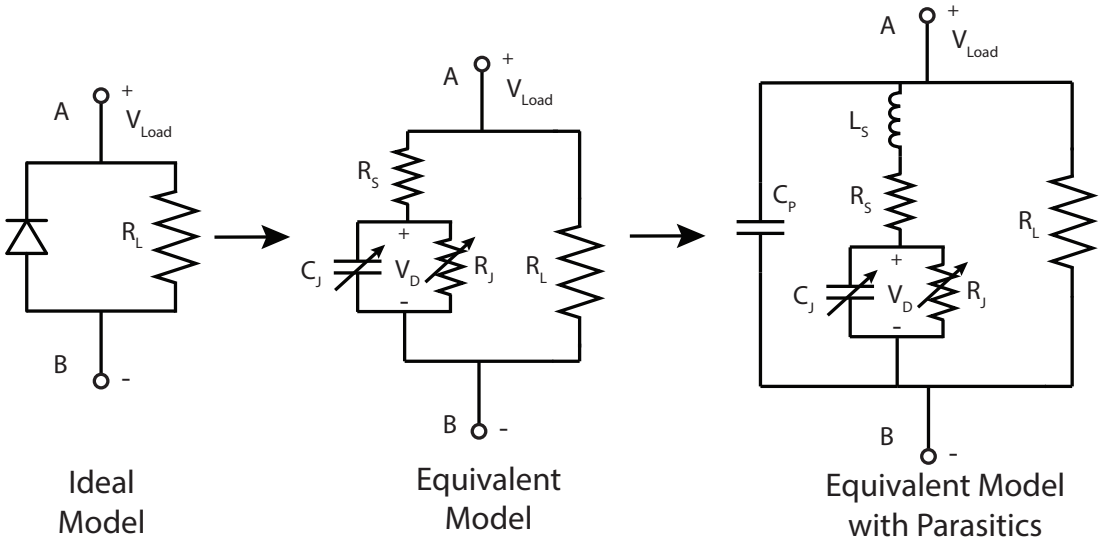

Figure 2.3. Ideal and non-ideal diode equivalent circuit model.

Therefore the largest DC voltage a diode can generate is

$$V_{DC(max)} = V_{br} \tag{2.3}$$

and

$$P_{DC(max)} = \frac{V_{DC(max)}^2}{R_L} = \frac{V_{br}^2}{4R_L}. \tag{2.4}$$

From this analysis, V_{br} and V_{th} from a datasheet can be used to select a diode depending on the expected RF input power level. For example, HSMS-282 in table 2.1, which has high breakdown voltage is more suitable for high RF input power application, and SMS7630, which has low threshold voltage and low breakdown voltage, is appropriate for low input power application.

2.2 Losses in RF Rectification

In the previous section, it was assumed that only the fundamental CW and DC existed in the analysis. In reality, there are a variety of loss mechanisms associated with the rectification process. An ideal diode model is equivalently expressed as a combination of a series resistance (R_S) and a parallel variable resistance (R_J) and a parallel variable capacitance (C_J) as depicted in Fig. 2.3. R_J and C_J are also known as a junction resistor and a junction capacitor, respectively, and their values vary depending on the applied voltage. In reality, there are parasitic inductance (L_S) and capacitance (C_P) associated with the package of actual diode. The loss factors can be generally classified into dissipative and non-dissipative losses. The dissipative losses associated with the non-linearity of a diode can be further separated to three; junction voltage (V_J) effect, breakdown voltage (V_{br}) effect, and harmonics effect, as depicted in Fig. 2.4 [24]. The non-dissipative loss is caused by a mismatch between a signal source and a rectifier. This impedance mismatch causes a reflection of incident signal reducing the RF power actually transferred to a diode. Following part of section discusses each loss factor in detail.

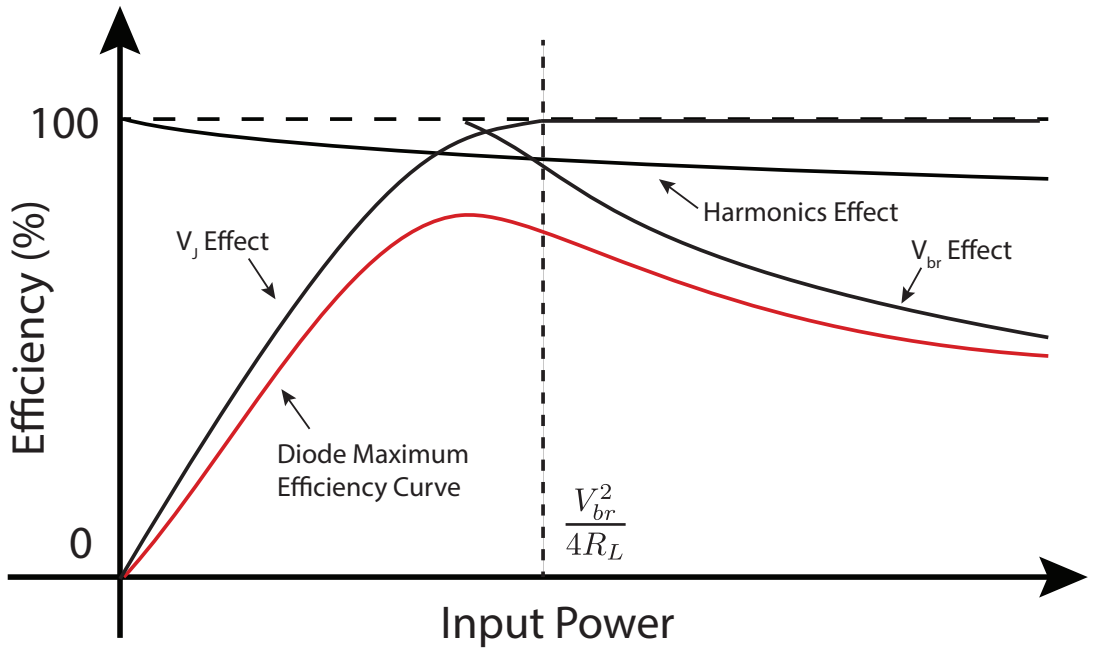

Figure 2.4. General relationship between RF-DC conversion efficiency and input power with the loss factors.

2.2.1 Junction and Breakdown Voltage Effects

As briefly discussed in Sec. 2.1, the junction and the breakdown voltage are major losses in a diode during the rectification process. The junction voltage is the voltage drop caused by the junction resistance (R_J) variation. When input power is low, the effect of junction voltage is the major loss factor. Unless sufficient power is applied to a diode, there is not enough energy to go over the sub-threshold region in the diode I-V curve. Also, in reality, the series resistance (R_S) is not negligible and this limits the maximum efficiency of RF-DC conversion. On the other hand, the breakdown voltage effect dominates the loss in a diode when input power is high. This is because the reverse direction leakage increases as the input power increases. In the steady state, the bias voltage heavily depends on the value of load resistance. Therefore, the selection of load resistance value is important to maximize the RF-DC conversion efficiency.

2.2.2 Harmonics Effects

During the rectification process, higher order harmonic components, which are another major loss in a diode, are generated because of non-linear behavior of a diode. The parasitic components can be eliminated by introducing a proper matching circuit, so the following analysis uses the diode equivalent circuit model without parasitics. If applied voltage is expressed as

$$V = V_0 + v, \tag{2.5}$$

where V_0 is a DC bias voltage and v is a small AC signal voltage. Then, Eq. (2.5) can be expanded in a Taylor series about V_0 as follows.

$$I(V) = I_0 + i \approx I_0 + v \left.\frac{dI}{dV}\right|_{V_0} + \frac{1}{2!}v^2 \left.\frac{d^2I}{dV^2}\right|_{V_0} + \frac{1}{3!}v^3 \left.\frac{d^3I}{dV^3}\right|_{V_0} + \cdots, \tag{2.6}$$

where $I_0 = I(V_0)$ is the DC bias current and i is AC current. The first derivative can be expressed as

$$\left.\frac{dI}{dV}\right|_{V_0} = \alpha I_s e^{\alpha V_0} = \alpha(I_0 + I_S) = G_d = \frac{1}{R_J}, \tag{2.7}$$

which defines $G_d = \frac{1}{R_J}$, which is called the dynamic conductance of the diode. The second derivative is

$$\left.\frac{d^2I}{dV^2}\right|_{V_0} = \left.\frac{dG_d}{dV}\right|_{V_0} = \alpha^2 I_s e^{\alpha V_0} = \alpha^2(I_0 + I_S) = \alpha G_d = G'_d. \tag{2.8}$$

Therefore, Eq. (2.6) can be rewritten as follows:

$$I(V) = I_0 + i \approx I_0 + vG_d + \frac{v^2}{2}G'_d + \frac{v^3}{6}G''_d + \cdots. \tag{2.9}$$

The first three term approximation for the diode current in Eq. (2.9) is called the small-

signal approximation, and is practically adequate for the explanation of diode current. If a diode is excited with a CW in Eq. (2.2), the diode current is

$$\begin{aligned} I(V) &= I_0 + V_a G_d cos(\omega_0 t) + \frac{V_a^2}{2} G_d' cos(\omega_0 t) \\ &= I_0 + \frac{V_a^2}{4} G_d + V_a G_d cos(\omega_0 t) + \frac{V_a^2}{4} G_d' cos(2\omega_0 t). \end{aligned} \tag{2.10}$$

In Eq. (2.10), I_0 is the bias current and $\frac{V_a^2}{4} G_d$ is the DC rectified current. Similarly, $V_a G_d cos(\omega_0 t)$ and $\frac{V_a^2}{4} G_d' cos(2\omega_0 t)$ are first and second harmonics, respectively. In reality, a diode generates higher order harmonics (more than 3rd), but they are typically negligibly smaller than the first and second harmonics. During the rectification, it is important to maximize the voltage difference between the anode and cathode of a diode, especially when input RF power is low. Therefore, harmonics are suppressed with a low-pass filter as depicted in Fig. 2.1 and usually only DC components travel to a load resistance. However, some applications actually utilize the second harmonic component for sensing and this type of circuit is called a frequency doubler. The further application of the second harmonic during rectification process is discussed in Chap. 4.

2.2.3 Impedance Mismatch

Impedance mismatch is another loss factor in a rectifier. Different from previously discussed losses in a diode, this loss is caused by a reflection between a signal source and a rectifier circuit because of impedance mismatch. This reflection reduces RF energy actually used for the rectification. Unlike the impedance matching of a passive RF circuit, the impedance matching of RF rectifier is very difficult because of the non-linearity of a diode. The impedance of a rectifier varies depending on the applied voltage, the load resistance value, and frequency of the incident signal. Especially in an wearable energy harvester circuit, which has a varying receiver antenna impedance value, to power real ICs, these three parameters vary drastically, making the impedance matching circuit design with a passive

circuit even more difficult. Therefore, use of an active matching circuit to compensate the impedance variation in the circuit is further discussed in Chap. 4. Also, as depicted in Fig. 2.3, a real diode chip has parasitic inductance (L_S) and capacitance (C_P) associated with the packaging and the lead of a bare die causing further impedance mismatch especially at high frequency when the effective impedance value gets larger. However, these parasitic components are passive circuit elements and their impedance value only depends on the frequency. Therefore, they can be eliminated by designing a matching circuit properly.

2.2.4 Other Losses in RF Circuits

Since an RF rectifier uses RF transmission lines for matching circuits and filters, there are losses associated with them. In general, the losses in RF transmission lines are classified into conductor loss, dielectric loss, and radiation loss. In rectifiers for VHF (30 to $300\,\mathrm{MHz}$) and UHF (0.3 to $3\,\mathrm{GHz}$) rectifiers fabricated utilizing standard RF substrates such as FR-4 with copper cladding, conductor loss and dielectric loss are typically negligibly small. These losses increase as the operation frequency increases especially in a material which has low conductivity and high loss tangent. The material properties of substrates for inkjet-/3D- printing are further described in Chap. 3. The radiation loss depends on the geometry of the circuit pattern, but it is also relatively small for transmission lines such as a microstrip line and a CPW. In general, for relatively low frequency rectifiers (below $1\,\mathrm{GHz}$), lumped components are used for the matching circuit and the low-pass filter because of the size limitation. Obviously, in a real circuit, these lumped components are non-ideal lumped elements which have resistive loss. Also, these lumped components also have parasitic components causing impedance mismatch if they are not taken into account. Therefore, during a rectifier design process utilizing a simulator software, non-ideal lumped component models and measured S-parameters from vendors are utilized to improve the accuracy of simulation.

When all these losses are considered, the RF input power (P_{in}) from a signal source can be expressed as following:

$$P_{in} = P_{out(DC)} + P_{DL} + P_{RL} = \frac{V_{out(DC)}^2}{R_L} + P_{DL} + P_{RL}, \tag{2.11}$$

where $P_{out(DC)}$ is DC output power, $V_{out(DC)}$ is DC output voltage, P_{DL} is dissipative loss, and P_{RL} is return loss. The most commonly used definition of RF-DC conversion efficiency (η_{RFDC}) is

$$\eta_{RFDC} = \frac{P_{out(DC)}}{P_{in}}. \tag{2.12}$$

If only the power conversion is considered, ignoring the return loss caused by the impedance mismatch, the power conversion efficiency (η_{PC}) is expressed as,

$$\eta_{PC} = \frac{P_{out(DC)}}{P_{in} - P_{RL}}. \tag{2.13}$$

In the literature, the analytical and experimental selection of optimal diodes depends on the target operation frequency and the input power level [25]–[27]. In terms of energy conversion efficiency, rectifiers for UHF band have achieved [28], [29] more than $80\,\%$ of conversion efficiency with an optimal load and input RF power above $20\,\mathrm{dBm}$. This is much higher than the other energy transducers for ambient energy harvesting. For example, the highest conversion efficiency of a solar cell, which is commonly used for ambient energy harvesting, does not exceed more than $50\,\%$. Therefore, a near-field RF EH, which can take advantage of this high RF-DC conversion efficiency, is further studied in Chap. 4. Since the available ambient RF energy density in the far-field is very low (below $1\,\mathrm{mW}$), diodes with a low threshold voltage and fast switching speed are preferable for ambient energy harvesting. From this perspective, Schottky diodes have been mainly used for RF energy harvesting. Off-the-shelf Schottky diodes are reaching the maximum theoretical RF-DC conversion efficiency because of inevitable series resistance, junction capacitance,

and high junction resistance, especially with low RF input power [25]. Therefore, several studies have recently applied special types of diodes such as the backward tunnel (Esaki) diodes and the metal-insulator-metal (MIM) diodes to rectify extremely low RF input power of below $1\,\mu W$ [25], [30].

2.3 Rectifier Topologies

In the previous sections, the rectification process of a single diode topology is discussed. However, there are several rectifier topologies, which have different characteristics, available in the literature to satisfy requirements as a power source in a system. Following sections summarize the characteristics of six major types of rectifier topologies; series, shunt, Cockcroft-Walton, modified Cockcroft-Walton, and Dickson voltage multiplier as depicted in Fig. 2.5 and Fig. 2.6. Rectifiers in Fig. 2.5 are single diode topologies, and Fig. 2.6 depicts voltage multiplier topologies, which have multiple diodes to generate high output voltage.

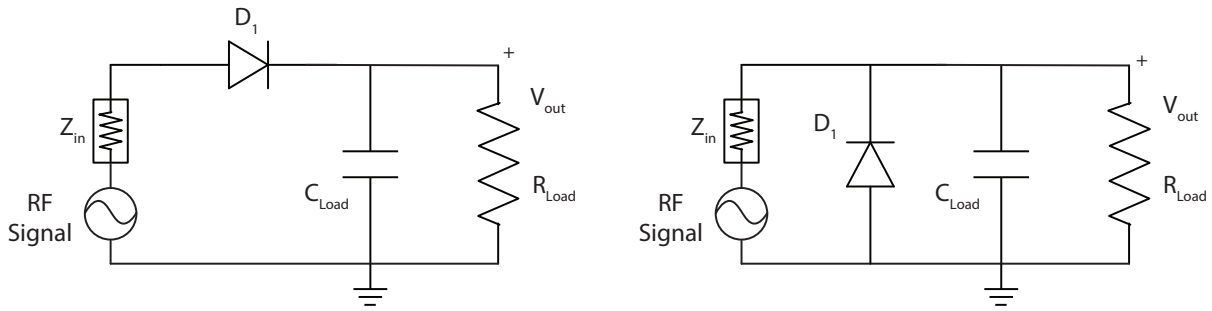

Figure 2.5. (a) Series rectifier. and (b) Shunt rectifier.

2.3.1 Series and Shunt Rectifiers

For maximum conversion efficiency, single-diode rectifier topologies, of a series type or a shunt type, are utilized because the dissipative loss, which is the limiting factor of

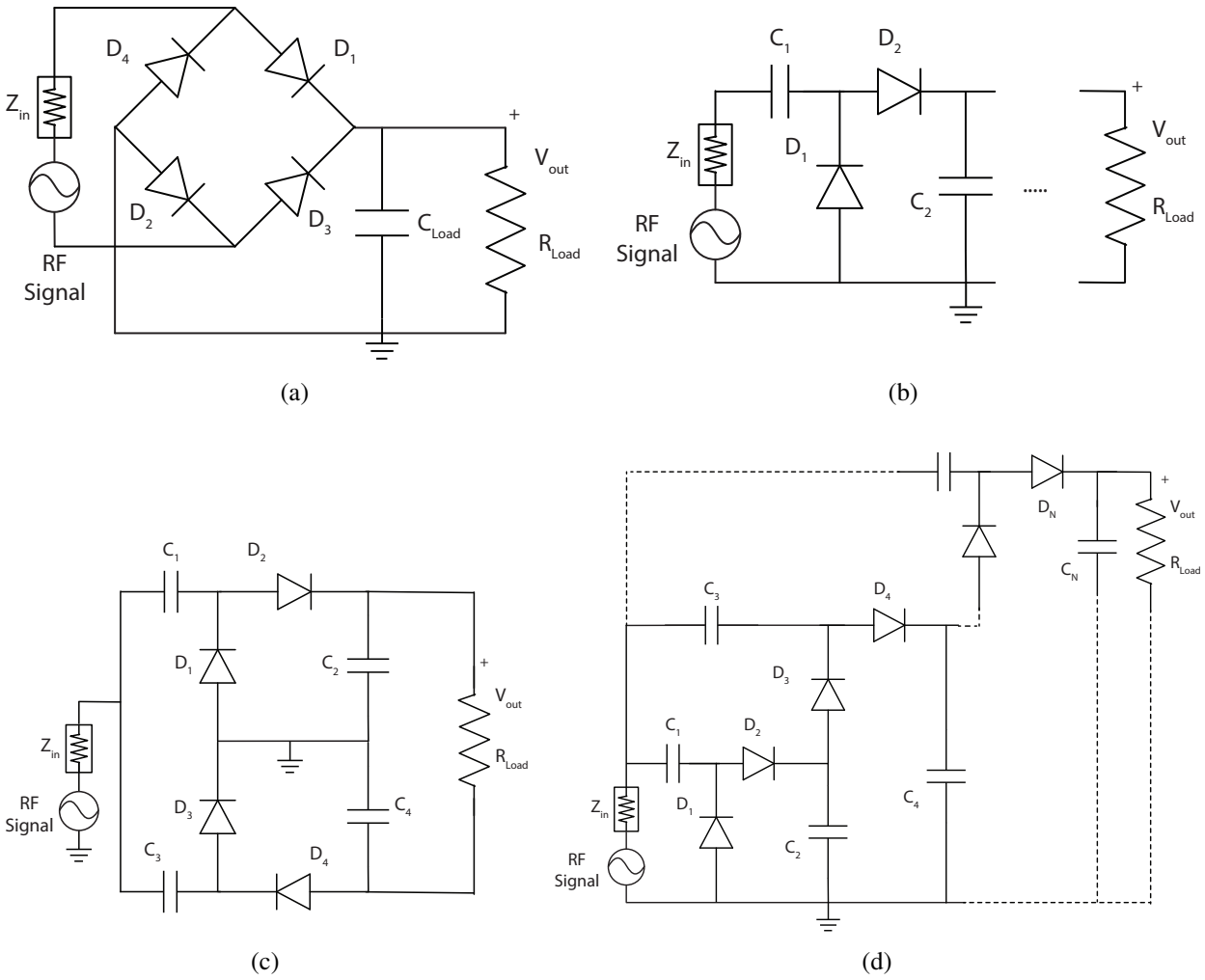

Figure 2.6. (a) Full-wave rectifier, (b) Cockcroft-Walton, (c) Modified Cockcroft-Walton, and (d) Dickson voltage multiplier.

maximum conversion efficiency can be minimized. Also, these topologies can reduce the cost and size of a rectifier. The principle of rectification is as described above. These single diode configurations are suitable for high power long range WPT application, which usually has plenty of RF input power that can sufficiently bias a diode to generate a high voltage. Since these are the most efficient RF-DC converter topologies, they are used for ultra-low-power (below $10\,\mu\mathrm{W}$) RF energy harvesting applications with a combination of a low-power high efficiency DC-DC converter. The comparison of RF-DC converter circuit topologies for ultra-low-power applications are discussed in Chap. 5.

2.3.2 Full-wave Rectifier

Full-wave rectifier topology is composed of a combination of four diodes as depicted in Fig. 2.6 (a). At low frequency, this topology can rectify both positive and negative applied voltage, and theoretically, the AC-DC conversion efficiency is higher than that of a half-wave rectifier. This is not always at RF frequency especially with low input power because of high dissipative loss and phase shift associated with the junction capacitance and parasitics [31]. However, this topology is useful as a frequency doubler, theoretically eliminating the odd-order harmonics leaving even-order harmonics. This is further discussed in Chap. 4.

2.3.3 Voltage Multipliers

A voltage multiplier is another category of rectifiers, which is composed of a cascade of unit-cells to generate relatively high voltage to power ICs with lower input power than a single diode rectifier. This is commonly used in RFID chips making it possible for the ICs to wake up and transmit signal from low RF input power. Well-known voltage multiplier circuits are the Cockcroft-Walton and Dickson charge pump shown in Fig. 2.6 (b) and (d). By cascading more than one single-stage voltage multiplier, the rectifier can step up the voltage by theoretically the multiple of the number of stages. However, especially at high frequency, stage capacitors must be sufficiently large to prevent leakage current, and because of parasitic impedance of lumped elements causing self-resonance, capacitance values cannot be arbitrary large. This makes impractical to use this topology above UHF band. Similarly, voltage multiplier topologies increase dissipative loss associated with the use of multiple diodes especially when input power is low, and this prevents the output voltage to be arbitrary high. One thing which is worth noticing is that the optimal output DC resistance value tends to increases as the number of stage increases. Therefore, if the output load has a known specific impedance value, the number of multiplier stage can be adjusted to shift the operation point. Note that, the peak RF-DC conversion efficiency degrades as

the number of stages increases. Another voltage multiplier topology, which is worth mentioning, is modified Cockcroft-Walton topology. This topology has a symmetrical structure with a multiple of four diodes in parallel compared to a regular Cockcroft-Walton charge pump. This causes a smaller input impedance, and this is useful for antenna matching. Furthermore, the symmetry helps to reduce the reflected harmonic content generated by the diode non-linearity.

2.4 Other Rectenna Design Aspects for Ambient RF Energy Harvesting/wireless Power Transfer

In previous sections, the operation principle and different topologies of a rectifier in a rectenna were discussed to design a high efficiency rectenna. In this section, some other rectenna design aspects to increase available RF input power and improve power conversion efficiency are discussed.

2.4.1 Wide-Band and High Gain Antennas for High RF Input Power

Since the ambient RF energy harvesting, unlike other wireless communication devices, scavenges RF energy generated from surrounding environmental RF energy sources, no legal operation frequency restriction applies. Therefore, one of the strategies to maximize available RF input power is to use multi-band frequencies by introducing an ultra wide band (UWB) antenna and a wide band matching circuit topology in the rectenna to maximize the aggregated input RF power [8], [32], [33]. However, UWB antennas require a wide band matching circuit for an RF-DC conversion circuit, causing relatively low return loss which decreases RF-DC conversion efficiency. To avoid this, Pinuela et al. reported a DC combination from multiple rectennas where each operates at different operation frequency [9], although, this implies the system requires the design of multiple rectennas and the physical size of the system enlarges as the number of bands used in the system increases. Another strategy is to introduce a directive antenna that has a high gain for cases that harvested

from a source whose direction is well known [34], [35], but this type of antenna tends to feature a narrow beamwidth and requires sensitive angular alignment to realize maximum performance. Also, the directive antennas are usually implemented in array topologies and reflectors, commonly with large physical dimensions. Therefore, the antenna design must be modified depending on size limitations, required power in a load, available RF signal frequencies and so on.

2.4.2 Wave-form Optimization to Improve Power Conversion Efficiency

In some situations, even for ambient RF energy harvesting, we can use modulated RF signals instead of CW to realize a higher RF-DC conversion efficiency and lower required RF power to activate the device. One example is to use multiple frequency signals for pulse shaping, which creates much higher peak voltage with the same average power per time as the CW signals, effectively resulting in higher efficiency of RF-DC conversion [36].

2.5 Friis Transmission Equation and Available Ambient RF Power

In most cases of ambient far-field RF energy, however, the energy density is low and the typical RF input power is below $100\,\mu\mathrm{W}$. Therefore, despite the engineering efforts to improve the RF-DC conversion efficiency, the output load voltage of a rectifier is often lower than the operation threshold voltage of a device connected as the DC load of the rectifier, thus, the device cannot be powered. For example, a typical transistor base-source voltage requires at least $0.5\,\mathrm{V}$, for switching operation, whereas typical voltages from the rectifier are below $0.3\,\mathrm{V}$. In free space, the available RF power from a receiver antenna can be theoretically calculated from the Friis transmission equation shown in Eq. (2.14) where P_r and P_t are the input power of the receiving and the transmitter antenna, respectively, G_t and G_r the antenna gains λ the wavelength, and R is the distance between the antennas. In decibel scale, relationship between the transmitted power and the received power is expressed as Eq. (2.15), where f is frequency and c is the speed of light. If the gain of the transmitter

and the receiver antenna and operation frequency are fixed, the received power decreases quadratically as the distance from the transmitter and the receiver increases. Fig. 2.7 depicts a general relationship between distance and path loss in VHF and UHF band. This is with respect of Therefore, as the minimum required power for a power management circuit increases, the operation distance of the RF harvester system decreases in proportion to the square of the required power increase. To overcome this low output voltage issue, voltage multiplier topologies are utilized [37]. However, because the operation frequency increases and the input power decreases, the voltage multiplier cannot generate arbitrary high voltage in a UHF far-field ambient RF EH. Generally, because of inevitable loss of energy in the diode, the RF-DC conversion efficiency decreases as the number of voltage multiplier stages increases. Also, to achieve high output voltage, the charge tank capacitor connected to the output of the voltage multiplier must be isolated from the DC load during charging, which implies that an external switching device is required.

$$\frac{P_r}{P_t} = G_t G_r (\frac{\lambda}{4\pi R})^2 \tag{2.14}$$

$$P_r = P_t + G_t + G_r - 20log_{10}(R) - 20log_{10}(f) - 20log_{10}(\frac{4\pi}{c}) \tag{2.15}$$

	Distance (m)			
Frequency (MHz)	1	10	100	1000
30	2 dB	22 dB	42 dB	62dB
300	22 dB	42 dB	62 dB	82 dB
3000	42 dB	62 dB	82 dB	102dB

VHF

UHF

Good

Moderatee

Not good

* If input power is 30 dBm and Gt & Gr are 0 dB

Figure 2.7. General relationship between distance and path loss in VHF an UHF band.

2.6 Power Management Circuit

In order to overcome the challenge of low RF input power, a power management circuit, which reduces the power consumption of a circuit by duty cycling, adjusting output voltage, and optimizing a battery/capacitor charging, is typically introduced in a system.

2.6.1 Duty Cycling

A duty cycling is one of the most commonly used techniques to reduce the average power consumption of a system. Most of MCUs have a multiple low power modes (LPMs), which have different power consumption depending on the function and clock frequency, and "sleep" while power hungry computation is not necessary. For example, one of the most commonly used low power MCU, the MSP430 Texas Instruments, consumes $390\,\mu\mathrm{A}$ at $3\,\mathrm{V}$ while in active mode with a $1\,\mathrm{MHz}$ clock, but it consumes $0.1\,\mu\mathrm{A}$ while LPM4, which is the lowest power consumption operation mode. The active mode operation time is usually in the order of millisecond to minimize the energy consumption. This is a digital approach to reduce the power consumption of the device, but not all sensor devices have an integrated MCU. Therefore, as an analog approach, an ultra-low power timer IC can be used. Actually, the power consumption of some analog low-power timer ICs are lower than that of a digital MCU in LPM. For example, the Texas Instruments TPL5010, consumes $0.035\,\mu\mathrm{A}$ at $2.5\,\mathrm{V}$, which is more than three times lower power consumption than the lowest power consumption of the MCU LPM4. A timer is an essential function to realize a duty cycling, and the total power consumption of the system cannot be lower than that. However, a power consumption below $100\,\mathrm{nW}$ is a reasonably low power which can be provided by ambient RF energy sources. This discussion is based on the performance of off-the-shelf ICs, but actually, in the literature, much low power required oscillators (timers) are reported in the solid-state circuit community. For example, Bandyopadhyay et al. have reported a power management IC which requires only $544\,\mathrm{pW}$ of power [38]. The issue

is the relatively high required voltage to drive these ICs. RF energy harvesters, even with a multi-stage voltage multiplier, typically cannot generate more than $1\,\mathrm{V}$ of output power with RF input power below $10\,\mu\mathrm{W} = -20\,\mathrm{dBm}$. Therefore, the use of a DC-DC boost converter is considered.

2.6.2 DC-DC Boost Converter

Another way to decrease the required RF power for harvesting is the integration of a DC-DC boost converters in a system [39]. The simplest form of DC-DC converter can be achieved with a combination of oscillators, a transistor switch, a diode, and an inductor. The principle of creating a high voltage from DC bias is basically following two steps; on and off, repeatedly. The current flow while in the on and off states is depicted in Fig. 2.8.

1. When the switch is closed, current flows through the inductor and a switch and the inductor stores some energy by generating a magnetic field. If the switch stays on and current keeps flowing, the magnetic field saturates at steady state.

2. After the magnetic field in the inductor reaches a steady state, when the switch is opened, current will be reduced as the impedance gets high. The magnetic field previously created will decrease to maintain the current towards the load. As a result, two sources (DC bias and the inductor) will be in series causing a higher voltage than the voltage of original DC bias to charge the capacitor through the diode D_1.

3. The switch turns on again to repeat the process again. Since the diode prevents the current flow from the C_{load} to a switch, the voltage of the charged capacitor remains high. The maximum voltage depends mostly on the switching frequency and the inductance value.

In a practical circuit, a MOSFET is used as a switch. The gate terminal of the FET is triggered by the control signal from an oscillator. The selection of each component and of the oscillation frequency is very important to maximize DC-DC conversion efficiency

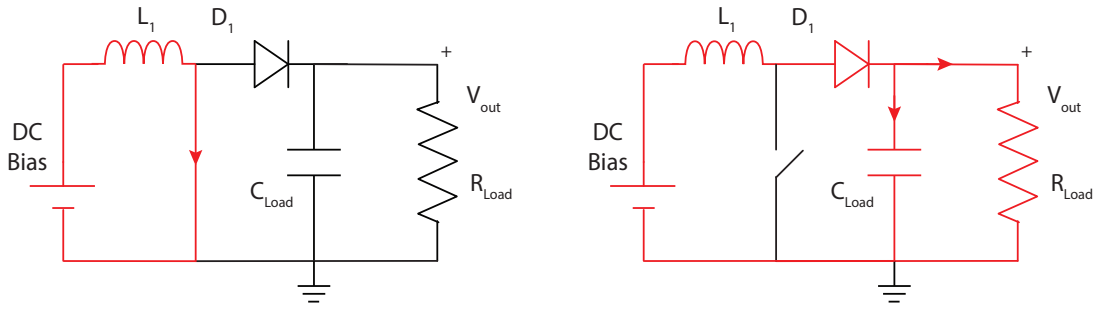

Figure 2.8. DC-DC converter circuit while a switch is (a) on and (b) off state.

and output voltage. The aggregated power loss (P_{loss}) in the circuit is the summation of the control (P_{ctrl}), conduction (P_{cond}), switching (P_{sw}), and leakage (P_{leak}) losses [39]. The control loss (P_{ctrl}), which is the minimum required power to operate the system, is associated with the power consumption of the timer and the oscillator ICs. The conduction loss is mainly caused by the series resistance of an inductor. High inductance can store more energy while charging and generate higher voltage. However, higher inductance value generally means larger number of turns causing a high series resistance value that increases the conduction loss. In addition, it takes more time to charge the high inductance and the optimal oscillation frequency decreases, reducing control loss. Therefore, the inductance and the oscillation frequency need to be selected carefully depending on the required output voltage and supplied DC voltage. The switching loss is caused by the series resistance of the transistor and the diode while conducting. Also, the diode causes a few hundred mV of voltage drop involving additional loss. Therefore, a transistor and a diode with low series resistance with low threshold voltage are preferred. Finally, the high output capacitor voltage negatively biases the diode while the transistor is on causing leakage current which is considered as leakage loss. The leakage loss increases as the output capacitance voltage increases. It heavily depends on the characteristics of a diode, but a diode which has low threshold voltage tends to have high leakage current, so there is also a trade off between switching loss and leakage loss. As a summary, available DC power from the DC-DC

converter is expressed as

$$P_{av} = P_{RFDC} - P_{loss}, \tag{2.16}$$

where P_{RFDC} is the average power of the RF-DC conversion circuit. With the help of DC-DC boost converters, output voltage values of more than $1\,\mathrm{V}$ can be generated from input power in the order of few $\mu\mathrm{W}$. Carlson et al. [40] reported a DC-DC boost converter which generates an output voltage of $1\,\mathrm{V}$ from an input voltage as low as $20\,\mathrm{mV}$ with a power consumption of $1.6\,\mu\mathrm{W}$. However, the voltage of the oscillator requires at least $0.6\,\mathrm{V}$ of start-up voltage in a capacitor to kickoff the operation of oscillators in its circuit. Another example is a self-powered DC-DC converter reported by Adami [41], which can generate an output voltage of $1\,\mathrm{V}$ from an input voltage close to $100\,\mathrm{mV}$ without any external power supply, but it requires at least $10\,\mu\mathrm{W}$ of input DC power. Practically, the minimum input RF power requirement increases to $30\,\mu\mathrm{W}$ for these DC-DC converters to realize a reasonably high output voltage of $1\,\mathrm{V}$ by taking into account the RF-DC conversion efficiency of the harvester. Gudan et al. [42], [43] reported an autonomous RF energy harvester which can operate with input RF power of $8\,\mu\mathrm{W}$ by combining a self-powered DC-DC boost converter and a low-voltage-required high efficiency DC-DC boost converter. However, these circuits still require a relatively high voltage at the very beginning of the DC-DC boost conversion cycle to reach a steady state. This dilemma is called "cold-start", which is also well known in the initial operation of digital MCUs.

2.6.3 Maximum Power Tracking and Battery Charging

Finally, after being captured, precious energy needs to be stored in energy storage devices such as a battery and a super capacitor to prepare for a much power hungry active operation. The equivalent DC resistance value of energy storage devices tend to vary significantly during their charging process. As previously mentioned, the RF-DC conversion efficiency of a rectifier heavily depends on the impedance of a load. Therefore, the huge

variation of load impedance value causes the degradation of RF-DC conversion efficiency. To solve this issue, we consider a maximum power tracking circuit, which can maximize the output power from the transducer without the effect of load variation. There are several different types of maximum power tracking circuits; a DC-DC converter is typically used for low power applications [39], [44], [45].

CHAPTER 3

REVIEW OF ADDITIVE MANUFACTURING TECHNOLOGIES

In the history of RF circuit fabrication, including RF ICs, passive components, antennas and PCBs, conventional fabrication processes include both additive and subtractive processes to create a 2D/3D structure. Depending on many different factors, such as scale, material, electrical/mechanical property requirement, and cost, the combination of a variety of fabrication processes, for example, mechanical milling, laser ablation, photolithography, PVD/CVD, spin-coating, and so on, is selectively used. However, these processes also produce toxic chemical/mechanical wastes and the cost of fabrication increases as the process of fabrication becomes more complicated.

Additive manufacturing technologies, including inkjet printing, 3D printing, and screen printing are becoming increasingly popular in industry because of their environmentally friendly and low-cost fabrication-process features. These emerging fabrication techniques can significantly decrease the number of fabrication steps, including the etching processes, and drastically improve the fabrication efficiency and scalability. The development of nanoparticle inks made of various materials such as metals, carbon-based nano-structures, polymers, and semiconducting materials, have further enhanced the capabilities of inkjet-printing technology. One of the fundamental advantages of inkjet printing is the capability of fabricating circuits on low-cost flexible substrates such as paper, Kapton, and LCP. The usage of inkjet printing is not only directly depositing inks, but also printing of copper catalyst inks for electroplating that can create robust conductive traces [46]. In addition, the wide variety of printable materials allows the easy realization of most typical passive components in the RF circuits such as capacitors, inductors, circuit traces including antennas, and even substrates, utilizing printing technology [12]–[14], [47]. Recently, Sani et al. have reported that diodes for RF rectification can be fabricated with a combination of printing technologies [15]. Furthermore, transducers for many energy sources [48]–[51], energy storage components such as supercapacitors and batteries [52], [53], and sensors, [54],

which are fundamental components of the autonomous sensor systems, can be also fabricated using additive manufacturing, implying the potential of fully additively-manufactured autonomous sensor platforms harvesting multiple energy sources.

In this section, two major additive manufacturing technologies of ink- and 3D- printing are reviewed and the potential applications of these techniques for ambient energy harvesting and energy storage along with the electrical property characterization methods of printed materials are discussed.

3.1 Inkjet-printing Technology

After the emergence of a printing press invented by Johannes Gutenberg around 1440 in Germany, the basic principle of conventional printing have remained the same for hundreds of years. Usually, this process involves the pattern transfer form the master pattern to the paper or other substrate through direct contact of liquid or semi-liquid ink. In contrast, the inkjet printer, which is now commonly used in the modern home and office, works on a fundamentally different operation principle. A printer of this type generates each small droplet of ink, typically 10 to $100\,\mu\mathrm{m}$ in diameter, and deposits them under the digital control enabling the patterning of arbitrary 2D images on a substrate. In addition, by printing a multi-layer of material repeatedly, it is possible to deposit a relatively thick material to create 2.5D objects. There are inkjet printers based on several different jetting system such as continuous jetting and different droplet formulation mechanism such as thermal inkjet, but in this research, one of the most commonly utilized piezoelectric DOD inkjet printing, adopted for Fujifilm Dimatix DMP-2850, is mainly discussed.

3.1.1 Operation of Piezoelectric DOD

Drop ejection using piezoelectric actuators was first reported in 1970s [55]. Piezoelectric-based printing head are commonly used in home and office inkjet printers and it has predominated in those print-heads developed for industrial applications as well. The piezoelec-

tric effect is the ability of certain types of materials to generate an electric field in response to mechanical strain. This effect actually happens in reverse order meaning the applied electric field changes the shape of piezoelectric material. One of the most commonly utilized piezoelectric material for inkjet printing is lead zirconate titanate (PZT) which is a ceramic material that exhibits a strong piezoelectric effect. Hence the PZT piezoelectric effect is anisotropic, and the material will change shape in a way which depends on the relative orientation of the applied field to the poling direction. If a field is applied in the same direction as the poling, the material will expand along that direction and contract in orthogonal direction and vise versa. By utilizing this characteristic, negative and positive voltage is sequentially applied to "fill" and "eject" the ink from a ink reservoir as depicted in Fig. 3.1.

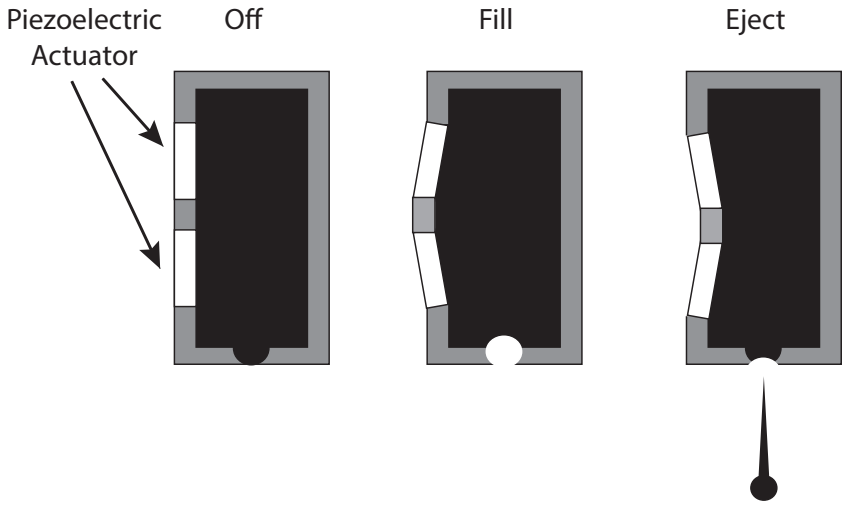

Figure 3.1. Phase of piezoelectric actuator movement while jetting a droplet.

3.1.2 Surface Tension and Viscosity for Droplet Formulating and Wetting

Surface tension and viscosity are two important physical properties that determine the behavior of jetting and droplet formation. Surface tension is the elastic tendency of a fluid surface which makes it acquire the least surface area possible. Therefore, if there is no

influence of external forces such as electrostatic or aerodynamic forces, a free liquid drop forms a spherical shape. If the liquid is in contact with a solid surface, then the equilibrium shape of the drop becomes a spherical cap because of the interference between the liquid, the surface of the substrate, and the air. Surface tension (δ [$\mathrm{N/m}$]) can be defined as the force per unit length and this is equivalent to surface energy (Δ [$\mathrm{J/m^2}$]) which is the work done in creating unit area of new surface. As examples, for pure water at $20\,^{\circ}\mathrm{C}$, δ is [$72.5\,\mathrm{mN/m}$], while for many organic solvent, δ lies in the range of [20 to $40\,\mathrm{mN/m}$]. The tendency of a liquid to form the spherical shape, which has the lowest total energy, is crucial to the processes of inkjet printing. A liquid flow coming out from the printing head is initially a cylindrical shape, but this is not stable. Under the effect of surface tension, the cylinder shape gradually transforms and will eventually break into a series of spherical drops.

The forces which resist the contraction of liquid through the action of surface tension have two types: the inertial force of liquid and its viscosity. Inertial forces are associated with a change in a momentum of an object. Viscous forces are caused by the interaction between molecules of the liquid and act between regions of liquid moving relative to each other. In the case of a rectangular parallelepiped which has a parallel plates distance of d and one of places is moving with the relative velocity of v with respect to the other , the dynamic viscosity of liquid is expressed as:

$$\eta = \frac{\tau}{\dot{\gamma}} \ , \tag{3.1}$$

where shear strain rate $\dot{\gamma}$ is

$$\dot{\gamma} = \frac{v}{d} \ , \tag{3.2}$$

and τ is the shear stress acting on the upper and lower surface.

To determine if the ink is jettable without causing satellite droplets and forming proper

spherical shape droplets, two important dimensionless numbers ; Reynolds (Re) and Weber (We) numbers, based on surface tension, inertial force, and viscosity can be used. The Reynolds number represents the ratio between inertial and viscous forces in a moving fluid and defined as:

$$Re = \frac{\rho d V}{\eta} \quad , \tag{3.3}$$

where ρ is the density of the fulid, V is its velocity, η is its viscosity, and d is a diameter of the nozzle or diameter of the droplet. The Weber number is the ratio between inertia and surface tension and expressed as:

$$We = \frac{\rho d V^2}{\delta} \quad , \tag{3.4}$$

where δ is the surface tension.

In order to expresses the properties of the ink without the influence of velocity in Reynolds and Weber number, Ohnesorge number (Oh) can be defined as:

$$Oh = \frac{\sqrt{We}}{Re} = \frac{\eta}{\sqrt{\delta \rho d}} \quad . \tag{3.5}$$

In terms of Ohnesorge number, which is only a function of material properties, the jettable ink needs to be in the range or $0.1 < Oh < 1$. If $Oh > 1$, the ink is too viscous preventing the ink droplets from separating [56], [57]. On the other hand, if $Oh < 0.1$, the jet will work a large number of satellite droplets, which are the undesired droplets generated during printing, especially for fine resolution printing. Similarly, the jet must possess enough kinetic energy to be ejected from the nozzle and it is also desirable to avoid splashing when the droplet hit with the substrate. These criterion provides other boundary in the relationship between Ohnesorge and Reynolds numbers. In the literature $Re = \frac{2}{Oh}$ and $Oh = \frac{50}{Re^{5/4}}$ are suggested [57]. The relationship between Reynolds and Ohnesorge numbers described above is visually depicted in Fig. 3.2 (reproduced from [56]).

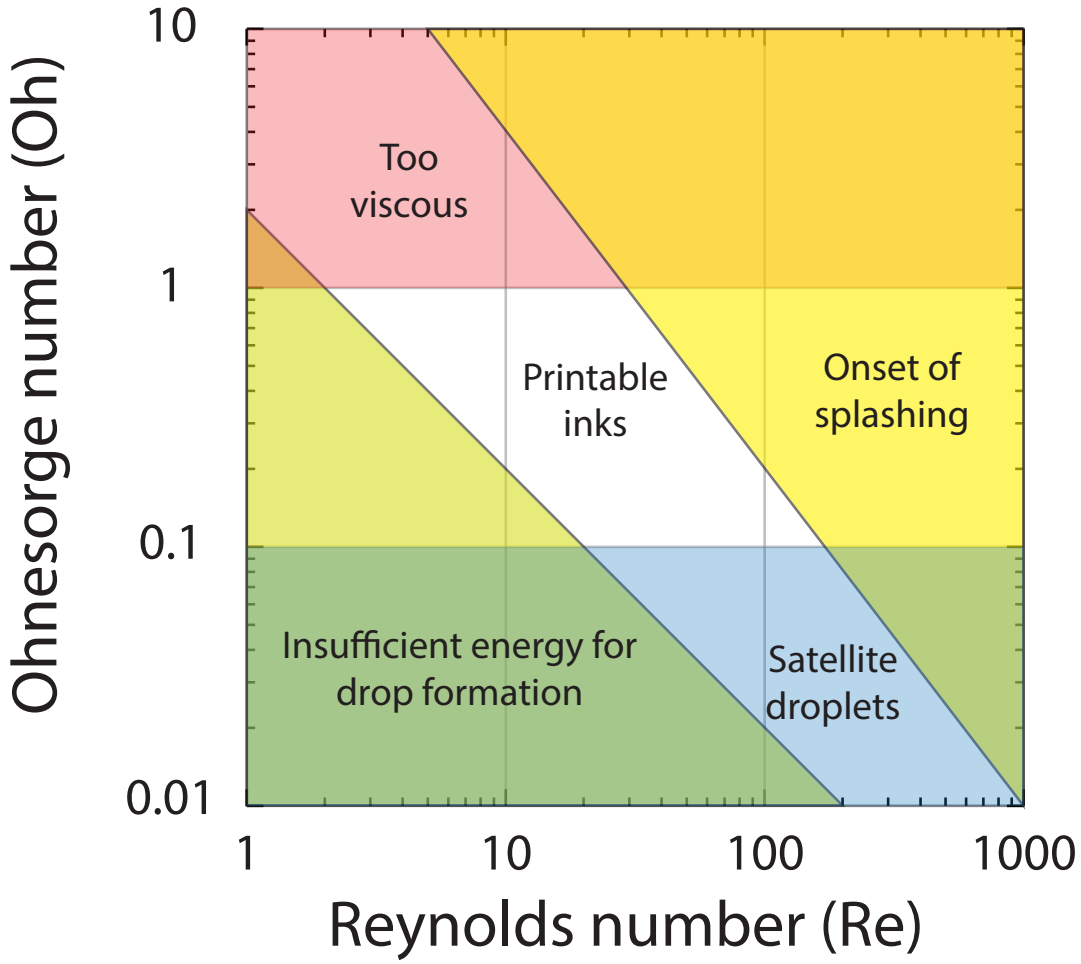

Figure 3.2. Schematic of stable inkjet droplet formulation in terms of Reynolds and Ohnesorge numbers.

Once a droplet is expelled from a cartridge, its interaction with a host substrate and the surrounding ink droplets must be also considered. The total free surface energy of the host substrate must be higher than the surface tension of the ink droplet to ensure good wetting between the two phases, where a difference of approximately $10\,\mathrm{mN/m}$ between the surface tension of ink and the surface energy of the substrate is desired to achieve stable wettability [58]. In order to increase or decrease the surface energy of the substrate, UV ozone and plasma surface treatments are conducted, respectively. Also, substrate temperature can be adjusted by heating the platen of the printer while printing.

TABLE 3.1TYPICAL DROP DIAMETERS AND EQUIVALENT DROP VOLUMES

Volume (pL)	0.1	1	10	100	1000
Diameter (μm)	5.76	12.41	26.73	57.59	124.07

3.1.3 Droplet Size and Resolution

Typical drop diameters in inkjet printing lie in the range from 10 to $100\,\mu\mathrm{m}$, corresponding to drop volumes from 0.5 to $500\,\mathrm{pL}$ as summarized in table 3.1. Although, depending on the material of solvent in an ink droplet, the volume of material actually deposited on a substrate may vary because of the solvent evaporation. The print head of a Dimatix inkjet printer material cartridge is available in $1\,\mathrm{pL}$ and $10\,\mathrm{pL}$ drop volume options which give $12.41\,\mu\mathrm{m}$ and $26.73\,\mu\mathrm{m}$ droplet diameter size, respectively. When the droplet hits the substrate, it spreads and contracts while releasing its mechanical energy and finally it stops on the substrate. Eventually, the maximum resolution of printing with Dimatix printer is about 20 to $50\,\mu\mathrm{m}$ depending on the ink. Recently, a special type of inkjet printer called electrohydrodynamic inkjet, which can achieve $1\,\mu\mathrm{m}$ order resolution is reported [59].

3.1.4 Printable Materials

Standard materials for the most common electronic inkjet printing processes can be separated into three general categories: conductive, dielectric, and reactive. Conductive inks are typically composed of suspensions of metallic nanoparticles in a low viscosity solvent solution. Noble metals, such as silver and gold, are preferred for dispersion-based inks because of their high resistance to oxidation in the ambient processing conditions, one of the highlighted advantages of inkjet printing processing. Additionally, metallic nanoparticle inks are advantageous for low-temperature and ambient sintering processes, including thermal ($< 200\,^{\circ}\mathrm{C}$, laser-based, and photonic solutions. Dielectric inks are commonly realized through organic polymer solutions with thermal or photoinitiated crosslinking agents. Polymeric dielectric inks are typically classified by their per-layer printed thickness, where a poly(4-vinylphenol) (PVP) polymer-based ink can be used to pattern films with thick-

nesses in the range of hundreds of nanometers while an SU-8 polymer-based ink can realize uniform films with thicknesses in excess of one hundred micrometers [60]. Dielectric materials that are well established and characterized within standard microelectronic fabrication processes, including PVP and SU-8, are popular targets for adoption within inkjet printing systems in order to facilitate integration with existing fabrication technologies. Finally, reactive inks are composed of materials that respond to certain environmental stimuli, such as temperature, strain, humidity, and the presence of a target gas. Many popular solutions for sensing inks consist of dispersions of carbon-based nanomaterials, such as reduced graphene oxide (rGO) flakes and carbon nanotubes (CNTs). With these inks, nanomaterials are suspended within an aqueous solution consiting of solvents and surfactants, allowing for low-temperature processing and good wetting with host substrates. The nanomaterials comprising these inks have the potential to be specifically functionalized to allow for selective sensitivity to a desired sensing target.

3.1.5 Inkjet Printing for Masking

Since it is possible to print SU-8 polymer, which is commonly used as a negative photoresist for PCB masking, it is possible to pattern copper clad substrate through wet etching process after printing the circuit trace with SU-8 polymer. This is not an additive manufacturing process, but is useful for initial prototyping purpose especially for circuit which has lumped components. For electrical connection between lumped components and inkjet printed conductive traces, usually conductive epoxy material is used. However, this material cannot be easily removed and redeposited. Therefore, printed conductor traces are not suitable for a circuit fabrication which involves changing of lumped components for fine tuning. On the other hand, clad copper on a substrate is designed for soldering and suitable for initial prototyping. The advantage of this approach is that it is possible to fabricate the initial and final design by utilizing the same printing platform by just changing ink.

There are four steps in the fabrication of flexible circuit traces utilizing inkjet printing

masking on copper clad LCP as are depicted in Fig. 3.3. The polymer ink is made of 35 $w\%$ SU-8 polymer from MicroChem, and was used as a mask on a copper-cladded liquid crystalline polymer (LCP) substrate from Rogers Corporation. Once the SU-8 ink was printed on the copper cladding layer, the substrate was soft baked at $120\,^{\circ}\mathrm{C}$ for 10 minutes before the masking was exposed to $365\,\mathrm{nm}$ UV light for cross linking. After the UV light exposure, the substrate was heated at $120\,^{\circ}\mathrm{C}$ for additional 5 minutes, yielding a 4 to $6\,\mu\mathrm{m}$ SU-8 layer thickness [61]. Two layers of SU-8 were printed and then the uncovered copper metallization was etched with ferric chloride ($FeCl_3$) solution. The etching time varied from 30 to 90 minutes depending on the temperature, size of substrate, thickness of metal layer and freshness of the $FeCl_3$ solution. After the etching, SU-8 mask is removed by using acetone. Fig. 3.4 shows the printed conductive traces for a $3\,\mathrm{mm}$ by $3\,\mathrm{mm}$ TDFN8 package that have been fabricated with the above additive fabrication approach. The resolution of the conductive patterning is effectively equal to the resolution of inkjet printing, making it possible to fabricate circuit traces width and spacing of less than $400\,\mu\mathrm{m}$ for the prototype in Fig. 3.4, although narrower spacings below $90\,\mu\mathrm{m}$ can be easily realized, which is sufficiently good for many commonly used packaged ICs.

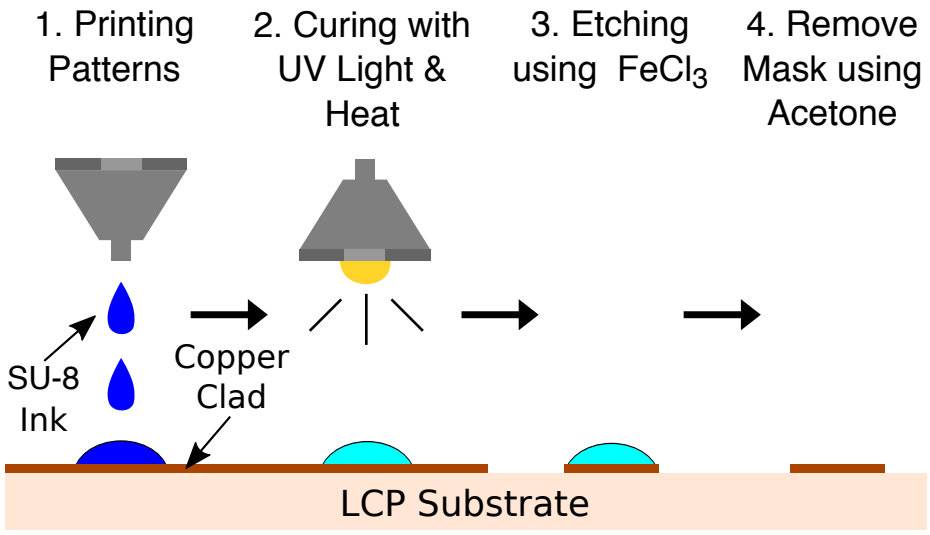

Figure 3.3. Fabrication process of flexible circuit traces utilizing inkjet printing masking.

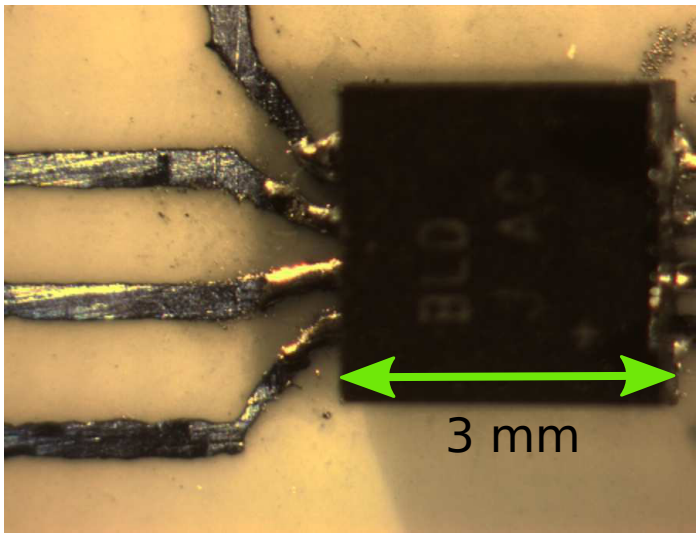

Figure 3.4. Circuit traces for a TDFN8 IC package fabricated with inkjet printing masking.

3.2 3D-printing Technology

3D printing has gained a significant amount of attention in the last half decade with the rapid expansion of affordable 3D printers, enabling the use of the printers in schools, developing areas, and wide adoption in prototyping labs and academia. There exists a wide variety of 3D printing techniques. Most commonly is Fused Deposition Modeling (FDM), the method where thermoplastic polymers are wound into a filament form, which is then deposited through a heated nozzle that moves in the XYZ dimensions. The filament needs to melt at relatively low temperature, so the compatible material for FDM printing is limited to polymers such as ABS and PLA. The second most adopted 3D printing technique is stereolithography (SLA), which exposes a bath of UV-curable photopolymer resins by either precisely tracing with a laser or displaying a cross section to be cured with a projector, layer by layer. Multijet and Polyjet 3D printing employ inkjet nozzles to deposit UV-curable photopolymer resins which are cured in-situ with a UV source alongside the inkjet nozzles. Selective laser sintering (SLS) and selective laser melting (SLM) enable 3D printing of metal powders which are sintered or melted together with a high powered laser.

Each of these printing techniques offer a unique set of advantages and disadvantages, ranging from resolution, surface roughness, strength, material selection and compatibility.

FDM printing enables an XYZ gantry that allows coexistence of direct write deposition tools, allowing the printing of both thermoplastic polymer alongside a wide variety of fluids, from conductive pastes to scaffolding gels for bio printing. This allows the printing of new unique materials, such as flexible and stretchable silver nanoflake pastes in combination with thermoplastic elastomers to print stretchable electronics. One of the biggest advantages of FDM printing over the other 3D printing technologies is this printing technology enables the simultaneous multi-material printing. By contrast, SLA printing has relatively high resolution of printing and stable operation, but it only allows a single material printing in the process.

In terms of electrical properties of these 3D printing materials, most of 3D printing polymers have similar dielectric constant in the range of 2 to 4. However, the loss tangent of polymers for 3D printing have relatively large variation. For example, ABS an PLA which are commonly used material for FDM printing has loss tangent of 0.005 to 0.019, but photo reactive polymers used for SLA printing has loss tangent of 0.01 to 0.05. In this research, 3D printing was mainly used for packaging application, and lower dielectric loss was preferred. Therefore, in this section, only FDM printing is discussed more in detail.

3.2.1 FDM Printing

FDM printing technology was developed by S.S. Crump in 1989 [62] and commercialized in 1990. The basic schematic topology of FDM 3D printer is depicted in Fig. 3.5. The printing process is based on the deposition of melt filament ejected from a printing head with an filament extruder. The printing head scans in the XY direction while printing to deposit material on each "layer" and the printer platen (or print head) moves in Z direction to start another layer in different relative height to form a 3D object. The XY direction resolution is mostly depending on the heated nozzle size and flow rate, and Z direction resolution is determined by the step motor resolution. Typically, the maximum resolution is in the order of hundreds of micron [63], [64].

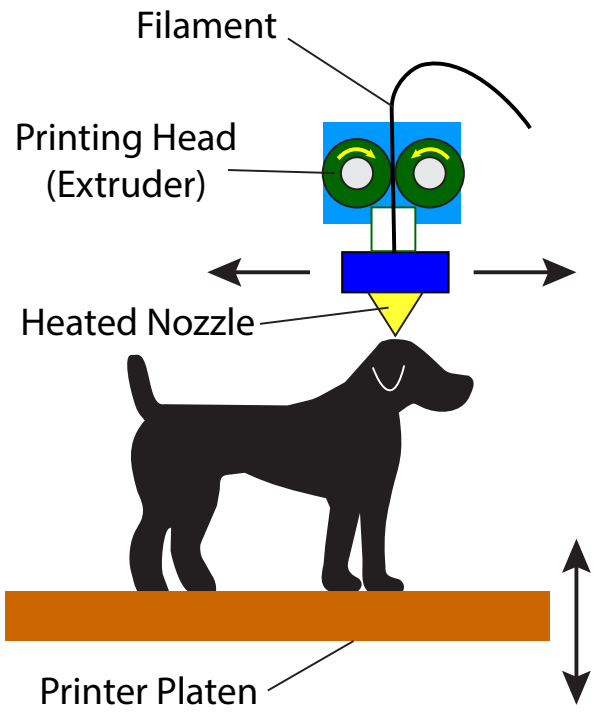

Figure 3.5. FDM 3D printing process.

3.3 Printed Material Electrical Property Characterization

For both inkjet and 3D printings, printed materials after curing do not necessary to have the same electrical properties as the original bulk condition. Therefore, printed materials need to be characterized for fine RF circuit design. In this section, the characterization of most important parameters in RF circuit design; conductivity, dielectric constant, and loss tangent of printed materials is discussed.

3.3.1 Sheet Resistance of Conductive Material

Since most of RF circuits utilize a thin sheet of metal as a conductor which has much smaller dimensions in the Z direction than the X and Y directions, the resistivity in a 3D structure is not a good metric because it is difficult to know the exact thickness of the metal. Therefore, sheet resistance (R_s), which is a measure of resistance of thin films that are nominally uniform in thickness, is commonly used. As depicted in Fig. 3.6, if the

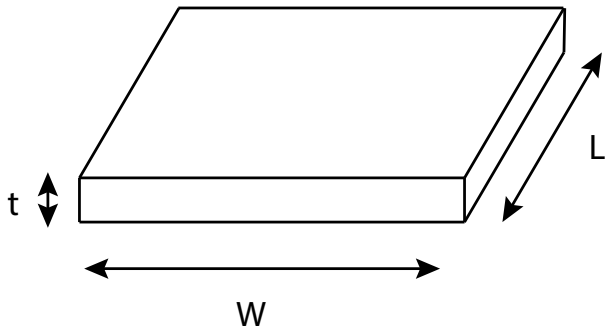

Figure 3.6. Model of sheet resistance.

thickness of a material is t, width is W, and length is L, the resistance (R) can be expressed as:

$$R = \frac{\rho}{t}\frac{L}{W} = R_S\frac{L}{W} \quad , \tag{3.6}$$

where ρ is the resistivity of the material and R_s is the sheet resistance. Sheet resistance has the unit of Ω that is the same as resistance, but to differentiate these two, conventionally, Ω □ (ohm square) or $\Omega/\square$ (ohm per square) are used. Typically, printed silver nano particle ink after curing has sheet resistance of 0.01 $\Omega/\square$.

3.3.2 Dielectric Constant

Dielectric constant (ϵ) , or permittivity, is a material property that effects the Coulomb force between two point charges in the material changing the electrical length of the field in the material. Usually, the dielectric constant of a substrate is expressed as $\epsilon = \epsilon_r\epsilon_0$, where ϵ_0 is the dielectric constant of air and ϵ_r is relative permittivity. In order to propagate RF signals, waveguide structures such as microstrip lines and CPWs are used in RF circuits, and the dielectric constant of a substrate is one of critical parameters to design these waveguides. Also, the physical dimensions of antennas are also heavily affected by the dielectric constant of the substrate, so it is critical to know the dielectric constant of the printed material. There are several methods to characterize dielectric constant of a substrate

utilizing resonator structures and waveguides, but it this research a two line method and a microstrip T-resonator method are described.

Two Line Method

The two line method is the most simplistic and universal method to characterize the dielectric constant of a substrate by using two waveguides with two different lengths. The velocity of light is a function of the permeability and permittivity of the medium and expressed as:

$$V_{light} = \frac{1}{\sqrt{\mu\epsilon}}. \tag{3.7}$$

Therefore, if the permeability of the medium is known and the difference between the time of travel in two different length waveguides is known from measurements, the permittivity of the material can be calculated with this equation. Although, it is hard to measure the time of travel directly, so the difference in phase is used. Practically, the permittivity of a waveguide is also dimension dependent and it is necessary to consider an effective permittivity (ϵ_{eff}). Therefore, the relationship between effective permittivity and phase difference is expressed as:

$$\epsilon_{eff} = \left(\frac{\Delta\theta \times c}{2\pi f(\Delta L)} \right)^2, \tag{3.8}$$

where $\Delta\theta$ is the difference in phase, c is the speed of light in free space, and ΔL is the difference in the length of two lines, assuming the relative permeability is 1 [65]. The phase difference is a function of frequency, but for practicality, the phase difference should be in the range of 10 to $170°$ to minimize the error. This implies that more than two lengths of waveguides are required to characterize the dielectric constant over a wide range of frequency.

In the case of microstriplines, the effective dielectric constant is approximated as:

$$\epsilon_{eff} = \frac{\epsilon_r + 1}{2} \frac{\epsilon_r - 1}{2} \frac{1}{\sqrt{1 + 12d/W}}, \tag{3.9}$$

where d is the thickness of substrate and W is the width of signal line [66].

Microstrip T-resonator Method

The microstrip T-Resonator is a transmission line with an open circuit stub as depicted in Fig. 3.7.

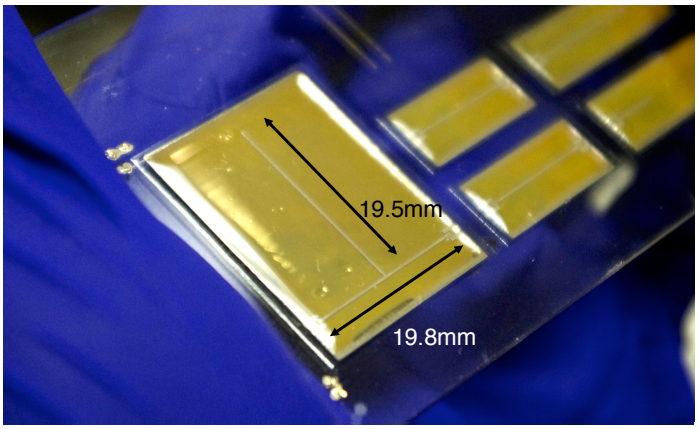

Figure 3.7. Fully printed T-resonator structure.

This type of resonator has a null in the insertion loss when the length of the stub (l) is approximately $l = \lambda/4 + n\lambda/2$, where $n = 0, 1, 2, ...$ The resonant frequency of T-resonator is expressed as

$$f_{r,n} = \frac{nc}{4(l + l_0)\sqrt{\epsilon_{eff}}} \quad , \tag{3.10}$$

where l_0 is the correction factor for the fringing capacitance at the tip of the open circuit stub [67]. The dielectric constant is calculated from the effective permittivity utilizing Eq. (3.9).

As an example, a fully printed $80\,\mu\mathrm{m}$ thick SU-8 substrate is characterized with both two line and microstrip T-resonator methods. As a result, a dielectric constant of about 3.2

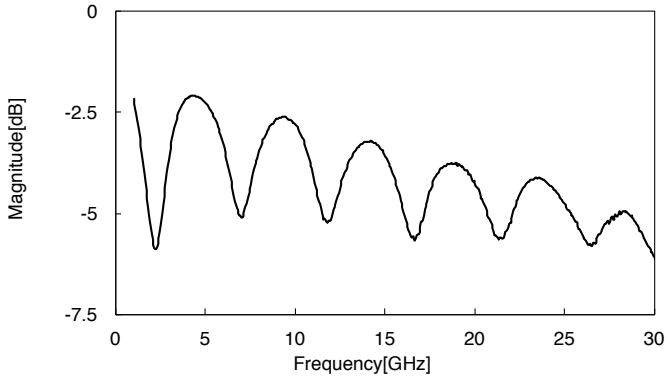

Figure 3.8. Measured S_{11} of fully printed T-resonator.

was obtained as shown in Fig. 3.9.

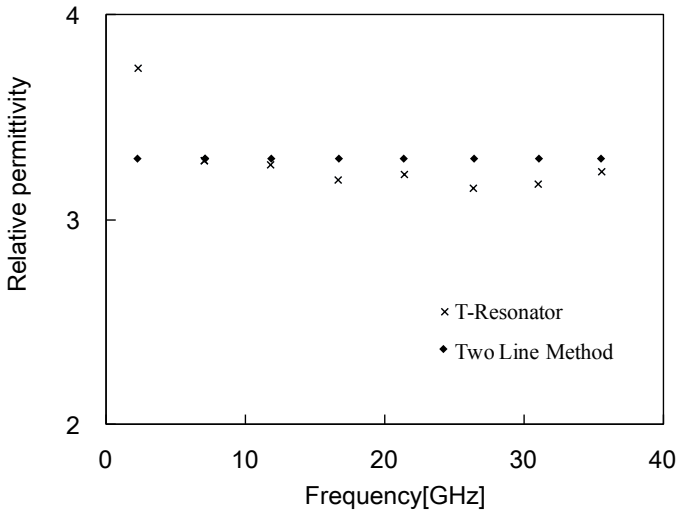

Figure 3.9. Dielectric constant of printed thick SU-8 substrate.

3.3.3 Loss Tangent

The losses in RF circuit are classified into conductor, radiation, and dielectric losses assuming there is not reflection loss. The dielectric loss is one of dissipative losses and becomes critical for high frequency circuits. This can be also calculated from the measurement of the insertion loss of the T-resonator. The loaded Q-factor of the resonator is

expressed as:

$$Q_{l,n} = \frac{f_{r,n}}{BW_{3dB,n}} \quad , \tag{3.11}$$

where BW_{3dB} is the $3\,\mathrm{dB}$ bandwidth from the resonance frequency. Then, the loaded Q-factor is converted to an unloaded Q-factor to eliminate the effects of measurement equipment by Eq. (3.12), where L_a is the insertion loss at each resonance frequency [67].

$$Q_{ul,n} = \frac{Q_{l,n}}{\sqrt{1 - 2\ exp(\frac{L_a}{10})}} \tag{3.12}$$

The unloaded Q-factor is converted into the scale of [dB/m] and expressed as a total loss $\alpha_{tot,n}$ as follows:

$$\alpha_{tot,n} = \alpha_{c,n} + \alpha_{r,n} + \alpha_{d,n} = \frac{8.686\pi f_{f,n}\sqrt{\epsilon_{eff}}}{c\ Q_{ul,n}} \quad , \tag{3.13}$$

where $\alpha_{c,n}$, $\alpha_{r,n}$, and $\alpha_{d,n}$ are conductor, radiation, and dielectric loss, respectively. Among these losses, the conductor loss is calculated using a simulation software, Keysight (Agilent) ADS LineCalc, and subtracted. For frequencies below $100\,\mathrm{GHz}$, radiation loss from a microstrip line is negligibly small. Finally, the dielectric loss can be related to the loss tangent ($tan\delta$) by using Eq. (3.14).

$$tan\delta = \frac{\alpha_{d,n}\lambda_0\sqrt{\epsilon_{eff,n}}(\epsilon_{r,n} - 1)}{8.686\pi\epsilon_{r,n}(\epsilon_{eff,n} + 1)} \tag{3.14}$$

From the measurement results in Fig. 3.8 and Eq. (3.14), the average loss tangent over frequency is approximately 0.055.

3.4 Additive Manufacturing for Energy Harvester Fabrication

Numerous renewable ambient energy sources such as solar, heat, vibration, and electromagnetic waves exist in nature. The characteristics of each widely utilized ambient energy

source in terms of potential power density, output DC voltage, availability, and compatibility with additive manufacturing are summarized in Table 3.2. Following is a brief explanation of solar, heat, and vibration energy harvesting. The explanation of ambient RF energy harvesting is skipped in this section since it is discussed in Chap. 2.

TABLE 3.2
COMPARISON OF AVAILABLE AMBIENT ENERGY SOURCES

	Solar Energy	**Thermal Energy**	**Piezoelectric Energy**	**Ambient RF Energy**
Potential Power Density	$100\,\mathrm{mW/cm^2}$ (Outdoor) $100\,\mu\mathrm{W/cm^2}$ (Indoor) [7], [68]	$60\,\mu\mathrm{W/cm^2}$ [5], [7]	4 to $800\,\mu\mathrm{W/cm^3}$ depending on activity [5], [7], [69], [70]	$2\,\mathrm{nW/cm^2}$ to $10\,\mathrm{mW/cm^2}$ [5], [26], [27], [71]
Output Voltage	$0.95\,\mathrm{V}$ (Perovskite) [72] $0.77\,\mathrm{V}$ (OPV) [73]	5 to $7\,\mathrm{mV}$ [48]	1 to $25\,\mathrm{V}$ [5], [49], [50], [70]	1 to $25\,\mathrm{V}$ (Open voltage) [5], [8], [71]
Conversion Efficiency (%)	10.14 (Perovskite) [72] 4.1 (OPV) [73]	< 1 [48]	< 25 (PVDF) [70]	< 90 (Frequency and input power dependent) [5], [8], [26], [27], [71]
Availability	Daytime (4 to $8\,\mathrm{h}$)	Continuous	Activity dependent	Continuous
Compatibility with Additive Manufacturing	Inkjet Slot-die Gravure Screen printing [51]	Dispenser printing [48]	Vapor deposition Screen printing [49], [50]	Inkjet Gravure Screen printing [10], [15], [74]

3.4.1 Solar

Solar power is one of the most commonly used sources, featuring high power. It has high power density of $100\,\mathrm{mW/cm^2}$ during daytime and $100\,\mu\mathrm{W/cm^2}$ in indoor environment with the maximum conversion efficiency of more than $45\,\%$ [75]. The conversion efficiency heavily depends on the materials used for the solar cells. Commonly used materials for low-cost printable solar cells are inorganic perovskite-based ink [72] and organic polymer-based ink [73], and each yields $10.1\,\%$ and $4.1\,\%$ of conversion efficiency. The conversion efficiency of printed solar cells is relatively low compared to silicon based solar cells, but the solar cells can operate in a hybrid mode in conjunction with other types of energy source to virtually increase the available power per area [76], [77].

3.4.2 Heat

Thermal energy of the power source is also widely utilized. Electrical power is directly generated by exploiting the temperature difference in thermoelectric devices taking advantage of thermoelectric effects, such as the Seebeck effect or the Thomson effect. In general, a thermoelectric generator produces an energy density of 20 to $60\,\mu\mathrm{W/cm^2}$ when a human body is a heat source yielding about 18 to $25\,^{\circ}\mathrm{C}$ temperature difference between room temperature. Thermoelectirc devices can operate continuously as long as the temperature difference is maintained, but the energy conversion efficiency is low if the temperature difference is small. Typically, the conversion efficiency is below $1\,\%$ when a human body is used as an energy source [7]. The thermoelectric devices can be also fabricated using additive manufacturing techniques [48].

3.4.3 Vibration

The piezoelectric effect generates electrical voltages or currents from mechanical strains, such as vibration or deformation. The potential power density varies depending on activities. For example, a human motion exhibits $4\,\mu\mathrm{W/cm^3}$, and a machine vibration can gener-

ate $800\,\mu W/cm^3$. The energy is usually not continuously available and intermittent, which causes a large dynamic range in generated power. The generated power typically consists of high voltage and low current which requires voltage regulation circuitry to protect a circuit from a voltage overshoot [78]. Flexible piezoelectric materials can be fabricated using chemical and physical vapor deposition and screen printing [49], [50].

3.5 Additive Manufacturing Technologies for Energy Storage Devices in Autonomous Systems

Once each transducer converts the ambient energy into electric energy, it is stored in the energy storage devices such as a battery and a capacitor. They can be classified into three types depending on the operation principle: dielectric capacitors, electrochemical capacitors (electric double layer capacitors and pseudocapacitors), and batteries. Each device has different area specific capacitance and discharge speed, which determines the maximum power.

3.5.1 Dielectric Capacitors

Dielectric capacitors are well known as parallel plate capacitors, which are composed of two metal plates separated by dielectric materials. In the presence of an electric field, charges are directly stored on the plates as free electrons. The amount of charge is determined by the size (A) and separation distance (d) of the electrodes and the dielectric constant of the material between two electrodes. Since this type of capacitor does not require any chemical reaction in the charge and discharge process, they have the highest power density as well as charge-discharge life cycle among three energy storage devices. Although, the area specific capacitance ($\epsilon_0\epsilon_r/d$) would be less than $0.02\,F/m^2$ even with very high dielectric constant materials (ϵ_r = 2000) for d = $1\,\mu m$. Cook et al. have reported dielectric capacitors fabricated only using inkjet-printing technology which can support the operation up to RF frequency range [13].

3.5.2 Electrochemical Capacitor

Electrochemical capacitors store charges on the surface/sub-surface rather than in a bulk material as in batteries. Depending on charge storage mechanism, electrochemical capacitors are classified into electric double layer capacitors (EDLCs) and psuedocapacitors. EDLCs store charges due to accumulation of ions on the surface without involving conventional dielectric materials. EDLCs do not have any chemical reaction, so the power density is as high as dielectric capacitors, and the area specific capacitance would be $0.1\,\mathrm{F/m^2}$ with ϵ_r = 10 and d = $1\,\mathrm{nm}$ because of the extremely small separation distance. However, the charge-discharge life cycle of EDLCs is as high as that of dielectric capacitors because this type of capacitor does not involve any chemical reaction. In contrast, pseudocapacitors, which are also known as supercapacitors, involve fast and reversible redox reaction on the surface/subsurface of the electrodes. The pseudocapacitors have higher energy density than EDLCs, and it can go up to $1500\,\mathrm{F/g}$ [79]. Chen et al. have reported supercapacitors, which have an energy density of $138\,\mathrm{F/g}$, fabricated using inkjet printer [52]. However, the charge-discharge life cycle is lower than dielectric capacitors and EDLCs.

3.5.3 Battery

Batteries charge and discharge electricity through chemical reactions. For energy harvesting applications, rechargeable (secondary) batteries need to be used. Since they involve chemical reactions, it requires relatively long charge/discharge times on the order of a few minutes to a few hours. A variety of materials such as nickel cadmium, or lithium ion can be used as electrolytes, but for printed batteries, a zinc polymer is typically used because of its low toxicity, thin form factor, and low cost [53]. Their energy density can be 100 to $300\,\mathrm{W\cdot h/L}$. Currently, the charge-discharge life cycle is low and it is necessary to improve the charge-discharge life cycle or eliminate the use of a battery in a system to realize long life-time IoT and WSN devices.

CHAPTER 4

WEARABLE FLEXIBLE NEAR-FIELD RF ENERGY HARVESTER

One of the unique properties of additive manufacturing technologies is the capability of fabricating circuits on flexible materials. By taking advantages of this unique property, it is possible to create wearable RF energy harvesters, which can be comfortably arranged near mobile communication devices unlike conventional rigid RF energy harvesters. Generally, energy density in the near-field of an RF transmitter is much higher than that in far-field. Therefore, this is one of potential solutions for the low output voltage associated with the low energy density of ambient RF energy harvesting. However, as depicted in Fig. 4.1, high RF energy in near-field is only available when the user of a mobile device is communicating and RF input power is not always high. Without loss of generallity, in this research, the duration of communication is assumed to be 10 to $100\,\mathrm{s}$ and each communication happens with the time interval of 1 to $10\,\mathrm{s}$. Therefore, it is critical to maximize RF input power and RF-DC conversion efficiency to increase the available DC energy. Also, with current technology, RF input power below $1\,\mu\mathrm{W}$ is almost impossible to be used except for some very limited conditions which are discussed in Chap. 5. In this chapter, a novel analytical near-field RF energy harvester design process based on measurements (Sec. 4.1), an active matching circuit design for wearable RF energy harvesters utilizing a genetic algorithm and a clustering (Sec. 4.3), and a backscattering-based on-body sensor network (Sec. 4.4) utilizing an wearable RF energy harvester are discussed.

4.1 Wearable Flexible RF Energy Harvester Design

4.1.1 Near-field Power Distribution Simulations and Measurements

These days, many mobile communication electronics use digitally modulated signals and base stations for communication to reduce transmitted energy. However, some mobile communication devices such as two-way talk radios still use analog signals to commu-

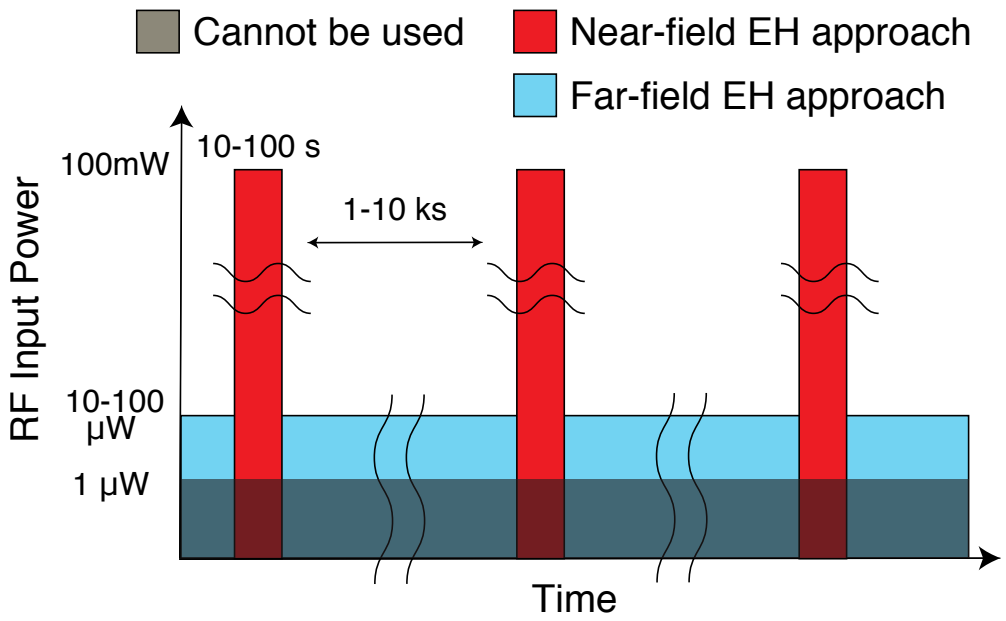

Figure 4.1. RF input power of near- and far-field RF energy harvesting with respect to time.

nicate directly with other devices, and they transmit relatively high energy continuously during communication. Therefore, this research used a Motorola RDU2020 two channel two-way talk radio ($2\,\mathrm{W}$) output power, which utilizes the continuous tone-coded squelch system (CTCSS) which is an analog squelch scheme at $464.5500\,\mathrm{MHz}$ (Channel 1) and $467.9250\,\mathrm{MHz}$ (Channel 2), as an RF power source. This study uses $2\,\mathrm{W}$ output power mode and Channel 1. The actual transmitted power was measured to be $2.2\,\mathrm{W}$ utilizing a power sensor (NRP-Z211 from Rohde & Schwarz) and a $30\,\mathrm{dB}$ attenuator. Since most people turn on the Walkie-Talkie with their hands, sufficient output power is available in the near-field of the radio by placing a harvester around a hand.

To estimate the E- and H-field distribution around the hand holding the radio, various simulations were run on CST STUDIO SUITE. In these simulations, a monopole antenna which has the same operation frequency as RDU2020 was placed near the thumb of the right hand model which features the human flesh electrical properties. Fig. 4.2 highlights the simulation results of E- and H-field distribution on the back and on the palm sides. As it can be easily observed in this figure, E-field intensity is generally much higher than that of H-field, but at some locations, H-field is locally high. Next, the intensity of electric

and magnetic fields around the wrist were measured with an ETS-Lundgren E-and H-field probe which was connected to a real-time spectrum analyzer, RSA3408A, from Tektronix to optimize the placement orientation of the wearable energy harvesting circuit. Fig. 4.3 (a) and (b) show the measurement setup and the measured E- and H-field values at 2 to $17\,\mathrm{cm}$ away from the radio at various angular positions, respectively. As a conclusion, the electrical field is stronger than the magnetic field around the wrist. However, because of the fundamental near-field E-field distribution around the monopole antenna, the optimum E-field receiver needs to be parallel to the two-way radio antenna, which is difficult because of typical motions and changes in the relative positions of the radio in common holding arrangements of the radio near the wrist. On the other hand, the power level of the magnetic field at $0°$ position is relatively higher than any other angles. Mounting the harvesting structure on the back of hand, which is vertically facing the expected H-field, can easily increase the receiving area of the H-field, instead of placing the receiver on the wrist. Based on this assumption, this study designed receiver circuits for both electrical field and magnetic field for proof-of-concept purposes.

4.1.2 E- and H-field Receiver Design

By taking into account the typical size of a hand and a wrist, this study adopted a width of $5\,\mathrm{cm}$ and length of $15\,\mathrm{cm}$ as the size constraints of the E-field receiver, and a width of $5\,\mathrm{cm}$ and a length of $8\,\mathrm{cm}$ for the H-field receiver expecting the E-field harvester is wrapped around a wrist and the H-field harvester is stuck on the back of a hand. Based on the near-field power simulations and measurements, and the above wrist-dependent restrictions, receiver circuits for both E- and H-field were designed. This work selected a dipole antenna for E-field and an open-type helical coil with four loops for H-field as the wearable harvesting receivers. Both were soldered with the balun (ADT1-1WT) from Coilcraft, Inc. Fig. 4.4 (a) and (b) show the dimensions of the E-and the H-field receiver prototypes, respectively.

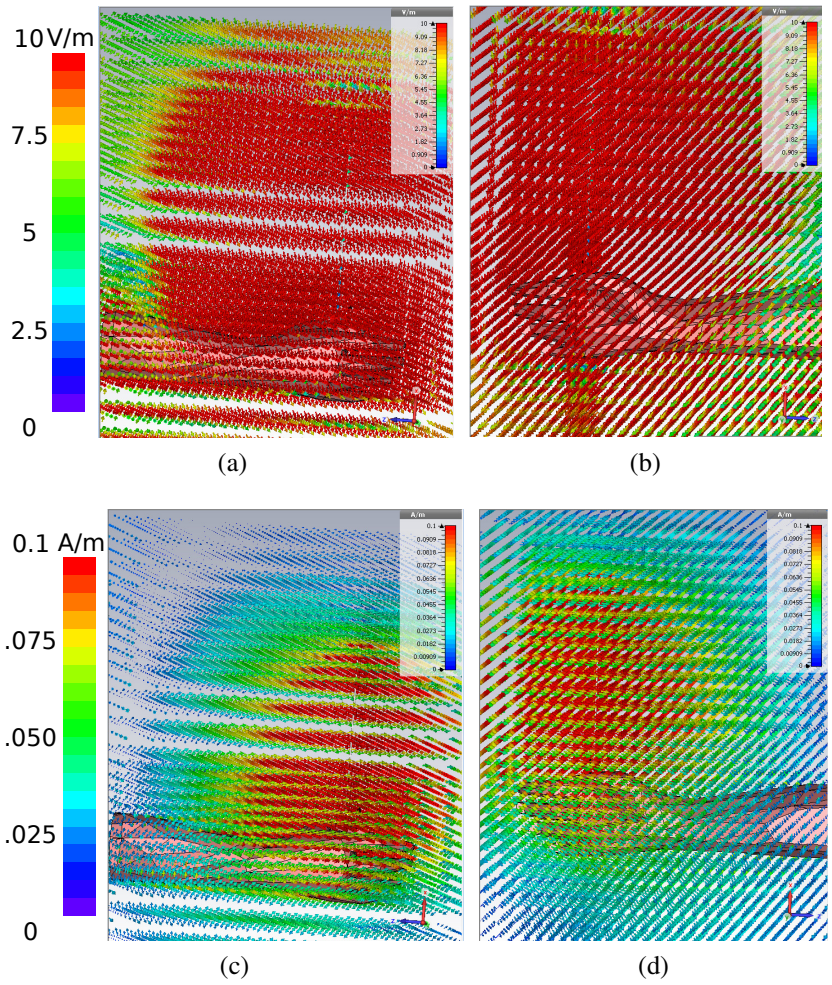

Figure 4.2. E-field distribution of (a) Back side. (b) Palm side. H-field distribution of (c) Back side. (d) Palm side.

4.1.3 Input Power Estimation and RF-DC Conversion Circuit Design

Since the transmitter and the receiver circuits are placed in the near field, it is very difficult to estimate how much power is actually transferred to the receiver through simulations. The requirement that the proposed receiver had to be wearable, as well as the detrimental proximity effect of the human body, further complicated this estimation. Therefore, in this paper, the power transferred to the receiver port was computed from 2-port S-parameter measurements with a vector network analyzer (ZVA8 from Rohde & Schwarz). The energy harvesting system can be generally modeled as shown in Fig. 4.5. In this figure, Z_S is the source impedance and Z_L is the load impedance. If input and output power at port1 and

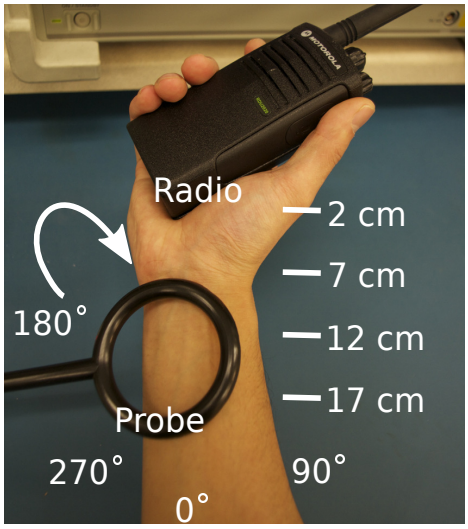

(a)

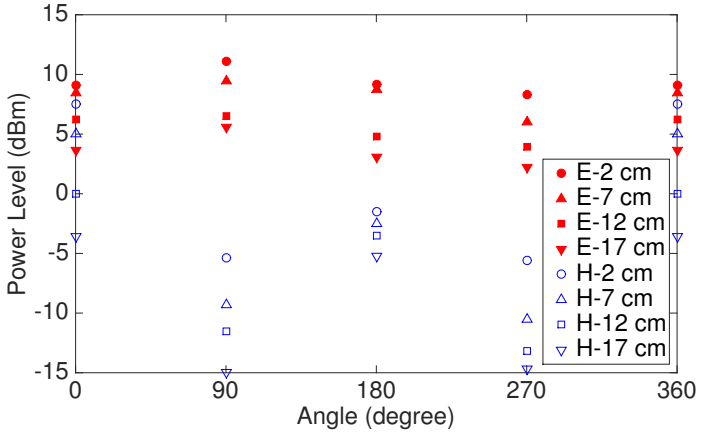

(b)

Figure 4.3. (a) Near-field probe measurement configuration. (b) Measured E- and H-field power levels at different relative angles and distances.

port2 are defined as a_1, b_1, a_2 and b_2, respectively, the topology of the transmitter antenna and of the harvesting receiver can be expressed as a S-parameter matrix. Once the power transferred to the load and the power from the source, defined as P_L and P_S, respectively, the power transfer efficiency from the source to the load can be determined as shown in Eq. (6.14). If the reflection coefficient from the source to port1 (Γ_{IN}) in Eq. (6.14) is substituted with Eq. (6.16), the efficiency can be expressed only as a function of the reflection coefficient from port2 to the load (Γ_L). Therefore, once the 2-port S-parameter matrix for the Tx-Rx propagation channel is calculated experimentally, the maximum power transfer efficiency can be analytically computed by sweeping the value of $\Gamma_L = Ae^{j\theta}$ in the range

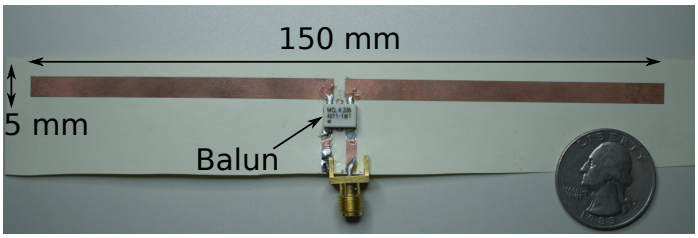

(a)

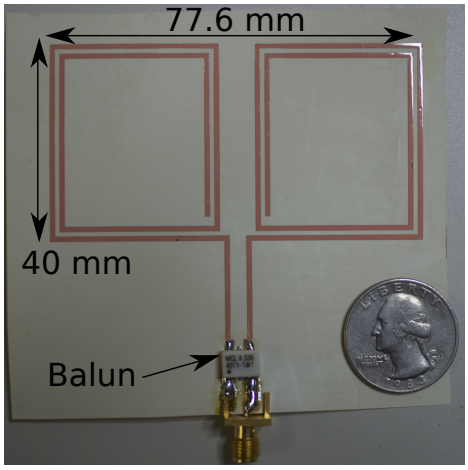

(b)

Figure 4.4. Additively manufactured receiver prototypes for (a) E-field, (b) H-field.

of $|A| = 1$ and θ =0 to 360°. At the same time, the load impedance value yielding the maximum efficiency can be computed from Eq. (6.16) [80].

$$\mu = \frac{P_L}{P_S} = \frac{b_2 b_2^* - a_2 a_2^*}{a_1 a_1^* - b_1 b_1^*} = \frac{(1 - |\Gamma_L|^2) S_{21}^2}{(1 - |\Gamma_{IN}|^2)|1 - \Gamma_L S_{22}|^2} \tag{4.1}$$

$$\Gamma_{IN} = S_{11} + \frac{\Gamma_L S_{21} S_{12}}{1 - \Gamma_L S_{22}} \quad Z_L = Z_0 \frac{1 + \Gamma_L}{1 - \Gamma_L} \tag{4.2}$$

In this research, the harvester circuit is expected to be placed on the human body. However, because of regulation issues related to human subject research, a bottle of water was adopted as the substitute material for the human forearm for the preliminary measurements. In reality, the human body has different electrical properties compared to the water. Therefore, in order to imitate the human body effects more accurately, a phantom should be used in future research efforts. However, as a first-order approximation and as a proof-of-

concept of the wearable near-field RF energy harvesting, and without loss of generality, a spindle-shape $20\,\mathrm{cm}$ tall water bottle, which has the smallest diameter of $17.5\,\mathrm{cm}$ at the middle and the largest diameter of $23\,\mathrm{cm}$ at the top and bottom, was used. In order to mimic the two-way talk radio, a stubby UHF antenna, RAN4033 from Motorola, which has similar physical dimension to the one on the 2-way talk radio, was placed at the bottom of the water bottle and was used for the S-parameter measurements. The E-field receiver was wrapped around the bottle at a distance of $7\,\mathrm{cm}$ from the bottom of the bottle in a configuration equivalent to the handheld 2-way radio and the "$7\,\mathrm{cm}$" position of the harvester in Fig. 4.3(a). Similarly, the H-field receiver was placed at $2\,\mathrm{cm}$ away from the bottom of the water bottle which is equivalent to the "$2\,\mathrm{cm}$" position in Fig. 4.3. The measured S-parameters for the transmitting monopole and for the E- and H-field receivers are plotted in Fig. 4.6 for this specific configuration. Using these data in Eq. (6.14) and (6.16), the maximum potential power transfer efficiency was determined to be $2.57\,\%$ and $7.55\,\%$ for the E-field and the H-field receivers, respectively. For the E-field harvester circuit, the maximum possible transferred power from the $2.2\,\mathrm{W}$ transmitter, $56.2\,\mathrm{mW}$, and the load impedance at the maximum power transfer condition, 202 - $j90$, were determined from Eq. (6.14) and (6.16), respectively. From the same equations, the H-field harvester maximum possible transferred power of $166.0\,\mathrm{mW}$, and the load impedance at the maximum power transfer condition, 10.7 - $j4.6$, were computed. In order to maximize the output voltage with the minimum possible circuit size, a single-stage Dickson voltage doubler with one Schottky diode chip, Avago HSMS282C, was used as the rectifier. Also in order to keep the size of harvester small, an L-shape LC network was adopted as the matching circuit. The circuit was initially designed with Keysight (Agilent) Advanced Design System (ADS) and the matching circuit was fine tuned during measurements. The configuration of the E and H-field rectifier prototypes is shown in Fig. 4.7 (a) and (b), respectively.

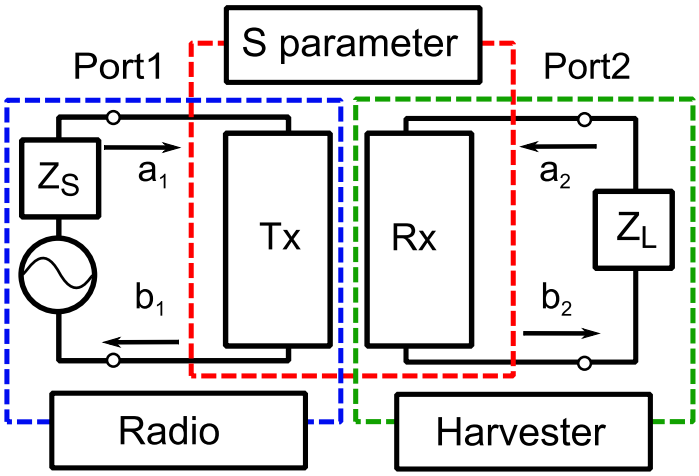

Figure 4.5. System configuration with equivalent S-parameters matrix.

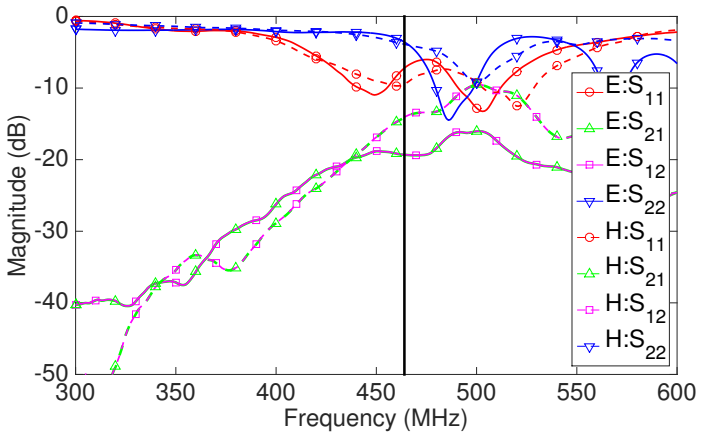

Figure 4.6. Measured S-parameters for E- and H-field receivers.

4.2 Wearable Energy Harvester DC and Communication Characterization

4.2.1 RF-DC Conversion Efficiency Measurements

The output voltage measurements were initially conducted with an RDU2020 hand-held radio by arranging the harvester and the radio on the side of the water bottle in a configuration similar to the one on the human arm holding the radio as shown in Fig. 4.8 (a) and Fig. 4.9 (a). The output voltage was measured by changing the load resistance of the circuit in the range of 100 to 6800 Ω, which fully covers the optimal load resistance value range of 1800 to 3000 Ω from ADS simulation. The input power is assumed to be 56.2 mW (17.5 dBm) for the E-field harvester, and 166.0 mW (22.2 dBm) for the H-field

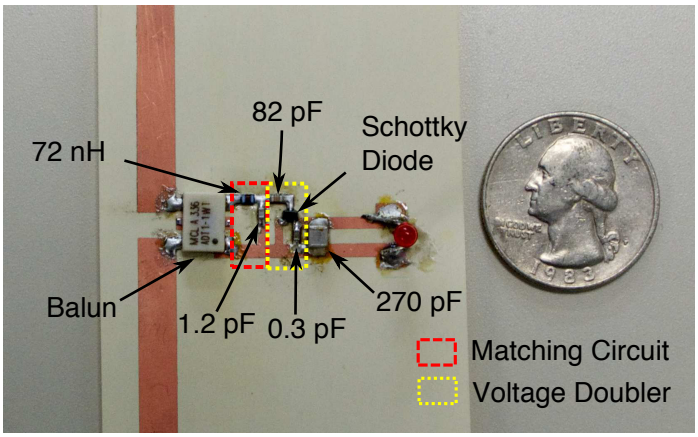

(a)

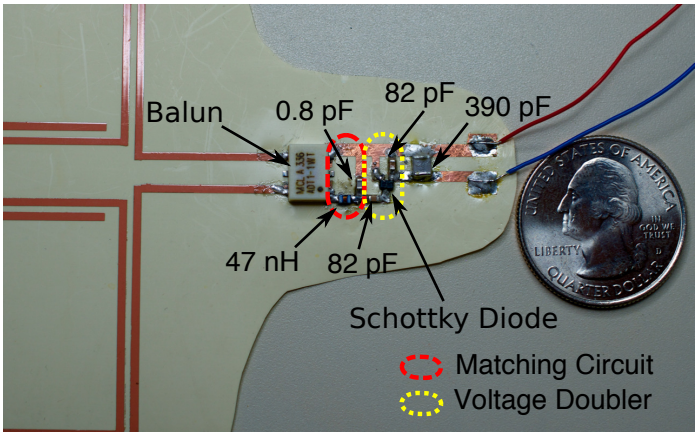

(b)

Figure 4.7. RF-DC conversion circuit topology for the wearable (a) E-filed energy harvester. (b) H-filed energy harvester.

harvester from the input power estimation based on the S-parameter measurements. The estimated RF-DC conversion efficiency from both the simulations and the measurements for E- and H-field harvesters as a function of the load resistance are depicted in Fig. 4.10 and Fig. 4.11, respectively. During the simulation, the matching circuit and the load resistance are optimized to achieve the highest DC output power for the estimated RF input power using ideal circuit components. The RDU two-way talk radios can potentially switch the transmitting power to $1\,\mathrm{W}$ and $4\,\mathrm{W}$. Therefore, the RF-DC conversion efficiencies when the input power is halved and doubled without changing the matching circuit design are also depicted in Fig. 4.10 and Fig. 4.11. According to the simulation results, the maximum RF-DC conversion at every input power level observation is almost the same for both E-

and H-field harvesters, and the optimal load resistance value shifts slightly lower as the input power increases. These are because the input power is pretty high and the junction capacitance of the diodes, which is input power dependent at low input power levels, is negligibly small, and only the real part of the diode impedance changes as the input power levels are varied.The sharp decrease in the RF-DC conversion efficiency for high load resistance values at high input power levels happens because the output voltage becomes larger than the breakdown voltage of the diode, resulting in limiting effects. As a result of the measurements, the estimated maximum RF-DC conversion efficiency of $76.3\,\%$ was achieved for the $1772\,\Omega$ load resistance for E-field harvester and $88.5\,\%$ was achieved for the $2996\,\Omega$ load resistance for H-field harvester based on the measurements. The reason why the simulation and measurement results for the E- and H-field harvester show minor disagreements in terms of the optimal load resistance is assumed to be the fact that the estimated input power from the S-parameters measurement is lower than the actual input power, practically causing some amount of mismatch between the receiver and the RF-DC conversion circuit. Also, the difference between the ideal and the actual lumped components could be the cause of the higher loss in the measurement. As depicted in Fig. 4.8 (b) and Fig. 4.9 (b), an operation test using a LED was conducted by replacing the load resistance with a LED while mounting the prototype of E-field harvester on the wrist, and sticking the H-field harvester prototype on the back of the hand. As a result, the LED was successfully turned on utilizing only the harvested energy from the handheld radio under the typical radio operation conditions for both scenarios [80], [81].

4.2.2 System-Level Operation Test Utilizing Micro-controller Module

One of the fundamental motivations of this research is to overcome the problem of the "cold start" of ICs by introducing a wearable flexible near-field energy harvesting circuit. To test the applicability of the proposed harvester to wireless autonomous sensing devices, this research conducted an operation test utilizing off-the-shelf micro-controller modules.

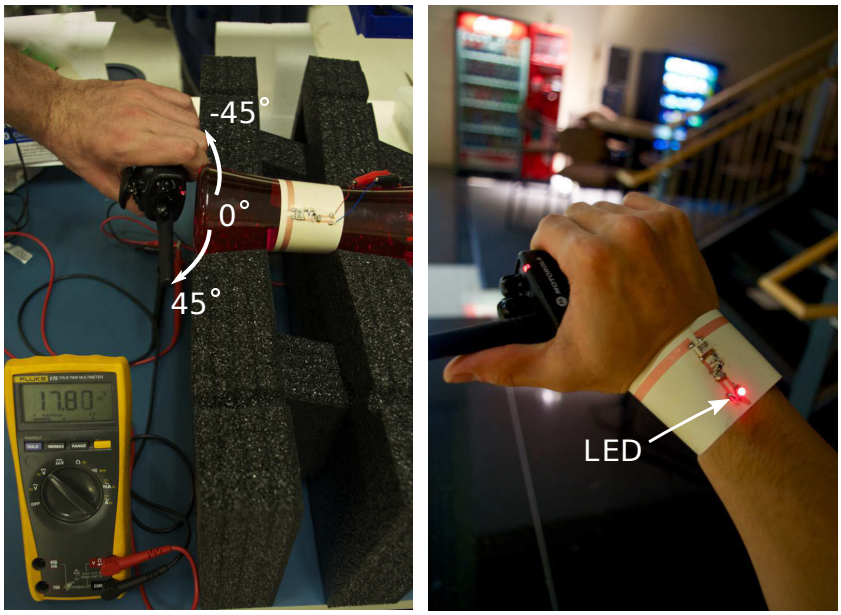

(a) (b)

Figure 4.8. (a) Open voltage measurement of E-field harvester with an on-bottle setup. (b) Operation verification of the E-field harvester on the wrist.

Fig. 4.12 shows the setup for the operation verification. The harvested energy was stored in the energy storage unit, which was composed of a $1000\,\mu\mathrm{F}$ Tantulum capacitor and voltage regulators to protect the capacitor and the micro-controller module. The MSP430 base micro-controller unit, eZ430-RF2500 provided by Texas Instruments, was used as the Access Point (AP) and the End Device (ED). The module has the functionality of wireless communication at $2.45\,\mathrm{GHz}$, while functioning as a thermometer utilizing an analog-to-digital converter (ADC). The operation and the duty cycle of the ED, which was powered by an H-field harvester, were optimized to realize a low power consumption. The current flow to the ED when the module was powered by a $3.3\,\mathrm{V}$ voltage source was measured by using a digital oscilloscope, Tektronix DPO7354, as is plotted in Fig. 4.13, which clearly shows an initial operation state and a normal operation state. During the initial operation, the ED sequentially performs the following four tasks: initializes the micro-controller, establishes communication between the ED and the AP, acquires the temperature data using ADC, and sends the data back to the AP by transmitting RF signals. Similarly, the ED acquires the temperature data and sends the data to the AP during the normal operation.

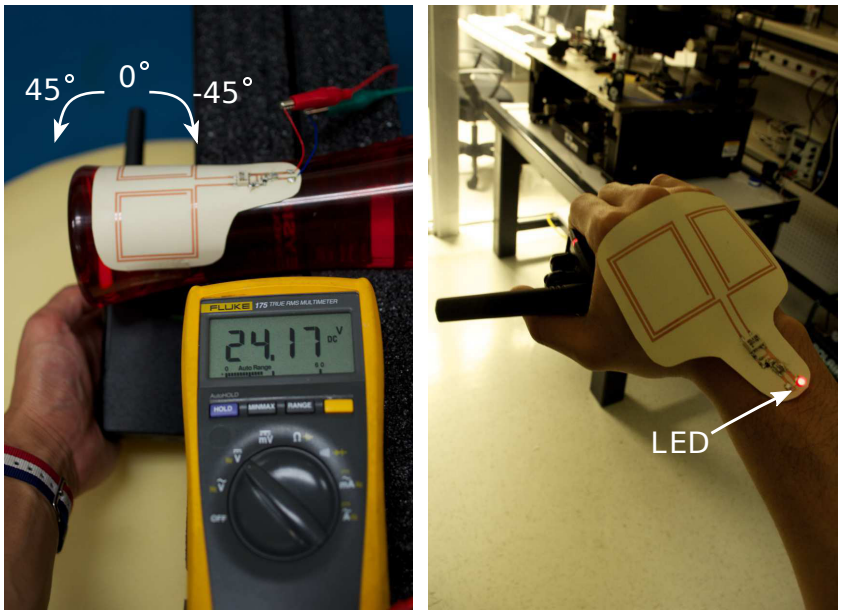

(a) (b)

Figure 4.9. (a) Open voltage measurement of H-field harvester with an on-bottle setup. (b) Operation verification of the H-field harvester on the hand.

In order to start up the operation, about $986\,\mu\mathrm{J}$ of energy is required at the supply voltage of $3.3\,\mathrm{V}$. At the normal operation, the module requires about $193\,\mu\mathrm{J}$ of energy for every measurement. These values are computed by integrating the instant power consumption during the initial and the normal operation states obtained from the previous oscilloscope measurement data. Also, the initial operation requires the maximum instantaneous power of $123.75\,\mathrm{mW}$, which is about 1.32 times larger than in the normal operation. Without loss

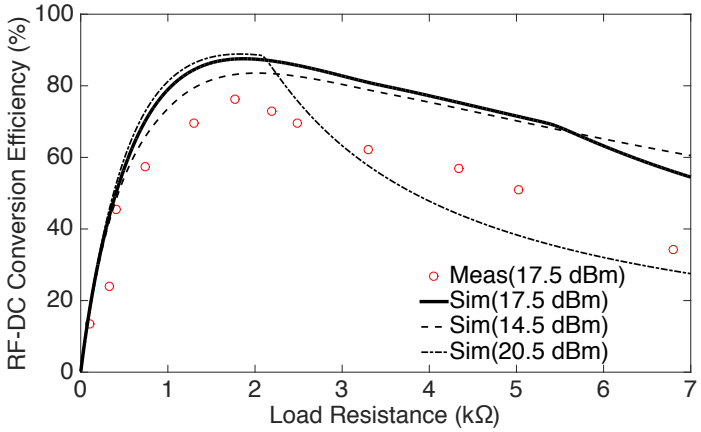

Figure 4.10. Simulated and estimated RF-DC conversion efficiency values from S-parameters measurements and the measured output DC power from E-field harvester prototype with respect to load resistance.

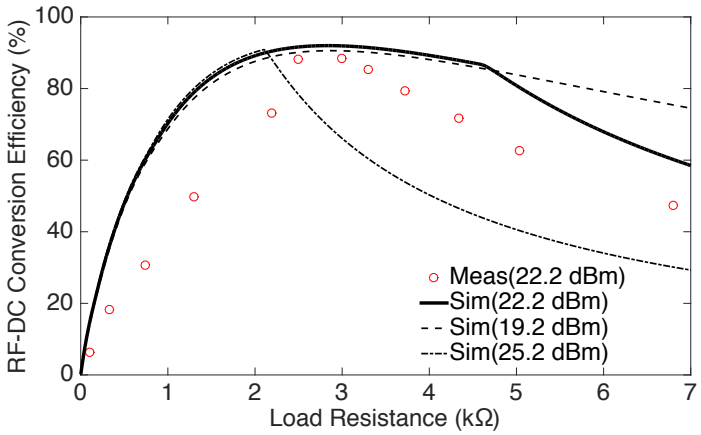

Figure 4.11. Simulated and estimated RF-DC conversion efficiency values from S-parameters measurements and the measured output DC power from H-field harvester prototype with respect to load resistance.

of generality, this work assumed that the temperature acquisition and data transmission are conducted at an arbitrary interval, which is represented as Td in the Fig. 4.13. For the operation verification test, the duty cycle was chosen as $5\,\mathrm{s}$ for practical proof-of-concept purposes. After each measurement, the ED stays in low power consumption mode until the next measurement, and consumes about $4.3\,\mu\mathrm{W}$ of power according to the application note [82]. As a result of the verification test, the ED turns on within $1\,\mathrm{s}$ from the "cold start" and starts sending the data once the two-way talk radio was turned on. After $1\,\mathrm{s}$ of charging, the ED can repeat the normal operation for 3 to 5 times at the duty-cycle of $5\,\mathrm{s}$. The number of operations was confirmed by counting the number of the communication logs shown on the computer. It can be assumed that the variation in the number of operations was caused by the variance in the stored energy in the capacitor after the charging because the DC power from the harvester varies depending on the load resistance and the misalignment. Also, the required energy for the ED to establish the communication with the AP changes depending on how fast they establish the communication link. The number of "autonomous" operations could not exceed 5 times even if the charging time was increased, which is implying that the capacitor in the energy storage unit had been already saturated after $1\,\mathrm{s}$ of charging. Therefore, it is assumed that it would be possible to extend the operation time by introducing a high-capacity energy storage device, such as a Lithium ion battery.

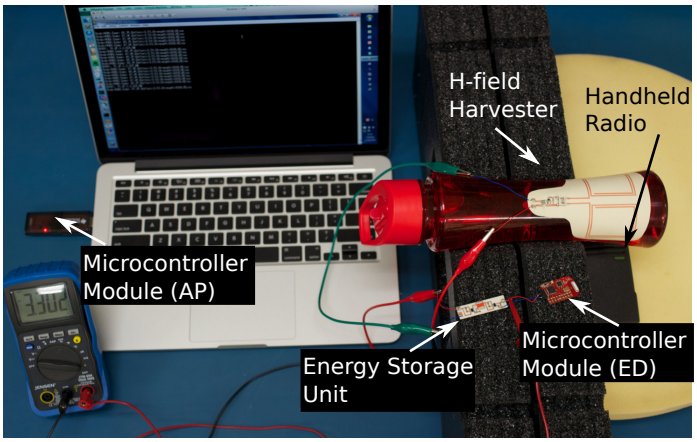

Figure 4.12. Setup for the operation test of H-field harvester using a micro-controller module.

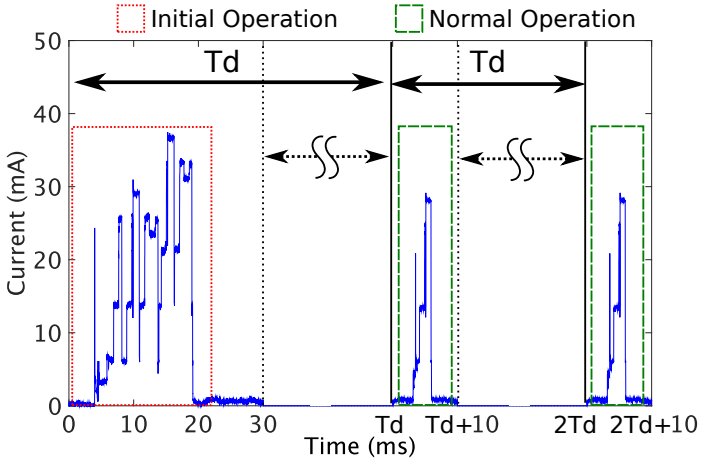

Figure 4.13. Measured micro-controller module (ED) current flow in the initial operation state and in the normal operation state.

4.2.3 Effect of Harvester on the Two-Way Radio Communication Quality

Since the energy harvester circuit is utilizing energy which is originally expected to be used for communication signals, it possibly degrades the quality of communication. To specify the effects of the energy harvesting circuit on the handheld radio communication performance, the received power, which represents the quality of communication, was measured in the anechoic chamber for the following three different conditions at $1\,\mathrm{m}$ and $2\,\mathrm{m}$ separation distances between the transmitter and the receiving antenna; (i) the harvester prototype on the water bottle is placed in the proximity of the radio as is Fig. 4.9, (ii) only the water bottle is placed near the radio and (iii) both the water bottle and the harvester

prototype are removed from the vicinity of the radio. The measurement setup is shown in Fig. 4.14[80] involving one prototype of the E-field harvester. For the measurement, one prototype of the E-field harvester was used. The receiving antenna was a monopole antenna, ANT-433-CW-QW from Linx Technologies Inc,. The measurement results are depicted in Fig. 4.15, verifying that the difference in the received power between the case (i) and the case (ii) at two different separation distances in the far field were quite small, meaning that the effects of adding a wearable harvester to a hand holding a radio are almost negligible. On the other hand, the difference between case (ii) and (iii) is quite significant, which implies that the effect of harvesting is small compared to the effect of existence of water bottle, which is probably causing fading. Therefore, it can be concluded that the degradation of the communication performances of the two-way talk radio by the presence of the energy harvesting circuit is much smaller compared to the human body effect.

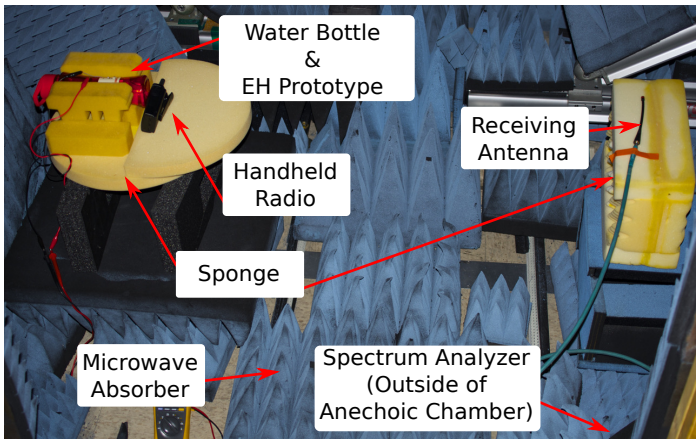

Figure 4.14. Received power measurement in an anechoic chamber.

4.3 Real-time Active Matching Circuit for Wearable Flexible RF Energy Harvester

In the previous section, it is proved that the wearable energy harvester can provide enough power to turn on an MCU. The major challenge in the realization of efficient harvesters of this type is the significant variation of Transmitter (Tx) and Receiver (Rx) network topology due to human movements and of the resulting change in the input power

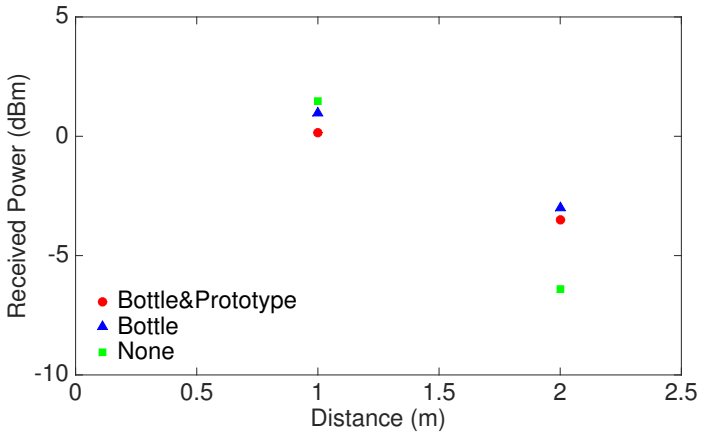

Figure 4.15. Effect of harvester prototype on received communication power.

levels of the harvester, along with the variations of harvester's load resistance during their actual operation. In the literature, some techniques, such as resistor emulation and resistance compression network, to overcome these input power and load resistance variations have already been reported [39], [83], [84]. However, even with these techniques, it is difficult to compensate the potential Tx-Rx network impedance variation, which can significantly degrade the performance of the wearable harvester especially when there is a high coupling between Tx and Rx. In order to overcome this mismatching problem, in this paper, a novel real-time active matching circuit design process based on measurements as well as on the hybridization of a genetic algorithm and a data mining method is discussed.

4.3.1 Real-time Active Matching System for Near-field RF Harvester

A typical near-field wearable energy harvesting system with a real-time active matching circuit can be generally modeled as shown in Fig. 4.16. For this research, a Motorola RDU4100 handheld radio (2 W mode), that operates at the fixed frequency of 464.5 MHz is expected to be the RF energy source to be harvested. From the measurement with a power sensor (NRP-Z211 from Rohde & Schwarz), the actual transmitted power from the hand held radio is 2.2 W. The values of each circuit component are summarized in Table 6.9. In our harvester, a voltage doubler topology using a two-diode package chip is used in order to achieve a high output voltage with a miniaturized feature size to solve the issues

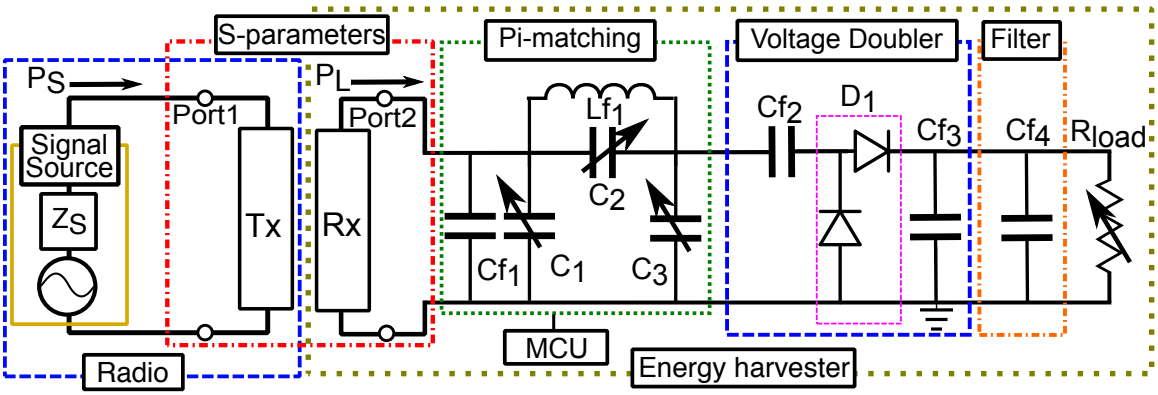

Figure 4.16. Generalized near-field wearable energy harvester system with real-time active matching circuit model.

of both "cold start" and limited available footprint. The variable capacitor can change its capacitance in the range of 6.4 to $13.3\,\mathrm{pF}$ by $0.22\,\mathrm{pF}$ steps, thus leading to 32 potential values.

TABLE 4.1
PARAMETERS OF RF-DC CONVERSION CKT COMPONENTS

Names	Part numbers	Values	Power
Cf_1	S 0603	$10.0\,\mathrm{pF}$	-
Cf_2 Cf_3	S 0603	$1.0\,\mathrm{pF}$	-
Cf_4	E 1111	$390\,\mathrm{pF}$	-
Lf_1	L 0603	$6.8\,\mathrm{nH}$	-
R_{load}	-	100 to $5000\,\Omega$	-
D_1	HSMS282C	-	-
C_1 C_2 C_3	MAX1474	6.4 to $13.3\,\mathrm{pF}$ $0.22\,\mathrm{pF}$ step	$660\,\mu\mathrm{W}$ (Active) $33\,\mu\mathrm{W}$ (Normal)
MCU	MSP430F2274	-	$<1.2\,\mathrm{mW}$ (Active) $<3\,\mu\mathrm{W}$ (LPM)

The basic design of the matching circuit is a Pi-network that is composed of two shunt variable capacitors and one series variable capacitor which is parallel connected to a fixed inductor (Lf_1), yielding 32^3 different impedance value combinations. In order to prevent the self-resonance of this parallel LC network at $464.5\,\mathrm{MHz}$, Lf_1 was chosen to be $6.8\,\mathrm{nH}$ [85]. The fixed-value parallel capacitor Cf_1 is used to shift the minimum capacitance value of C_1. The value of the other fixed parallel capacitors are chosen from the list of Johanson

Technology's lumped components to maximize the output DC power at the load in ADS simulation. The basic operation of the active matching circuit is a simple "brute force" method[86]. The micro-controller unit (MCU) tries a list of preassigned capacitor values combinations to decide the best capacitor combination featuring the highest load DC power ("selection" state), keeps this combination for a while ("execution" state), and finds the best combination again after a certain amount of time. The genetic algorithm and the clustering are used to identify the optimum list of capacitor value combinations over time-varying conditions. In terms of the power consumption, both the MCU and the variable capacitors need to be in active mode during the "selection" state and consume about $3.15\,\mathrm{mW}$ of power. During the "execution state", the variable capacitors are in normal mode and the MCU is in low power mode (LPM), consuming about $100\,\mu\mathrm{W}$ of power.

4.3.2 Characterization of Effect of Human Movement for Tx-Rx Network

The transducer gain G_T in Eq. (4.3), which is the ratio of the power delivered to the load P_L and the power from the signal source P_S, is one of the most commonly used expressions to evaluate the quality of power transfer. Since the reflection coefficient Γ_L in Eq. (4.3) is a function of load impedance Z_L, there is an optimal load impedance value that gives the maximum RF power transfer to the load [71]. Therefore, in order to characterize the effect of the human body movement on the Tx-Rx network, the S-parameters of the Tx-Rx network were periodically measured using a vector network analyzer, ZVA8 from Rohde $\&$ Schwarz, which was controlled by using LabVIEW. As a proof-of-concept and without loss of generality, a coil shape flexible receiver fabricated on a liquid polymer crystal (LCP) substrate utilizing inkjet printing technology was wrapped around a spindle-shaped plastic bottle filled with water with a separation distance of about $7\,\mathrm{cm}$ and a model of the two-way talk radio with a whip antenna (RAN4033A) was randomly tilted within the range of movement of human wrist as depicted in Fig. 4.17(a). The S-parameters were sampled every $0.25\,\mathrm{s}$ for about $25\,\mathrm{s}$ to obtain 100 sample data, to represent the full range of

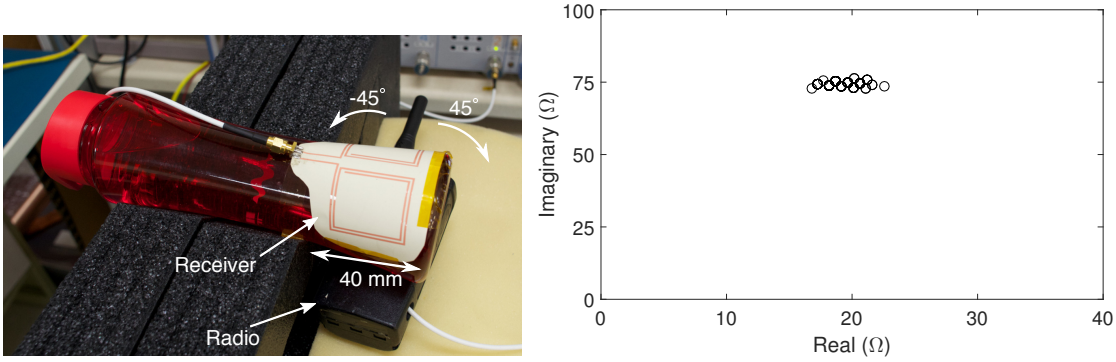

(a) (b)

Figure 4.17. (a) Tx-Rx network characterization measurement with an on-bottle setup. (b) Optimal load impedance value for each of the 100 sampled S-parameters with an on-bottle setup.

possible configurations of the handheld two-way talk radio. For each sample, the optimal load impedance was computed and the results are depicted in Fig. 4.17(b). As can be seen in the figure, the impedance variation in this Tx-Rx configuration is $\pm$ 20 % around the average value of the real part.

$$G_T = \frac{P_L}{P_S} = \frac{|S_{21}|^2(1-|\Gamma_L|^2)}{|1-S_{22}\Gamma_L|^2} \quad Z_L = Z_0\frac{1+\Gamma_L}{1-\Gamma_L} \tag{4.3}$$

4.3.3 Matching Circuit Design using GA and Clustering

From the previous S-parameter measurements, it is determined that the impedance variation in the Tx-Rx network because of human movement is limited. However, there are still the effects of the load resistance variation and input power level variation, which cannot be optimally compensated using a passive matching circuit[71]. One of the commonly used techniques to compensate these effects is to stabilize the load impedance value by using a DC-DC converter. However, by using this technique, we would typically be able to achieve only below 70 % of RF-DC-DC conversion efficiency[45], which can be significantly improved by using the real-time active matching circuit. Since the RF-DC conversion circuit includes active circuit components, the analytically computed maximum transducer gain value does not always guarantee the highest power transfer to the DC load. In order to

properly assess the quality of the harvesting circuit, the measured S-parameters are integrated in the circuit simulation utilizing Keysight ADS2015, and the actual available DC power is used as a measure for quality assessment. The final goal of this matching circuit design is to determine a reasonable number of capacitor value combinations which can match as many as possible Tx-Rx network conditions and uncertainties as well as the load resistance value variations out of the potential 32^3 discrete capacitor value combinations. The first stage involves the identification of the best capacitance value combination for each S-parameter sample with different load resistance values. For the proof-of-concept harvester presented in this paper, the load resistance variation included 14 different resistance values from 100 to $5000\,\Omega$ (from 100 to $2000\,\Omega$, $200\,\Omega$ step and from 2000 to $5000\,\Omega$, $1000\,\Omega$ step) are used, which implies there are 1400 sample-resistance value combinations to be optimized. For this stage, the genetic algorithm solver in the optimization function in ADS was utilized. Genetic algorithms (GA) are widely used heuristic search methods, and by introducing this solver, the simulation time and required memory are reduced drastically (more than 5 times) compared to trying all 32^3 possible capacitance value combinations. This GA process utilizing the 100 measured S-parameter samples reported above requires about $4\,\mathrm{h}$ to optimize all the sample-load resistance combinations. Because of the limited amount of available memory on the computer, the number of iterations for each optimization was restricted to 30, but the practical cases that the solution does not converge within 30 iterations were quite rare. In Fig. 4.18, the comparison between an ideal RF-DC conversion, which is equivalent to the P_L when the transducer gain is the highest, a typical RF-DC-DC conversion efficiency of $70\,\%$ and our genetic algorithm simulation results are depicted. For simplicity and fair comparison, the delivered load power benefits from the genetic algorithm were reduced by the matching circuit power consumption in the active mode. As can be easily observed, the proposed real-time matching circuit can deliver a higher amount of power at 1289 out of 1400 data points ($92.0\,\%$), for a maximum additional power delivered to the load of $34.1\,\mathrm{mW}$. Similarly, in Fig. 4.19, the comparison

between the case of the active matching circuit and the case of one fixed capacitor combination, which is optimized to give the highest output power among all the sample-load resistance combinations is plotted. At 975 out of 1400 data points ($69.6\,\%$), the additional power delivered to the load was positive for the proposed active matching circuit with a maximum value of $56.3\,\mathrm{mW}$. In Fig. 4.20, the distribution of the available DC power increase for both the RF-DC-DC converter case and the fixed matching circuit case are shown with their arithmetic mean values. The highest number of counts can be seen at the bin of 10 to $15\,\mathrm{mW}$ for the case of RF-DC-DC, which is implying that the degradation of matching and power dissipation associated with the use of DC-DC conversion circuit can be improved. Similarly, in the case of fixed matching, the highest number of counts can be seen at the bin of -10 to $0\,\mathrm{mW}$. This is mainly because of the power consumption of the micro-controller and the active matching circuit. On average, about $14.9\,\mathrm{mW}$ and $10.2\,\mathrm{mW}$ available DC power increases can be achieved, respectively. These results imply that the there is a high potential of a significant increase in available DC power using the proposed active matching circuit.

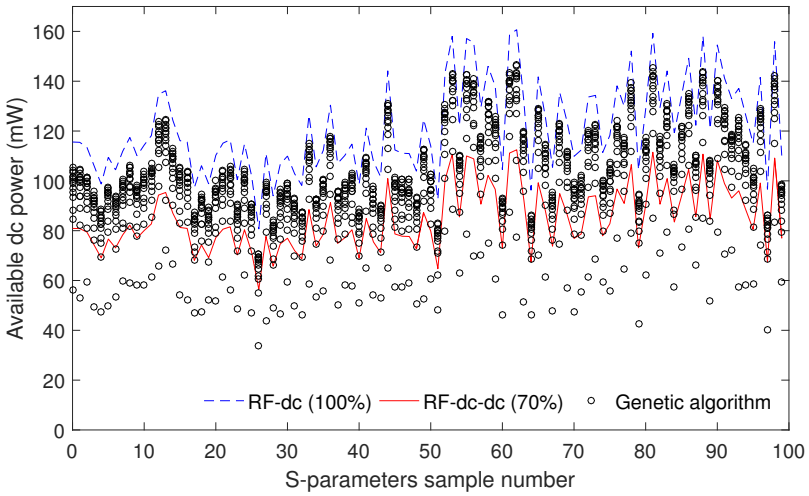

Figure 4.18. Available DC power with ideal RF-DC conversion, typical RF-DC-DC conversion and GA optimized capacitor combinations.

However, we still have 1400 choices of capacitor value combinations as the candidates of the final list of capacitance combinations, which is not a practical number of combina-

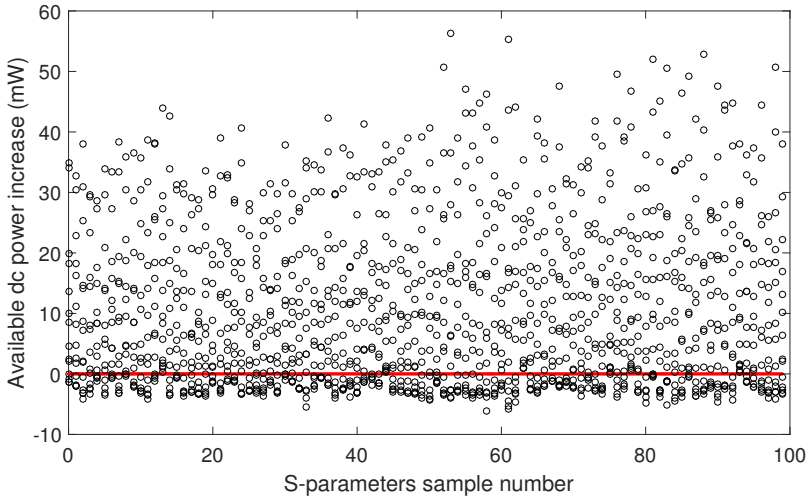

Figure 4.19. Delivered DC power increase with GA optimized capacitor combinations compared to one fixed capacitor combination.

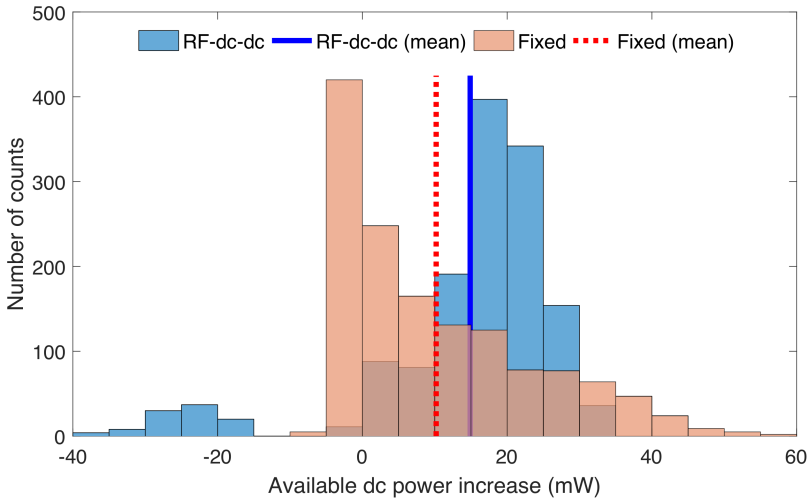

Figure 4.20. Distribution of available DC power increase for RF-DC-DC converter case and fixed matching circuit case, and their arithmetic mean values.

tions that can be tried one-by-one during the "brute force" real-time matching operation, especially with a low computational power micro-controller unit. In order to choose a much smaller but almost equally efficient subset of value combinations out of these 1400 cases, we employed the k-means clustering method, which is commonly used for the data mining from big data, utilizing MATLAB. At the beginning of the data mining, we have set automatically generated 1000 replicates as starting points in order to increase the accuracy of the clustering[87]. For the proof-of-concept of clustering data mining method, 64 and 27 representative data points, that are equivalent to using 4 and 3 different capacitor values for

each variable capacitor, are chosen as the the cluster sizes. In Fig. 4.21, all potential candidates from the genetic algorithm, and 64 and 27 clusters cases are plotted, and in Table 4.2, the figure of merit for all three cases listing the percentage of practical configurations "coverage" of the proposed active matching features better than conventional approaches as well as the maximum additional power delivered to the load using this approach. As can be easily concluded from the table, the degradation of performance in terms of coverage and maximum power gain are less than $3\,\%$ and $13.8\,\mathrm{mW}$, respectively, even with the drastic decrease of the number of combinations enabled by the k-means clustering approach. In actual operation, the MSP430F2774 chip is capable of 200 ksps analog-to-digital conversion (ADC), which implies that the required time for matching is less than $1\,\mathrm{ms}$ for both 64 and 27 cluster cases. This is expected to be sufficiently fast enough to real-time match and compensate the effects of load resistance variations and human movement.

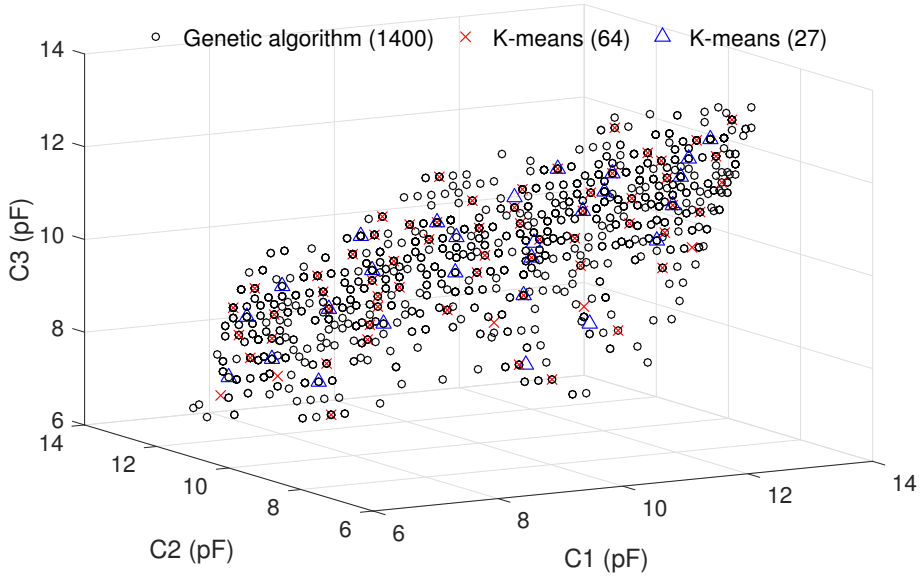

Figure 4.21. Capacitor value combinations with and without clustering.

4.4 Backscattering-based On-body Sensor Network

In previous sections, the basic operations of wearable RF energy harvesters and the real-time active matching circuit design to maximize the output DC power were discussed.

TABLE 4.2
FIGURE OF MERIT OF GA AND CLUSTERING

	DC-DC matching		Fixed passive matching	
	Coverage	Max power increase	Coverage	Max power increase
GA (1400)	92.0 %	34.1 mW	69.6 %	56.3 mW
K-means (64)	92.7 %	33.9 mW	68.4 %	45.8 mW
K-means (27)	89.4 %	30.4 mW	67.4 %	42.5 mW

Similarly, for most of the ambient RF energy harvesters in the literature, output filters are used while designing energy harvesting circuits to eliminate harmonics created during rectification to maximize the output DC power [26]. This is a reasonable circuit design choice because of the low RF input power of typical ambient RF energy harvesting systems. However, wearable RF energy harvesters in this research have extremely high RF input power compared to typical ambient RF energy harvesters and a rectifier generates harmonic signals, which also have non-negligible amount of power, during rectification processes. In stead of wasting these precious harmonic signals, in this research, a novel on-body sensor network system utilizing harmonics for backscattering communication is designed as depicted in Fig. 4.22.

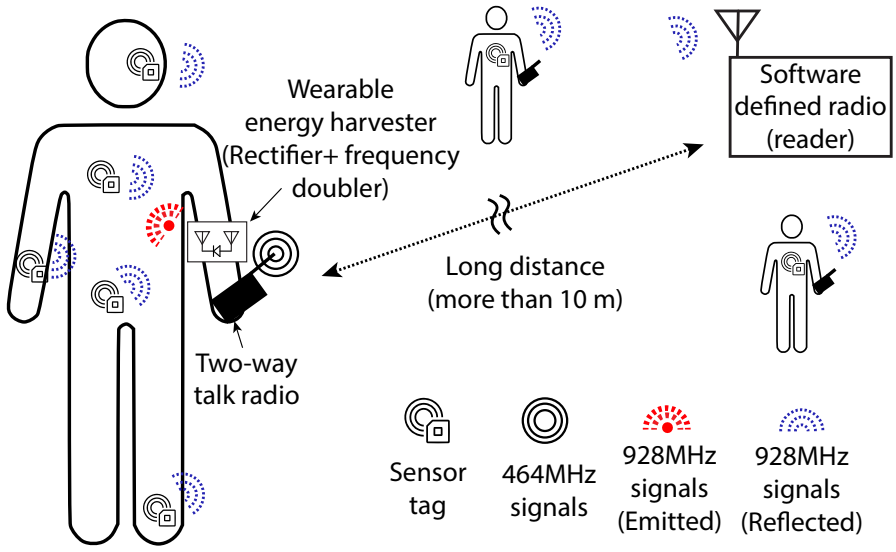

Figure 4.22. Proposed wearable energy autonomous on-body wireless sensor network system.

The basic operation principle of wireless sensing utilizing backscattering modulation [2] and the reading range extension of passive RFID tags utilizing a bistatic RFID reader with external carrier emitters [3] have been proven in literature. In this proposed research, the energy harvester simultaneously plays two roles: a DC power source and carrier emitter. Since the two-way talk radio is utilizing analog modulated signals at $464\,\mathrm{MHz}$ [71], the second harmonic from the energy harvester includes continuous RF signals at $928\,\mathrm{MHz}$, which fits in the frequency range of the conventional $900\,\mathrm{MHz}$ band UHF RFIDs. Therefore, the second harmonics from the harvester are re-emitted by a secondary antenna to illuminate backscattering sensor tags arranged on-body. Fig. 4.23 shows the detailed block diagram of the proposed system. As shown in the Fig. 4.23, the energy source is a 464 MHz two-way talk radio with $36\,\mathrm{dBm}$ output power. The energy harvester section is composed of three main components; a $464\,\mathrm{MHz}$ receiver, a proposed rectifier, and a $928\,\mathrm{MHz}$ antenna. The $464\,\mathrm{MHz}$ near-field receiver is used to harnesses the power radiated from the radio and the power is sent to the rectifier. There are two outputs generated by the proposed rectifier. The DC power is used to drive a DC load and the RF output is fed to a $928\,\mathrm{MHz}$ antenna. Each tag is composed of a rectifier for $464\,\mathrm{MHz}$ to power an oscillator, which triggers an RF transistor in the tag to create a modulation. The oscillation frequency varies depending on the resistance value of a sensing element, which is connected to the oscillator IC to enable a sensing. Thus, this energy harvesting design can enable three different applications simultaneously to establish an on-body autonomous sensing network. The following subsections describes more detailed designs each component of the system.

4.4.1 Energy Harvester Design and Measurement

Since one of the most commonly used frequency bands for RFID tags is 860 to $960\,\mathrm{MHz}$, the second harmonics from the rectifier $928\,\mathrm{MHz}$ would be a good choice for the carrier emitter. Thus, the main goal of the proposed rectifier is to generate as large power as possible at the DC and the second harmonic frequencies. Therefore, a full-wave rectifying

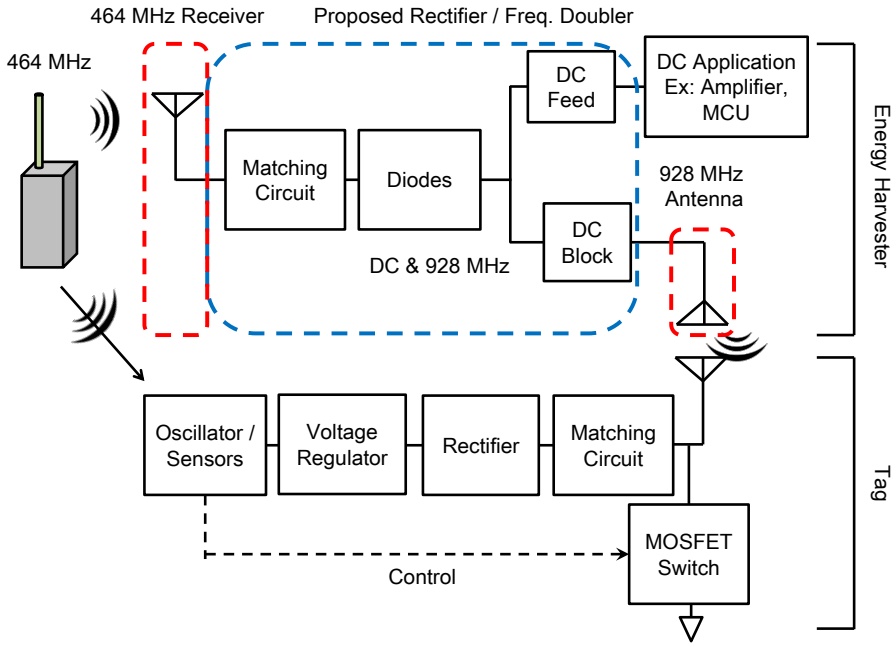

Figure 4.23. Block diagram of energy autonomous on-body wireless sensor network system.

topology is applied theoretically allowing for the elimination of the odd harmonics. Hence, the largest remaining harmonic is the second harmonic.

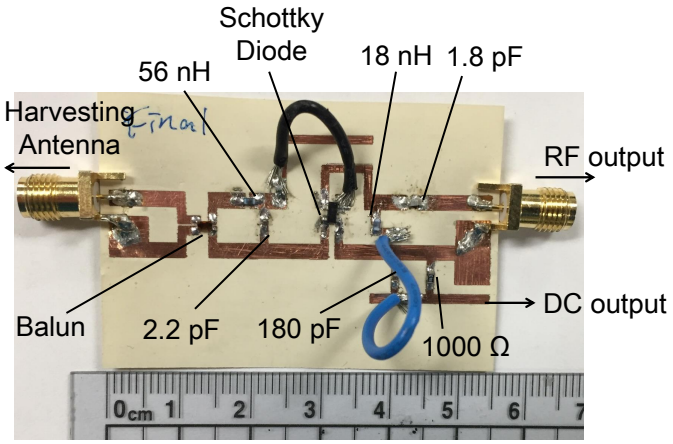

Figure 4.24. Prototype of proposed full-wave rectifier.

Fig. 4.24 shows a prototype of the proposed rectifier. A balun is used, as demonstrated in Fig. 4.24, to guarantee the differential feeding of the full-wave rectifier. The matching circuit is composed of a $56\,\mathrm{nH}$ series inductor and a 2.2 pF parallel capacitor. The HSMS 2828 Schottky diode package is used to perform the full-wave rectification. The $1.8\,\mathrm{pF}$ capacitor and the $18\,\mathrm{nH}$ inductor are serving as a DC block and a DC feed, respectively.

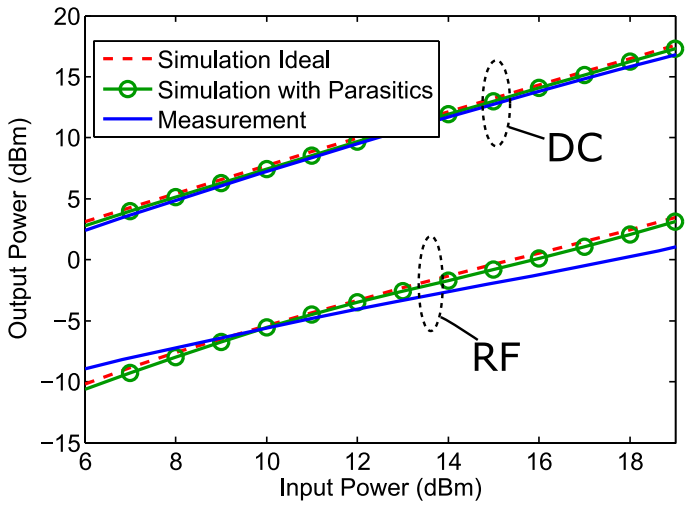

Figure 4.25. Simulated and measured output DC and RF power from the proposed rectifier with respect to the input power.

Finally, a $180\,\mathrm{pF}$ capacitor is used to eliminate higher order harmonics and a $1000\,\Omega$ resistor acts as a load.

The measured DC and RF outputs from the proposed rectifier with respect to the input power are shown in Fig. 4.25. The simulated results using Advanced Design System (ADS) are also included for comparison. Good agreement between the simulated and measured results can be observed. As shown in Fig. 4.25, the maximum DC conversion efficiency is about 61 % and the maximum RF conversion efficiency is about $3.8\,\%$. The maximum total efficiency is $63.1\,\%$ when $18\,\mathrm{dBm}$ RF input power is provided.

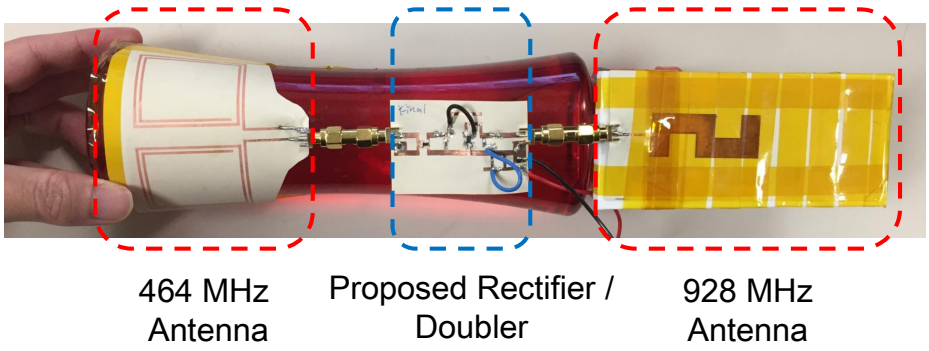

Figure 4.26. Prototype of the energy harvesting circuit for carrier emission.

The topology of the energy harvesting composite circuit including the $464\,\mathrm{MHz}$ and the $928\,\mathrm{MHz}$ antennas is shown in Fig. 4.26. The circuit is put on a water bottle filled with

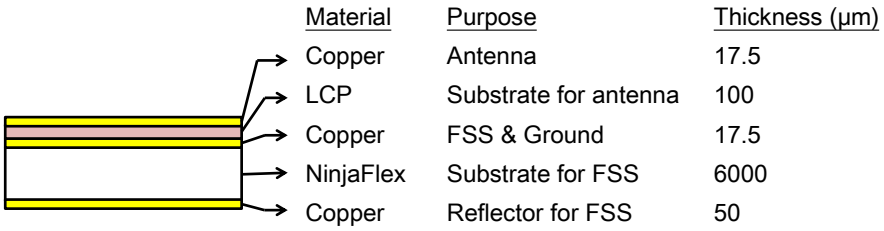

(a)

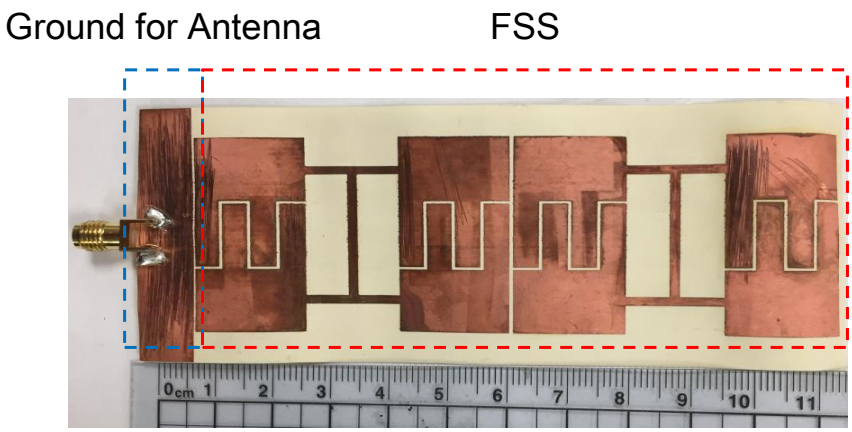

(b)

Figure 4.27. (a) Side view of the wearable 928 MHz antenna (b) prototype of the FSS.

water to mimic the effects of human body [71]. The 464 MHz near-field coupling receiver, as depicted in Fig. 4.26, is the same design as the one described above. The 928 MHz antenna is a Z-shaped monopole antenna with an artificial magnetic conductor (AMC) on the back that is used to eliminate the effects of the human body on the antenna [88]. The side view of this antenna is shown in Fig. 4.27a. It is composed of 5 layers. The top copper layer is used for the Z-shaped monopole antenna. The second layer is the LCP substrate. The AMC structure is composed of a frequency selective surface (FSS), a spacer, and a metal reflector which are corresponding to the third, fourth, and fifth layer, respectively. The thickness and the purpose of each layer are also included in Fig. 4.27a. The pattern of the FSS and the ground plane for the monopole are contained in the third layer as shown in Fig. 4.27b.

The fourth layer is a spacer between the metal reflector and the FSS. The thickness of this layer is extremely important since it affects significantly the bandwidth and the oper-

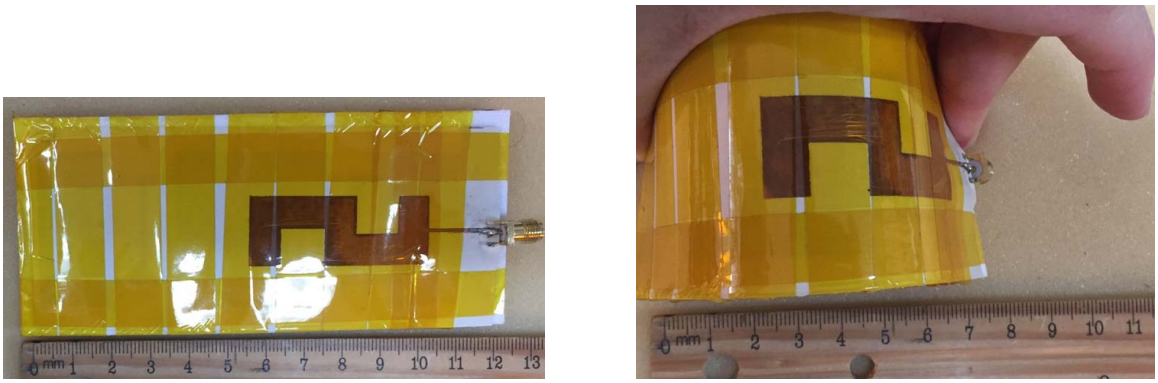

(a) (b)

Figure 4.28. Prototype of the (a) unfolded and (b) folded 928 MHz antenna.

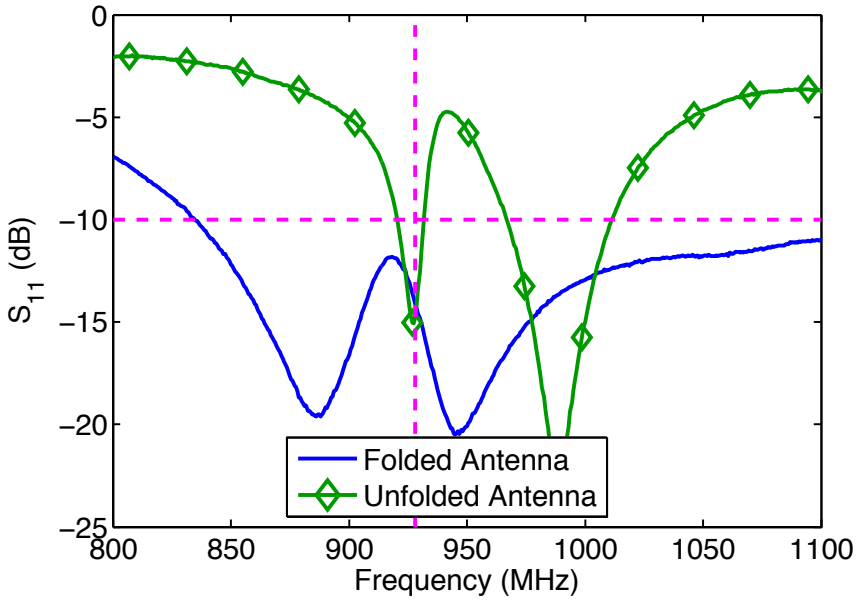

Figure 4.29. Measured S_{11} of the folded and unfolded 928 MHz wearable antenna.

ating frequency of the AMC plane [88]. However, the thickness of this layer can not be designed arbitrarily if off-shelf substrates are used. The reason is that the thicknesses of off-shelf substrates are limited to specific discrete values and it is hard to realize substrates with custom/optimized thicknesses. The 3D printing technique offers a good solution to this problem. The minimum and maximum thickness that can be realized using 3D printing are $127\,\mu\mathrm{m}$ and $25\,\mathrm{cm}$, respectively. Thus, by 3D printing flexible NinjaFlex [89], almost any arbitrary thickness values can be realized and a more optimal design of the AMC plane can be achieved. The final layer is a reflector fabricated using copper tape. The

prototype of the $928\,\mathrm{MHz}$ antenna is shown in Fig. 4.28a. Furthermore, since the $928\,\mathrm{MHz}$ antenna is wearable and flexible, the prototype under the folded condition is also shown in Fig. 4.28b demonstrating a very good flexibility. As demonstrated in Fig. 4.28b, good flexibility can be observed. The length of the unfolded one is about $12.5\,\mathrm{cm}$ and can be folded to about $8\,\mathrm{cm}$. The measured scattering parameter values of the wearable $928\,\mathrm{MHz}$ antenna are shown in Fig. 4.29. Measured results under both folded and unfolded conditions are included. As demonstrated in Fig. 4.29, the return loss values at $928\,\mathrm{MHz}$ for folded and unfolded conditions are $14.1\,\mathrm{dB}$ and $14.8\,\mathrm{dB}$, respectively.

4.4.2 Backscattering Sensor Tag Design

For on-body communication and sensing applications, a custom backscatter tag was designed and fabricated as depicted in Fig. 4.30. The power received by the Z-shaped antenna of the tag is rectified by the voltage doubler. Then a 3.3 V voltage regulator (Linear technology LT3009) is connected between the voltage doubler and the oscillator to protect the oscillator. The output signal from the Silicon Labs TS3006 oscillator is applied to trigger an RF switching MOSFET (NXP BF1118) to create modulated backscattered signals. The design was based on the MOSFET front-end from [90], used in the cutoff and saturation region. The modulation frequency varies depending on the value of a sensing element connected to the oscillator and this enables wireless sensing [2]. From a measurement utilizing VNA, the input impedance of each input power and MOSFET bias voltage condition are obtained as depicted in Fig. 4.31. For 928 MHz with -20 dBm of RF input power, the difference in the magnitude of the normalized input impedance between 0 V and 2 V bias voltage conditions is 0.775 and the phase difference is $112.3°$ from the measurement. Also, the input impedance with respect to each input power level of 928 MHz signal (-5, -10, and -20 dBm) at the MOSFET bias voltage conditions of 0 and 1.55 V is obtained as depicted in Fig. 4.32.

As shown in Fig. 4.31, the impedance value difference while the MOSFET is on and off

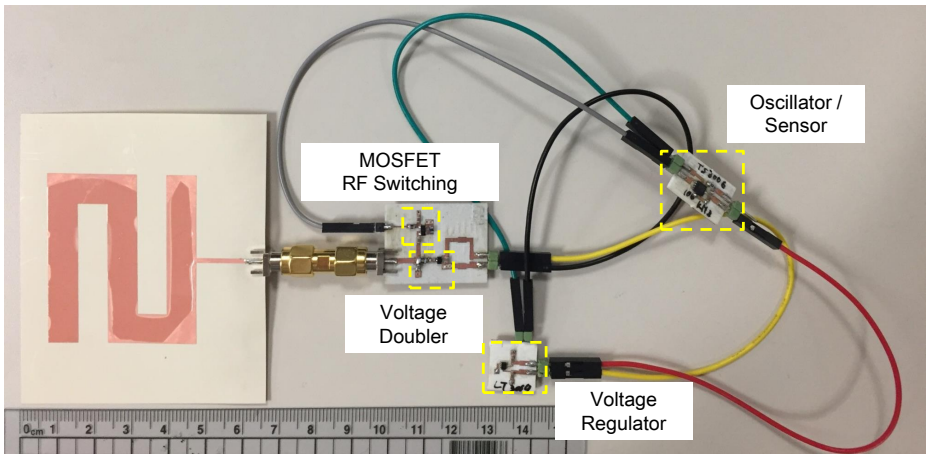

Figure 4.30. Prototype of the custom RFID tag for on-body sensing.

are sufficiently large to create modulation even if input RF power level is varied. Fig. 4.33 depicts the measured output voltage from the voltage regulator connected with the voltage doubler with respect to RF input power level ($464\,\mathrm{MHz}$) at each MOSFET bias voltage condition when $824\,\mathrm{k\Omega}$ resistor, which is expected equivalent DC resistance of the oscillator IC, is connected as a load. According to the measurement results, the tag requires about $-5\,\mathrm{dBm}$ of input power to achieve $1.55\,\mathrm{V}$ to start the operation of the oscillator IC. From Friis transmission equation, by taking advantage of relatively low frequency and high transmitted power from the two-way talk radio, the tag operation distance of 1 to $2\,\mathrm{m}$, which can cover the entire human body, can be realized even with the antenna realized gain of -17 to $-11\,\mathrm{dBi}$. This offers the flexibility of using practical on-body antennas without the need for high gain and large form-factors.

Integration with Ammonia Sensor

The modulation frequency is determined by the oscillation frequency which varies as a function of the external load resistance value of the oscillator IC. Therefore, it is possible to integrate arbitrary sensors (in this case a gas sensor) that changes its impedance when it is exposed to certain chemicals, into the custom backscattering tag in Fig. 4.30 to detect the existence of specific gases by measuring the change in oscillation frequency. Therefore, the resistor in the previous prototype shown in Fig. 4.30 was replaced with a printed anmonnia

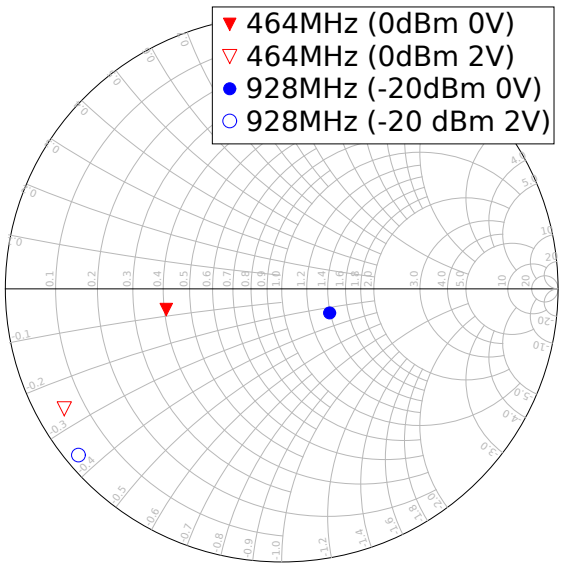

Figure 4.31. Measured S-parameters of 464 MHz and 928 MHz with each expected input power and MOSFET bias voltage.

sensor reported in [91] as depicted in Fig. 4.34. The impedance of the ammonia sensor increases when it is exposed to ammonia gas and the oscillation frequency is expected to decrease due to the change of the impedance. Experimental results shown in Section 4.4.6 confirm this assumption.

4.4.3 DC and RF Performance Evaluation

To evaluate the performance of the energy harvester shown in Fig. 4.26, the ambient RF source (two-way talk radio) is placed at a distance of 9 cm from the frequency doubler/rectifier. The measured DC voltage at the output of the proposed rectifier is 7.53 V with a 1 kΩ resistor which equals 17.5 dBm. Moreover, the measured 928 MHz signal at the output of the proposed rectifier is 1.43 dBm. To evaluate the link budget, the antenna of the tag is placed 30 cm away from the energy harvester, where it measured a received 928 MHz level of -22.2 dBm. The measurement setup of the entire system is shown in Fig. 4.35. As depicted in Fig. 4.35, with the help of the 928 MHz carrier emitted from the proposed energy harvester, the backscattered signal from the proposed RFID tag can be detected by the software defined reader which is located at 17 m away.

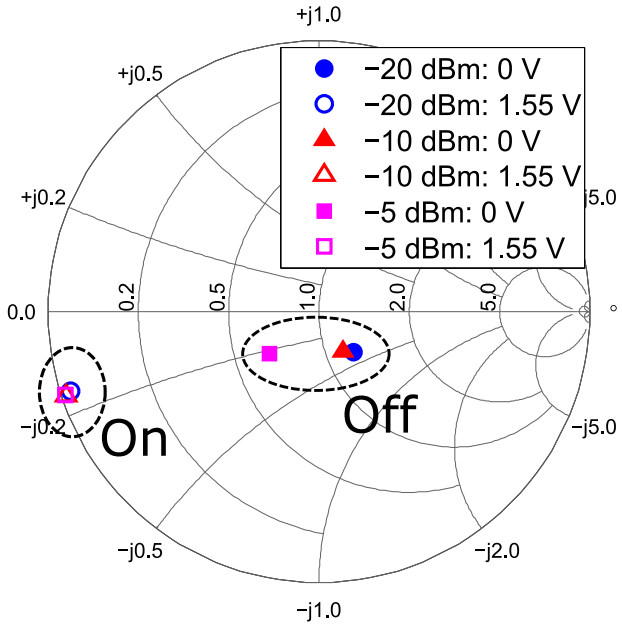

Figure 4.32. Measured S-parameters of 928MHz with each expected input power and MOSFET bias voltage.

4.4.4 Operation Range Extension Using an RF Amplifier

In the previous subsection, it is proved that the entire system properly operates, but the DC power is not fully utilized. Also, the second harmonics are relatively low power and this limits the separation distance between the harvester and the tag to below $30\,\mathrm{cm}$. Therefore, as one of potential usages of the DC power, the integration of RF amplifier for the operation range extension is discussed. The new block diagram of the proposed energy harvester with the amplifier is depicted in Fig. 4.36.

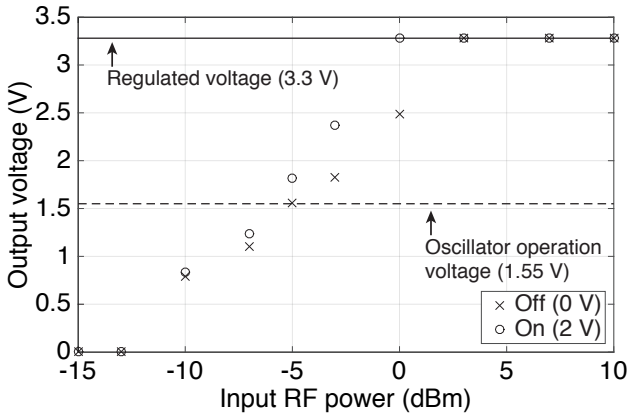

Figure 4.33. Measured output voltage from the voltage regulator connected with the voltage doubler with $464\,\mathrm{MHz}$ RF input signal at each input power and MOSFET bias voltage.

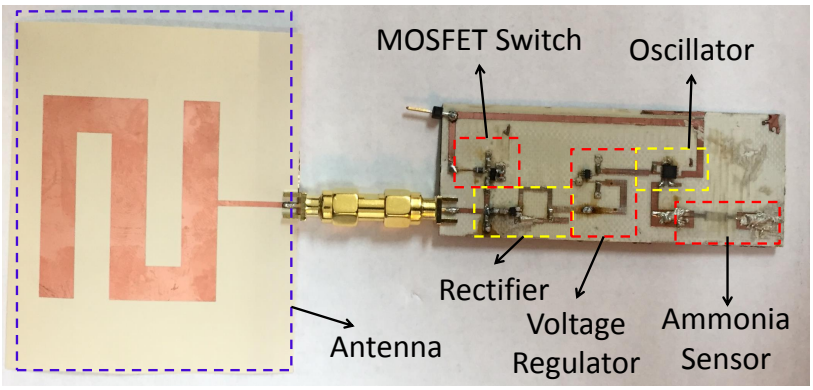

Figure 4.34. Prototype of the custom backscattering RFID tag with a printed ammonia sensor.

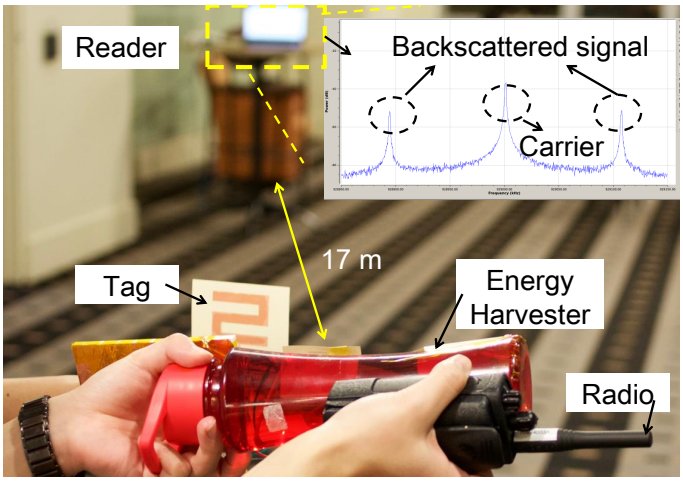

Figure 4.35. Measurement setup for the wearable RF energy harvester powered on-body backscattering sensing system.

The first step is to select an appropriate RF amplifier chip for this application. As discussed in previous sections, near-field RF energy harvesting can generate relatively high power compared to far-field RF energy harvesting. Having that said, the available DC power is below $100\,\mathrm{mW}$, so it is critical to choose an RF amplifier IC which operates with the budgeted DC power. Also, the device supply voltage needs to be low so that the harvester can generate voltage high enough to drive the IC with the relatively low expected equivalent DC load resistance value. By considering all these aspects, MGA-68563 chip, which has the typical supply voltage and current of $3\,\mathrm{V}$ and $15\,\mathrm{mA}$ ($45\,\mathrm{mW}$ with $200\,\Omega$), respectively, from Avago (Broadcom) was selected for this application. According to the datasheet, the gain at $900\,\mathrm{MHz}$ with the typical operation conditions ($3\,\mathrm{V}$ and $15\,\mathrm{mA}$) is

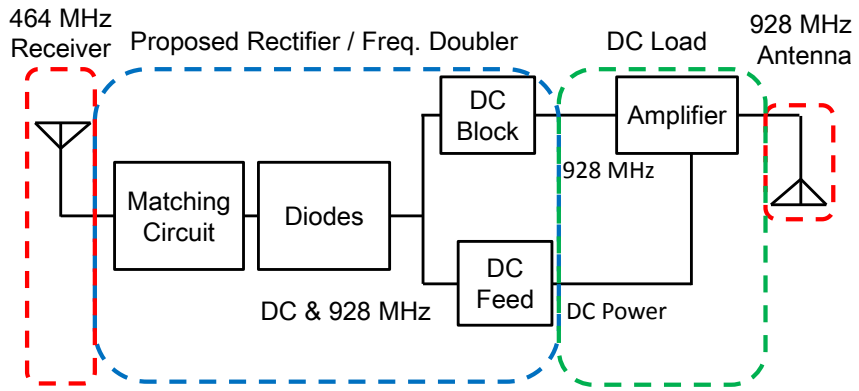

Figure 4.36. Block diagram of the proposed energy harvester with enhanced RF output by driving an RF amplifier using DC output power.

$18\,\mathrm{dB}$ with P1dB compression point of $17.5\,\mathrm{dBm}$, which is above the RF output from the energy harvester. Therefore, theoretically the use of this RF amplifier can extend the operation range by about eight times making the maximum harvester to tag separation distance more than $2\,\mathrm{m}$, which can sufficiently cover the entire body of most human beings.

Fig. 4.37 and Fig. 4.38 depict measured supply current and equivalent load resistance with respect to supply voltage of the RF amplifier, respectively. Similarly, Fig. 4.39 shows the measured power consumption of the RF amplifier with respect to the supply voltage. From these figures, it is clear that the equivalent resistance saturates at $200\,\Omega$ and the power dissipation increases as the supply voltage increases. Although the power consumption is much lower than the expected DC power from the harvester, the circuit can accommodate to slight shift in equivalent load resistance value.

Fig. 4.40 shows measured amplifier gain with respect to the RF input power with supply voltages of $2\,\mathrm{V}$ and $3\,\mathrm{V}$. According to the measurements, the maximum amplifier gain is about $10\,\mathrm{dB}$, which is still capable of extending the maximum operation rage to about $1\,\mathrm{m}$. The difference in maximum gain from the datasheet and the mesurement is assumed to be caused by mismatch between the output of the harvester and the input of the amplifier, and this can be improved by changing the matching, but this slight modification of the circuit is beyond the focus of this research.

Next, the amplifier was integrated in the RF energy harvesting capable RF carrier emit-

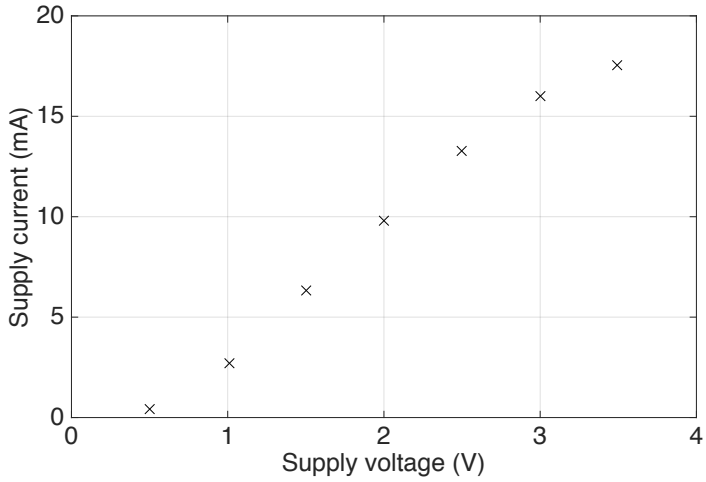

Figure 4.37. RF amplifier's supply voltage vs. supply current.

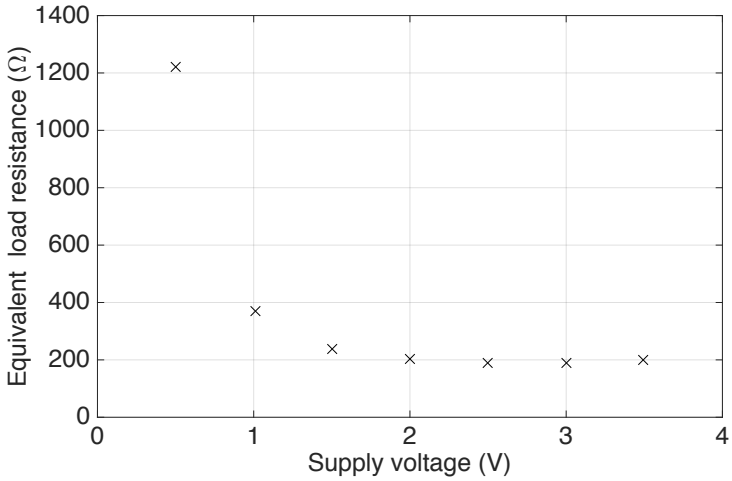

Figure 4.38. RF amplifier's supply voltage vs. equivalent load resistance.

ter as depicted in Fig. 4.41 and the comparison of the 928 MHz output between the harvesters with and without the amplifier is shown in Fig. 4.42. The output 928 MHz power is much larger with the help of the amplifier and the effect is more significant when the input power is larger. The 928 MHz output power is about 9 dB larger when the input 464 MHz signal is about 19 dBm. One thing to note is the maximum conversion efficiency from $464\,\mathrm{MHz}$ RF input to $928\,\mathrm{MHz}$ RF output is about $16\,\%$, which is much higher efficiency than the typical off-the-shelf voltage controlled oscillator (VCO) ICs' DC-RF conversion efficiency of 5 to $10\,\%$. Therefore, it is more efficient to utilize both the DC and second harmonics instead of maximizing the RF-DC conversion efficiency to directly feed VCO ICs,

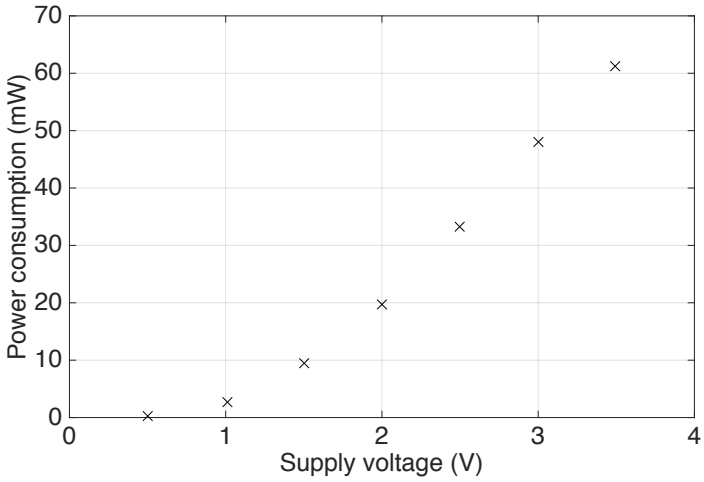

Figure 4.39. RF amplifier's supply voltage vs. power consumption.

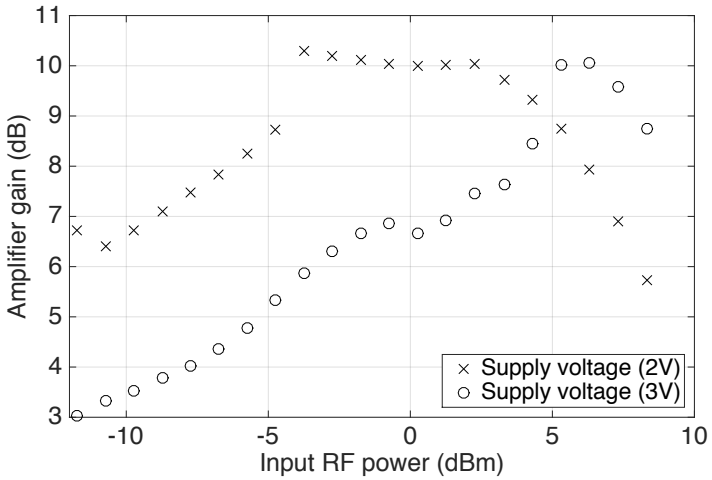

Figure 4.40. Amplifier gain vs. RF input power with supply voltage of $2\,\mathrm{V}$ and $3\,\mathrm{V}$.

especially the RF-DC conversion loss during the rectification is also taken into account.

Finally, a long-range field measurement was conducted in an office area as depicted in Fig. 4.43 [92]. As a result of the measurement, a tag to reader separation distance of more than $75\,\mathrm{m}$ was confirmed in while maintaining an signal to noise ratio (SNR) is more than $10\,\mathrm{dB}$ with the noise floor of -80 to $-70\,\mathrm{dBm}$. As the typically required signal-to-noise ratio for detection is 3 dB, there is still a margin of 7dB. According to Friis equation, this implies the reading range can be extended more than 2.2 times, i.e. more than $165\,\mathrm{m}$. Similarly, as depicted in Table 4.3, the maximum distance between the tag and the energy harvester is also extended to $80\,\mathrm{cm}$ which is long enough to cover all on-body

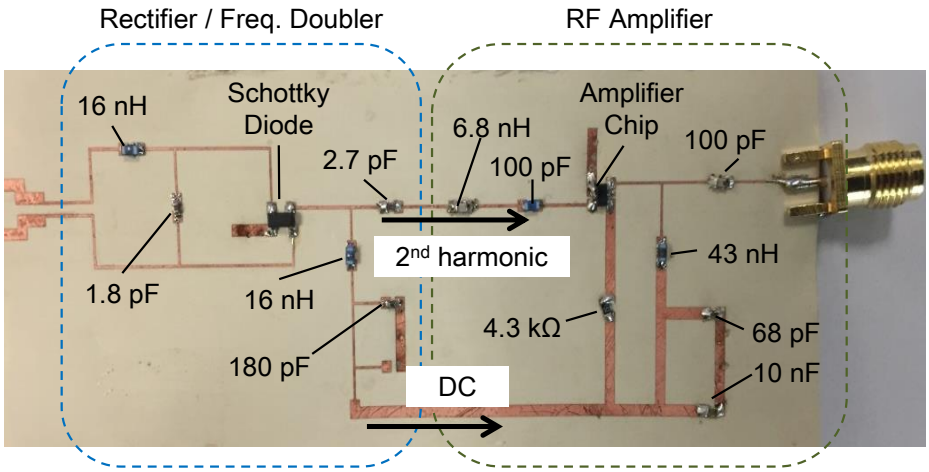

Figure 4.41. Proof-of-concept prototype of the proposed rectifier/frequency doubler including a DC power enabled amplifier.

backscattering sensor tags.

TABLE 4.3THE PERFORMANCE COMPARISON BETWEEN THE ENERGY HARVESTERS WITH AND WITHOUT AN RF AMPLIFIER

	With Amplifier	**Without Amplifier**
Max. Distance Tag-EH	80 cm	10 cm
Max. Distance Reader-Tag	>75 m	17 m

4.4.5 Multiple Backscattering Tags

Since the proposed on-body wireless sensor network system typically consists of multiple sensor tags, different modulation frequencies are assigned for each sensor tag to enable simultaneous multiple sensor detection. Therefore, an experimental setup shown in Fig. 4.44 was used to demonstrate that multiple tags operating at different modulation frequencies can be detected by the reader at the same time. As shown in Fig. 4.44, two tags are placed on the two sides of a sponge and interrogated with the carrier emitter (energy harvester). The software defined reader is placed around 60 cm away from the tags. The measured results using the software defined reader is shown in Fig. 4.45. As demonstrated in Fig. 4.45, two tags with different modulation frequencies (50 kHz and 100 kHz) were successfully detected simultaneously. Moreover, five spikes can be observed. The center spike is the carrier and the two symmetric spikes with 25 dB signal-to-noise ratio which

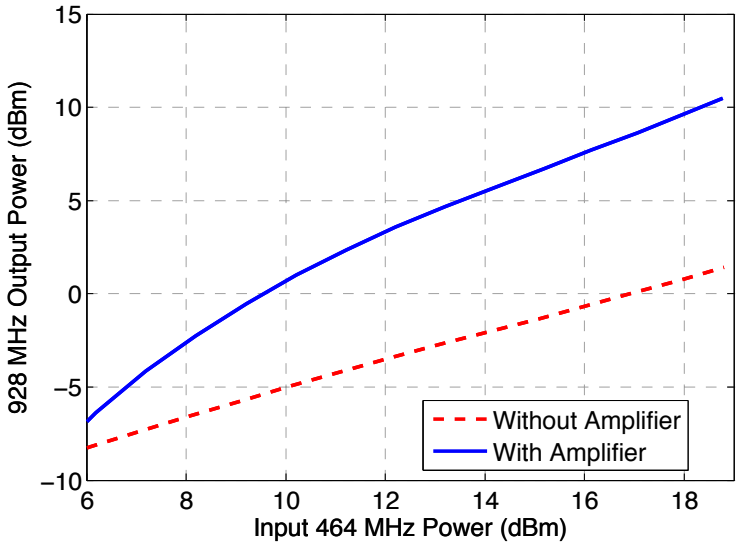

Figure 4.42. Comparison of the 928 MHz output power between the harvesters with and without an RF amplifier.

are located at $50\,\mathrm{kHz}$ away from the carrier are the backscattered signals from the first tag. The remaining two spikes with 40 dB signal-to-noise ratio which are located at $100\,\mathrm{kHz}$ away from the carrier are the backscattered signals from the second tag. The difference of the signal-to-noise ratio between two tags is because the distant between "On" and "Off" states resistances on the Smith chart as shown Fig. 4.31 are different for two tags.

4.4.6 Ammonia Sensor

The backscattering tag that was integrated with the ammonia sensor is tested with the similar experiment setup shown in Fig. 4.44. The only difference is that there is only one sensor tag and the tag is exposed to ammonia gas during the measurement. The measured results of the tag before and after being exposed to ammonia gas are shown in Fig. 4.46 and Fig. 4.47, respectively. As shown in Fig. 4.46, the modulation frequency of the ammonia sensor tag is $50\,\mathrm{kHz}$ before the tag is exposed to the ammonia gas. The impedance of the ammonia sensor is increased after the ammonia gas exposure effectively decreasing the modulation frequency to $7\,\mathrm{kHz}$ as shown in Fig. 4.47. Due to the frequency change of the backscattered signals, the ammonia gas can be easily detected by processing the received data.

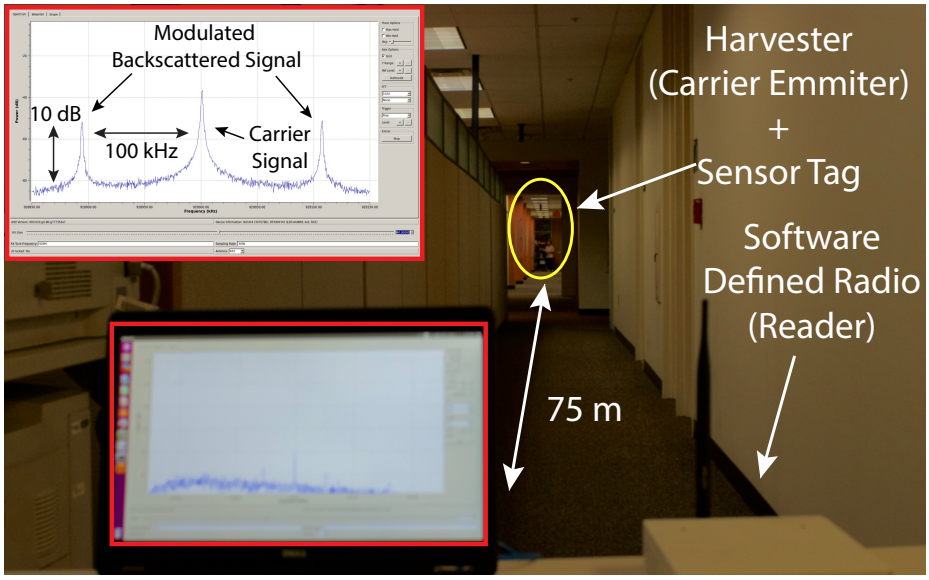

Figure 4.43. Long-range operation test of the wearable RF energy harvester powered on-body backscatter sensing system with an integrated RF amplifier.

4.5 Discussion for Further Applications

In this chapter, the fundamental operation, characterization, and several practical applications of the near-field wearable RF energy harvester are discussed and have proved that the wearable RF energy harvester can be used as a DC power source for a conventional MCU and an RF amplifier, and an RF transmitter for sensing applications. These are the essential components of a typical RFID reader, so this implies that the wearable RF energy harvester can be low-cost RFID reader, which is a hub of sensing capable RFIDs and correct information from each RFID more efficiently. This kind of system is a practical and reasonable solution for a continuous monitoring of biological and environmental characteristics such as glucose level, eye pressure, heart rate, gas exposure, humidity, and temperature.

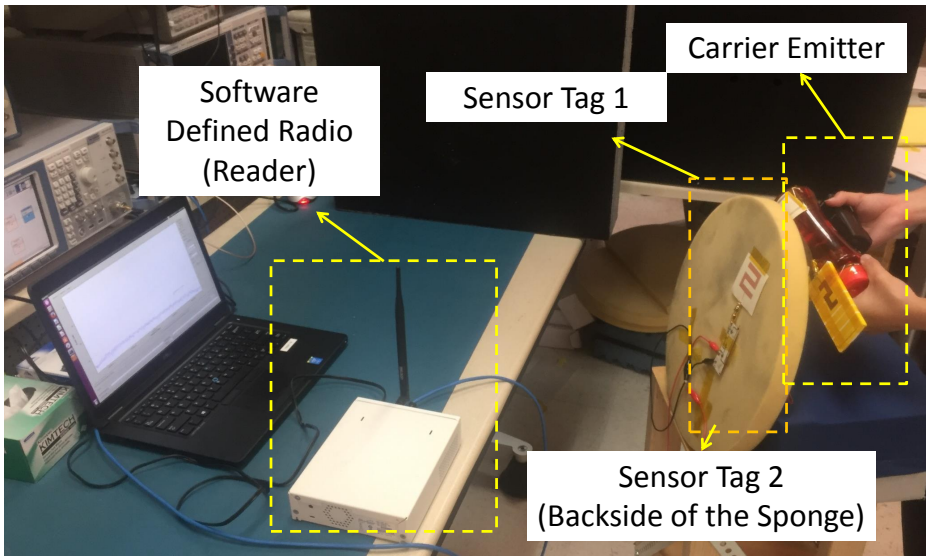

Figure 4.44. Measurement setup for the multiple sensors test.

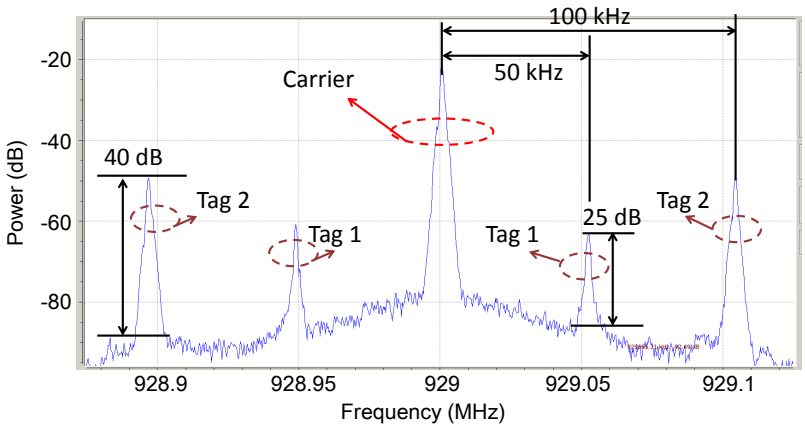

Figure 4.45. Measured result for multiple sensors test.

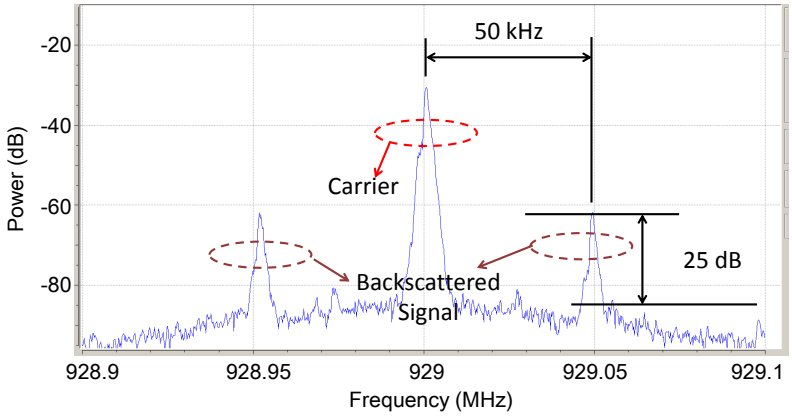

Figure 4.46. Measured result for the ammonia sensor tag before exposure to ammonia.

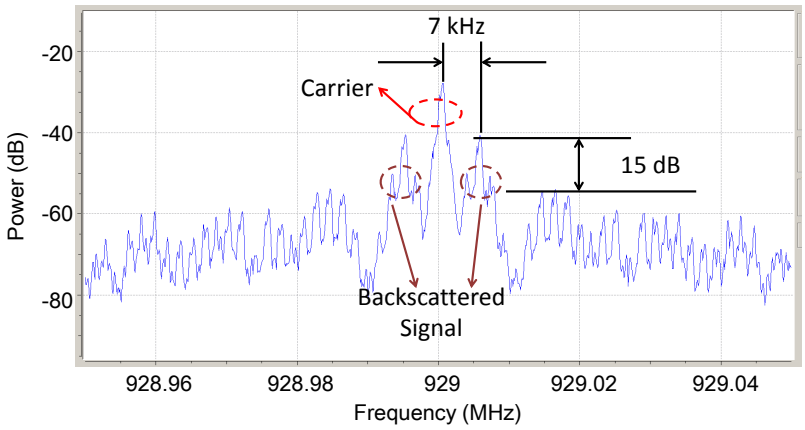

Figure 4.47. Measured result for the ammonia sensor tag after exposure to ammonia.

CHAPTER 5

HYBRID RF/SOLAR ENERGY HARVESTING

5.1 Energy Harvesting from Ambient Energy Sources

As summarized in Table 3.2, each ambient energy source, which exhibits distinct characteristics, has both advantages and disadvantages. In reality, when the ambient energy sources are integrated in autonomous systems, these disadvantages can cause critical issues. For example, a solar panel cannot generate sufficient power during the night time. Therefore, as mentioned in [5], each energy source can compensate for the challenges of other energy sources by combining multiple energy sources. Fig. 5.1 shows a block diagram of a typical multiple-source energy-harvesting-enabled autonomous sensor device. One of the most attractive combinations, especially for additive manufacturing, is solar and RF energy because they are both compatible with inkjet-printing technology. Photovoltaic devices are used to directly convert the electromagnetic energy contained in the solar spectrum to electricity. The power conversion efficiency of this process depends on the level of illumination, the photoactive material and device architecture used. At low irradiance levels, like the ones found indoors (ca. $100\,\mu\mathrm{W/cm^2}$), the performance of a photovoltaic device becomes limited by increased power losses that arise as the value of shunt resistance of the device becomes comparable to that of the characteristic resistance of the cell; defined as the ratio between the open circuit voltage and the short-circuit current. Among current photovoltaic technologies, those based on organic semiconductors have been shown in [93], [94] particularly suitable for low-light level operation. In addition, organic photovoltaic devices are compatible with all-additive manufacturing methods such as ink-jet printing [73] and are therefore attractive for integration with an RF energy harvester to increase the available power per unit area [76], [77], [83].

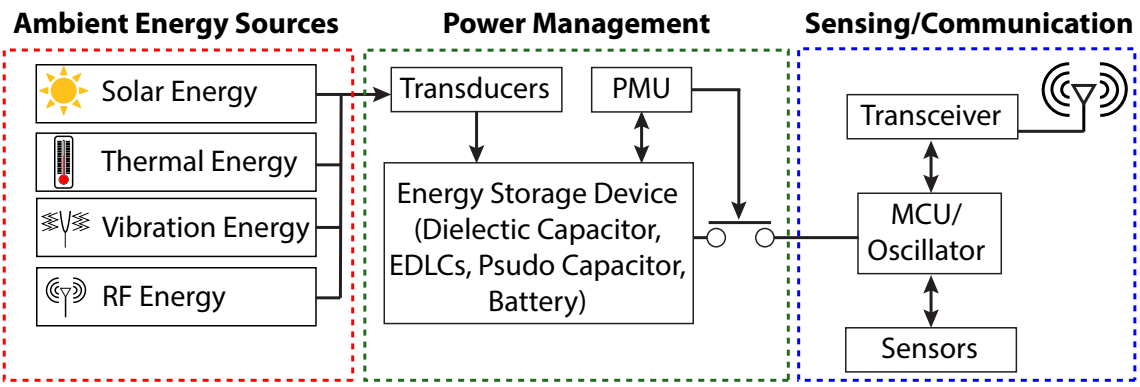

Figure 5.1. Block diagram of a typical multi-form-energy harvesting enabled autonomous sensor device.

5.2 Hybrid RF Solar Energy Harvesting System

Regardless of the typically low energy density of ambient RF, RF energy harvesting is an attractive ambient energy source. However, as discussed in Chap. 2, the output voltage from RF energy harvester is typically low because of the low energy density of ambient RF signals and cannot drive conventional ICs for power management to boost the voltage level. To sufficiently address the main challenges of RF energy harvesting, by taking advantage of the unique features of additive manufacturing, one possible solution is the combination of multiple source ambient energy harvesting. In particular, this research proposes the hybridization of RF energy harvester and solar cells, which generate a nearly constant voltage under sufficient illumination conditions, can enable the "cold start" start-up operation of a DC-DC converter allowing RF energy harvesters to then scavenge low power energy, in modules/topologies that can be fabricated utilizing additive manufacturing technology. As a proof-of-concept prototype that can be easily implemented in a compact form factor, this research utilized a TI bq25504 ultra low power boost converter with a battery management IC, which has a self-powered DC-DC converter for "cold start" operation and a high efficiency DC-DC converter with maximum power point tracking for "hot start" operation [95]. Fig. 5.2 shows the block diagram of an autonomous hybrid RF solar powered sensor device (mote). The device consists of a dual port antenna both for harvesting and communication at the $2.4\,\mathrm{GHz}$ ISM band, a solar cell, a matching circuit, an RF-DC conversion

circuit, a bq25504 power management unit (PMU), a capacitor/battery for energy storage, a MOSFET switch, an MSP430 micro-controller unit (MCU) [96], and a CC2500 transceiver for communications [97].

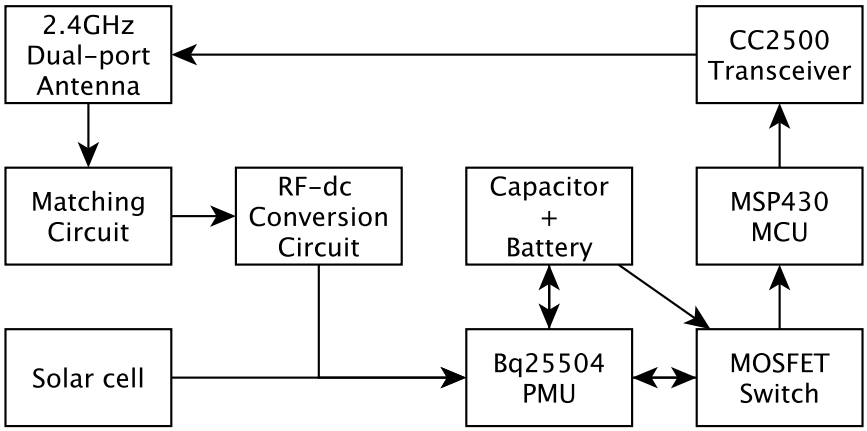

Figure 5.2. Block diagram of a hybrid RF solar powered autonomous mote.

5.2.1 Antenna Design and Measurement

This proposed system uses the $2.4\,\mathrm{GHz}$ ISM band for both energy harvesting and communications. Therefore, the antenna requires a dual port configuration with a high two-port isolation. In addition, circular polarization is suitable for RF energy harvesting as it allows the rectenna to capture signals with arbitrary linear polarization. In this scenario, a properly excited rectangular shorted slot antenna [98], [99] was identified as a strong candidate which also exhibits a good impedance and polarization bandwidth. The biggest novelty and challenge in designing the antenna for our energy harvesting capable mote is to feature a simultaneous two-port operation; one port for energy harvesting and another port for communication while sharing the same rectangular slot. The design and location of the feeding transmission lines as well as the size and height of the ground plane are critical to realize a good matching for both ports and a simultaneous high isolation between the two ports. Since the rectangular shorted slot antenna is an omnidirectional antenna, a reflector was placed on the bottom of the package in order to increase the gain. The package was printed

utilizing a 3D printer to precisely control the distance between the ground of the antenna and the reflector. The antenna was designed utilizing HFSS and fabricated on a $0.762\,\mathrm{mm}$ FR4 substrate with dielectric constant of 4.4 and loss tangent of 0.002 utilizing an LPKF ProtoMat S60 mechanical milling machine. Fig. 5.3 shows the side and top view of the rectangular shorted antenna and Table 5.1 summarizes the antenna design parameters. In this research, port1 is for harvesting and port2 is for communication. Fig. 5.4 shows the pictures of the prototype of the solar antenna, i.e., an antenna with an embedded solar cell. The package was created utilizing a fused deposition modeling (FDM) printer with poly-lactic acid (PLA) based-material. For an initial simulation, a dielectric constant of 3.1 and the loss tangent of 0.01 [100] were adopted.

The design goals of the antenna are the following: (1) S_{11} and S_{22} below $-13\,\mathrm{dB}$ ($5\,\%$), (2) S_{21} below $-13\,\mathrm{dB}$ ($5\,\%$), and (3) axial ratio below $3\,\mathrm{dB}$ in the frequency range of 2.4 to $2.5\,\mathrm{GHz}$. To satisfy these design goals, the length (L) of the sides of the square slot and the length of the gap (G) were determined to obtain a resonance at $2.45\,\mathrm{GHz}$. In terms of impedance matching, the length and the width of the feeding signal lines can be adjusted to control the center frequency of operation. In addition, the proposed antenna design can adjust the center frequency of the two-port isolation (the peak of transmission loss) almost independently from the matching condition by varying the length of the square side of the ground plane (L_{in}). As illustrated in Fig. 5.5, preliminary simulations varied L_{in} from 42 to $48\,\mathrm{mm}$, while a value of $45\,\mathrm{mm}$ was adopted for the initial antenna prototype. Fig. 5.6 (a) depicts the simulated (design and post fabrication) and measured S_{11} and S_{22}, respectively. From the measurement, the antenna features the operation range of 2.28 to $2.55\,\mathrm{GHz}$, and the simulation results match well with the measurement results. However, as depicted in Fig. 5.6 (b), the frequency at the peak of transmission loss ($|S_{21}|$) was slightly shifted to lower frequency. This is expected to be caused by slight fabrication errors, but the isolation at the target frequency is about $15\,\mathrm{dB}$, and practically, there is almost no coupling between two ports. Over all, the measured S-parameters satisfied the

design goals (1) and (2).

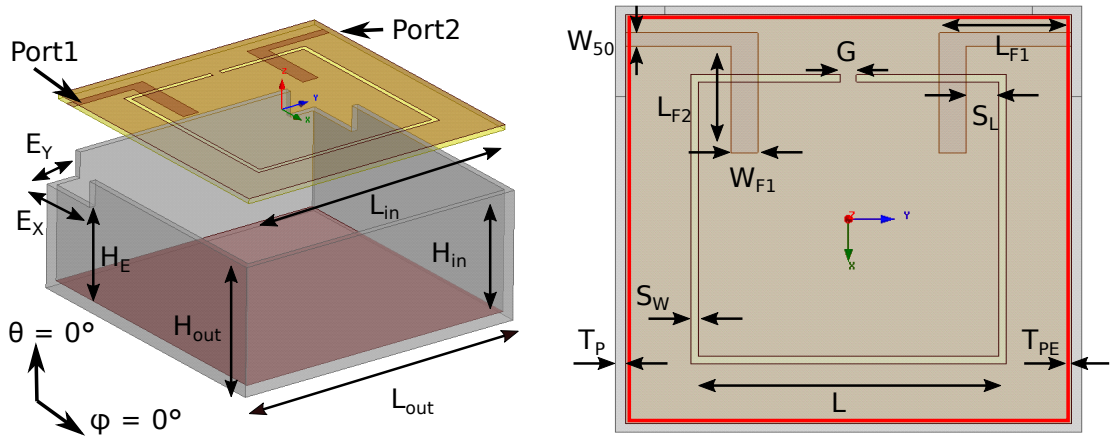

(a) (b)

Figure 5.3. (a) Side and (b) top view of the prototype of the rectangular shorted antenna.

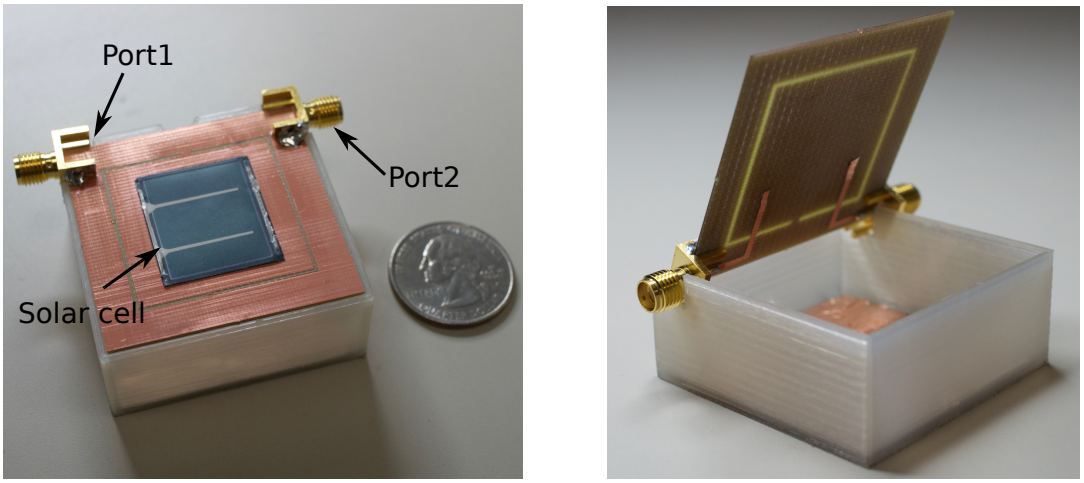

(a) (b)

Figure 5.4. Prototype of the dual-feed rectangular shorted slot solar antenna with a filexible film solar cell (a) top and (b) inside.

In addition to the S-parameters, this study characterized the other properties of the antenna through simulations and measurements. Fig. 5.7 (a) and (b) show the simulated axial ratio with respect to frequency at broadside (θ = 0°) and θ direction rotation angle at $2.45\,\mathrm{GHz}$, respectively. The axial ratio is about $3\,\mathrm{dB}$ in the frequency range of 2.4 to $2.5\,\mathrm{GHz}$, which almost satisfies the design goal (3). Also, Fig. 5.8, which plots simulated total realized gain as a function of frequency, yields a value of $7.4\,\mathrm{dB}$ at the center

TABLE 5.1
PRELIMINARY DIMENSIONS OF THE DUAL-FED RECTANGULAR SHORTED ANTENNA.

Parameter	H_{in}	H_{out}	H_E	L_{in}	L_{out}	E_X	E_Y
Length (mm)	18	20	14	45	47	10	5
Parameter	L_{F1}	L_{F2}	L	W_{F1}	W_{50}	S_W	S_L
Length (mm)	13.35	7	11.81	31	1.46	0.9	3.1
Parameter	G	T_P	T_{PE}				
Length (mm)	1.6	1	0.5				

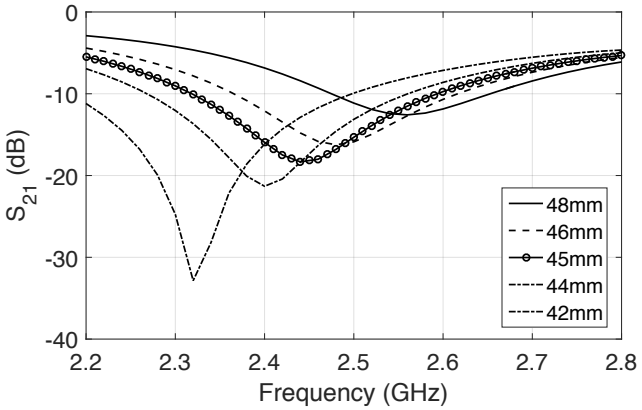

Figure 5.5. Simulted S_{21} with respect to frequency with varied ground size.

frequency of $2.45\,\mathrm{GHz}$. For the final prototype, a thin film solar cell, which Section 5.2.2 explains the detail, is placed on top of the conductive area inside the slot without significantly disturbing its radiation characteristics. Therefore, the radiation patterns, depicted in Fig. 5.9, were also measured utilizing a LabVIEW controlled automatic rotation setup and a vector network analyzer (Anritsu 37369d). The measurement utilized a broadband horn antenna (AINFO LB-20245) as a reference. The measurements depicted on Fig. 5.9 show that the solar cell does not have a significant effect on the performance of the dual-feed rectangular antenna. Fig. 5.10 shows the side and the top view of the rectangular shorted antenna for the final prototype and Table 5.2 summarizes the final antenna design parameters. For simplicity in measurements, SMA connectors were connected to the edges of the antenna, but the final prototype of the sensor device (mote) was designed to have all electronics connected to the antenna on the bottom layer near the center of the rectangular slot. Therefore, as shown in Fig. 5.10 the design of the excitation lines were modified for

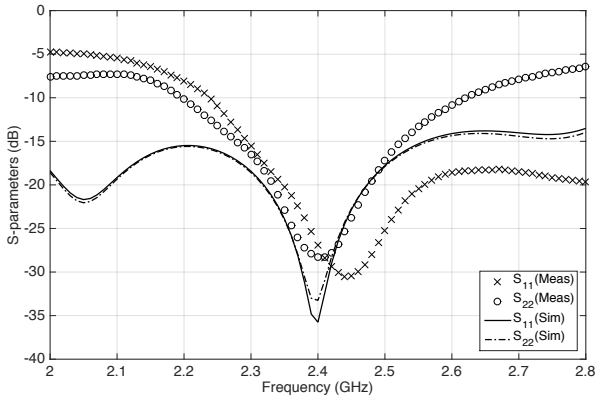

(a)

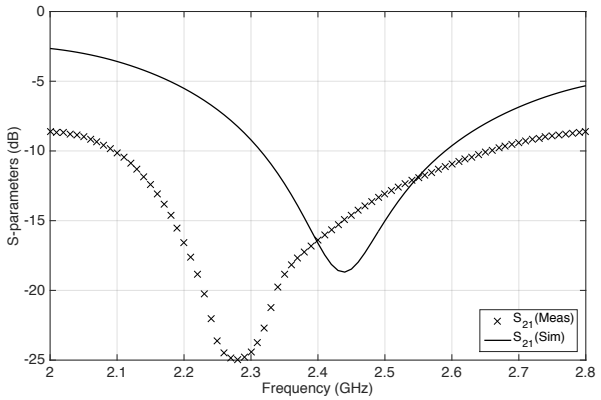

(b)

Figure 5.6. Measured and simulated (design and post fabrication) (a) S_{11}, S_{22}, and (b) S_{21} of the dual-feed rectangular shorted slot antenna.

the final prototype. Fig. 5.11 shows the simulated S-parameters of the final antenna design.

TABLE 5.2
DIMENSION OF THE RECTANGULAR SHORTED ANTENNA FOR THE FINAL PROTOTYPE.

Parameter	H_{in}	H_{out}	L_{in}	L_{out}	L_{F1}	L_{F2}	L
Length (mm)	18	20	45	47	13.5	10	31
Parameter	W_{F1}	W_{F2}	W_{50}	S_W	S_L	T_P	G
Length (mm)	4	7	1.46	0.9	4.6	1	1.6

5.2.2 RF-DC Conversion Circuit Design and Measurement

The solar cell selected for the proof-of-concept prototype was the Power Film MP3-25 solar cell which has dimensions of $114\,\mathrm{mm}$ x $24\,\mathrm{mm}$, short circuit current I_{sc} = $48\,\mathrm{mA}$,

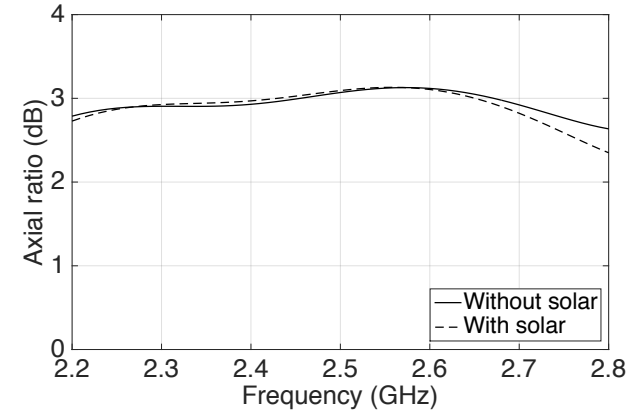

(a)

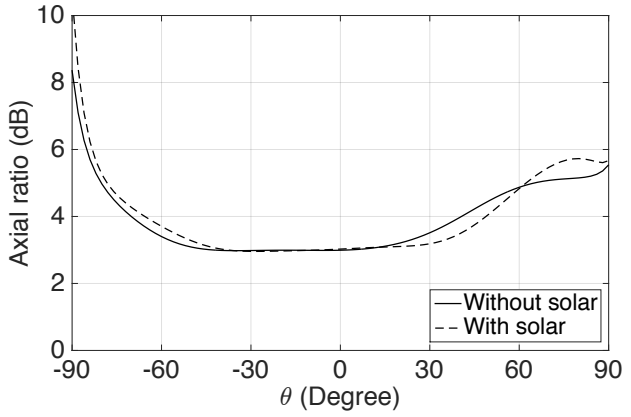

(b)

Figure 5.7. Simulated axial ratio of the rectangular shorted antenna with and without the solar cell with respect to (a) frequency and (b) θ direction rotation angle.

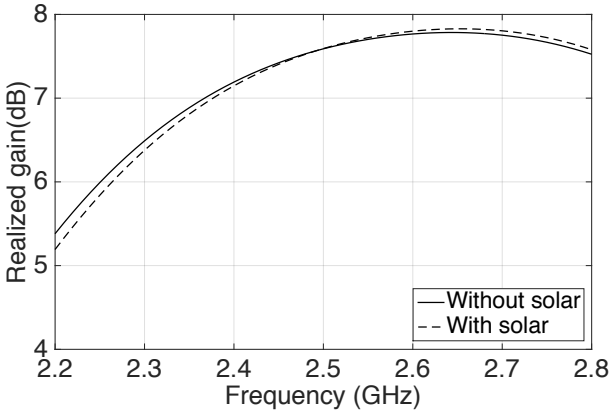

Figure 5.8. Simulated total realized gain of the rectangular shorted antenna with and without the solar cell.

open circuit voltage V_{oc} = $4.1\,\mathrm{V}$, and can provide up to $93\,\mathrm{mW}$ at $3\,\mathrm{V}$ under 1 sun irradiance of $100\,\mathrm{mW/cm^2}$. Specifically for the 3D printed prototype discussed in this paper, only

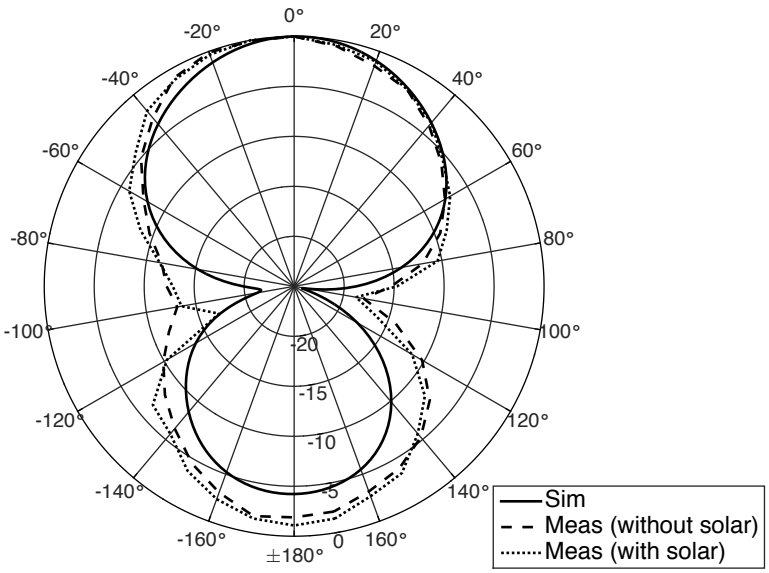

(a)

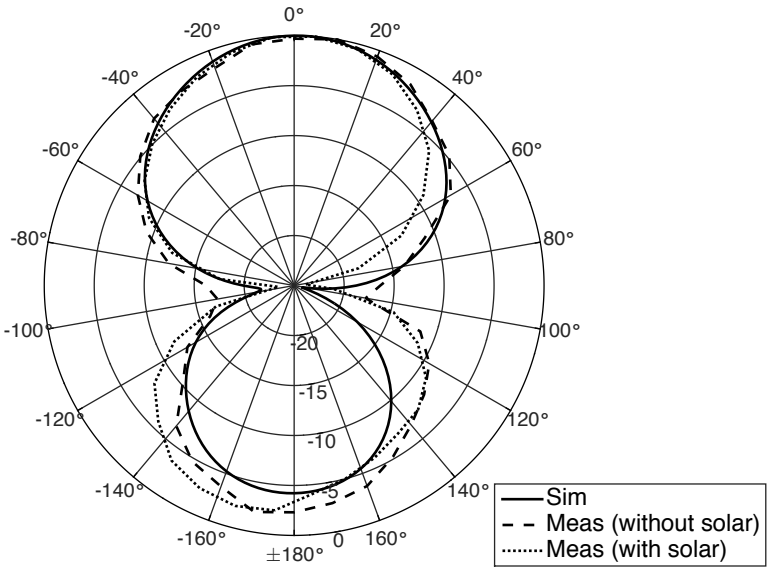

(b)

Figure 5.9. Measured and simulated normalized radiation patten of the rectangular shorted antenna with and without the solar cell (a)$\phi = 0°$ and (b)$\phi = 90°$.

one fifth of the length of the solar module, which exhibits about $0.68\,\mathrm{V}$ of open voltage and about $70.5\,\mu\mathrm{W}$ of maximum power under a room light condition ($334\,\mathrm{lx} = 49\,\mu\mathrm{W/cm^2}$) with a DC load resistance of $3.8\,\mathrm{k\Omega}$, was utilized in order to fit within the conductive surface inside the dual-fed slot antenna, as shown in Fig. 5.4 (a). The equivalent circuit model of the solar cell was utilized to design the harvester circuit in ADS. To begin with, this work

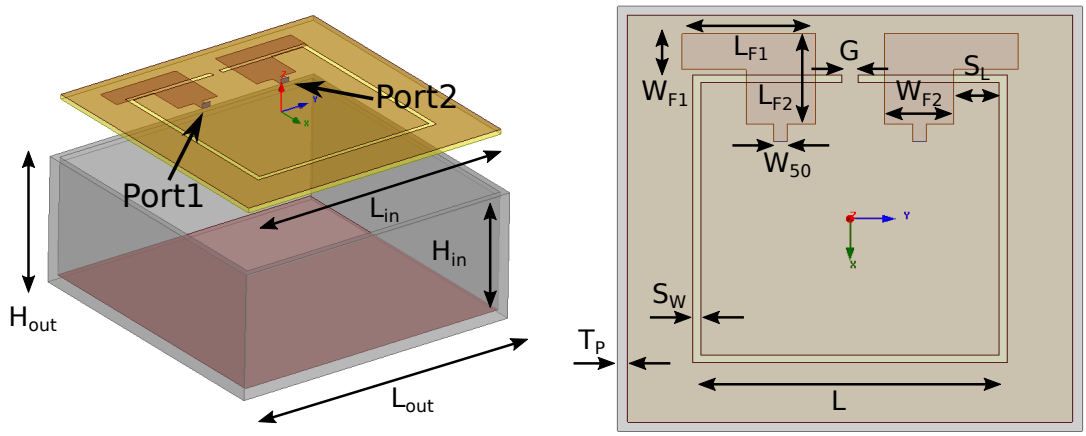

(a) (b)

Figure 5.10. (a) Side and (b) top view of the rectangular shorted antenna for the final prototype.

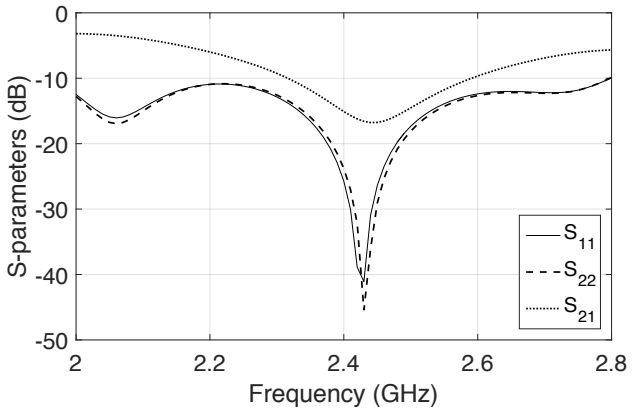

Figure 5.11. Simulated S-parameters of the final antenna design with respect to frequency.

initially characterized the RF-DC conversion circuit independent from the solar cell.

The goal of the RF-DC conversion circuit design was to produce sufficient voltage and power to drive the PMU. Specifically, the bq25504 IC requires $330\,\mathrm{mV}$ and $15\,\mu\mathrm{W}$ to start up from a "cold state", and it can sustain operation for a minimum input voltage of $80\,\mathrm{mV}$. Also, the IC has an integrated maximum power point tracking function which optimally adjusts the load resistance value for the maximum output power [95]. This work utilized a two diode RF rectifier (voltage doubler) circuit, which was necessary to accommodate a sufficiently high voltage to facilitate the start-up of the DC-DC converter circuit, as shown in Fig. 5.12 (a). To simplify the layout, the solar cell output was connected using a series diode at the output of the RF rectifier circuit as depicted in Fig. 5.12.

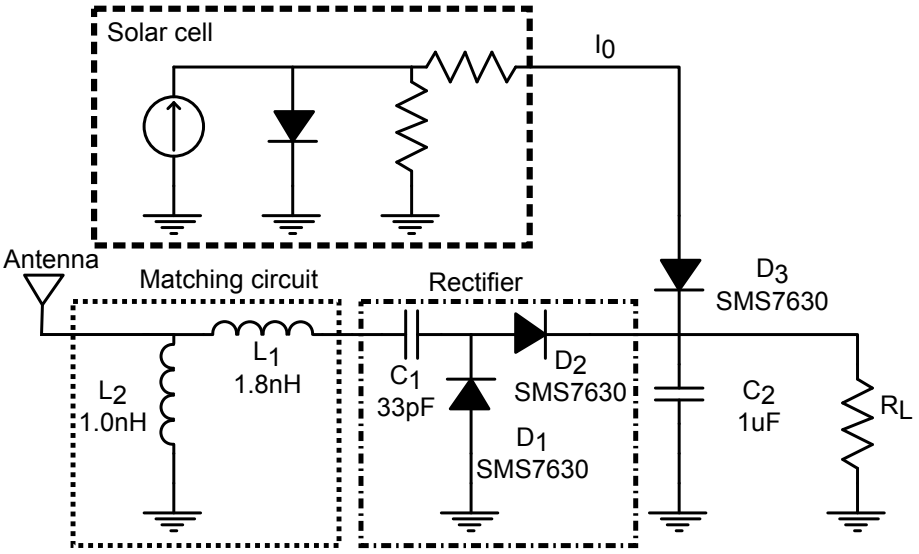

(a)

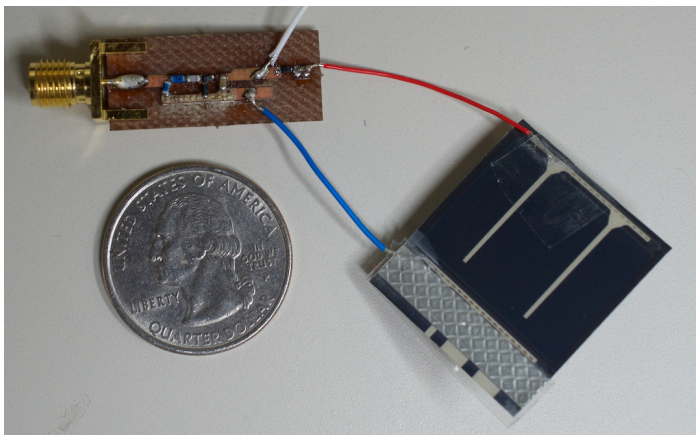

(b)

Figure 5.12. (a) Circuit diagram of the hybrid RF solar harvester and (b) picture of the complete harvester prototype.

The matching circuit design was optimized to maximize the DC output power for a given RF available input power of -17 dBm. This is the minimum required RF input power to generate the minimum DC input voltage ($80\,\mathrm{mV}$) of the PMU in the "hot state", according to preliminary simulations for different DC output current values from the solar cell, corresponding to different solar light irradiation conditions. Fig. 5.13 and Fig. 5.14 show the RF-DC conversion efficiency and the output voltage of the rectifier prototype

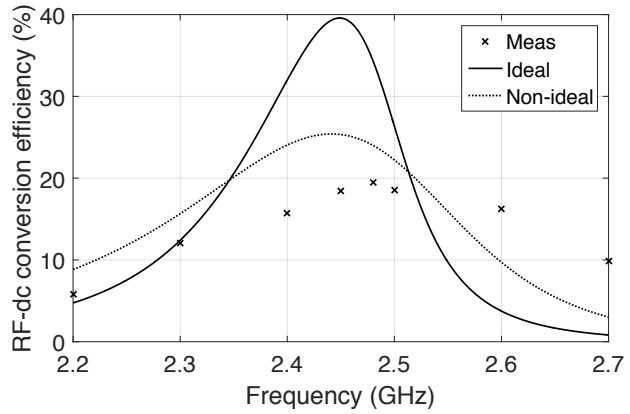

(a)

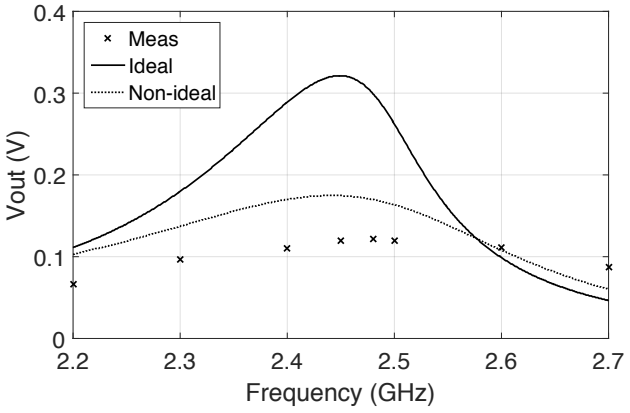

(b)

Figure 5.13. Measured and simulated (a) RF-DC conversion efficiency and (b) DC output voltage with respect to frequency with optimal load resistance at -17 dBm RF input power.

without connecting a solar cell as a function of the frequency for an input RF power level of -17 dBm and as a function of the power level of the input (harvested) RF signals at the frequency of $2.45\,\mathrm{GHz}$, respectively. In these figures, both "ideal" and "non-ideal" are simulation results with ADS. "Ideal" simulations use ideal lumped component models and "non-ideal" simulations use non-ideal lumped component models, provided by Johanson Technology for the components used in the prototype. For these measurements, RF power was measured using an RF power meter (NRP-Z211 from Rohde and Schwarz). The aggregate DC output power (P_{out}) from the RF energy harvester and the solar cell was calculated using the following Eq. (5.1), where V_{out} is the measured output voltage and R_{load} is the load resistance. The RF energy harvester exhibits about 20 to $45\,\%$ RF-DC conversion

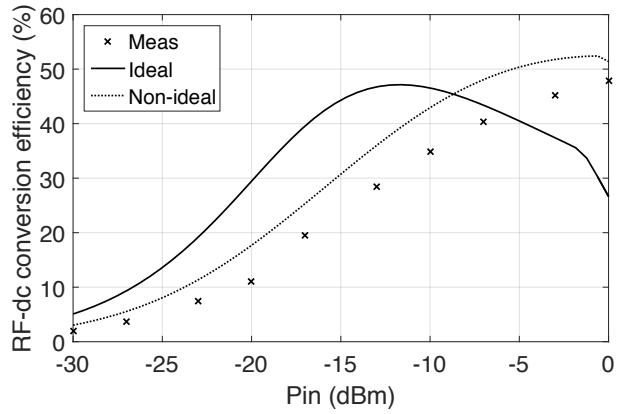

(a)

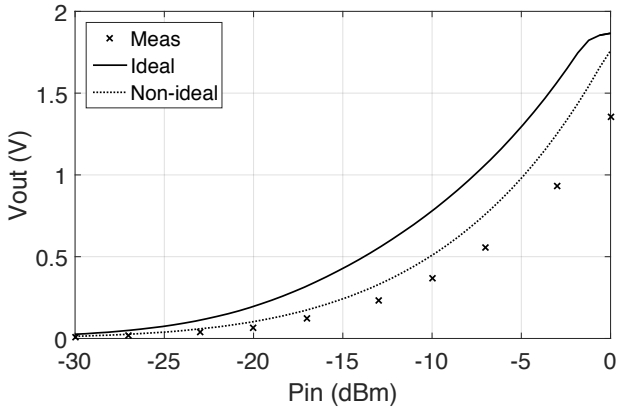

(b)

Figure 5.14. Measured and simulated (a) RF-DC conversion efficiency and (b) DC output voltage with respect to input power with optimal load resistance at $2.45\,\mathrm{GHz}$.

efficiency depending on the RF input power in the range of -17 to 0 dBm.

$$P_{out} = \frac{V_{out}^2}{R_{load}} \tag{5.1}$$

Next, the performance of the RF-DC conversion circuit including the solar cell was characterized through simulations and measurements. Fig. 5.15 (a) and (b) depict the output power and the output current from the solar cell for the optimal load resistance of $3.8\,\mathrm{k\Omega}$ with reference to the ambient light intensity, respectively. The light intensity, measured utilizing a luminometer, was controlled by adjusting the distance between a table lamp and the solar cell. From these measurements, the solar cell yielded $70.5\,\mu\mathrm{W}$ of output DC power and $135.5\,\mu\mathrm{A}$ of output DC current at the room light condition of $334\,\mathrm{lx}$ irradiation.

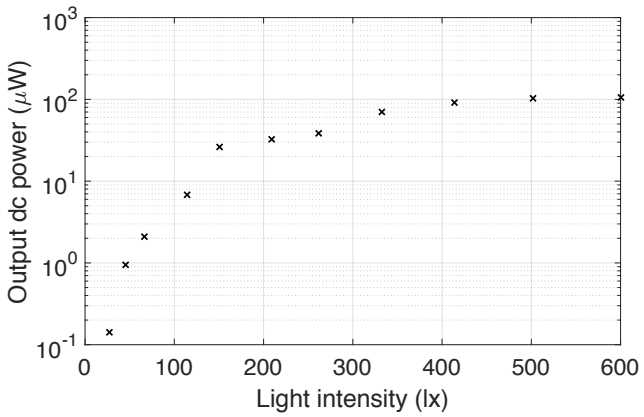

(a)

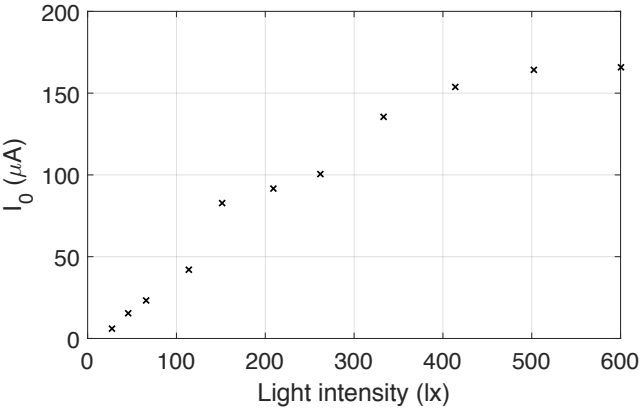

(b)

Figure 5.15. Measured (a) output DC power and (b) DC current (I_0) from the soalr cell with respect to the light intensity for the load resistance of $3.8\,\mathrm{k}\Omega$.

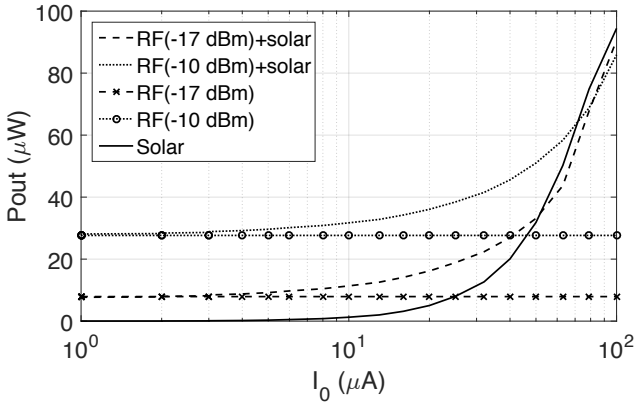

Figure 5.16. Simulated output DC power with respect to the output DC current from the solar cell (I_0) for RF input power of -17 dBm and -10 dBm.

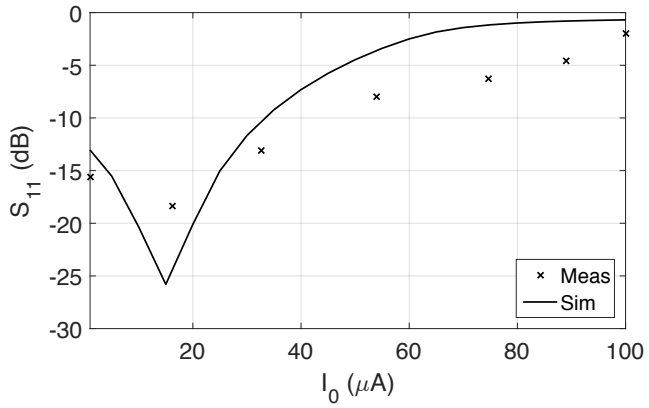

Figure 5.17. Simulated and measured S_{11} with respect to output current from the solar cell (I_0).

In addition, this work simulated the output power from the hybrid RF solar harvester with respect to the current from the solar cell (I_0) for the RF power levels of -17 dBm and -10 dBm for the optimal load at $2.45\,\mathrm{GHz}$ as shown in Fig. 5.16. The simulation results confirm that the DC combination of the solar cell and the RF circuit exhibits a higher output DC power without affecting the performance of the RF-DC conversion circuit and the solar cell. However, if the solar energy is dominant, the performance of the solar cell slightly degrades. Finally, Fig. 5.17 shows the simulated and the measured S_{11} of the harvester for the input RF power of -17 dBm at $2.45\,\mathrm{GHz}$ when the input current from the solar cell is varied. The current from the solar cell was varied by changing the light intensity in the same manner as described above. The return loss ($|S_{11}|$) increases first as I_0 increases, but it decreases if the input current is too large and the solar power is dominant.

5.2.3 Module-level Operation Test

After optimizing the subsystems of the proposed hybrid harvester, a module-level operation test of the RF solar harvester utilizing a bq25504 module as a load resistance R_L in Fig. 5.12 (a) was performed to evaluate the capability of the harvester to "cold" start up the PMU. Fig. 5.18 shows the voltage of the $100\,\mu\mathrm{F}$ capacitor that is integrated in the bq25504 PMU during charging. The dashed line expresses the threshold of $1.5\,\mathrm{V}$ when the IC switches the operation mode from the cold start to the hot start. Similarly, the dotted

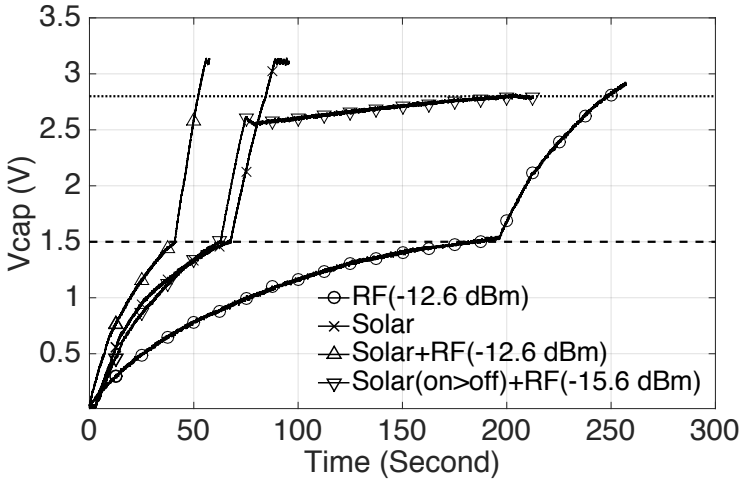

Figure 5.18. Voltage in the $100\,\mu\mathrm{F}$ capacitor that is integrated in the bq25504 PMU during charging under different RF and solar conditions: (1) -12.6 dBm RF input power, (2) solar under room light condition, (3)-12.6 dBm RF input power + solar under room light condition, and (4) -15.6 dBm RF input power + solar under room light condition until cold start mode is over.

line indicates the threshold of $2.8\,\mathrm{V}$ when VBAT_OK signal, which is a digital output for a battery good indicator, from the PMU is sufficiently high so that the capacitor voltage is adequate and the energy storage capacitor is ready to power the external DC load by turning on a MOSFET switch. The maximum output voltage is regulated at $3.3\,\mathrm{V}$ to protect a battery which can be externally connected, but this voltage can be arbitrary selected within the range of 2.4 to $5.3\,\mathrm{V}$. The first three traces in Fig. 5.18 represent three different charging conditions: (1) -12.6 dBm RF input power, (2) solar cell at room light condition, and (3) aggregate DC combining the two harvesters, respectively. The input RF power of -12.6 dBm is the minimum required RF power to start the operation of the bq25504 module from the "cold start" condition without using any solar cell. The comparison between (2) and (3) in Fig. 5.18 suggests that the charging time significantly decreases combining the DC output of the solar and the RF harvesters. More specifically, the time to charge the capacitor from $0\,\mathrm{V}$ to $2.8\,\mathrm{V}$ under the charging conditions (2) and (3) is $86\,\mathrm{s}$ and $51\,\mathrm{s}$, respectively. Therefore, $40\,\%$ of capacitor charging time reduction is confirmed through the measurement. The last trace in Fig. 5.18 shows another charging condition (4) by combining the DC outputs of the solar and the RF harvester for the lower input power level of

-15.6 dBm. In this trace, the change in slope around $2.5\,\mathrm{V}$ indicates that the light intensity was drastically reduced from 334 to $18.9\,\mathrm{lx}$ at this point by covering the solar cell. The input RF power of -15.6 dBm, which is the half of -12.6 dBm, cannot support alone the operation of the "cold start" operation mode. However, with the help of solar energy, this hybrid energy harvesting system can go over the "cold start" mode. For non-sufficient light irradiation conditions (e.g. in the night or in completely dark rooms), even a solar panel may not be used to "cold start" the system. However, once the IC starts operating with "hot start" mode after an initial relatively strong light irradiation, the input RF power of -15.6 dBm can maintain the perpetual operation of the IC, while the PMU gradually charges the capacitor using the ambient RF energy even under dark conditions. Finally, all the components are integrated into two PCBs as shown in Fig. 5.19 (a) and assembled as Fig. 5.19 (b). The charging of battery and wireless communication were tested by loading the program used for the circuit in Fig. 4.12.

5.3 Hybrid RF Photovoltaic Energy Harvesting System

In the previous section, the solar cell was utilized as a power source to go over the "cold start" operation of the power management IC by only using a single cell solar cell. The system successfully managed to kick start the operation of the circuit even under the room light irradiation, though, with even lower irradiance levels such as the ones found in darkroom (ca. below $10\,\mu\mathrm{W/cm^2}$), the energy conversion efficiency of a photovoltaic device becomes limited by increased power losses that arise as the value of the devices shunt resistance becomes comparable to that of the characteristic resistance of the cell. However, the photovoltaic effect is inherently suitable to generate high voltage by connecting multiple cells in series, especially with near open voltage condition. The open voltage (V_{OC}) of an ideal solar cell is expressed as Eq. (5.2), where k is Boltzmann's constant, T is temperature in kelvin, q is electronic charge, I_{SC} is short circuit current, and I_0 is reverse saturation current, respectively. For example, $\frac{kT}{q}$ at room temperature ($25\,^{\circ}\mathrm{C}$) is 0.0257. As

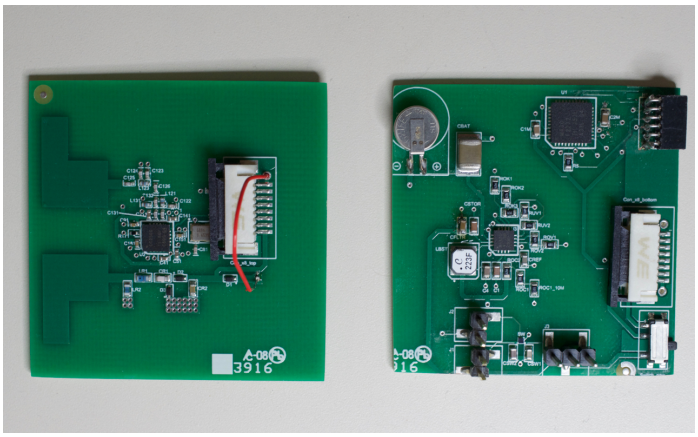

(a)

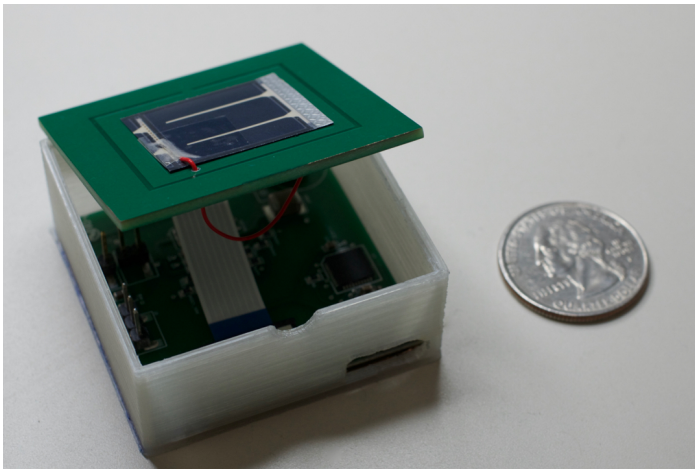

(b)

Figure 5.19. (a) PCBs for the final prototype. (b) Prototype of integrated hybrid energy harvesting system.

depicted in Fig. 5.20, the short circuit current and the available DC power from a solar cell more or less linearly decrease with respect to the light intensity. On the other hand, open voltage of a solar cell decreases linearly with respect to the logarithmic scale reduction of the light intensity [93], [94]. These imply that a solar cell can provide sufficiently high voltage while output power is very limited under a low-light level operation. Therefore, a solar cell is better to be used as a voltage source to operate a extremely low-power-required power management circuit to convert the energy from an RF-DC conversion circuit, which is a main energy source in the system, into high voltage usable form increasing the RF

sensitivity of the system.

$$V_{OC} = \frac{kT}{q} \ln(\frac{I_{SC}}{I_0} + 1) \tag{5.2}$$

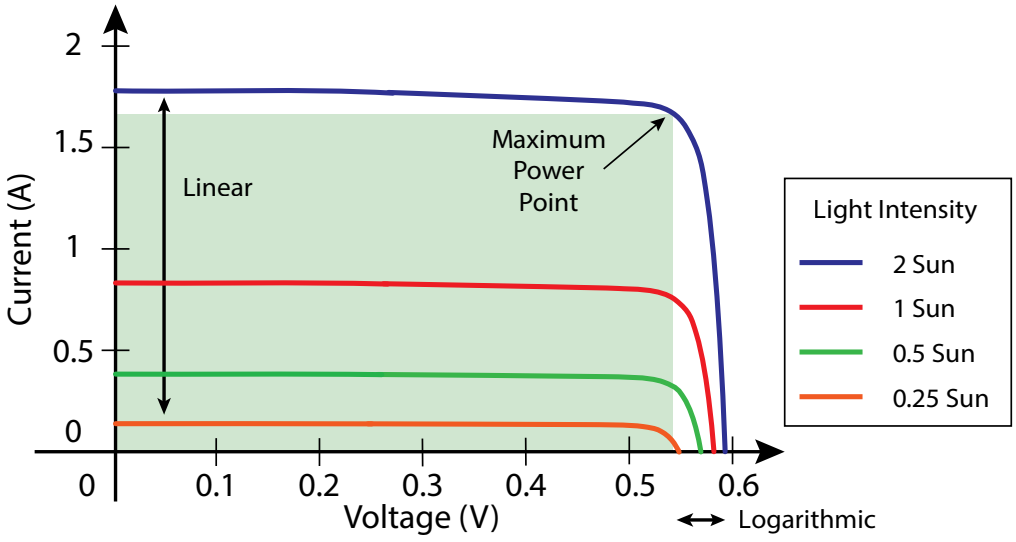

Figure 5.20. Simulated current and voltage output of a single solar cell under varying light levels.

In this section, an ultra-low power hybrid RF solar energy harvesting system is presented utilizing a Texas Instruments TPL5100 nano-timer and Silicon Labs TS3001 oscillator ICs. The PV-powered timer, which consumes power below $50\,\mathrm{nW}$, generates short duration pulse signals with operation frequency below $0.1\,\mathrm{Hz}$ to trigger the operation of a relatively high-power and frequency (1 to $5\,\mu\mathrm{W}$ at 5 to $90\,\mathrm{kHz}$ oscillation frequency) oscillator to minimize the power consumption of entire system. This low required energy allows the operation of the system even under extremely low light irradiation condition without having the issue of cold start. Fig. 5.21 depicts the block diagram of the system. The expected RF input power level is $-20\,\mathrm{dBm}$ at the $2.4\,\mathrm{GHz}$ ISM band.

5.3.1 Selection of Rectifier Topology and Charge Tank Capacitor Value

There are several rectifier topologies available which exhibit different maximum RF-DC conversion efficiency, optimum load resistance, and open voltage values. This re-

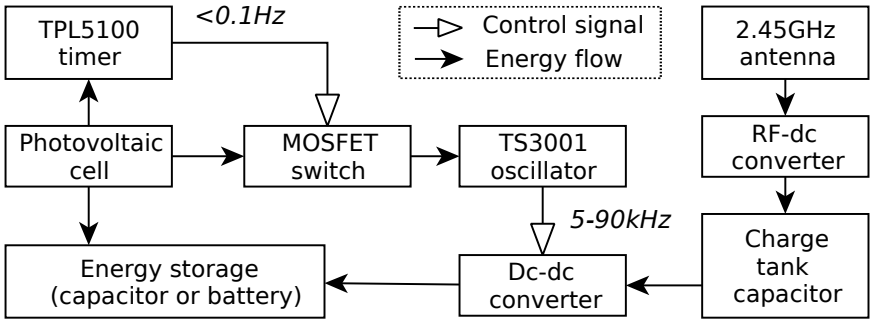

Figure 5.21. Block diagram of the proposed hybrid RF/PV powered energy harvesting system.

search compares the performance of a series rectifier, a one-stage and a two-stage voltage multiplier to select the optimal RF-DC conversion circuit topology, which exhibits the highest RF-DC conversion efficiency, and charge tank capacitor value for long-term duty cycling through simulation and analytical estimation. In the proof-of-concept simulation with Keysight Advanced Design System (ADS), an Avago HSMS285 Schottky diode and $0.5\,\mathrm{mm}$ thick Rogers RO4003 substrate were utilized. For impedance matching, a radial stub with optimized length (S_L), distance from the anode of the diode (S_P), and the stub angle (S_A) was utilized. The microstrip line width and the width of stub input line is $1.15\,\mathrm{mm}$ making the characteristic impedance of the lines to be $50\,\Omega$. Table 5.3 summarizes the results of simulation. As a clear trend, the peak RF-DC conversion efficiency decreases and the open voltage increases as the number of diodes increases. To maximize the energy available in a capacitor within a specific time period, the transient behavior of the charging of the capacitor needs to be simulated. However, since the RF-DC conversion circuit is a load resistance dependent power supply, the charging of the capacitor, which changes its equivalent impedance value continuously while charging, cannot be simply modeled with well known capacitor charging models with a perfect voltage or current source. Similarly, in ADS transient simulation, from Shannon's sampling theorem, the time step needs to be at least $0.2\,\mathrm{ns}$ to express $2.5\,\mathrm{GHz}$ signals making practically impossible to simulate the behavior of the capacitor for a time period more than $1\,\mathrm{s}$ because of the simulation time and the memory requirement, especially with a varied charge tank capacitance value. On the other hand, the steady state voltage at each given load resistance value can be immediately

simulated from harmonic balance simulation in ADS. From Ohm's law and the definition of current in a capacitor, the capacitor impedance variation over the time can be expressed as shown in Eq. (5.3) where $V(t)$, $Z(t)$, and C are the output voltage, load resistance, and charge tank capacitance, respectively. From the relationship between the output voltage and the load resistance, the slope of voltage for each given load resistance ($\frac{dV}{dZ}$) can be easily calculated. If the output voltage, load resistance and the slope of the voltage at $t = 0$ are given as initial conditions, the capacitor impedance and voltage variation over time can be numerically calculated utilizing Eq. (5.3). Once the output voltage at each time step is determined, the energy stored in the capacitor ($E = \frac{1}{2}CV^2$) can be also easily calculated. Practically, the output voltage of the rectifier cannot be measured with a continuously changing load resistance, and the relationship is typically calculated at discrete data points. Therefore, without loss of generality, the measured output voltage and its relationship with the load is approximately expressed as closed form equations shown as Eq. (5.4) where p_1, p_2, and q_1 are arbitrary constant terms derived through MATLAB polynomial fitting functions. Fig. 5.22 shows the average RF-DC conversion efficiency ($\eta_{avg} = \frac{E}{t_p}$) for every rectifier topology with varied capacitance value at selectable operation time period (t_p) of TPL5100 timer: 16, 32, and 64s. From Fig. 5.22, the series type rectifier exhibits the highest average conversion efficiency with the optimal capacitance. Regarding the timer operation time periods and capacitance value, the use of long time periods, which requires larger capacitance to maximize the efficiency, reduces the power consumption of the oscillator. However, the use of larger capacitor causes a higher leakage current loss. Therefore, this research adopted a t_p of $16\,\mathrm{s}$ and a $2\,\mathrm{mF}$ capacitor to minimize capacitor leakage loss.

TABLE 5.3
RECTIFIER PERFORMANCE COMPARISON

Topology	No. of diodes	Peak eff (%)	Avg eff (%)	Open voltage (V)
Series	1	21.9	17.3	0.21
One	2	16.7	13.3	0.29
Two	4	10.2	8.2	0.35

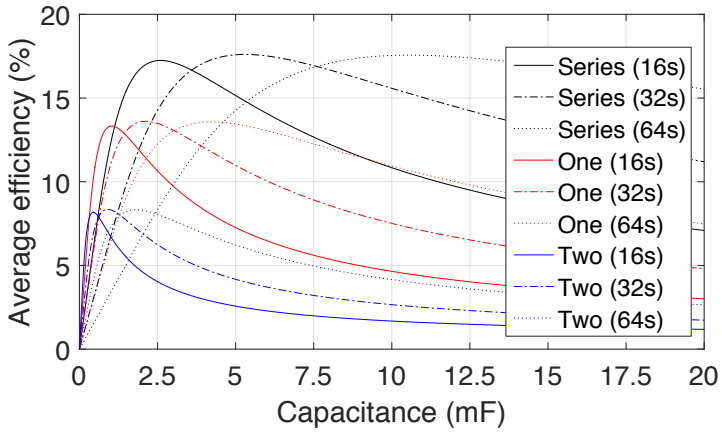

Figure 5.22. Comparison of average RF-DC conversion efficiency with respect to the charge tank capacitance values and different timer operation periods with a series rectifier, a one-, and a two-stage voltage multiplier.

$$I = \frac{V}{Z} = C\frac{dV}{dt} = C\frac{dV}{dZ}\frac{dZ}{dt} \qquad \frac{dZ}{dt} = \frac{V(t)}{Z(t)}\frac{1}{C\frac{dV}{dZ}(Z(t))} \tag{5.3}$$

$$V = \frac{p_1 Z + p_2}{Z + q_1} \qquad \frac{dV}{dZ} = \frac{p_1 q_1 - p_2}{(Z + q_1)^2} \tag{5.4}$$

Based on the analysis, a series type rectifier was fabricated as depicted in Fig. 5.23. For this prototype, S_L, S_P, and S_A are $17.6\,\mathrm{mm}$, $13.2\,\mathrm{mm}$, and $80.3°$, respectively. Fig. 5.24 (a) shows simulated and measured output voltage with respect to load resistance, and the curve fitting from the measurement is also depicted, and they have a good agreement. Fig. 5.24 (b) is the measured and estimated $2\,\mathrm{mF}$ capacitor voltage with at each time while charging with the fabricated rectifier prototype with $-20\,\mathrm{dBm}$ RF input power. The measurement and estimation exhibits a good agreement proving the accuracy of the estimation model. The peak and average RF-DC conversion efficiency are $24.0\,\%$ and $17.6\,\%$ with $2\,\mathrm{mF}$ capacitor and t_p of $16\,\mathrm{s}$ from the measurements of the rectifier prototype.

5.3.2 DC-DC Conversion Circuit Design and Characterization

Since the output voltage from the rectifier is too low to directly drive practical ICs, a DC-DC boost converter circuit is required. From preliminary measurements, the TPL5100

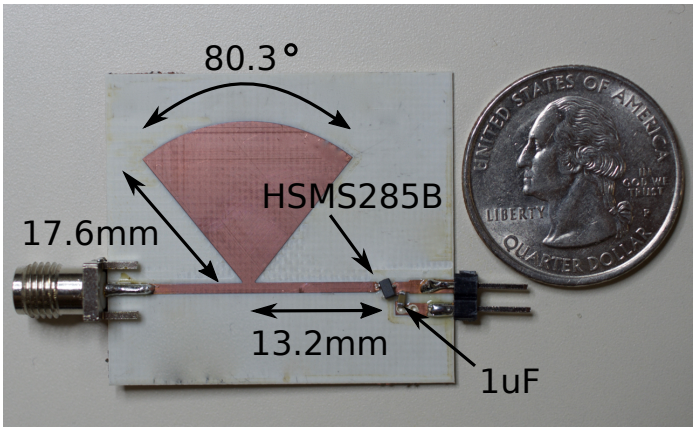

Figure 5.23. Picture of series rectifier prototype optimized for $-20\,\mathrm{dBm}$ input power at $2.45\,\mathrm{GHz}$.

timer requires $1.5\,\mathrm{V}$, which is the highest required voltage in the system, to start the operation. Therefore, the goal of this study is to generate more than $1.5\,\mathrm{V}$ from a DC-DC converter. Fig. 5.25 shows a typical DC-DC converter circuit topology, which is composed of a charge tank capacitor (C_t), an inductor (L), an N-MOSFET (Q_1), a Schottky diode (D_1), and an output capacitor (C_{out}). The gate terminal of the FET is triggered by the TS3001 oscillator. The selection of each component and of the oscillation frequency is very important to maximize DC-DC conversion efficiency. The aggregated power loss (P_{loss}) in the circuit is the summation of the control (P_{ctrl}), conduction (P_{cond}), and switching (P_{sw}) losses [39]. Therefore, $P_{av} = P_{RFDC} - P_{loss}$ where P_{av} is available power from the system and P_{RFDC} is the average power of the RF-DC conversion circuit. The control loss, which is the minimum required power to operate the system, is associated with the power consumption of the timer and the oscillator ICs. To minimize the oscillator power consumption without degrading the performance of the DC-DC converter, the operation frequency was selected to be $10\,\mathrm{kHz}$ [39]. Table 5.4 summarizes measured current consumption and operation time of each IC with in t_p of $16\,\mathrm{s}$. The TPL5100 timer IC has the fixed MOSFET switch drive time of $31.25\,\mathrm{ms}$ which limits the operation time of the oscillator. However, a decoupling capacitor (C_d) connected to the V_{dd} of the oscillator circuit can extend the operation time of the oscillator. Using the datasheet recommended value of $0.1\,\mu\mathrm{F}$ sustains the operation of the oscillator for extra $30\,\mathrm{ms}$, making the total operation time to be about $60\,\mathrm{ms}$ with $1.5\,\mathrm{V}$

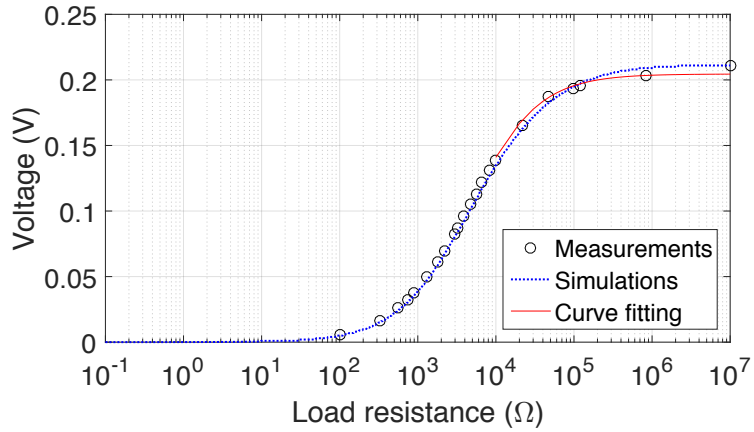

(a)

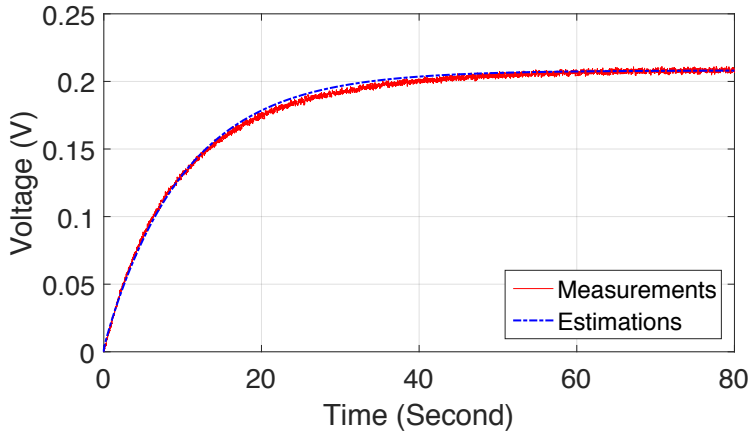

(b)

Figure 5.24. (a) Measured, simulated, and curve fitted output voltage of the recfier with a varied load resistance. (b) Measured and estimated $2\,\mathrm{mF}$ capacitor voltage while charging with respect to time.

input voltage. The minimum P_{ctrl} is $59\,\mathrm{nW}$, which is an ultra low value that is another goal that needs to be achieved to realize positive available power. Regarding other components, an Avago HSMS282 Schottky diode, a Vishay Si2302CDS N-MOSFET, and a Coilcraft DO5022P-104 ($100\,\mu\mathrm{F}$) inductor were chosen to minimize P_{cond} and P_{sw}.

5.3.3 Selection of PV cell and Operation Test

Since the control system requires only $59\,\mathrm{nW}$ of power to operate, the output voltage, instead of the output power, under low light irradiation is a key factor in the selection of a PV cell. Therefore, a Panasonic AM-5610CAR $25\,\mathrm{mm}$ by $20\,\mathrm{mm}$ amorphous silicon solar cell which exhibits $5.1\,\mathrm{V}$ open voltage under 1 sun irradiation was selected. As depicted

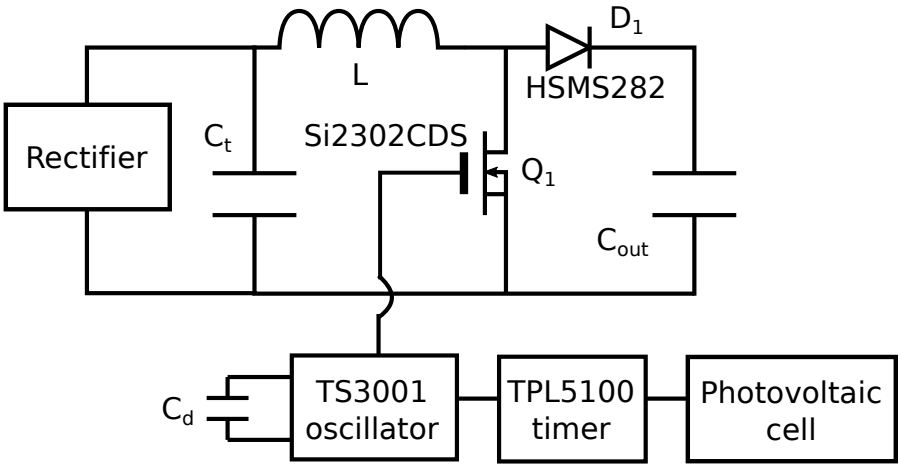

Figure 5.25. Circuit schematic of a DC-DC boost converter.

TABLE 5.4
COMPONENTS OF DC-DC CONVERTER

Component	Part no.	Operation time	Current
Timer	TPL5100	Continuous (31.25 ms MOSFET drive time)	32.6 nA @1.5 V 36.4 nA @1.8 V
Oscillator	TS3001	60 ms @1.5 V	1.34 µA @1.0 V 1.8 µA @1.5 V 2.4 µA @1.8 V

in Fig. 5.26 (b) the PV cell, which can be mounted on a $2.4\,\mathrm{GHz}$ patch antenna, exhibits $1.9\,\mathrm{V}$ of open voltage which supports the operation of the system under $3\,\mathrm{lx} = 440\,\mathrm{nW/cm^2}$ irradiation, which is 10^2 and 10^4 times weaker than office lighting and direct sunlight, respectively. $3.4\,\mathrm{lx}$ is dark limit of civil twilight under a clear sky, so $3\,\mathrm{lx}$ light irradiation is considered as night time. Fig. 5.26 (c) shows the output voltage from the DC-DC converter, the rectifier, the timer, and the PV cell during operation under these darkroom irradiation conditions for $-20\,\mathrm{dBm}$ ambient RF input power. The DC-DC converter successfully charges $100\,\mu\mathrm{F}$ capacitor to more than $2.4\,\mathrm{V}$ within $450\,\mathrm{s}$ with the DC-DC conversion efficiency of $38\,\%$ and a maximum output voltage of $3\,\mathrm{V}$. The average system output power is $643\,\mathrm{nW}$ which is 10.9 times higher than the minimum required system power. By gradually reducing the RF input power, the net positive output power with output voltage of $1.5\,\mathrm{V}$ was confirmed from $-25.0\,\mathrm{dBm}$ of RF input power which is $4\,\mathrm{dB}$ and $9.4\,\mathrm{dB}$ lower than

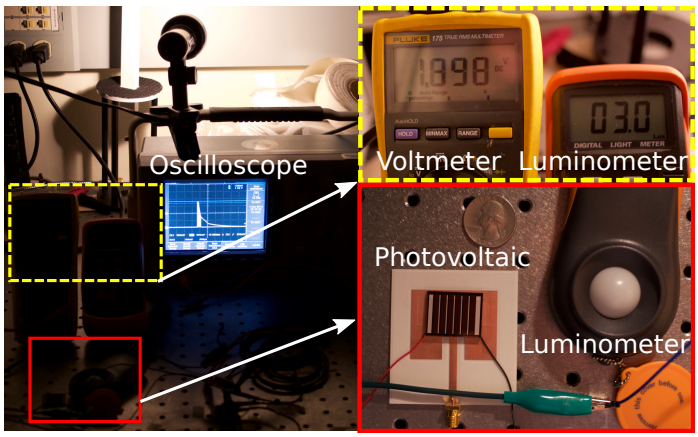

(a)

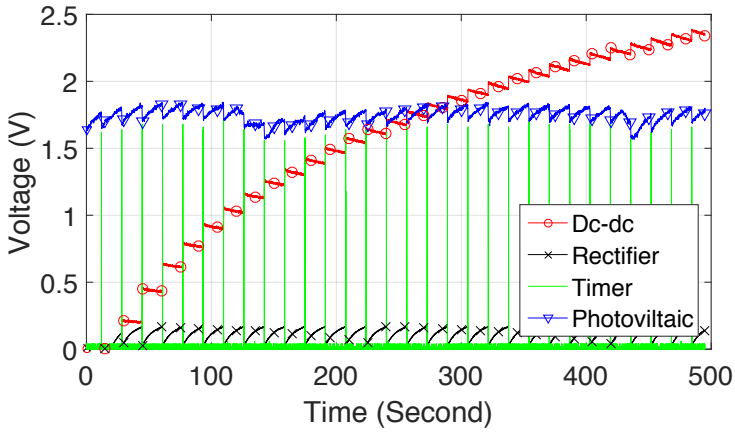

(b)

Figure 5.26. (a) Operation test of the DC-DC converter prototype in a darkroom. (b) Measured output voltage from the DC-DC converter, the rectifier, the timer, and the PV during operation test.

state-of-the-art autonomous RF energy harvester [43] and hybrid RF/solar energy harvester [101], respectively.

5.4 Power Management System for Overnight Operation of Long-range Active Van-Atta RFID Sensor

In the previous sections, ultra low power far-field RF energy harvesting systems were discussed.These energy harvester systems have very high RF sensitivity, but available power is still very limited. For example, an eZ430-RF2500 MCU module with a transceiver, which is discussed in Chap. 4, consumes about 200 µJ per data transmission even for low RF power transmission mode. This limits the cycle of data transmission and the communi-

cation range to below once in a few minute and the communication range to below $10\,\mathrm{m}$, respectively, even with $-20\,\mathrm{dBm}$ RF input power. This is because of the module system configuration relying on a power hungry RF transceiver. The application of these sensors are limited to data logging which requires relatively slow data acquisition such as structural health monitoring. In order to realize an ultra long range high duty cycling sensing system for such as hazardous gas detection, recently an active Van-Atta array backscattering RFID at mm-wave frequency [102] was reported. This system utilizes a high gain cross polarized Van-Atta array antenna with RF transistors for $28\,\mathrm{GHz}$ 5G network. Because of low spill over loss associated with the use of high gain antennas for both a transmitter and a sensor tag, theoretically, it can achieve a kilometer range wireless sensing [102]. Also, an intrinsic self-mixing operation of backscattering communication systems allows one to use a VLF oscillator for modulation without the fine tuning of a carrier emitter in a sensor tag. Therefore, technically, the VLF oscillator used for the DC-DC boost converter can simultaneously do a backscattering modulation. In this section, a energy autonomous power management circuit design, which allows a continuous sensing during day-time and high duty cycling ($> 20\,\%$) during night-time, is discussed.

5.4.1 System Overview

The block diagram of this system is depicted in Fig. 5.27.

This power management circuit has two operation states; normal operation and power saving mode. During normal operation mode, the system bypasses a power saving circuit and powers VLF oscillator (TS3001 Silicon Labs), which triggers the RF transistors in an active Van-Atta RFID chip to create the modulation. The modulation frequency depends on the resistance of a resistive sensing element (R_s) such as PEDOT:PSS, rGO, and CNT for temperature, humidity, and gas sensing [54]. Also, some energy is stored in an energy storage device. As discussed in Chap. 2, it is preferred to avoid the use of an energy storage device which involves chemical reactions because of short charge-discharge life

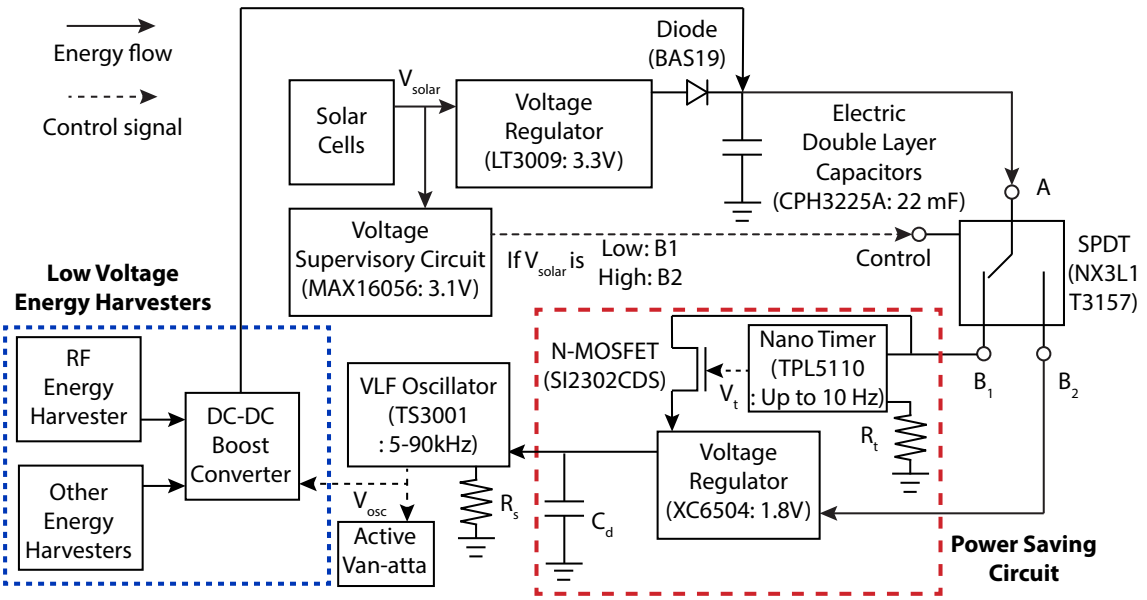

Figure 5.27. Circuit schematic of a DC-DC boost converter.

cycle, especially for a long life-time IoT applications. Therefore, two paralleled EDLCs (CPH3225A Seiko Instruments), which have total capacitance of $22\,\mathrm{mF}$ and rated voltage of $3.3\,\mathrm{V}$ were selected to be used. The voltage from the solar cells is regulated at $3.3\,\mathrm{V}$ to protect the EDLCs and an additional voltage drop because of a diode, which prevents the leakage from the capacitors, limits the capacitor voltage to $3.1\,\mathrm{V}$. On the other hand, during the power saving mode, a nano timer (TPL5110 Texas Instruments) drastically reduces the power consumption while the gate of N-MOSFET (SI2302CDS Vishay) is off. The timer opens the gate of N-MOSFET for a short amount of time to charge a capacitor (C_d) and to power the VLF capacitor. The timing of the N-MOSFET switching is determined by the value of the timer resistance (R_s), and the duration of VLF oscillator operation is determined by the value of a decoupling capacitor (C_d). These two parameters are used to control the timing and duty-cycling rate.

The operation modes are switched based on the output voltage from solar cells by utilizing a voltage supervisory circuit (MAX16056 MAXIM) and an SPDT switch (NX3L1T3157 NXP). When output voltage from the solar cells is more than a threshold voltage of the voltage supervisory circuit ($3.1\,\mathrm{V}$ for the prototype), the operation is switched to the power

saving mode by toggling the SPDT switch.

The selection of duty cycling period heavily depends on the power the consumption of the system, especially that of VLF oscillator, and available ambient energy. According to preliminary measurements, the system consumes about $3.11\,\mu\mathrm{A}$ of current while the oscillator is on with the oscillation frequency is $10\,\mathrm{kHz}$ and $37.6\,\mathrm{nA}$ while the oscillator is off. Therefore, the power consumption of each state is roughly 4.67 to $9.64\,\mu\mathrm{W}$ and 56.4 to $116.6\,\mathrm{nW}$, respectively, assuming the operation voltage varies from 1.5 to $3.1\,\mathrm{V}$. Therefore, if RF input power is $-20\,\mathrm{dBm}$, it will support about $10\,\%$ duty cycle operation. Also, the available energy from capacitor E_{avg} can be determined from

$$E_{avg} = \frac{1}{2}C(V_h^2 - V_l^2), \tag{5.5}$$

where C is capacitance, and V_h and V_l are the upper and lower voltages of the capacitor. Therefore, the charged EDLCs can provide $81\,\mathrm{mJ}$ of energy assuming V_h is $3.1\,\mathrm{V}$ and V_l is $1.5\,\mathrm{V}$, and this supports an additional 20 to $30\,\%$ of duty cycling rate for the expected night time of $10\,\mathrm{h}$. However, there is a trade-off between the available power from ambient energy harvesters and the duty cycling rate. The use of higher duty cycling rate reduces the time for charging of a charge tank capacitor in a DC-DC converter and reduces available power. Therefore, for an initial prototype, $20\,\%$ duty cycling with $4\,\mathrm{s}$ period were selected. To achieve these values, R_t and C_d are chosen to be $8.3\,\mathrm{k\Omega}$ and $1\,\mu\mathrm{F}$, respectively. With this setting, the expected average power consumption of the system during the power saving mode is about $1.5\,\mu\mathrm{W}$. The output voltage from an oscillator during the power saving mode is depicted in Fig. 5.30.

5.4.2 Operation Test with a DC-DC converter

The fabricated prototypes of the power management circuit, VLF oscillator, DC-DC boost converter, and the off-the-shelf solar cells (AM-5610CAR) are depicted in Fig. 5.29.

The control pin of the DC-DC converter discussed in the previous section was con-

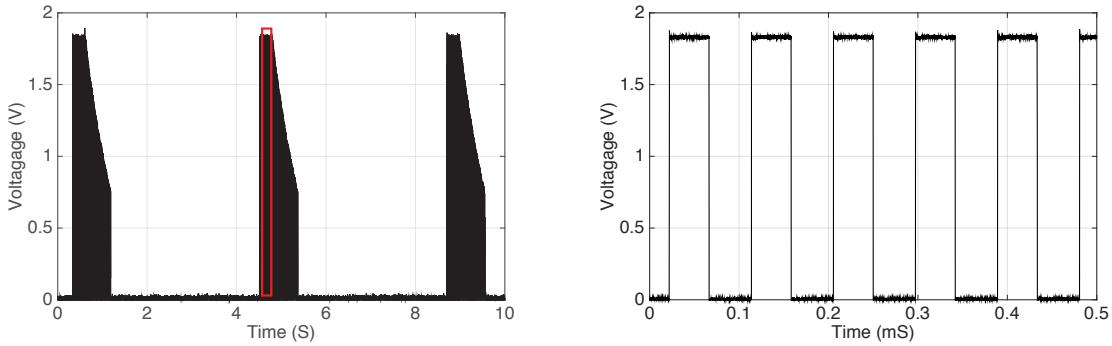

(a) (b)

Figure 5.28. (a) Measured VLF oscillator output voltage while power saving mode. (b)Close-up view of VLF oscillator output voltage (red line in (a)).

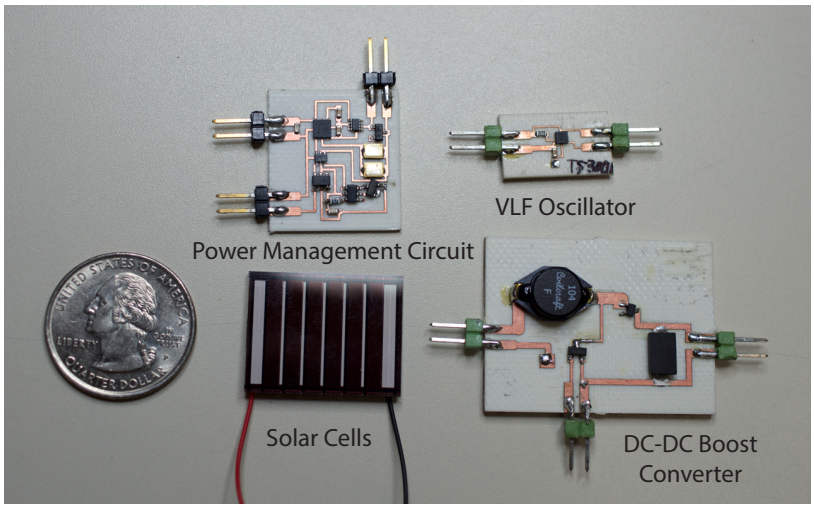

Figure 5.29. Picture of the fabricated prototypes of the power management circuit, VLF oscillator, DC-DC boost converter, and the off-the-shelf solar cells (AM-5610CAR).

nected to the output of the VLF oscillator, and the output voltage from the RF energy harvester for $2.45\,\mathrm{GHz}$ in Fig. 5.23 was connected to a charge tank capacitor of the DC-DC converter. Since the timing of operation was changed from 16 to $4\,\mathrm{s}$, a $390\,\mu\mathrm{F}$ capacitor was used for the charge tank capacitor. The operation of the DC-DC converter circuit and the VLF oscillator while the power management circuit is in the normal operation mode and the low power mode is shown in Fig. 5.30. The circuit successfully operates and generates a boosted voltage from $-20\,\mathrm{dBm}$ of RF input power. As expected, while the system is in the normal operation mode, the charge tank capacitor cannot store enough energy and the output voltage from the RF energy harvester cannot be boosted. The input power from the

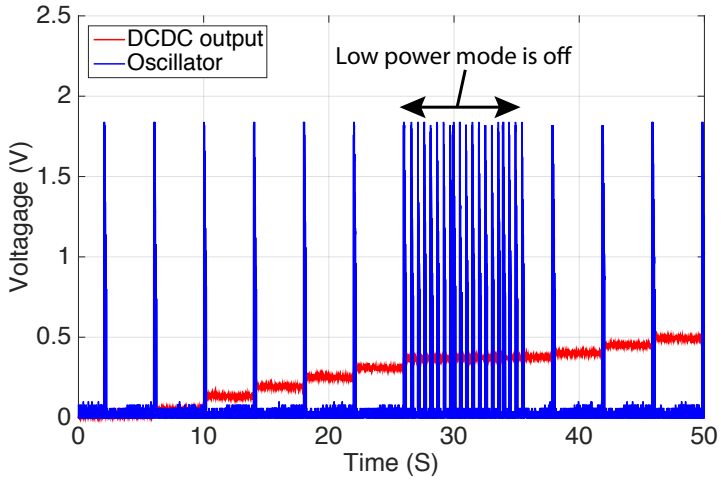

Figure 5.30. Operation of the DC-DC converter circuit and the VLF oscillator while the power management circuit is in the normal operation mode and the low power mode.

solar cells can generate high enough power to operate the oscillator, so practically, there is no DC-DC boost conversion is needed for the normal operation.

5.4.3 Field test in the office environment

Finally, the operation of the designed prototype was confirmed through a field test in a clattered office environment. As depicted in Fig. 5.31 (a), a charging of EDLCs with power from the RF energy harvester was confirmed at $8\,\mathrm{m}$ from a transmitter antenna (MODEL 3115 ETS LINDGREN), which has a gain of $9\,\mathrm{dBi}$ at $2.45\,\mathrm{GHz}$ with RF input power of $29\,\mathrm{dBm}$ (EIRP $38\,\mathrm{dBm}$) that is the maximum output power under the FCC regulation. The operations of the VLF oscillator at daytime, evening, and sunrise are depicted in Fig. 5.31 (b) to (d). During daytime, the oscillator operates continuously, and the power saving operation starts from a few hours after sunset to sunrise.

5.5 Inkjet Printed Organic Solar Cell

The last missing part of the printed hybrid RF solar energy harvester is the inkjet printed solar cell. In this section, the inkjet printing process to create a fully printed flexible organic solar cell is discussed.

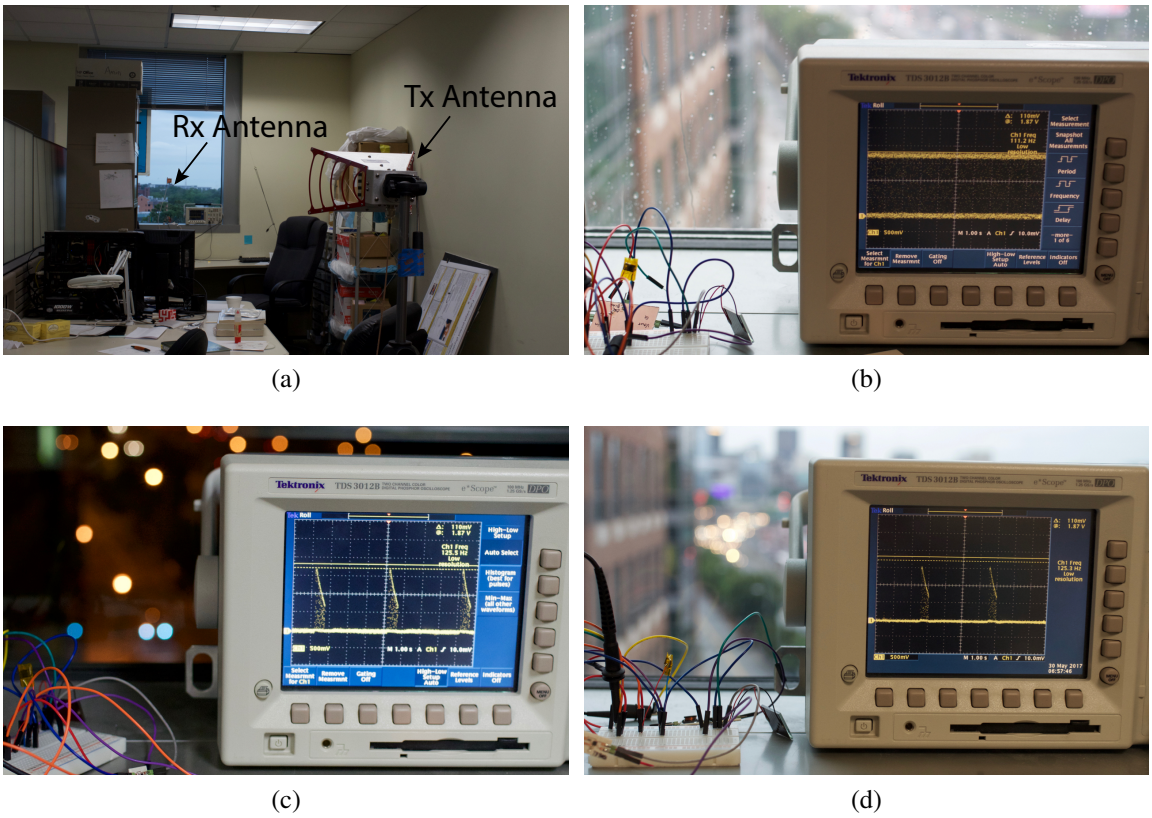

Figure 5.31. (a) Operation test of the power management system with the RF energy harvester powered by a RF transmitter at 8 m away from the receiver. The VLF oscillator output voltage at (b) daytime, (c) midnight, and (d) sunrise.

5.5.1 Operation Principle of Organic Solar Cell

As summarized in table 3.2, there are several different types of printed solar cells depending on the light absorbing material used as an active layer. However, in this research organic semiconductor material is the main focus. Organic photovoltaic (OPV) provides low-cost and low-temperature process along with possibility of large area fabrication on flexible substrates. The basic structure of OPV is an organic active material layer sandwiched between two different electrodes which have different work functions. Because of its operation principle, at least one of electrodes needs to be made of a (semi) transparent conductive material such as Indium Tin oxide (ITO) or poly(3,4-ethylenedioxythiophene):poly(styrenesulfonate) (PEDOT:PSS). Another electrode does not need to be transparent, so metal, such as silver and aluminum, is typically used.

The first prototype of an organic thin-film solar cell, which has a heterojunction of p- and n-type organic semiconductors, was first demonstrated by C.W. Tang in 1986 [103]. The conversion efficiency of this is not more than $1\,\%$ and this had not been improved until the development of bulk heterojunction material by Hiramoto et.al in 1991 [104]. After the further optimization and selection of materials, P3HT-PCBM is the standard bulk heterojunction material, which can achieve more than $5\,\%$ of power conversion efficiency, for organic solar cell in these days [105]. The basic electricity generation principle is as following.

1. Light penetrates a transparent electrode and illuminates a bulk heterojunction semiconductor material.

2. P-type semiconductor material in the bulk heterojunction semiconductor material is excited by the light irradiation and electrons in the highest occupied molecular orbital (HOMO) move to the lowest unoccupied molecular orbital (LUMO) and excitons, which are hole-electron pairs, are created.

3. Exitons travel through the P-type semiconductor and reach the p-n junction.

4. Exitons are separated into electrons and holes. Electrons travel through n-type semiconductor and reach cathode (low work function) and holes travel through p-type semiconductor and reach anode (high work function).

5. An external circuit is connected to the electrodes and creates current flow. The maximum open voltage is the potential difference between the HOMO of donor material and the LUMO of acceptor material.

5.5.2 Characterization of P3HT:PCBM material

Photoconductive blend material consists of regioregular poly(3-hexylthiophene) (rr-P3HT, Rieke Metals, Inc., USA) and [6]-phenyl C61 butyric acid methyl ester (PCBM,

Solenne, The Netherlands), dissolved in a mixture of ortho-dichlorobenzene (oDCB, anhydrous 99%, Sigma-Aldrich, USA) and 1,3,5- trimethylbenzene (mesitylene, anhydrous 99%, Sigma-Aldrich, USA).Typically, P3HT:PCBM solution is deposited utilizing screen printing and spin coating processes. Since this research utilizes inkjet printing for the deposition of P3HT:PCBM material, a special formulation of P3HT:PCBM solution is required. According to [106], a mixture of high and low boiling solvent such as 68 % of ortho-dichlorobenzene (oDCB) and 32 % of 1,3,5-trimethylbenzene (mesitylene), respectively, enables the inkjet printing of P3HT:PCBM material. This solvent mixture controls wetting properties of ink and drying process of printed film. The oDCB with higher boiling point (b.p. = $180\,^{\circ}\mathrm{C}$) provides reliable and jettable ink to prevent nozzles from clogging. Moreover, mesitylene has a lower boiling temperature, which enables a fast drying process and results in uniform morphologies, along with lower surface tension ($28.8\,\mathrm{dynes/cm}$, which provides better wetting properties of ink. Therefore, in this research, the mixing weight ratio of P3HT:PCBM:solvent is 1:0.75:98.25, with solvent mixture of oDCB: mesitylene (68:32 wt%) used for the active layer ink.

During the electricity generation process described above, the exition generation happens mostly near the transparent electrode and separated charges have to travel to each electrode before the recombination. Therefore, the thickness of the active layer is very important to realize a high power conversion efficiency. To figure out the optimal numbers of layer for P3HT:PCBM material, two and three layers of P3HT:PCBM ink was printed on ITO coated glass and on top of the printed P3HT:PCBM material, while two layers of silver nano particle ink was printed and annealed with a hot plate at $100\,^{\circ}\mathrm{C}$ for $5\,\mathrm{min}$ and $120\,^{\circ}\mathrm{C}$ for $10\,\mathrm{min}$, respectively. After the initial trial of printing test, the surface of P3HT:PCBM material was hydrophobic and the wetting property of the silver ink was poor. Therefore, the surface was treated with UV ozone for $30\,\mathrm{s}$ before the printing of silver ink. Fig. 5.32 shows printed solar cells of different conditions. Both sample (c) and (d) exhibited photovoltaic reaction and open voltage under sunlight irradiation was $0.037\,\mathrm{V}$

and $0.054\,\mathrm{V}$, respectively. Even if sample (d) has slightly higher open voltage, the wettability of P3HT:PCBM material did not improved significantly with UV ozone treatment. On the other hand, samples (a) and (b) did not show any photovoltaic reaction. Therefore, the minimum required number of layers for the P3HT:PCBM material is concluded to be three.

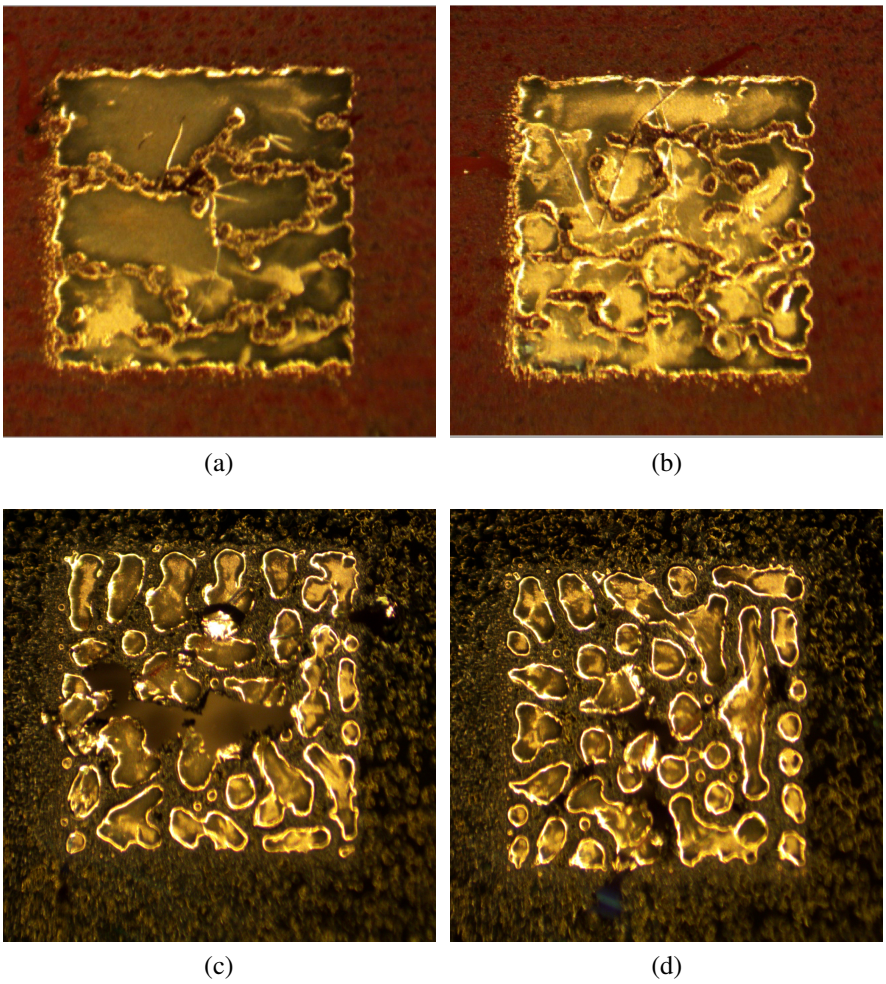

(a) (b)

(c) (d)

Figure 5.32. Printed organic solar cell samples with (a) Two layer P3HT without UV ozone treatment. (b) Two layer P3HT with UV ozone treatment, (c) Three layer P3HT without UV ozone treatment. and (d) Three layer P3HT withUV ozone treatment.

5.5.3 Work Function Characterization of Top and Bottom Electrodes

In the previous section, the printability and minimum required thickness of P3HT:PCBM were confirmed by using a ITO coated glass as a transparent electrode. However, the ulti-

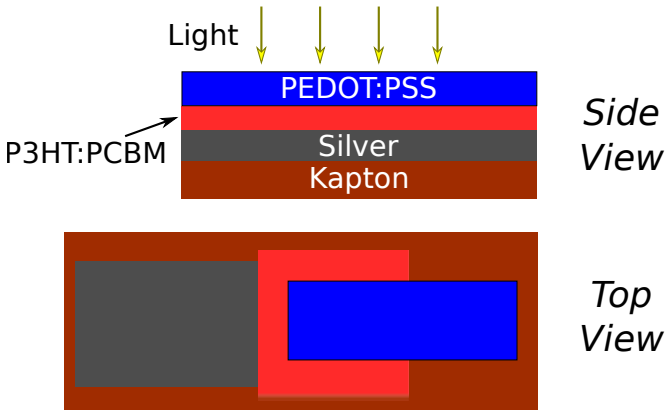

Figure 5.33. Printed solar cell structure.

mate goal of this research is to create a fully printed flexible solar cell, so in this part, the structure of a fully printed organic solar cell is discussed. In organic solar cells, one of the important issues is to create a high work function difference between two electrodes. For example, silver and PEDOT:PSS, which are expected to be used as electrodes, have work functions of approximately 4.26 and 5.2 eV as a bulk, respectively. To support the solar cell structure, Kapton HN substrate, which can stand up to $400\,^{\circ}\mathrm{C}$, from DuPont is used because of high process temperature handling capability. Since silver and PEDOT:PSS have a relatively large work function difference, the simplest possible organic solar cell structure is composed of silver as a bottom electrode and PEDOT:PSS as a top electrode as depicted in Fig. 5.33. Since silver ink typically requires a relatively high annealing temperature (more than $150\,^{\circ}\mathrm{C}$), this printing process is better than the other printing order to prevent printed organic material layers from damaging because of heat.

In order to test the work function of printed electrodes, a $1\,\mathrm{cm}$ by $1\,\mathrm{cm}$ square pattern of silver nano particle and PEDOT inks were printed on ITO coated glass and the work function of each material was measured utilizing a Kelvin meter. For the fabrication, Novacentrix JS-B40G nano silver ink and Heraues Clevios PEDOT:PSS ink were used. Two layers of each ink were printed by utilizing a Dimatix inkjet printer and cured at $250\,^{\circ}\mathrm{C}$ for $30\,\mathrm{min}$ and at $120\,^{\circ}\mathrm{C}$ for $5\,\mathrm{min}$, respectively. The work function of graphene ($4.6\,\mathrm{eV}$) was used as the reference of measurement. Each material was probed at four points near the

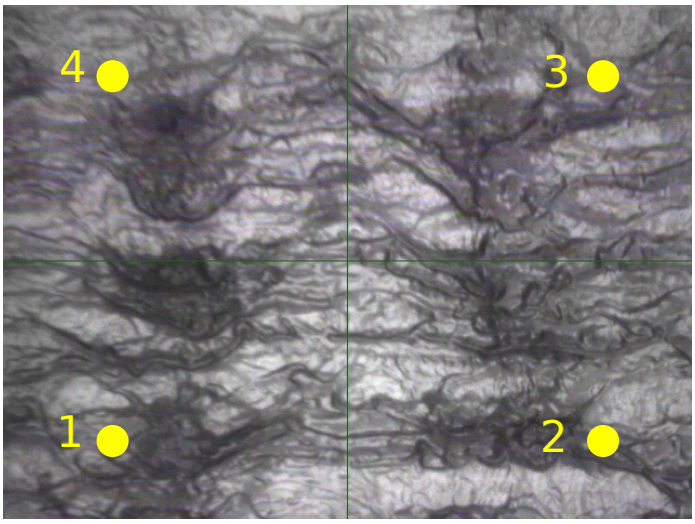

Figure 5.34. Printed PEDOT:PSS ink after curing and work function measurement points.

corner of the square. The picture of printed (two layers) PEDOT:PSS material and work function measurement points order is depicted in Fig. 5.34. Also, the measurement results of the work function are summarized in table 5.5. The average of measured work function for printed silver and PEDOT:PSS films is $5.07\,\mathrm{eV}$ and $5.05\,\mathrm{eV}$, respectively. Also, the sheet resistance of each material is 1.1 and $364\,\Omega/\square$.

TABLE 5.5
WORK FUNCTION OF PRINTED SILVER AND PEDOT:PSS

Data point	1	2	3	4	**Average**
Work function of silver without PEI (eV)	5.00	5.20	4.92	5.14	5.07
Work function of PEDOT:PSS (eV)	5.04	5.08	5.04	4.98	5.05
Work function of silver with PEI (eV)	4.15	4.15	4.15	4.15	4.15

According to the work function measurement results, there is no significant difference between the work function of printed silver and that of PEDOT:PSS. Therefore, somehow the work function of one of electrodes need to be modified. Recently, the method of reducing the work function by applying a thin layer of polymeric material on top of an electrode has been reported [107]. This is known as polymeric work function modification. Generally, polyethylenimine (PEI) has been widely used to produce low-work-function electrodes. Therefore, in this research, the device topology in Fig. 5.35, which has PEI layer on top of silver, is adopted.

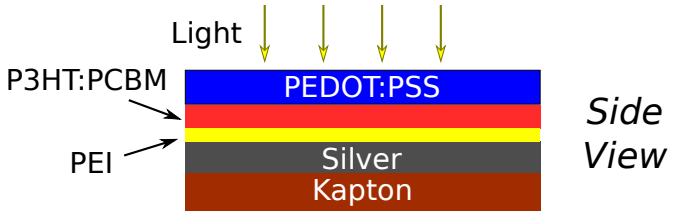

Figure 5.35. Printed solar cell structure with polymetric work function modification.

For the printable PEI ink, 70000 molecular weight poyethyleneimine $30\,\%$ aqueous solution ink from Alfa Aesar (part number 40529) was utilized. The ink was first dissolved with distilled water to reach $0.4\,\%$ weight percent and further diluted with glycerol to reach $0.18\,\%$ weight percent, to adjust the viscosity, making the ink compatible with the Dimatix printer. One layer of PEI ink was deposited on a cured silver ink on an ITO coated glass and baked in a vacuum oven overnight with $95\,°\mathrm{C}$ to evaporate the solvents. The work function of the PEI coated silver is $4.15\,\mathrm{eV}$, which is more than $0.9\,\mathrm{eV}$ lower than silver without PEI, according to the measurements with a Kelvin meter as shown in table 5.5.

5.5.4 Fully Inkjet Printed Solar Cells

Based on the characterizations of each material, fully inkjet printed solar cells were fabricated on a Kapton HN substrate with the following printing processes:

1. Print the 2 layers of silver nano particle ink.
2. Cure the sample in an oven at $250\,°\mathrm{C}$ for $30\,\mathrm{min}$.
3. UV ozone treatment for $60\,\mathrm{s}$ and print 1 layer of PEI ink on $40\,°\mathrm{C}$ platen.
4. Bake the sample in a vacuum oven at $95\,°\mathrm{C}$ for $1\,\mathrm{h}$ or longer.
5. Print the 3 layers of P3HT:PCBM ink on $40\,°\mathrm{C}$ platen with $5\,\mathrm{min}$ delay between each layer.
6. Dry the sample on a hot plate at $100\,°\mathrm{C}$ for $100\,°\mathrm{C}$ and bake the sample in an oven at $120\,°\mathrm{C}$ for $10\,\mathrm{min}$.

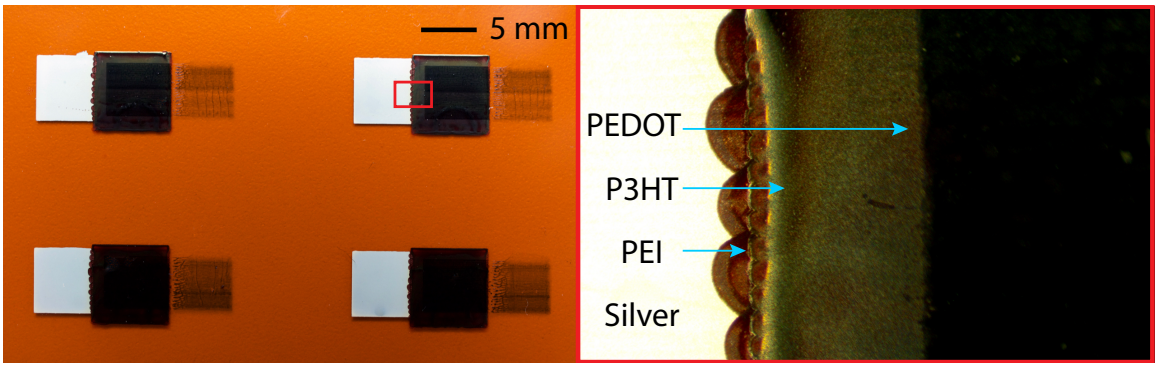

Figure 5.36. Fabricated fully inkjet printed solar cells.

7. UV ozone treatment for $60\,\mathrm{s}$ and print the 4 layers of PEDOT:PSS ink (2 layers from silver to PEI direction and 2 more layers from the opposite direction), and bake the sample in an oven at $120\,^{\circ}\mathrm{C}$ for $5\,\mathrm{min}$.

The picture of fabricated samples of fully inkjet printed solar cell is shown in Fig. 5.36.

As shown in Fig. 5.37 (a), the sample of solar cell exhibited about 0.2 to $0.25\,\mathrm{V}$ open voltage as a single cell under the normal office light intensity of about $350\,\mathrm{lx}$. Also, if two of these samples are cascaded in series, they exhibited almost doubled open voltage of a single cell open voltage. This implies that cascading of 4 to 5 cells of printed solar cell will be able to create $1\,\mathrm{V}$ of open voltage.

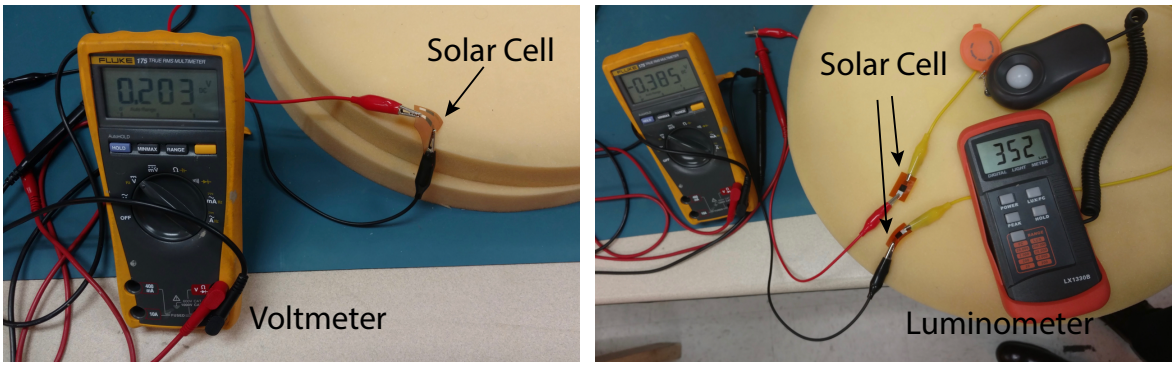

(a) (b)

Figure 5.37. Open voltage measurement of printed .

Next, the current density of a solar cell with respect to bias voltage was measured at three different light intensity levels as depicted in Fig. 5.38. According to the measure-

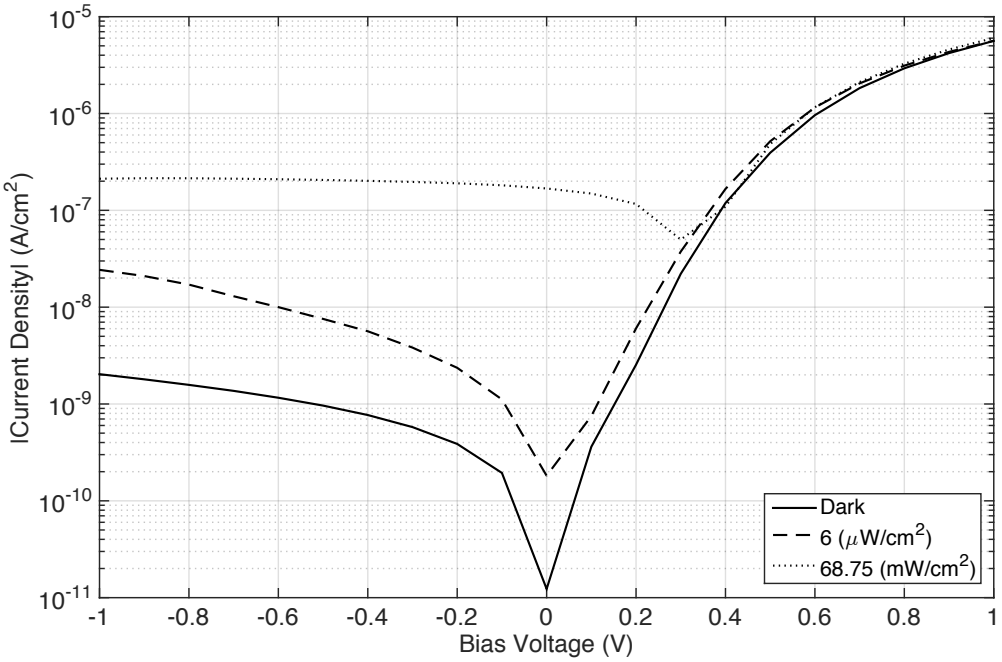

Figure 5.38. Current density of a printed solar cell with respect to bias voltage at dark, medium ($6\,\mu\mathrm{W/cm^2}$), and strong ($68.75\,\mu\mathrm{W/cm^2}$) light irradiation.

ment, the dark current performance is at least 10 times lower than reported printed organic solar cells [108], which implies that this printed solar cell can be used as a photo detector. However, the PCE is less than $1\,\%$ under the room light condition, and the sample does not generate more than $100\,\mathrm{nW/cm^2}$.

The possible cause of this low PCE is the thickness of active layer and the low conductivity of the top PEDOT:PSS electrode. As mentioned above, a too thick active layer causes high recombination of excitons reducing the PCE, but if the number of layers is reduced, the roughness of previously printed materials is too high and this causes the shorting of top and bottom electrodes. As depicted in Fig. 5.39, the coating of PEI material is not a perfect film and the printed surface became rough. This is one of the main causes of roughness. Also, as can be seen in Fig. 5.36, since the printed active layers are relatively thick, there is slight height difference between the P3HT layer and the Kapton making the printed PEDOT:PSS layer on the transition between these two very thin. This causes high resistance at the middle of top electrode reducing the PCE. Therefore, further process optimization is

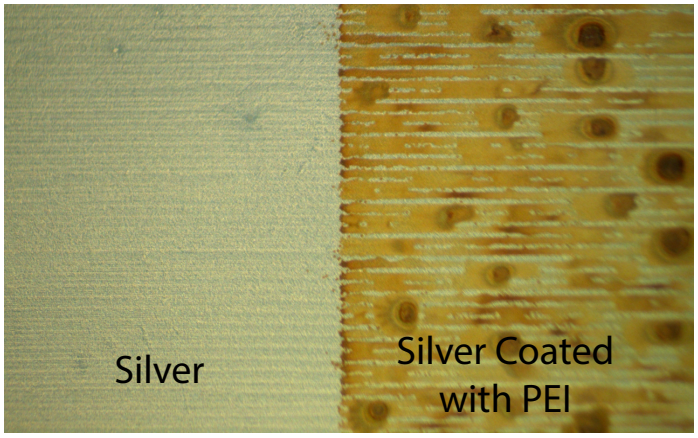

Figure 5.39. Printed silver with and without the coating of PEI polymer.

required to improve the PCE and achieve high output voltage.

5.6 Discussion for Future Extensions

In this chapter, the hybrid RF/solar energy harvester designs for ultra-low power IoT sensor devices were discussed. As a result, it was proved that the combination of a far-field RF energy harvester and solar cells allows one to use a high conversion efficiency DC-DC boost converter without the challenge of "cold-start" operation of ICs. This system architecture can improve the RF sensitivity up to $-25\,\mathrm{dBm}$, which is one of the highest RF sensitivities reported in the literature, by minimizing the power consumption of a DC-DC boost converter. Since required power is extremely low, the system can be operated in a dark light condition of $3\,\mathrm{lx}$, which is equivalently considered as night. In terms of operation distance, it is reported that the channel power level of about $-9\,\mathrm{dBm}$ is available from digital TV signals (400 to $700\,\mathrm{MHz}$) at $6.3\,\mathrm{km}$ away from a TV tower in Tokyo, Japan utilizing a $7.3\,\mathrm{dBi}$ gain antenna [8]. With the same condition, according to Friis transmission equation, the operation range of the RF energy harvester with $-25\,\mathrm{dBm}$ RF sensitivity is expected to be about $40\,\mathrm{km}$. Similarly, a power management circuit for continuous operation of Van-Atta array active RFID with simultaneous DC-DC boost conversion and modulation was demonstrated. This system supports an overnight duty-cycle operation of more than $20\,\%$ with the energy stored in small EDLCs and ambient RF energy. One of

the major limiting factors prevent 24/7 continuous operation is the relatively high power consumption of a VLF oscillator IC available in market. If the power consumption of this type of oscillator can be decreased by one order of magnitude, it is possible to eliminate the use of power saving mode and related circuit components in the system, and this will drastically simplifying the system.

Finally, a fabrication process of fully printed organic solar cells with a work function modification layer was developed and its performance was tested. It successfully generates 0.2 to $0.25\,\mathrm{V}$ of open output voltage with a single cell under the room light condition. For further PCE improvement, the printing process needs to be optimized to create a thinner layer of P3HT:PCBM and a more conductive electrodes. Also, for a system integration, a series connection of multi-cells for higher output voltage and a solar cell integrated antenna design are required.

CHAPTER 6

REAL-TIME ACTIVE MATCHING FOR NEAR-FIELD WIRELESS POWER TRANSFER

Near-field WPT technology is one of the most highly demanded technologies to realize truly cableless/batteryless mobile devices and wirelessly connected electronics, that are required for practical implementations of Internet of Things (IoT) devices, and could alleviate the typical issues of the short cruising range as well as the inconvenience of wired charging of electrical vehicles [5], [17], [109]. In addition to these applications, the medical field is one of the most important application areas of this technology. For hygienic purposes, the unique capability of EM waves to transfer power to sealed devices in a contact-/cable-less way is a major advantage. Furthermore, WPT could have a significant impact in health and biomonitoring applications, virtually eliminating the need for painful and infection-prone surgical procedures, which are currently necessary for periodical battery replacement, by wirelessly charging in-vivo implanted electronics. Associated with the development of flexible and wearable electronics, the importance of this technology getting higher and higher.

The resonant coupling, especially the magnetic resonant coupling method which belongs to the inductive power transfer techniques, has attracted the interest of the research community because of its relatively large operation distance and high maximum power transmission efficiency [16]. Also, the magnetic coupling is preferred to satisfy the fundamental requirement of penetrating the human body, which is electrically lossy conductor, to provide the power to the receiver in the human body. A two-frequency split, called the "horn effect", is usually associated with the fundamental operation of the magnetic resonance wireless power transmission in configurations with very small separation distances between transmitter and receiver coils [17]. This can be a major issue for WPT applications on moving or non-stationary platforms, such as the human body, typically pushing the values of the resonance frequency outside the allowable frequency bands or drastically

deteriorating the coupling efficiency. In order to compensate for the effect of human body part movements (e.g. breathing and turning), a real-time active matching circuit (MC) has to be inserted between the signal source and the transmitter coil. The overview of a typical magnetic resonant wireless power transmission system with real-time matching circuits on the transmitter side is depicted in Fig. 6.1. The matching circuit decreases the mismatch between a signal generator and a transmitting coil to maximize the power transfer efficiency to a receiver coil. In this chapter, first, Sec. 6.1 describes the fundamental operation principle of the magnetic resonant coupling type WPT. Sec. 6.2 shows active matching circuit design utilizing a GA and Sec. 6.3 further discusses the application of the active matching circuit design method for moving objects utilizing K-means clustering. In order to minimize the power consumption of the active matching system, the controller of the system focuses only on choosing the best matching circuit states among the set of preselected impedance values through GA and clustering processes. This allows to use an off-the-shelf MCU as a controller and a simple brute force selection process realizing a "real-time" operation of active matching circuit system.

6.1 Operation Principle of Magnetic Resonant Coupling Wireless Power Transfer

6.1.1 Wireless Power Transfer Efficiency and Horn Effect

Resonant coupling WPT utilizes at least one resonator for a transmitter and another resonator for a receiver to wirelessly transfer energy. There are magnetic and capacitive resonant coupling, but the magnetic flux dominates the energy transfer in magnetic resonant coupling WPT. In this research, an open-helical type resonator, which does not require any external circuit component and self-resonates, is mainly discussed as a resonator. The design of this type of resonator is based on the same operation principle as a dipole antenna, which resonates at the frequency that is determined by the length of dipole elements. A dipole antenna resonates when the total length of the two elements is equal to the half of the wavelength (λ) and radiates EM waves. The main difference between dipole antenna

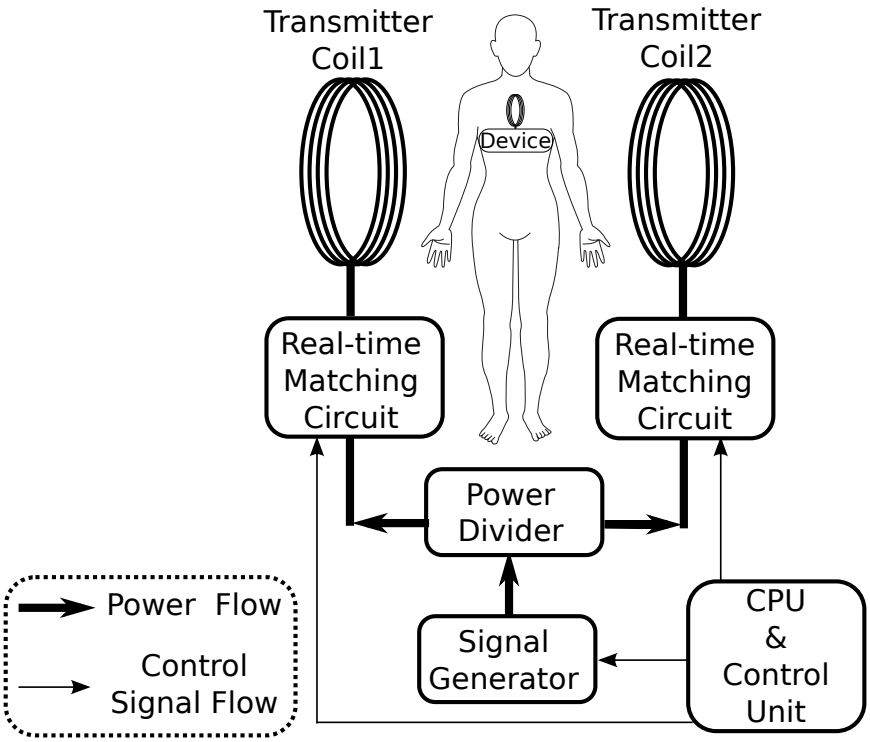

Figure 6.1. Block diagram of a dual-transmitting-coil wireless power transmission system with on-transmitter real-time matching circuits.

and open-helical coil is whether the resonating structure radiates EM waves or not. In the case of open-helical coil, it preserves EM energy in the structure and does not radiate while the resonator is independent from another resonator even if the resonator is connected to a signal source which generates signals with the resonance frequency. This is because the size of coil is electrically very small with respect to wavelength because of the winding of metal wires. Once the receiver reaches to the proximity of the transmitter, mutual coupling between two resonator electrically bridges two coils and energy transfers to the receiver.

An open helical coil can be approximated with an equivalent series RLC circuit as depicted in Fig. 6.2. In the figure, Z_0 is the characteristic impedance of the transmission line. If the resistance, the inductance and the capacitance of the single coil are R, L and C, the impedance of the coil, Z_{in}, is given by Eq. (6.1) where ω is an angular frequency. Specifically, the imaginary part of the coil impedance, X_{in}, can be expressed as shown in Eq. (6.2). At the self-resonance, $X_{in} = 0$ leaving the real part of impedance, which is

corresponding to the sum of copper loss and radiation loss of the resonator.

$$Z_{in} = R + j\left(\omega L - \frac{1}{\omega C}\right) \tag{6.1}$$

$$X_{in} = \omega L - \frac{1}{\omega C} \tag{6.2}$$

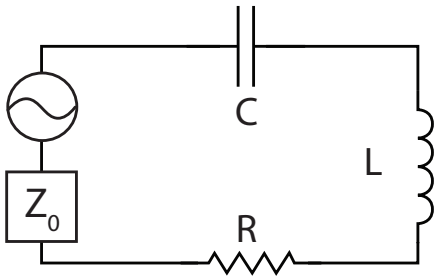

Figure 6.2. Equivalent circuit of open-helical type coil

In the case of two resonators, the equivalent circuit of a Tx-Rx network is expressed as Fig. 6.3 (a). In the figure, R_n, L_n, and C_n (where n = 1: Tx and 2: Rx) are the resistance, inductance, and capacitance of the resonator. Also, L_m is the mutual inductance between two resonators. Without the loss of generality, Fig. 6.3 (a) can be converted to a T-shaped equivalent circuit as depicted in Fig. 6.3 (b). Under the ideal condition of $Z_0 = Z_L = R = 0$, the reactance of the circuit is expressed as Eq. (6.3). If the Tx and Rx coils are the same, $R = R_1 = R_2$, $L = L_1 = L_2$, and $C = C_1 = C_2$ and the Eq. (6.3) = 0 at the resonance. By solving this equation, two angular frequency values ω_l and ω_u, which makes $X_c = 0$, can be found as described in Eq. (6.4) and Eq. (6.5), respectively. In Eq. (6.6), k_m is the coupling coefficient of two coils. From these equations, it can be conjectured that two frequency values, which maximize the WPT efficiency, appear while Tx and Rx coils are arranged at proximity and coupling coefficient is high. On the other hand, while the distance between Tx and Rx coils is high and $L_m = 0$, $\omega_l = \omega_u = \omega_0 = \frac{1}{\sqrt{LC}}$ and the circuit resonates at only one frequency value. Usually, the operation frequency of wireless system is limited by regulations and the operation frequency cannot be arbitrary swept to track the peak

maximum efficiency point. For example, the $13.56\,\mathrm{MHz}$ band, which is one of typically used ISM bands for near-field WPT is 13.553 to $13.567\,\mathrm{MHz}$. Therefore, an undesired two-frequency split, called the "horn effect" degrades the WPT efficiency at the center frequency when Tx and Rx coils are too close with each other.

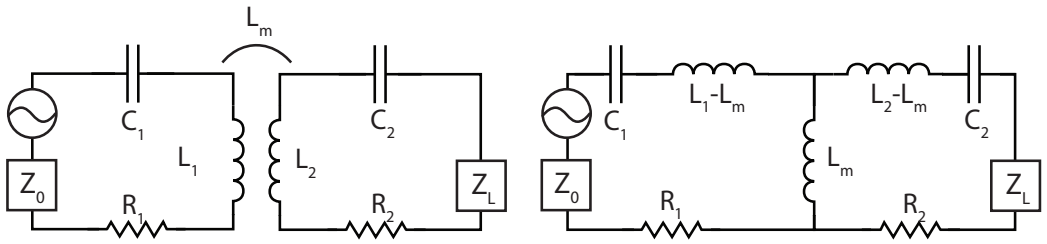

Figure 6.3. (a) Equivalent circuit of Tx-Rx coil network. and (b) T-shaped equivalent circuit of Tx-Rx coil network.

$$X_c = \frac{1}{\omega L_m} + \frac{1}{\omega(L_1 - L_m) - \frac{1}{\omega C_1}} + \frac{1}{\omega(L_2 - L_m) - \frac{1}{\omega C_2}} \tag{6.3}$$

$$\omega_l = \frac{\omega_0}{\sqrt{1 + k_m}} = \frac{1}{(\sqrt{L + L_m})C} \tag{6.4}$$

$$\omega_u = \frac{\omega_0}{\sqrt{1 - k_m}} = \frac{1}{(\sqrt{L - L_m})C} \tag{6.5}$$

where

$$k_m = \frac{L_m}{L} = \frac{\omega_u^2 - \omega_l^2}{\omega_u^2 + \omega_l^2} \quad and \quad \omega_0 = \frac{1}{\sqrt{LC}} \tag{6.6}$$

In two-port network, WPT efficiency (η_{21}) can be expressed as Eq. (6.7), where S_{21} in Eq. (6.8) is the transmission coefficient of the two-port network. From these equations, it is also recognized that the WPT efficiency has two peaks when L_m is high and gradually

merges into one peak. Eventually as L_m reaches 0, WPT efficiency also becomes 0.

$$\eta_{21} = |S_{21}|^2 \times 100\% \tag{6.7}$$

$$S_{21}(\omega) = \frac{2jL_mZ_0\omega}{L_m^2\omega^2 + \left\{(Z_0 + R) + j(\omega L - \frac{1}{\omega C})\right\}} \tag{6.8}$$

In order to confirm the transition from the strongly coupled regime to the weakly coupled regime in the small coil separation distance range, for proof-of-concept purposes and without loss of generality, an open type helical coil which has the self-resonance frequency of $13.56\,\mathrm{MHz}$ was designed on CST STUDIO SUITE within the size restriction in the diameter of $10\,\mathrm{cm}$. In the preliminary measurement setup, in order to simplify the experiments, the same coil design was adopted for both transmitter and receiver coils. The extension of the presented approach to coils of different size is straightforward. During the simulation process, the gap between each coil wire was optimized to reduce the radiation loss in given specific fabrication limitations. In order to reduce the simulation time, the integral solver was adopted. The simulation results yielded the following coil dimensions as summarized in Table 6.1; the radius of the coil is $50\,\mathrm{mm}$, the diameter of the copper wire is $1\,\mathrm{mm}$, the gap between consecutive turns is $0.2\,\mathrm{mm}$, and the number of turns is 26, to achieve the operation frequency of $13.56\,\mathrm{MHz}$. Based on the simulation results, the transmitter and the receiver coil prototypes were fabricated with $1\,\mathrm{mm}$ diameter copper wire utilizing laser cut acrylic boards for support purposes. The picture of the fabricated Transmitter (Tx) and Receiver (Rx) coils, the simulated and the measured S_{11} values of the single coil without any other coil in its proximity and the measured S_{21} value values for different center-to-center coil distances (identical Tx and Rx coils) are shown in Fig. 6.4, Fig. 6.5, and Fig. 6.6, respectively. The higher loss in the measurement results is assumed to be associated with greater radiation loss because of the fabrication error, the conductor loss associated with the copper wires and the dielectric loss because of the acrylic board supporters. As depicted in

Fig. 6.6, two frequency peaks can be seen at coil separation distances up to $12\,\mathrm{cm}$.

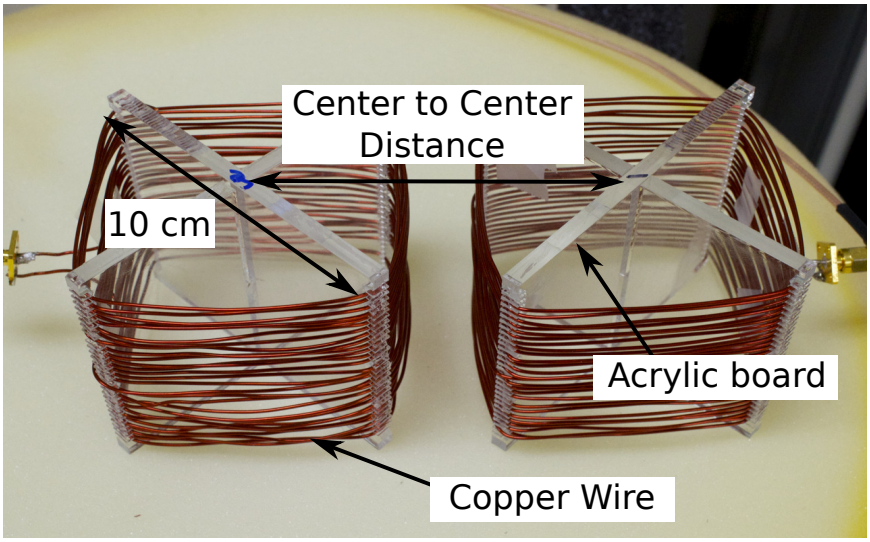

Figure 6.4. Open-helical-coil wireless power transfer system prototype.

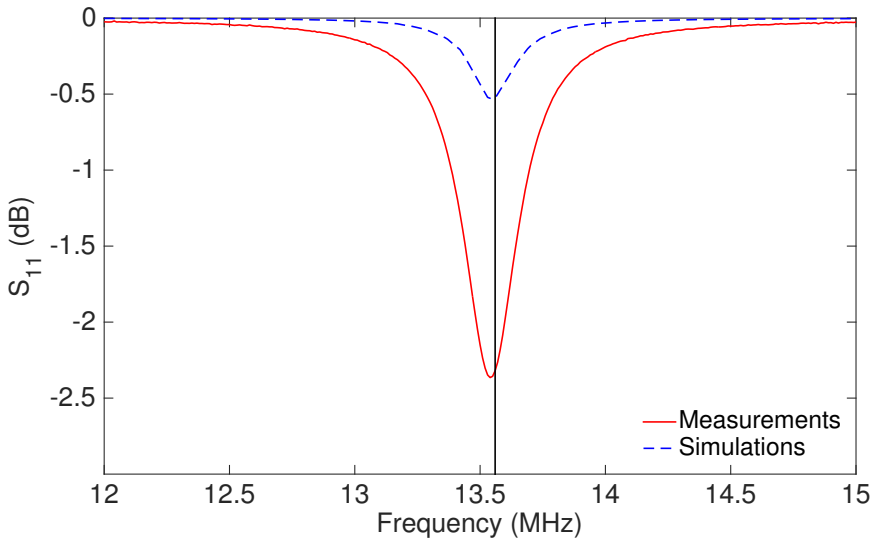

Figure 6.5. Measured and simulated S_{11} of the single open helical coil prototype.

6.1.2 Numerical Analysis of an Open-helical Coil

Practically, the values of the self-inductance and self-capacitance of the coil remain constant over the frequency range of operation allowing us to derive their values from the imaginary part of the measured coil impedance at two frequency points. The input impedance of a coil can be expressed as Eq. (6.9), where S_{11} is the reflection coefficient of

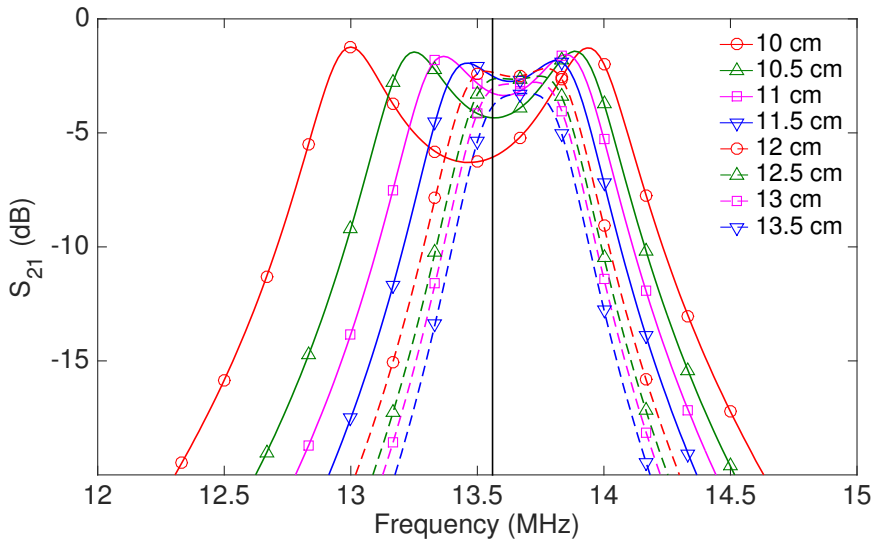

Figure 6.6. Measured S_{21} of the open-helical-coil wireless power transfer coil network at different separation distances.

TABLE 6.1
PARAMETERS OF THE OPTIMIZED OPEN HELICAL COIL FOR THE PROPOSED WPT SYSTEM

Parameters	**Values**
Radius of coil	50 mm
Diameter of wire	1 mm
Gap between loops	0.2 mm
Number of turns	26
Height of coil	60 mm
Self-resonance frequency	13.56 MHz

the coil. Since Eq. (6.1) is equivalent to Eq. (6.9), the imaginary part of input impedance is written as Eq. (6.10). Therefore, from measured S_{11} values at resonance frequency f_0 and slightly higher frequency $f_0 + \delta$, C and L can be calculated by solving simultaneous equations. If the mutual inductance between the two coupled coils is L_m, its value can be derived from the self-resonance frequency of the single coil, f_0, and the upper and lower resonance frequency of two coupled (Tx and Rx) coils, f_u, f_l, using Eq. (6.11)[110], [111]. From the measurement data, the inductance and the capacitance of the open helical coil prototype have been derived to be equal to 21.8 µH and 6.34 pF, respectively. Also, the

mutual inductance at $10\,\mathrm{cm}$ coil distance, for example, is $1.51\,\mu\mathrm{H}$.

$$Z_{in} = \frac{1 + S_{11}}{1 - S_{11}} Z_0 \tag{6.9}$$

$$Im[Z_{in}] = Im\left[\frac{1 + S_{11}}{1 - S_{11}} Z_0\right] = \omega L - \frac{1}{\omega C} \tag{6.10}$$

$$L_m = \left(\frac{f_u^2 - f_l^2}{f_u^2 + f_l^2}\right) L \tag{6.11}$$

6.2 Active Matching Circuit Design utilizing a Genetic Algorithm

6.2.1 Fundamentals of an Active Matching Circuit and a Genetic Algorithm

In order to overcome the "horn-effect", an active matching circuit can be utilized to improve the WPT efficiency at the designed self-resonance frequency while Tx-Rx coils are at the proximity. In ideal cases, a dynamically changing matching circuit can be easily implemented as a π network which has variable component values. However, in reality, it is quite challenging to change the impedance values arbitrarily within a wide dynamic range using off-the-shelf components. There are various different ways to realize arbitrary different impedance values by utilizing electrically controlled variable circuit components, for example by using relays [112] or varactor diodes [113]. However, in this research, a discrete value impedance matching circuit with p-i-n diode switches is adopted because of its fast switching speed, small feature size and relatively high power handling capability [114]. The matching circuit topology is based on the on the cascading of a unit cell consisting of a series inductor and a shunt capacitor in L-shape. The L-type topology was chosen to make the unit cell configuration as simple as possible to minimize the simulation and the optimization time for matching circuit design. Ideally, the range of impedance values created by the variable matching circuit unit increases as the number of stages increases. However,

in reality, this value range saturates at some point because of the discrete available circuit component values. At the same time, the loss associated with the lumped circuit components increases as the number of stage increases. Therefore, the number of stages (six in the prototype presented in this work) was eventually chosen to satisfy the practical matching circuit constraints described below with the minimum number of stages [86]. Each capacitor can be grounded through a p-i-n diode, which acts as the switching element. Since every switch provides 2 states, 6 switches can provide a total of 64 states. The p-i-n diodes are controlled by a microcontroller unit to choose the best configuration for the matching circuit by changing the combination of "on" and "off" states of the p-i-n diodes. In this work, the p-i-n diode SMP1340 from Skyworks is adopted in order to achieve a high-speed matching circuit operation. In this effort, GA were utilized in order to determine the optimal lumped component values for typical WPT matching applications out of the available standard "off-the-shelf" discrete component values aiming at achieving an effective matching over a large part of the Smith chart, virtually covering most impedance values to match in the practical WPT configurations.

A genetic algorithm (GA) is one of heuristic search methods, which have been widely used to solve electromagnetic optimization problems [115]. A GA is a method for solving both constrained and unconstrained optimization problems based on a natural selection process that mimics biological evolution. The algorithm repeatedly modifies a population of individual solutions. At each step, the genetic algorithm randomly selects individuals from the current population and uses them as parents to produce the children for the next generation. Over successive generations, the population "evolves" toward an optimal solution by minimizing the value of an arbitrary set evaluation function. Here, for the easy and quick implementation of GA into the matching circuit design, the Global Optimization Toolbox of MATLAB was utilized. The procedure to design and to evaluate the performance of the matching circuit is depicted in Fig. 6.7 [114]. In summary, the MATLAB code generates discrete load impedance values, which are evenly distributed around the

center of the Smith chart, and check how well the matching circuit at each on/off p-i-n diode combination can match these different impedance values to $50\,\Omega$ or not. The return loss (R_L) and the transducer gain (G_T), which are expressed in Eq. (6.12) and (6.13), are used as the criteria to assess the performance of matching circuit. These can be expressed as a function of the two-port S-parameters, and the load reflection coefficient (Γ_L) [116]. The return loss indicates the quality of matching to the load impedance. This is a necessary condition to check if port1 (signal generator: $50\,\Omega$), is actually matched to port2 (Tx coil), which has an arbitrary impedance, or not. However, this condition is not a sufficient condition to guarantee the improvement in power transfer from port1 to port2 because there is a dissipative loss associated with the insertion of the matching circuit and a load mismatch [117].

$$R_L = -20\ log(S_{11} + \frac{S_{12}S_{21}\Gamma_L}{1 - S_{22}\Gamma_L}) \quad (dB) \tag{6.12}$$

$$G_T = -10\ log(\frac{|S_{21}|^2(1 - |\Gamma_L|^2)}{|1 - S_{22}\Gamma_L|^2}) \quad (dB) \tag{6.13}$$

From the literature, it is possible to achieve the maximum Smith chart coverage (up to $70\,\%$) under the conditions, $R_L < -10\,\mathrm{dB}$ and $G_T > -2\,\mathrm{dB}$, which guarantees the sufficient improvement of matching by utilizing arbitrary circuit component values [114]. The proposed method can effectively realize a Smith chart coverage of 50 to $60\,\%$ satisfying the same criteria by modifying the combination of a discrete set of circuit components. Each component value in these sets is chosen from commercially available lumped component values. For both inductors and capacitors, 28 consecutive commonly used circuit values, which cover a lumped element value range of 1000:1 for the operation frequency of $13.56\,\mathrm{MHz}$ were considered. By limiting the number of components in the matching circuit in such a way, the simulation time was significantly reduced.

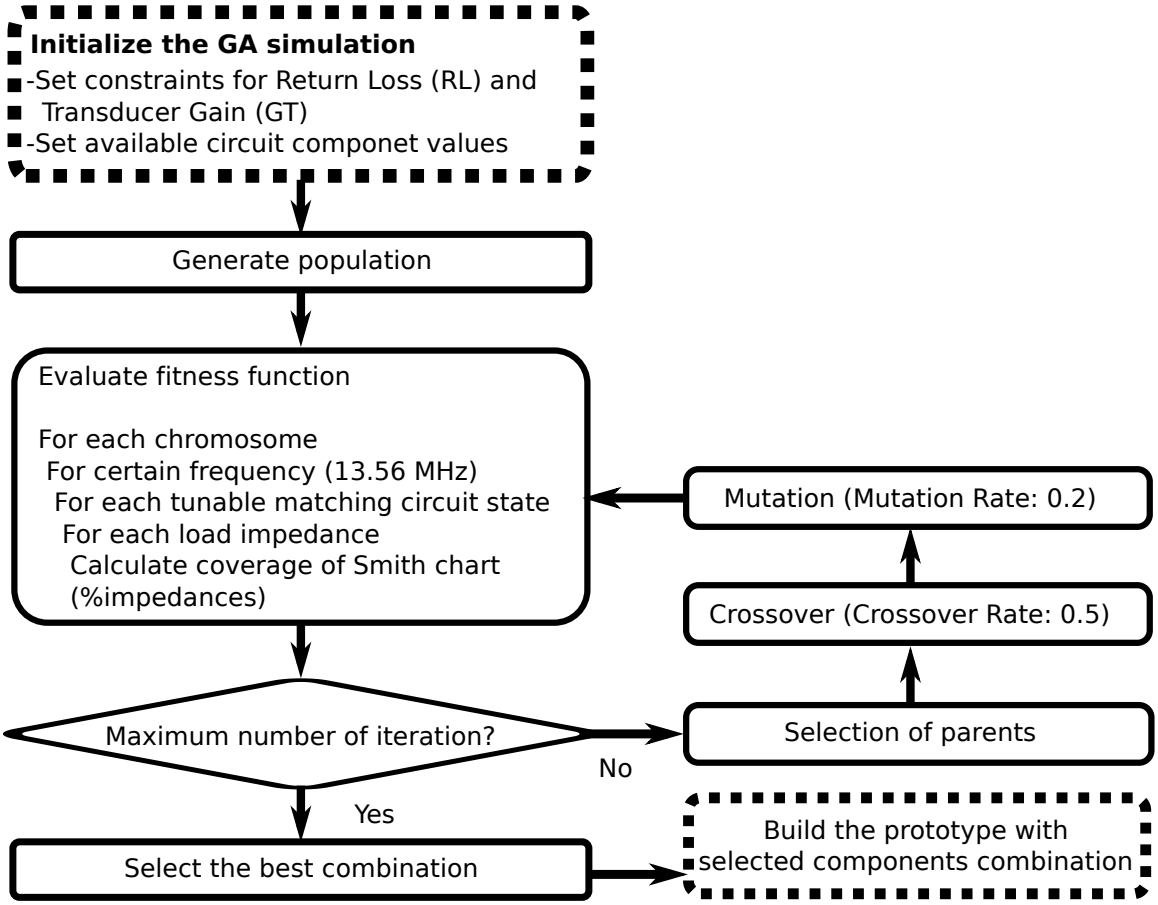

Figure 6.7. Flow chart of the GA optimization for the matching circuit design.

Characterization of Matching Circuit

During the GA simulations, based on the available lumped component values, the center of the Smith chart was targeted, offering a 50 to $60\,\%$ Smith chart coverage at $13.56\,\mathrm{MHz}$. The input impedance values of the matching circuit at each on/off state generated by MATLAB are shown in Fig. 6.8. However, the inductive component value of the fifth cell was changed from $27\,\mathrm{nH}$ to $560\,\mathrm{nH}$ through the simulations utilizing Advanced Design System (ADS) 2013 in order to fine tune the optimization process for the measured coil S-parameters.This improved the matching circuit performance at the short coil separation distances, and eventually increased the range of coil separation distance that can be matched. In Fig. 6.9, the schematic of the GA-designed matching circuit after the fine tuning and the picture of the matching circuit prototype are depicted. The circuit prototype was fabricated

on a $1.5\,\mathrm{mm}$ thick substrate, RO4003C, which features a dielectric constant of 3.38, provided by Rogers Cooperation. The measured and simulated reflection coefficient values for the designed matching circuit after the fine tuning are shown in Fig. 6.10. During the measurements, bias circuits, each composed of a series inductor and a parallel capacitor, were connected to each pin of the matching circuit prototype to isolate Arduino Uno microcontroller board's General Input Output Pins (GIOP), which provide the DC voltage for each p-i-n diode, from the rest of the matching network. As can be easily observed in Fig. 6.10, the simulation and the measurement results agree quite well.

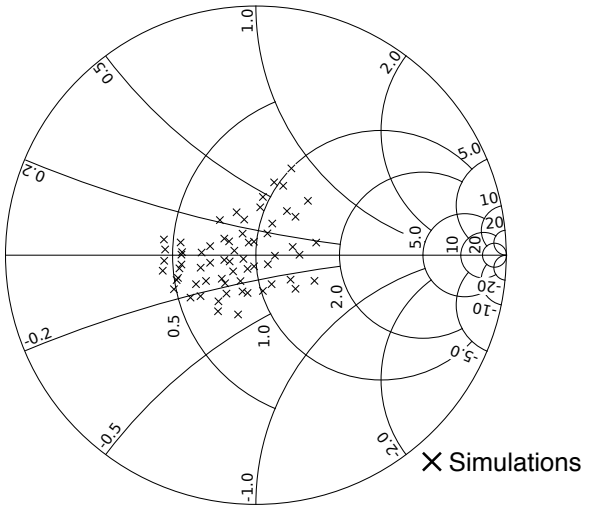

Figure 6.8. Simulated input impedance values on a Smith chart generated by MATLAB's GA algorithm.

6.2.2 Real-time Matching Circuit System

One of the easiest and most accurate ways to assess the quality of the matching and operate the system at the maximum power transfer point is to monitor the S-parameters values and modify the configuration of the active matching circuit in real time to achieve the highest value of the transmission coefficient (minimum reflection coefficient) for time-changing topologies. However, in reality, introducing a network analyzer into the system is not a practical choice in terms of cost and flexibility. Also, in practical implantable systems, it is virtually impossible to have a physical connection between the receiver device

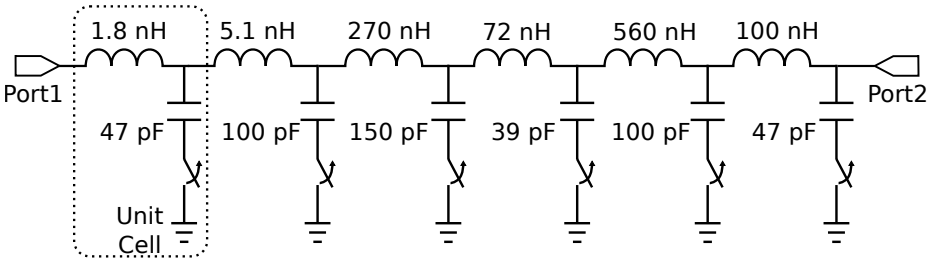

(a)

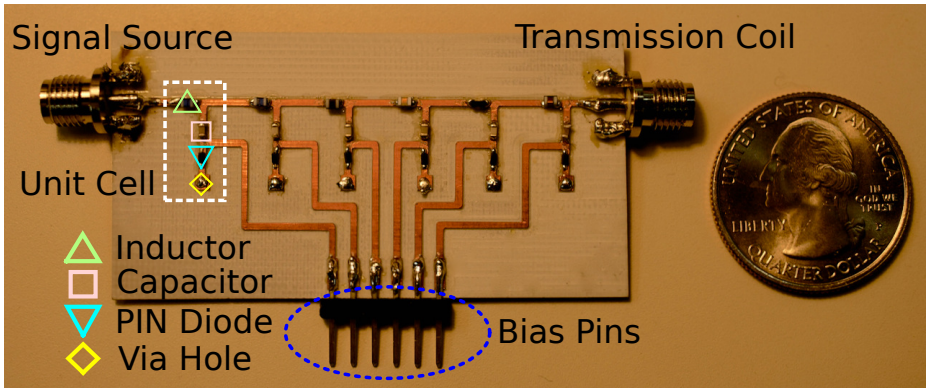

(b)

Figure 6.9. (a) Tunable 6-stage matching circuit schematic derived using the GA and ADS. (b) Prototype of the tunable matching circuit with modified components value.

and the matching quality control unit, thus making it difficult to directly measure the received power. In order to overcome this problem, a maximum power to the transmitter, that is measured by utilizing a directional coupler and an RF detector IC, which is mainly composed of a detector diode, was designed as shown in Fig. 6.11. In this system, a fraction of the reflected signal from the Rx coil is fed through the coupled port of a directional coupler to a detector diode, and the output DC voltage from the diode is measured by utilizing an analog to digital converter (ADC) in the microcontroller module. With this method, the system does not require any RF measurement equipment, which usually increases the system cost and complexity while limiting its applicability. If the output voltage of the detector diode is at the minimum value, it can be assumed that the reflection from the Tx coil is minimized, which equivalently means the highest power transmission in the ideal magnetic resonant Tx-Rx coil network.

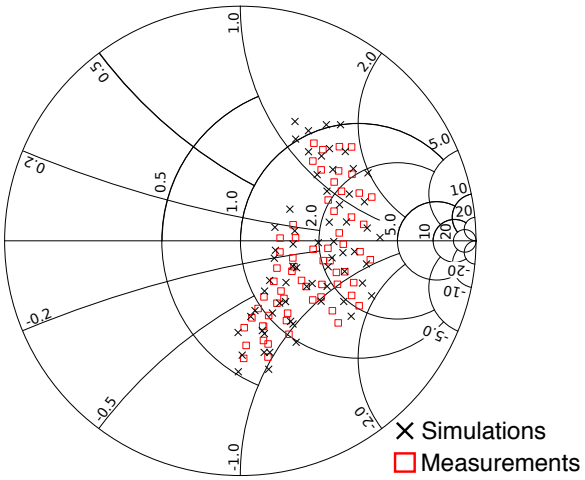

Figure 6.10. Measured and simulated input impedance values of tunable matching circuit prototype on a Smith chart.

Practical Limitations of Real-time Matching Circuit System

In practical implementations, due to the requirements for the optimal operation of the directional coupler as well as due to the performance characteristics of the detector diodes, there exist numerous fundamental system limitations. The efficient operation of the directional couplers is guaranteed only when all their ports are matched [66]. Therefore, if the active matching circuit cannot sufficiently match the Tx coil to the directional coupler, the reflected power estimation is no longer accurate, while the insertion loss of the directional coupler increases. In addition, the impedance of commercial detection diodes strongly depends on the input power level, thus drastically affecting the system performance. In the proof-of-concept prototype presented in this research the $-15\,\mathrm{dB}$ directional coupler, ZEDC-15-2B from Mini-Circuits, and the RF detector IC, LTC5507 from Linear Technology Cooperation, were used. In order to identify the practical system limitations, the output voltage and the impedance of the RF detector IC were measured for different input power levels within the range of -34 to $14\,\mathrm{dBm}$ with values plotted in Fig. 6.12. As a result, it can be said that the RF detector IC covers a quite wide dynamic range of input power levels providing an easily detectable output voltage change. The real part of input impedance varies from about 160 to $230\,\Omega$ depending on the input power level, and the imaginary part

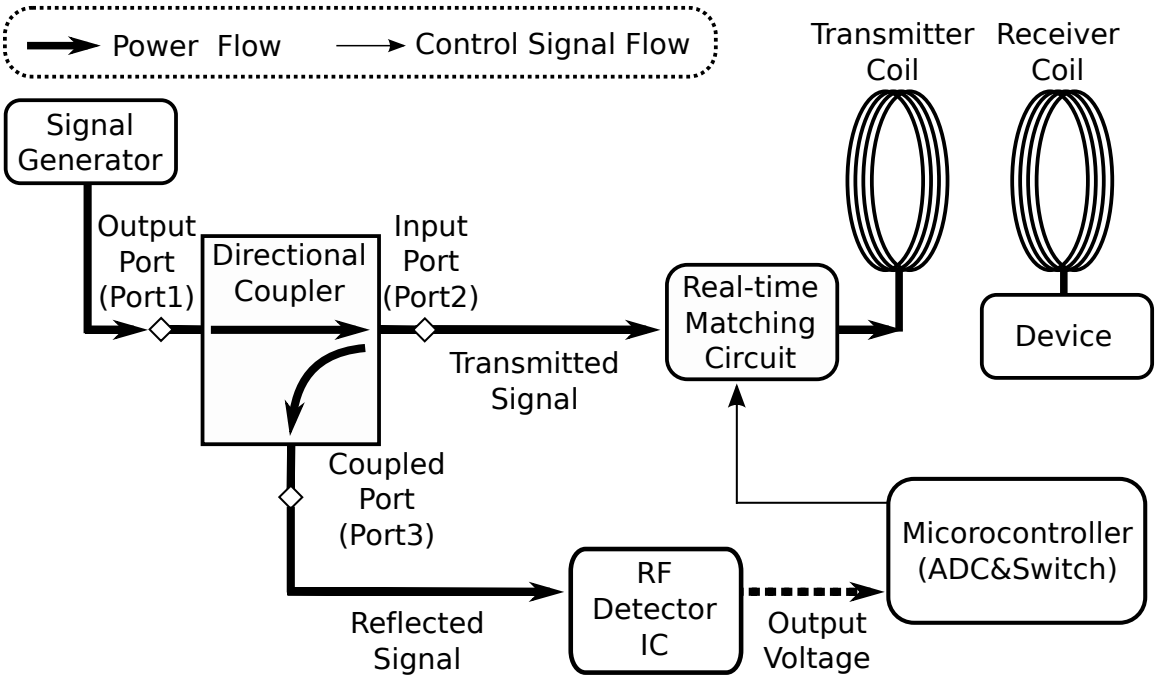

Figure 6.11. Block diagram of a matching circuit quality assessment system utilizing a directional coupler and an RF detector IC.

of the impedance is almost constant around $-10\,\Omega$. Next, based on these measured values, the effect of the directional coupler on the system performance was investigated through simulations on ADS by using the measured S-parameters of the coupler. For convenience, the output port, the input port and the coupled port of the directional coupler are named as port1, port2 and port3, respectively. In the actual real-time matching system, port1, which is connected to the signal generator, is assumed to be always matched. Therefore, the S-parameters of the coupler were simulated by changing the impedance of port2 and port3. After performing numerous simulations, it was observed that the impedance change at port3 over the above measured range of the impedance variation of the detector IC does not significantly affect the S-parameters of the coupler. However, the impedance mismatch at port2 drastically changes the S-parameters. The Fig. 6.13 (a) and (b) show the values of S_{21} and S_{32} of the coupler when the real and the imaginary part of the terminal impedance at port2 were varied from 20 to $130\,\Omega$ and 0 to $200\,\Omega$, respectively, by assuming that this is the change of input impedance of the Tx coil caused by the coil separation distance change. As it can be easily concluded from the numerical simulations shown in Fig. 6.13 (a), the

insertion loss increases as the mismatch at port2 increases. For a practical system implementation, up to $1\,\mathrm{dBm}$ worsening of the matching performance, which is equivalently 20 to $130\,\Omega$, must be satisfied to guarantee the effective system performance. At the same time, Fig. 6.13 (b) implies that there is an undetectable region near the perfectly matched condition because of too low reflected power below $-34\,\mathrm{dBm}$, which is the lower boundary of the detectable RF signal utilizing the RF detector IC. Whether, if this happens or not depends on the level of input power to the system, in general.

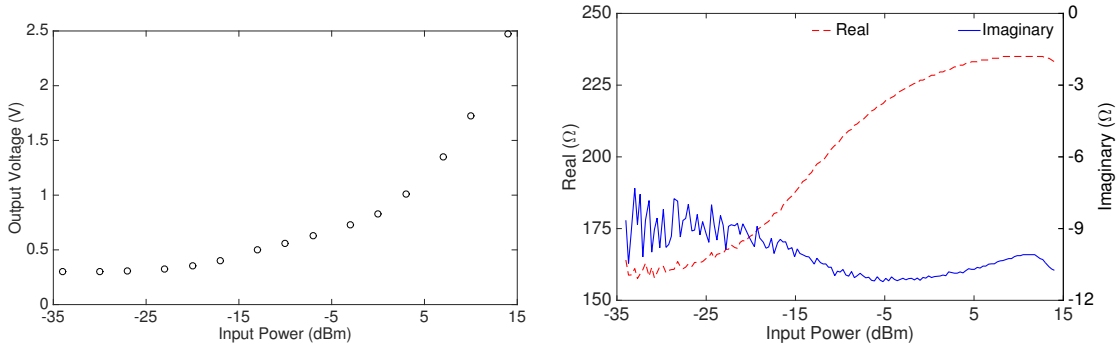

(a) (b)

Figure 6.12. (a) Measured output voltage from the RF detector IC with respect to the input power. (b) Measured impedance of the RF detector with respect to the input power .

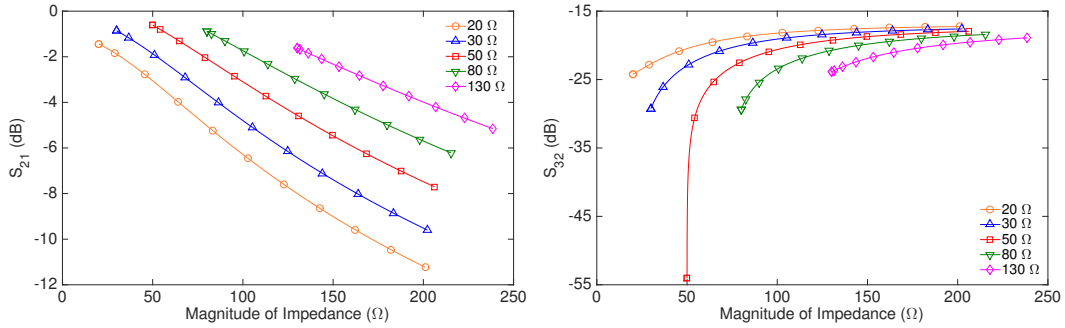

(a) (b)

Figure 6.13. (a) S_{21} of the directional coupler for different terminal impedance values of port2. (b) S_{32} of the directional coupler for different terminal impedance values of port2.

Automated Real-time Maximum Power Transfer Point Search

Based on the assumption that the lowest output voltage from the RF detector IC is correlated with the highest transferred power, the brute force real-time matching algorithm as shown in Fig. 6.14 was implemented by utilizing a microcontoller module, Arduino Uno. The major limitations for a fast real-time matching circuit operation are the switching speed of the p-i-n diode and the reading rate of the ADC in the microcontroller. From the datasheet, the switching time of the p-i-n diode in our system prototype, SMP1340, is in the range of hundreds of nano seconds [118], [119]. However, the maximum reading rate of ADC in Arduino is about $10\,\mathrm{kHz}$. In our matching circuit prototype, there are 64 states by using six p-i-n diodes. Therefore, the minimum required time for the matching is about $6.4\,\mathrm{ms}$ by taking only one ADC measurement for each state. In actual operation tests, ten measurements are conducted for each state for enhanced smoothing in order to increase the measurement accuracy. Therefore, the expected required time for the optimum operation point search is about $64\,\mathrm{ms}$. Ideally, the required time can be reduced by introducing fast ADC's potentially reducing the time to less than $1\,\mathrm{ms}$. By taking into account the fast switching time of the p-i-n diode, the time for matching can be less than $1\,\mathrm{ms}$.

6.2.3 Operation Test of the Automated Real-Time Matching System

Performance Characterization of Automated Real-Time Matching System

In order to test the performance of the developed automated real-time matching system, all the components are arranged as shown in Fig. 6.15, and the received power at different separation distances was measured by utilizing a real-time spectrum analyzer, RSA3408A from Tektronix, Inc., with and without a matching circuit. The input power to the matching circuit and the Tx coil is adjusted to be $0\,\mathrm{dBm}$ in both cases of with and without the matching circuit, respectively. The received power with respect to the coil center to center separation distance with and without an automated matching system is depicted in Fig. 6.16.

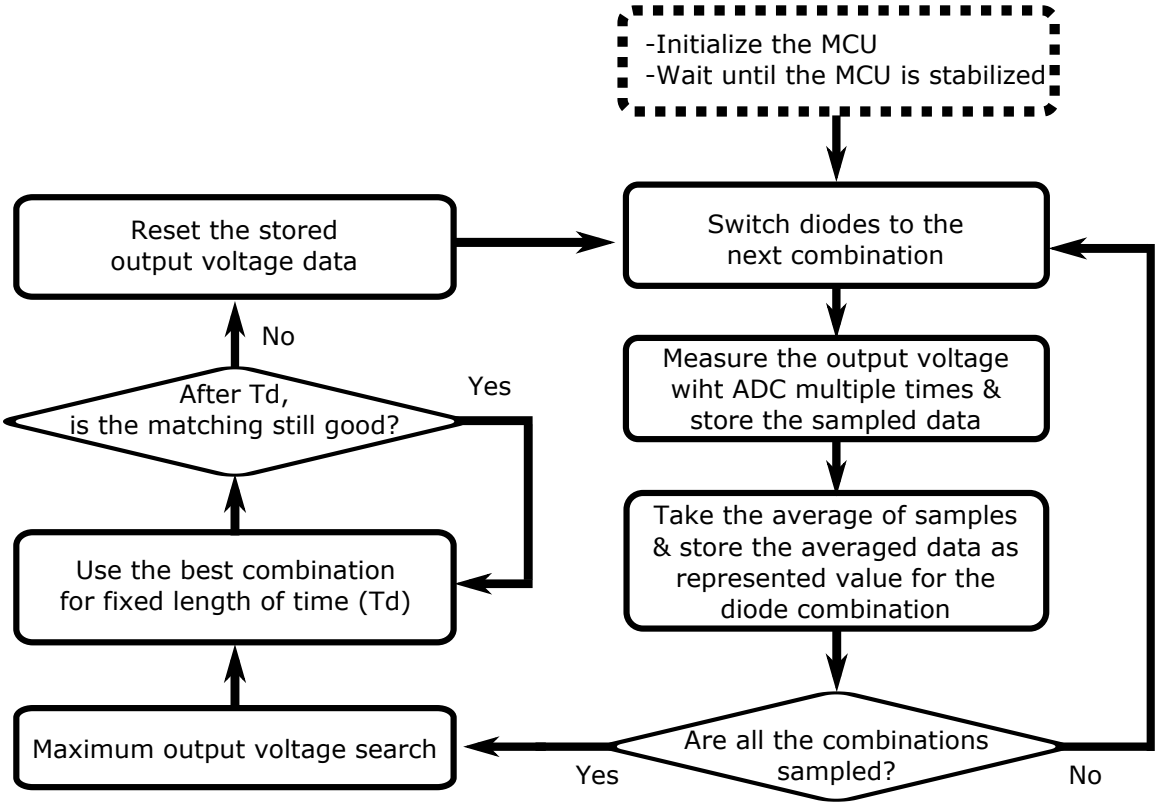

Figure 6.14. Flow chart of the automated real-time matching procedure utilizing a microcontroller.

It can be easily concluded that the received power increases by utilizing the matching circuit for separation distances in the range of 10 to $16\,\mathrm{cm}$ with a maximum received power improvement of $3.2\,\mathrm{dB}$. In order to specify the quality of the real-time matching circuit, the S_{11} of the Tx-Rx coil network with and without a matching circuit operating at the best/optimum performance state automatically chosen by the microcontroller at different coil separation distances are measured by using a vector network analyzer, ZVA8 from Rohde $\&$ Schwarz, and results are shown in Fig. 6.17. After $16\,\mathrm{cm}$, there is no significant change in S_{11} for both with and without matching circuits. Since the diameter of the coil is $10\,\mathrm{cm}$ and it is the minimum possible center to center separation distance between two coils, the coil's matching is improved over the entire separation distance range from 10 to $16\,\mathrm{cm}$ or more.

Finally, the output voltage from the detector IC and the received power are measured at different coil separation distances by changing the configuration of the matching circuit

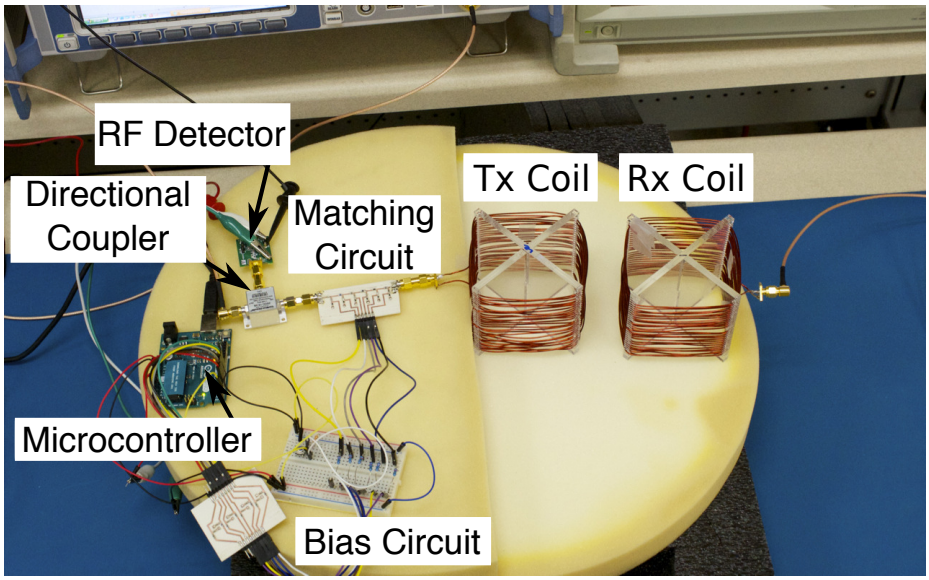

Figure 6.15. Complete setup of the automated real-time matching system for operation testing purposes.

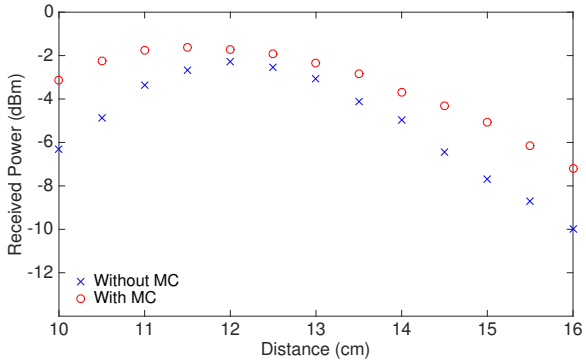

Figure 6.16. Measured received power with and without the automated matching circuit at different coil separation distances.

by manually turning on/off the switches to emulate all possible states in order to confirm whether the automated matching circuit is actually choosing the optimal combination of on/off states or not. The received power at 10, 12, 14.5 and $16\,\mathrm{cm}$ are shown in Fig. 6.18 (a) to (d), respectively. From the figures, it can be said that at $12\,\mathrm{cm}$, the voltage reading of microcontroller is not accurate because of the too low reflected power associated with the good matching, as previously explained in the section of the system limitation. This can be the reason why the S_{11} is high at $12\,\mathrm{cm}$ in Fig. 6.17. This can be prevented by using a coupler which has a high coupling coefficient or using high input power to the system. Similarly, at $16\,\mathrm{cm}$, the high mismatch at the input port of the coupler breaks the correlation

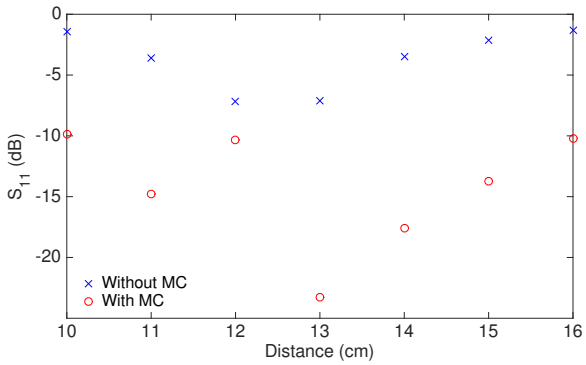

Figure 6.17. Measured S_{11} of coil with and without the matching circuit at the optimal power transfer state that is automatically chosen by the microcontroller at different coil separation distances.

of low reflected power and high transferred power, and the automated matching circuit cannot choose the best combination from the readout voltage data anymore. Therefore, technically 10 to $16\,\mathrm{cm}$ is the operation range of automated real-time matching system, although the variable matching circuit unit can cover the entire separation distance range.

6.2.4 Operation Tests under Rugged Conditions

Misalignment

One of the fundamental motivations for this research was to create a real-time matching circuit system which can compensate the effect of human movements for Tx-Rx coil networks in practical biomedical WPT systems. One of the potential causes for the change of the Tx input impedance is the resulting Tx-Rx misalignment. Because the geometrical symmetry of the designed coil, the effect of the misalignment in 2D radial direction can be assumed to be limited. Therefore, in order to examine the capability of our real-time matching system to handle the misalignment, the received power with and without the matching circuit was measured for misaligned positions caused by changing the elevation of the receiver coil. The Tx-Rx coil network setup testing the effect of the misalignment is shown in Fig. 6.19(a), and the received power with respect to the coil separation distance at different Rx coil elevations is depicted in Fig. 6.19(b). From these measurements, it appears that the automated real-time matching circuit system can improve the power transfer at all data

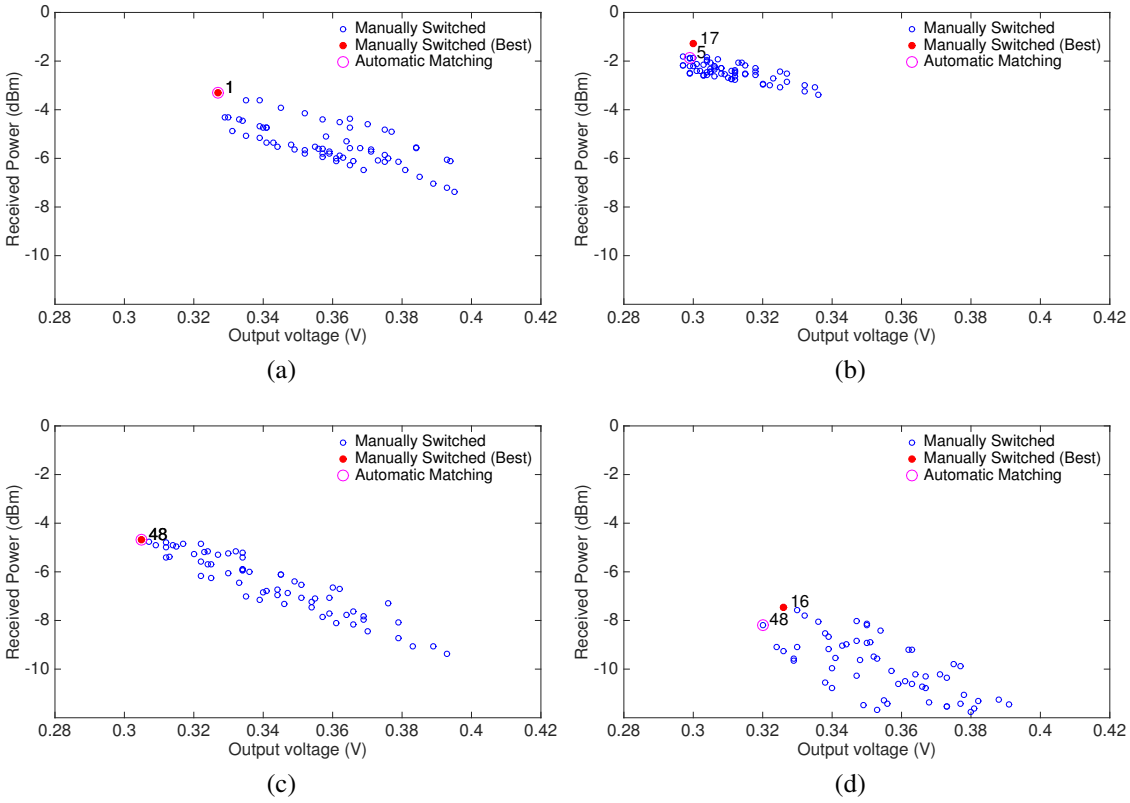

Figure 6.18. Measured received power from the receiver coil and the output voltage from the RF detector IC at each p-i-n diode on/off state with coil separation distance of (a)10 cm. (b) 12 cm. (c)14.5 cm. (d) 16 cm.

points implying the potential matching capability of our system in three dimensional coil movement.

Non-symmetrical Tx-Rx Coil Network

Most biomedical WPT systems are expected to feature non-symmetrical Tx-Rx coil topologies to increase the power transfer efficiency under the strict size constraints for the implantable receiver coils [120]. Therefore, in order to further investigate the potential of the automated real-time matching system for biomedical applications, additional operation tests using non-symmetrical Tx-Rx coil networks were conducted. For proof-of-concept purposes and without loss of generality, a larger planar loop open helical coil was utilized as the transmitter coil. The minimum and the maximum radii of the coil loop are 12 cm and 14 cm, respectively, the diameter of the copper wire is 1 mm, the gap between planer

loop is $4\,\mathrm{mm}$, and the number of turns is 5 for the Tx coil. A polystyrene foam was utilized as the supporting material for this coil, and the self-resonance frequency of the coil is $13.7\,\mathrm{MHz}$. The slight self-resonance frequency shift from the expected operation frequency of $13.56\,\mathrm{MHz}$ was caused by the fabrication errors. The non-symmetrical Tx-Rx coil testing setup is shown in Fig. 6.20(a), and the received power with respect to the coil separation distance is depicted in Fig. 6.20(b). As a result, the improvement in the received power was confirmed in the entire range from $20\,\mathrm{cm}$ or more. By introducing the larger Tx coil, the edge-to-edge coil separation distance range which achieves a certain received power level, for example above $-3\,\mathrm{dBm}$, increased compared to the symmetrical small Tx-Rx coil network. These preliminary promising results suggest the potential applicability of the proposed automated real-time matching system to non-symmetrical WPT systems in biomedical implants.

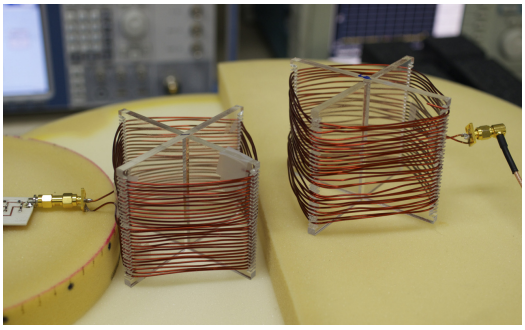

(a)

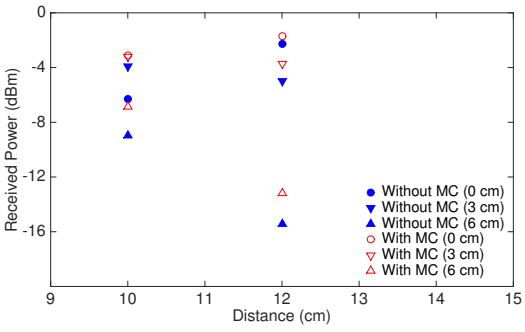

(b)

Figure 6.19. Tx-Rx coil network under misaligned conditions caused by relative elevation. (b)Measured received power as a function of the coil separation distance for different Rx coil elevation levels.

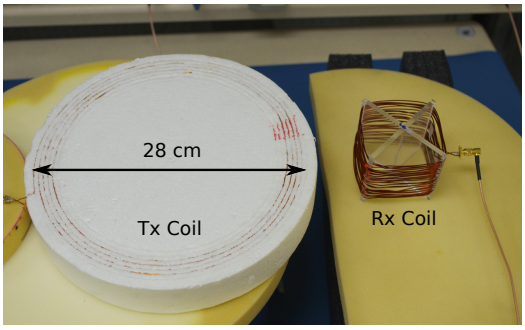

(a)

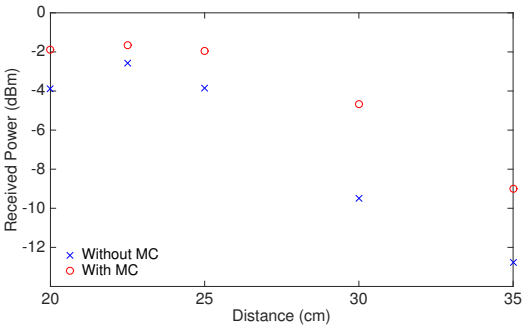

(b)

Figure 6.20. (a) Non-symmetrical WPT coil system with a large Tx coil and a small Rx coil. (b) Measured received power of the non-symmetrical Tx-Rx coil network with respect to the coil separation distance.

6.3 Active matching circuit for moving object

In the previous section, the main goal was to design an active matching circuit which can be used for different types of coils. To achieve this goal, a matching circuit which has an evenly distributing impedance when coil-coupling is high and therefore wireless power transfer efficiency is potentially high, was designed. However, with this design goal, the active matching circuit ended up using six cells whose non-ideal lumped components caused inevitable losses and discrepancies between modeled and effective impedance values. Also, the matching circuit combination selection time, while operating the active matching system utilizing brute force selecting, is relatively long. However, in more realistic situations, the impedance of the Tx-Rx coil network continuously changes because of the coils movements, and the reconfigurability speed of the utilized matching network needs to be drastically improved. Therefore, a novel matching circuit design method utilizing the combination of a genetic algorithm with clustering, which can maximize the performance of both fixed-value passive matching circuits or active matching circuits that are composed of a combination of inductors, capacitors and p-i-n diodes, is analytically discussed in this section. This method is based on the measured coil configuration S-parameters under real-time moving conditions, which displayed tendencies/unven space distribution in the coil impedance values. This is used to minimize the number of cells in the active matching circuit, which eventually reduced the brute force matching circuit selection process while the system is operating. As depicted in Fig. 6.21, the designed matching circuits are connected between the signal source and the Tx coil. In this work, the matching circuit design accuracy has been further enhanced by introducing the measured S-parameters of the utilized lumped components, and the performance of the designed matching circuit is validated through the comparison between the simulations and the experiments. Also, this study discusses the bias circuit design for the active matching circuit to minimize the discrepancy in impedance value while RF input power is high.

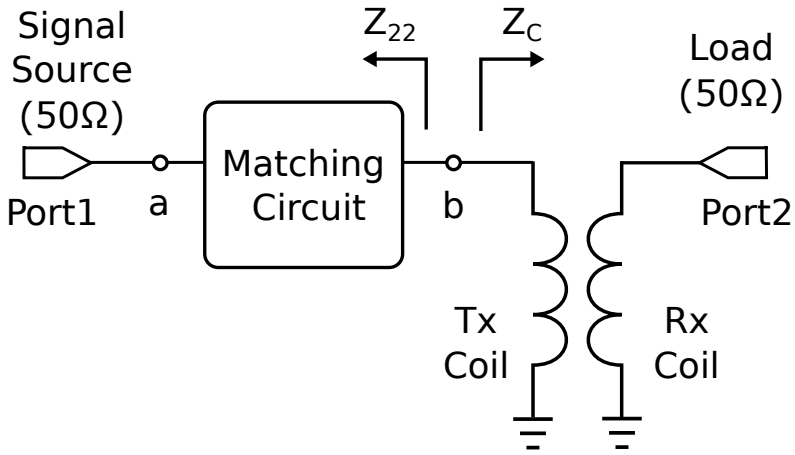

Figure 6.21. Block diagram of the wireless power transfer (WPT) system with the optimized matching circuit in the transmitter (Tx) side.

6.3.1 Characterization of Tx-Rx Coil Impedance under Moving Condition

In order to characterize the effect of the movements of the Tx-Rx coils on the coil input impedance for a proof-of-concept topology, the S-parameters of the Tx-Rx topology were periodically measured using a vector network analyzer (VNA), ZVA8 from Rohde & Schwarz, which was controlled by using LabVIEW. Without loss of generality, $10\,\mathrm{cm}$ diameter open helical coils with the resonance frequency of $13.6\,\mathrm{MHz}$ were used as both Tx and Rx coils. The S-parameters of the time-changing Tx-Rx topologies were measured 100 times with the time interval of $250\,\mathrm{ms}$ by randomly changing the distance and the elevation without rotating the coil within the coils for center-to-center coil distances in the range of about 10 to $20\,\mathrm{cm}$. The coil orientation change associated with the rotation of the coils typically changes the mutual inductance between two coils. Therefore, similar change in impedance value while changing the separation distance may happen because of the coil rotation. However, rotating the coil adds more complexity in measurement and it was difficult to rotate the coil without adding the effects of a mechanical coil holder to the electrical property of the coils. Thus, this research did not consider the rotation of the coil. During the measurements, the coils were placed on sponges, avoiding their interaction with hands, and manually moved. The same experiment was repeated four times, and the

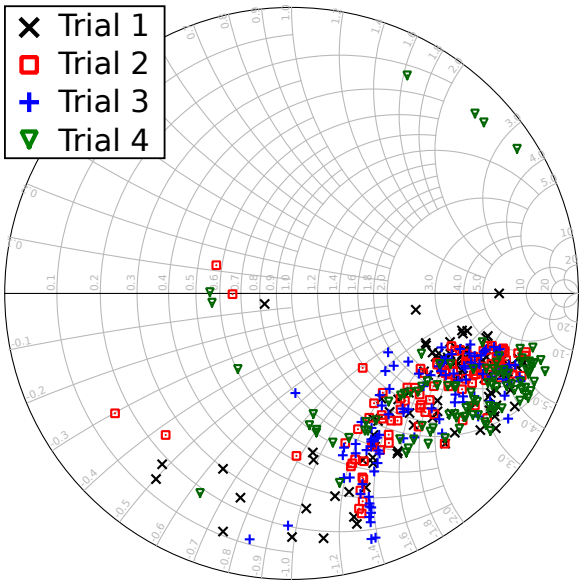

Figure 6.22. Measured input impedances of Tx-Rx coil topology under random coil movements in 4 trials of 100 measurements each.

measured Tx-Rx coil topology input impedance (Z_c) values for all trial measurements are shown in Fig. 6.22. As it can be easily observed, Z_c varies in a quite wide range, but there is a clear tendency/space concentration in the distribution of the coil impedance values. In Fig. 6.23, the distribution of power transfer efficiency, $|S_{21}| \times 100$ $(\%)$, of the above described 400 (4×100) measurements along with their arithmetic mean are depicted. The average power transfer efficiency without any matching circuit is about $60.8\,\%$.

6.3.2 Matching Circuit Design using Genetic Algorithm

For this research, first, the fixed-value passive matching circuit topology is discussed and evaluated in terms of the optimization of the power transfer efficiency to moving coils. Next, the GA-based matching circuit design process is extended to active matching circuit designs. In general, a cascaded two-port network/topology can be modeled through the multiplication of the respective stage transmission (ABCD) matrices. The ABCD matrix of each trial measurement (sample) can be obtained from the measured S-parameters of the corresponding Tx-Rx coil network by converting the S matrix to the ABCD matrix. Once the ABCD matrix of the matching circuit is determined by choosing the values of its

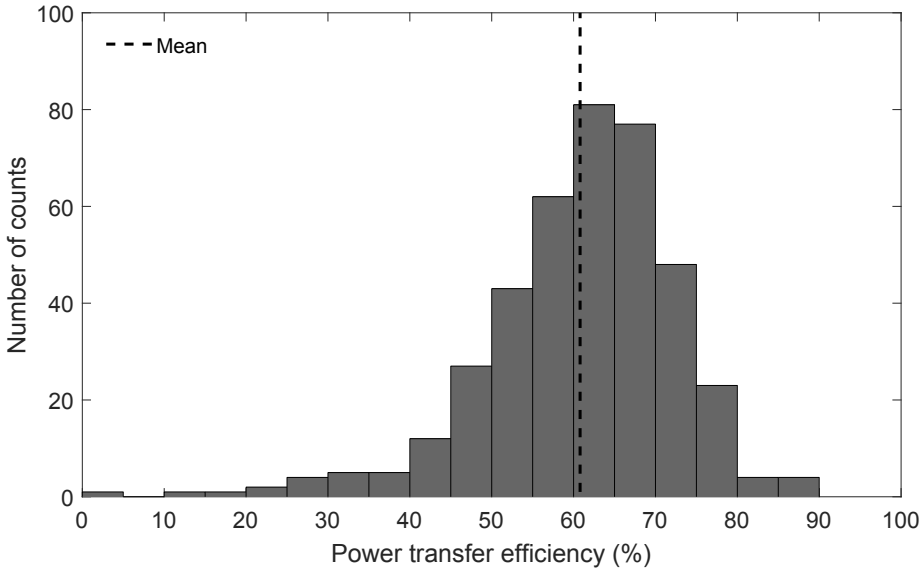

Figure 6.23. Distribution and arithmetic mean of the measured power transfer efficiency values for 4 trials with 100 measurements each (total of 400 counts).

lumped components, the S-matrix of the cascade of the matching circuit and the Tx-Rx coil topologies can be computed from the total transmission matrix [114]. Assuming that there are M samples of S-parameters for the time-changing coil configurations, the probability of choosing the i-th sample (P_i) is $\frac{1}{M}$. In the presented approach, the power transfer efficiency (η) is defined as the expected value of $|S_{21}|$ for the composite matching+coil configuration, as described in Eq. (6.14). For active matching circuits that feature more than two potential matching circuit configurations, the maximum $|S_{21}|$ value among all possible $|S_{21}|$ values for the i-th sample topology is chosen. The fitting function for the GA simulation is defined as F in Eq. (6.14), and the matching circuit component values which can minimize the value of F have to be identified and selected.

$$F = 100 - \eta \;\; where \;\; \eta = \sum_{i=1}^{M} |S_{21}|^{i}_{Max} \, P_i \times 100 \; (\%) \tag{6.14}$$

Fixed-Value Passive Matching Circuit

In order to determine the optimal fixed-value passive matching circuit topology, two π matching circuits, one featuring a series inductor with two parallel capacitors (Ser L),

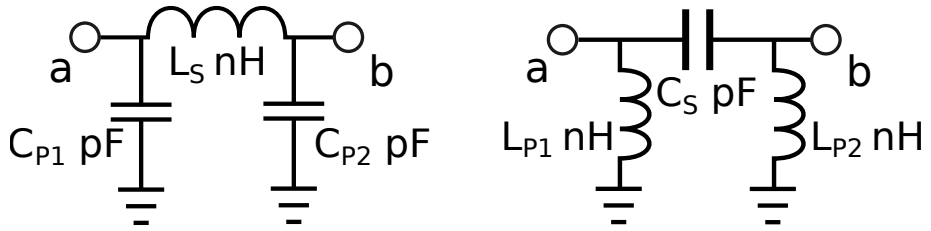

Figure 6.24. π matching circuit topologies with a series inductor (left) and a series capacitor (right).

TABLE 6.2
CIRCUIT COMPONENT VALUES FOR OPTIMIZED FIXED π MATCHING CIRCUIT TOPOLOGIES USING IDEAL LUMPED COMPONENT MODELS

Ser L		Ser C	
L_S	$1000\,\mathrm{nH}$	C_S	$10.0\,\mathrm{pF}$
C_{P1}	$0\,\mathrm{pF}$	L_{P1}	$1000\,\mathrm{nH}$
C_{P2}	$39\,\mathrm{pF}$	L_{P2}	$720\,\mathrm{nH}$

and another one featuring a series capacitor with two parallel inductors (Ser C) are defined. The two π matching circuits are depicted in Fig. 6.24. For the sake of practicality, for both inductors and capacitors, 29 consecutive commonly used circuit values (10 to $2000\,\mathrm{nH}$ for inductor and 10 to $2000\,\mathrm{pF}$ for capacitor), which cover a lumped element value range of more than 100:1 for the operation frequency of $13.6\,\mathrm{MHz}$ were considered. The range of lumped component values were chosen after less than ten iterations of GA simulations, confirming the values out of this range have never been used. Lumped component values below this range do not make sufficient change in impedance value, and the values above potentially cause too much change in impedance value as a single step. Also, the parallel components are allowed to be placed in an "open circuit" position, which can virtually lead to L-type matching circuits. The "ideal" circuit component values that minimize the fitness function for each fixed-value π matching circuit topology are shown in Table 6.2.

Active Matching Circuit

For proof-of-concept demonstration purposes, in this work, a discrete value impedance matching circuit including p-i-n diode switches is adopted because of its fast switching speed, miniaturized size, and robustness [114]. The matching circuit topology is based

on the N-stage cascading of a unit cell consisting of an L-type unit cell comprising of a series inductor, a shunt capacitor, and a switch as shown in Fig. 6.25. Without loss of generality and to facilitate the fabrication, the additional DC blocking capacitors have not been included in the preliminary design process discussed in this section. Their concurrent optimization will be described in Section 6.3.5. The utilized N stages can create 2^N different impedance values. For both inductors and capacitors, 29 consecutive component values were used, which are the same as those in the case of the fixed-value passive matching circuits. In this case, the inductance values are allowed to be 0 ("short circuit"). The circuit component values which minimize the fitness function for 1 (1C) - 4 (4C) utilized stages/cells are shown in Table 6.3.

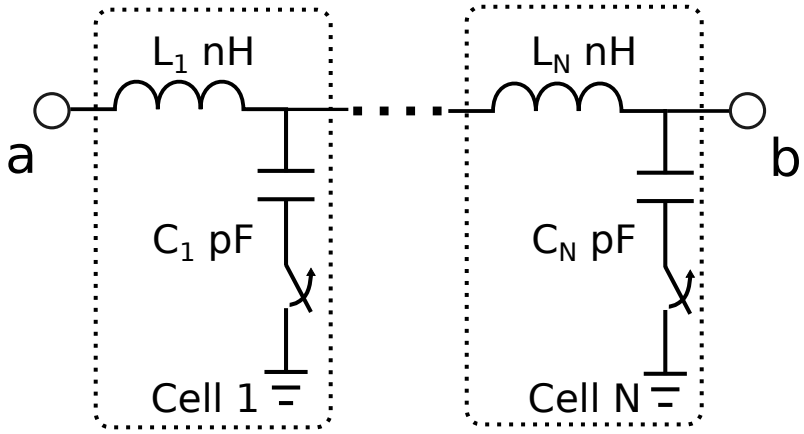

Figure 6.25. N-stage active matching circuit schematic.

In Table 6.4, the figure of merit (power transfer efficiency) for each optimized matching circuit topology is summarized. The improvement is obvious in the significant difference of the power transfer efficiency value compared to the case of no matching circuit (No MC). The "error" represents the number of data points where the power efficiency is lower than that for the case of no matching circuit within the 100 samples in Trial1. As the table clearly displays, the active matching circuit is much more efficient in improving the power transfer efficiency compared to the passive fixed-value matching circuit. As the number of the stages/cells increases, the efficiency increases while simultaneously reducing the "error" rate. From this simulation, it can be deduced that 3 cells or 4 cells are sufficient

TABLE 6.3
CIRCUIT COMPONENT VALUES FOR OPTIMIZED ACTIVE MATCHING CIRCUITS WITH DIFFERENT NUMBER OF CELLS USING IDEAL LUMPED COMPONENT MODELS

	Inductors (nH)				Capacitors (pF)			
	L_1	L_2	L_3	L_4	C_1	C_2	C_3	C_4
cell (1C)	1000	-	-	-	47	-	-	-
cell (2C)	330	820	-	-	390	47	-	-
cell (3C)	330	330	820	-	150	330	39	-
cell (4C)	330	470	0	820	180	330	82	33

TABLE 6.4
FIGURE OF MERIT OF EACH MATCHING CIRCUIT TOPOLOGY

	No MC	Ser L	Ser C	1 C	2 C	3 C	4 C
Efficiency (%)	61.5	76.4	76.4	78.3	80.8	82.2	82.9
Improvement (%)	-	14.9	14.9	16.8	19.3	20.7	21.4
Error (%)	-	15	13	10	4	1	1

to optimally improve the power transfer efficiency as the improvement saturates for larger number of stages, where an efficiency of 78.3 to $82.9\,\%$ is achieved. As a comparison, the power transfer efficiency using the previously designed 6 cell active matching circuit is $72.2\,\%$ [121]. This implies that a higher power transfer efficiency can be achieved even with a significantly smaller number of cells compared to previously reported matching circuits. Although, the matching circuits in the previous section were designed to improve the power transfer efficiency of different generic types of coils, the matching circuits introduced in this research can be easily customized and optimized for specific coil configurations. This design approach difference is one of the main causes for enhanced power transfer efficiency.

In order to confirm whether the designed matching circuits that are based on the measured data (100 measurements) of Trial1 can also work for other sets of sampled data, the power transfer efficiencies for each trial is computed and summarized in Table 6.5. It can be easily observed that there is no significant performance degradation of the data for different trials.

TABLE 6.5
POWER TRANSFER EFFICIENCY COMPARISON USING MEASURED S-PARAMETERS FOR TRIALS 1-4

	No MC	Ser L	Ser C	1 C	2 C	3 C	4 C
Efficiency (Trial1) (%)	61.5	76.4	76.4	78.2	80.8	82.2	82.9
Efficiency (Trial2) (%)	60.1	73.6	73.6	75.4	76.8	78.1	78.5
Efficiency (Trial3) (%)	59.9	72.8	72.9	75.4	77.4	78.3	79.2
Efficiency (Trial4) (%)	61.6	79.2	79.1	80.6	82.9	85.6	86.2
Degradation (%)	-	2.0	1.9	1.4	2.6	2.7	2.9

6.3.3 K-means Clustering

Since there is a clear trend in the distribution of coil impedance values over the Smith chart, it is possible to drastically reduce the time for GA simulation by selecting only representative impedance values as targets instead of using all sampled/measured data. Also, the fitness function calculation, which includes numerous S-to-ABCD matrix conversions, is not very computationally efficient. In order to choose a much smaller but almost equally efficient subset of coil configuration impedance values, we employed the k-means clustering method, which is commonly used for the data mining from big data, utilizing MATLAB. K-means clustering is an iterative, data-partitioning algorithm that assigns n observation points to exactly one of k clusters defined by centroids. The algorithm works with following three steps as summarized in Fig. 6.26.

1. Set clusters (G_i).

2. Calculate the coordinate of the centroid of each cluster.

3. Repeat step 1 and 2 to minimize the evaluation function C described in Eq. (6.15).

In the k-means clustering method, the program selects an arbitrary positive integer (K) of clusters which are the subsets of data points by minimizing the function C expressed in Eq. (6.15). In Eq. (6.15), $d(x, g_i)$ is the distance between each data point (x) in i-th cluster (S_i), and the centroid of i-th cluster (g_i). At the beginning of the data mining, we

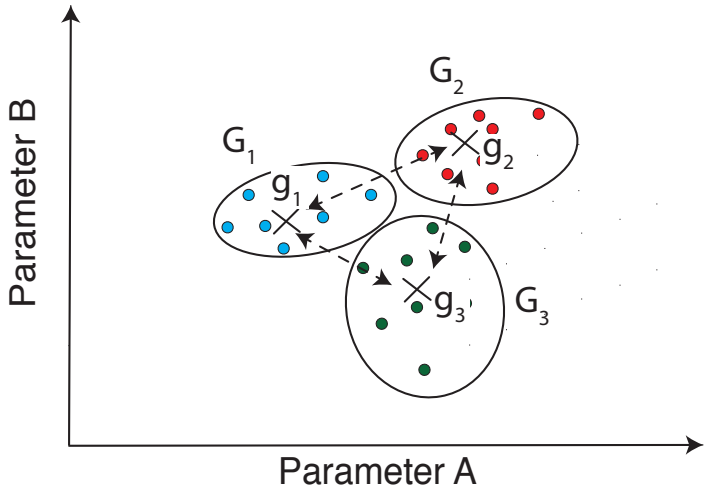

Figure 6.26. N-stage active matching circuit schematic.

have automatically generated 100 replicates as starting points of the clustering in order to increase the accuracy of the clustering [87], [122]. In this case, replicates are 100 complex numbers whose upper and lower boundary values are determined from the measured coil configuration impedance values (Z_c) in Trial1. The values of replicates are automatically selected minimizing the sum of distances between each replicate in the complex plane. For the proof-of-concept demonstration of the implementation of the clustering data mining method, 4, 8 and 16 representative coil topology input impedance values are chosen by using the 100 measured S_{11} values in Trial1. In Fig. 6.27, the Trial1's 100 sampled impedance values are plotted along with 4 (K-4), 8 (K-8) and 16 (K-16) clustered impedance values.

$$C = \sum_{i=1}^{K} \sum_{x \in S_i} (d(x, g_i))^2 \tag{6.15}$$

Since the power transfer to the load can be maximized when the input impedance of the matching circuit looking from port 2 (Z_{22}) in Fig. 6.21 is the complex conjugate of the Tx-Rx coil topology impedance input (Z_C), the sum of the reflection coefficient between the i-th clustered (coil topology) impedance value and Z_{22} is introduced as a new fitness function (G) as described in Eq. (6.16). In the equation, Z^*_{Ci} is the complex conjugate of the imaginary part of Z_C, and $|\Gamma|^i$ is the reflection coefficient for the i-th sample. Since

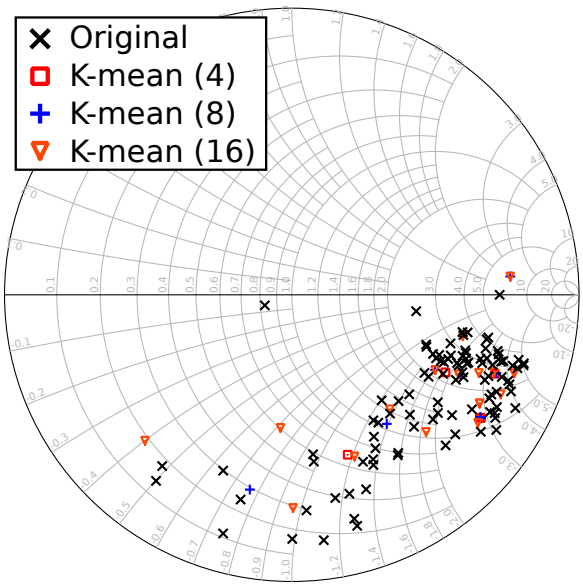

Figure 6.27. Measured 100 input impedance values of Tx-Rx coils configurations under random movements in Trial1 and representative impedance values selected by using K-means clustering.

active matching circuits have more than two potential matching circuit configurations, the minimum reflection coefficient among all potential matching circuit states ($|\Gamma|^i$) was chosen.

$$G = \sum_{i=1}^{L} |\Gamma|^i_{Min} \quad where\ \Gamma = \frac{Z^*_{Ci} - Z_{22}}{Z^*_{Ci} + Z_{22}} \tag{6.16}$$

In Table 6.6, the power transfer efficiency values for the matching circuit topologies optimized using only the clustered data (4, 8 and 16 points) as the target impedances in the GA simulation is summarized. From the table, it can be easily concluded that there are some cases that the clustered data do not work as proper targets, especially for the series inductor π matching circuit case, and degrade the performance of matching as the cluster size decreases. However, in most cases (series C passive and 1- to 4- stage active matching circuits) the clustering of impedance values does not have a significant effect on the matching circuit design performance.

TABLE 6.6
POWER TRANSFER EFFICIENCY COMPARISON BETWEEN ALL 100 MEASURED DATA VS 4, 8 AND 16 CLUSTER REPRESENTATIVE IMPEDANCE VALUES

	No MC	Ser L	Ser C	1 C	2 C	3 C	4 C
Efficiency (100) (%)	61.5	76.4	76.4	78.3	80.8	82.2	82.9
Efficiency (K-4) (%)	-	35.5	75.2	78.3	79.6	81.6	82.0
Efficiency (K-8) (%)	-	62.6	76.0	78.0	79.5	81.7	82.5
Efficiency (K-16) (%)	-	62.6	75.8	77.6	79.5	81.6	82.3

6.3.4 Matching Circuit Design using Non-ideal Lumped Component Models

In order to further increase the accuracy of the matching circuit design using genetic optimization algorithms, the measured S-parameter data for each non-ideal utilized lumped element provided by the vendors are introduced in MATLAB simulations. Each matching circuit component was replaced by its 2-port S-parameter model, and the impedance of the entire matching circuit network was represented as a cascade of ABCD matrices derived from the S-parameters. For a proof-of-concept simulation, the utilized series inductor and parallel capacitor in the L-shape matching unit cells of Fig. 6.25 are Coilcraft 0603CS and 0603HL, and Taiyo Yuden UMK105CG series, respectively. For this simulation, 55 inductor values (1.6 to $1800\,\mathrm{nH}$) and 29 capacitor values (12 to $1000\,\mathrm{pF}$) in the design kits were used. The circuit component values which are used for the final design of every matching circuit topology are summarized in Table 6.7 and Table 6.8. There are slight changes in the optimized component values compared to Table 6.3 and Table 6.4 due to the parastics of the non-ideal lumped components compared to the original capacitance and inductance values in the ideal matching circuits. The performance of the matching circuits using non-ideal lumped component models is discussed in Section 6.3.6.

6.3.5 DC Bias Circuit Design

In previously reported results, it has been confirmed that the RF isolation of DC bias circuits in the active matching configurations has not been good enough and has typically

TABLE 6.7
CIRCUIT COMPONENT VALUES FOR OPTIMIZED FIXED π MATCHING CIRCUIT TOPOLOGIES USING NON-IDEAL LUMPED COMPONENT S-PARAMETERS MODELS

Series L		Series C	
L_S	1000 nH	C_S	120 pF
C_{P1}	12 pF	L_{P1}	1800 nH
C_{P2}	39 pF	L_{P2}	820 nH

TABLE 6.8
CIRCUIT COMPONENT VALUES FOR OPTIMIZED ACTIVE MATCHING CIRCUITS WITH DIFFERENT NUMBER OF CELLS USING NON-IDEAL LUMPED COMPONENT S-PARAMETERS MODELS

	Inductors (nH)				Capacitors (pF)			
	L_1	L_2	L_3	L_4	C_1	C_2	C_3	C_4
1 cell	1000	-	-	-	47	-	-	-
2 cell	820	820	-	-	270	56	-	-
3 cell	560	4.3	820	-	100	330	33	-
4 cell	560	4.3	820	5.6	100	330	39	22

led to slight shifts in the impedance values of the matching circuits as to an increased dissipative loss. Therefore, the DC bias circuits of the p-i-n diode switches, which are typically composed of a series inductor (L_b), a parallel capacitor (C_b) and a current limiting resistance (R_b), as depicted in Fig. 6.28, are also optimized in our proposed approach by changing the values of the lumped components to reduce the undesired impedance value shift and dissipative loss. The S_{11} and S_{21} of both the original (initial design before optimization) and the optimized bias circuits are depicted in Fig. 6.29 (a) and (b), respectively assuming that the port1 is T_1 and the port2 is T_2 in Fig. 6.28 and both are connected to $50\,\Omega$ [123]. From Fig. 6.29 (a), it can be easily observed that the return loss of the original bias circuit is not as high as for the optimized circuit, thus being one of the main causes of undesired impedance value shifts. For the new design, a $100\,\mu\mathrm{H}$ inductor, DLW43SH101 from Murata, which provides the highest series inductance satisfying the self-resonant frequency above $13.6\,\mathrm{MHz}$, was used.

Due to the main operation principle of previously reported real-time matching systems, the switching speed must be faster than the reading of analog to digital converter (ADC) vir-

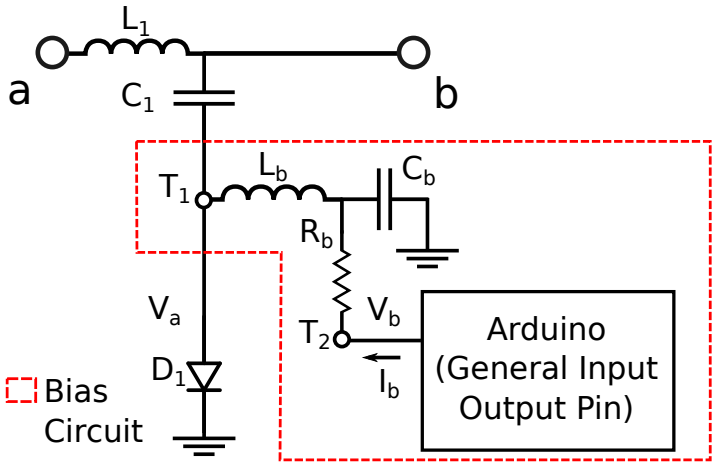

Figure 6.28. Circuit topology of the active matching circuit unit cell including the switch-controlled DC bias circuit.

tually controlling the switching status [121]. In the presented proof-of-concept prototype, an Arduino Uno micro-controller unit was used for the control of the p-i-n diode switches of the active matching circuit stages. From its datasheet, the sampling speed of Arduino is 9.6 ksps, which implies that the response time of the diode switch must be below $100\,\mu\mathrm{s}$. The value of C_b was chosen to be the highest capacitance value that satisfies the limitation of $100\,\mu\mathrm{s}$ LC response time for further RF isolation as can be seen in Fig. 6.29 (a) and (b). In Fig. 6.29 (c), the transient of the diode anode voltage (V_a) is depicted. The response time can be improved by removing C_b without a significant effect on RF isolation, and this can be an option when a micro-controller chip which features the capability of faster ADS reading, for example MSP432 (200 ksps), is used.

From the datasheet, the Arduino module has a rated output current of $20\,\mathrm{mA}$ with $5\,\mathrm{V}$ output voltage, and the value for R_b needs to be adjusted to satisfy this condition. The simulation results of the bias current (I_b) for an input power level of $30\,\mathrm{dBm}$ and bias voltage is $5\,\mathrm{V}$ is shown in Fig. 6.29 (d), and it turns out that the resistance in the original design is too high and the resulting current is unstable. R_b can be further lowered to $200\,\Omega$ for further stabilization. The original and the optimized value of each circuit component are summarized in Table 6.9.

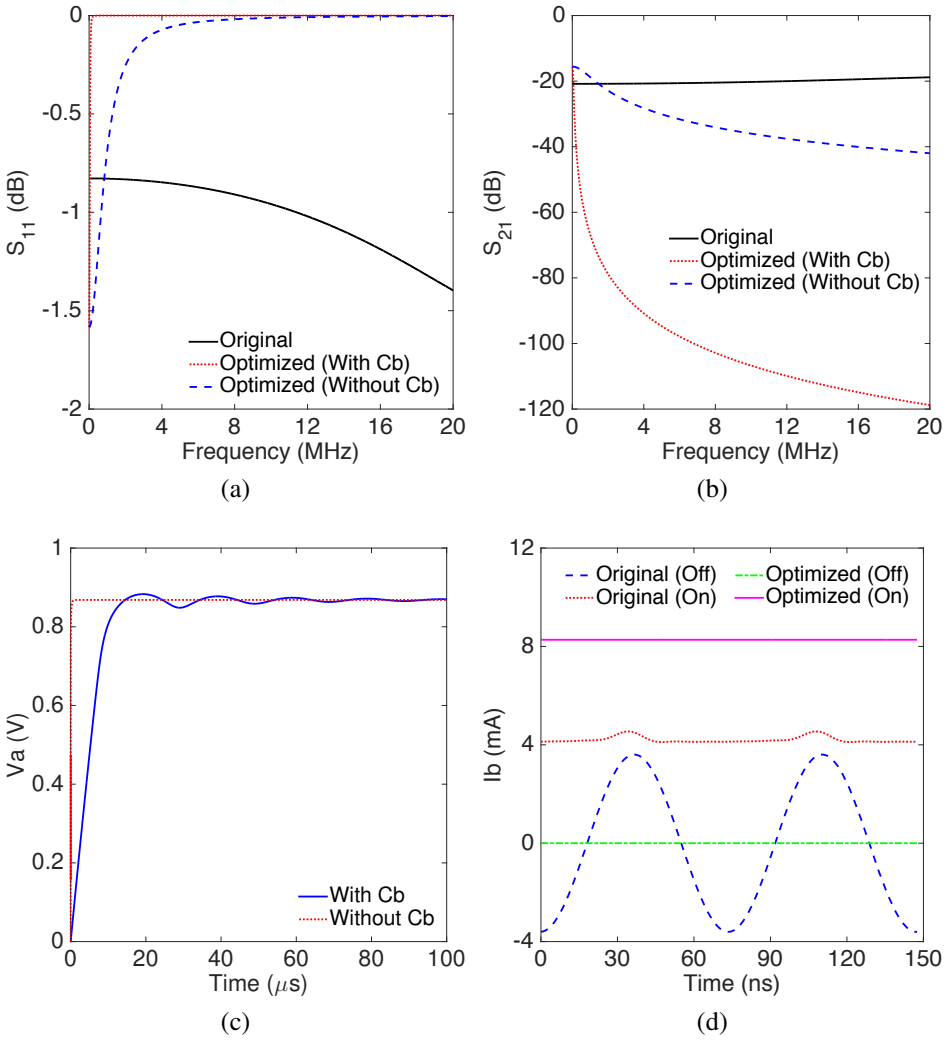

Figure 6.29. (a) S_{11} of the original and of the optimized bias circuits. (b) S_{21} of the original and of the optimized bias circuits. (c) Transient of the diode anode voltage after switching. (d) Steady state bias current at on/off states for the original and the optimized bias circuit.

6.3.6 Measurement Results and Discussion

Active Matching Circuit Operation Tests

Based on the optimized active matching circuit design using GA on MATLAB, the prototype of an 1-cell active matching circuit was fabricated as shown in Fig. 6.30. The series inductor and the parallel capacitor in the L-matching unit cell network, shown in Fig. 6.28, are Coilcraft 0603HL and Taiyo Yuden UMK105CG series, respectively. Also, the p-i-n diode is Skyworks SMP1340.

TABLE 6.9
PARAMETERS OF ACTIVE MATCHING CIRCUIT UNIT CELL DC BIAS COMPONENTS

	L_b	C_b	R_b
Original	330 nH	82 pF	1 kΩ
Optimized	100 µH	0.1 µF	500 Ω

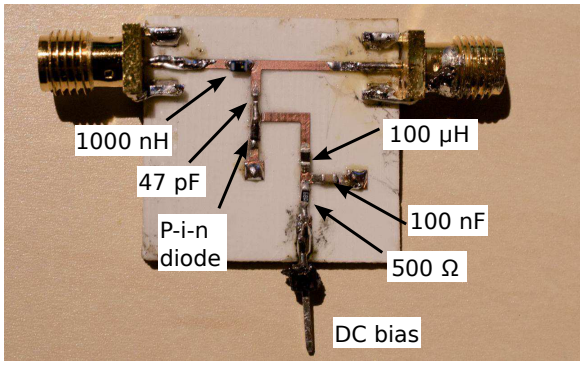

Figure 6.30. Prototype of an 1-cell active matching circuit.

The two port S-parameters of the 1-cell matching circuit at "on" and "off" states were measured using the VNA for an input power level of 0 dBm at 13.6 MHz and the S_{11} measured values for both states are plotted in Fig. 6.31. The bias voltage at "on" condition is 5 V from Arduino Uno module. For comparison purposes, ADS simulation results for the same matching circuit topology with ideal components ("Ideal") and non-ideal components utilizing their respective S-parameters ("S-parameter") are also depicted in the same figure. As can be easily observed from the figure, there are slight differences between the simulation results with ideal components and the measurement results. The simulation results using the non-ideal components' S-parameters and the non-ideal diode model are closer to the measurement results, which implies that GA matching design process can be improved by integrating S-parameters of each lumped component instead of using ideal values.

The S_{11} values of the matching circuit at "on" and "off" states were also measured for different input power levels. The output power from the VNA was calibrated using the power sensor, NRP-Z211 from Rohde & Schwarz, at 15 dBm which is the maximum output power from the VNA at 13.6 MHz. The measurement results for the input power levels of 15, 0, and -10 dBm are depicted in Fig. 6.32 (a) and (b). It can be easily recognized from the

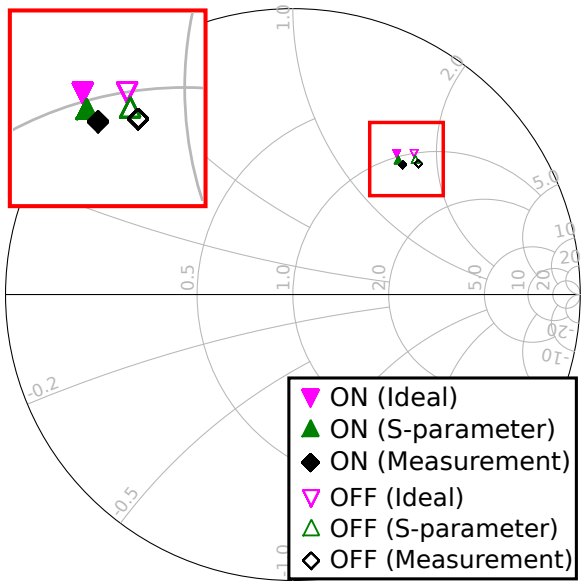

Figure 6.31. Measured and simulated input impedances of 1-cell active matching circuit at on and off conditions.

figures that there are slight differences in the input impedance values in the case of the input power level of 15 dBm compared to the other input power levels, but these differences are very small and can be omitted throughout the whole input power level range; this difference can increase for higher power levels (that are closer to the rated power of $250\,\mathrm{mW}$ for the SMP1340 p-i-n diode). For more practical applications such as the charging of electric vehicle and UAVs, which require a power handling capability that is typically more than $250\,\mathrm{mW}$, p-i-n diodes or other switching elements such as mechanical arrays, which have higher rated power, should be used. Even if different switching elements are used, the proposed matching circuit design method can be applied as long as the characteristics of the switching elements are close enough to that of an ideal switch.

Passive and Active Matching Circuits Performance Comparison

In addition to the 1-cell active matching circuit, five other matching circuit topologies were also fabricated based on the simulation results shown in Table 6.7 and Table 6.8. The measured input impedance of each matching circuit at all possible switching conditions are depicted in the Smith charts in Fig. 6.33. The bias circuit design is the same for all active

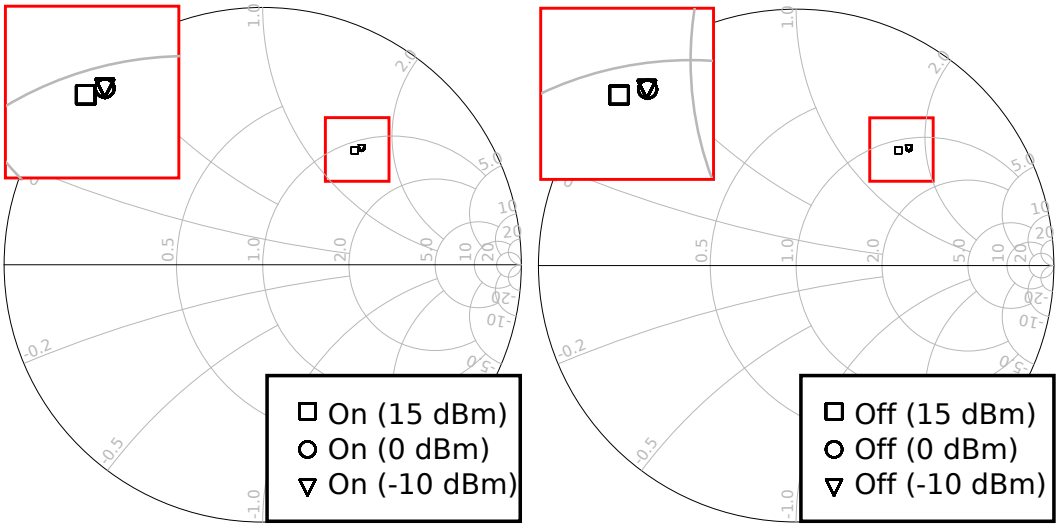

(a) (b)

Figure 6.32. Measured input impedance of the 1-cell active matching circuit for different input power levels at (a) "on" and (b) "off" switch conditions.

matching circuits. At the end, the power transfer efficiency for the six fabricated matching prototypes when connected to the Tx-Rx coil configurations described by the 100 samples of Trial1 was calculated using Eq. (6.14). The results for the implementations with ideal lumped circuit models, non-ideal lumped component S-parameter models and measured S-parameters are summarized in Table 6.10. From the table, it can be easily concluded that the measurement results are matching well with the simulation results in the cases of the passive matching circuit, and of the 1- and 2-cell active matching circuits. However, as the number of the stages/cells increases, the improvement of the measured power transfer efficiency saturates faster than the simulations, an effect that can be attributed to the increased dissipative loss associated with the increased number of non-ideal lumped components and p-i-n diodes in the circuit.

6.4 Discussion for Practical Applications

For more practical applications, ideally, it is better to use an active matching circuit which has a very wide variety of impedance values and then downselect the optimal impedance combinations for different coil combinations using a genetic algorithm or a machine learn-

TABLE 6.10
POWER TRANSFER EFFICIENCY COMPARISON WITH EACH MATCHING CIRCUIT WITH IDEAL LUMPED COMPONENTS, NON-IDEAL S-PARAMETERS MODELS AND MEASURED S-PARAMETERS

	No MC	Ser L	Ser C	1 C	2 C	3 C	4 C
Efficiency (Ideal) (%)		76.4	76.4	78.2	80.8	82.2	82.9
Efficiency (Non-ideal) (%)	61.5	73.2	70.7	75.1	76.3	77.4	77.9
Efficiency (Measurement) (%)		72.3	61.7	73.8	75.2	72.8	73.1

ing process as discussed in [124]. However, typically "off-the-shelf" trimmable capacitor ICs similar to the one used in [125] have a relatively low power handling capability and cannot be used for high power applications. Therefore, the proposed method requires the preliminary measurements of coil impedance to decide the combination of lumped components in the matching circuit which cannot be changed after the fabrication. Thus, one of the practical approaches is to standardize the coil design and make a library of measured impedance values for different coil combinations to avoid the repetitive coil impedance measurements. Also, for the charging of actual moving objects, the adjustment of time interval between each brute force matching circuit combination selection depending on the speed of the moving object to maximize the performance of the active matching may be required. Furthermore, the transition of the coil impedance value while the object is moving is expected to have a tendency depending on the type of movement. Therefore, some active learning process, such as a machine learning, and the real-time prediction of coil impedance value can be introduced in the system to further improve the performance of the matching circuit combination selection process rather than a simple repetitive brute force selection method.

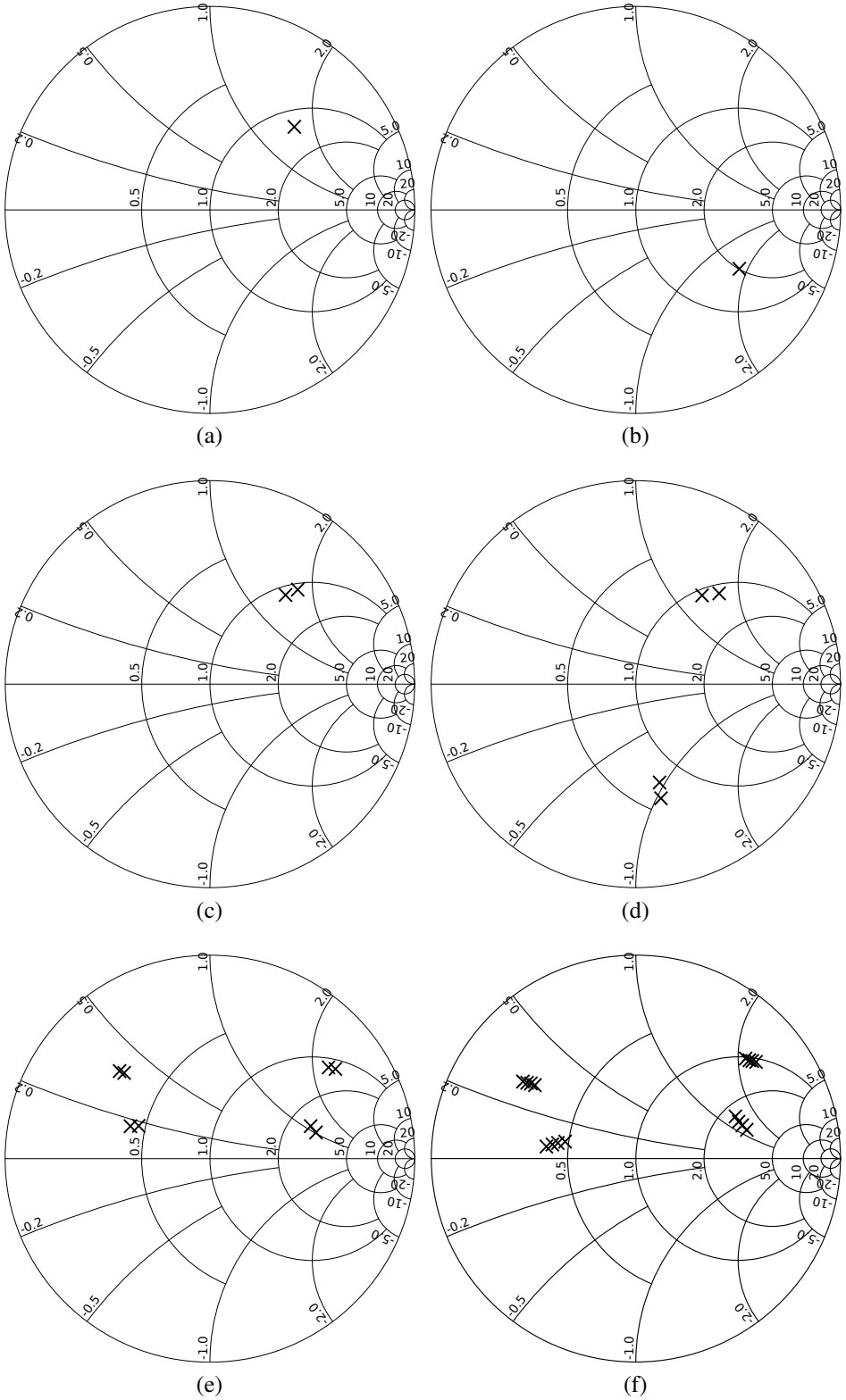

Figure 6.33. Measured input impedance of (a) L- and (b) C- series passive (c) 1-cell (d) 2-cell (e) 3-cell (f) 4-cell matching circuit.

CHAPTER 7

CONTRIBUTION AND CONCLUSION

7.1 Conclusion

The work presented in this dissertation encompasses the potential extension of additive manufacturing technologies for ambient RF energy harvesting and wireless power transfer systems. Ambient RF energy harvesting and wireless power transfer technology is one of the key technologies to realize a society based on IoTs, WSNs and wearable electronics in a truly wireless manner by eliminating the needs of wired powering and charging of batteries.

In this research, there are three major contributions. First, flexible wearable energy harvesters for off-the-shelf UHF ($464\,\mathrm{MHz}$) two-way talk radio which can generate $147\,\mathrm{mW}$ of output DC power and $24\,\mathrm{V}$ of open voltage was developed to power a conventional MSP430 MCU without the issue of cold start operation. The MCU and trimmable capacitor ICs, which are also powered by the wearable harvester, were utilized to improve the power transfer efficiency during human movement. By introducing novel hybrid GA and clustering matching circuit selection method, the power transfer loss was reduced by the maximum of $45.6\,\mathrm{mW}$. The harvester was also used to realize a fully autonomous on-body sensor network by utilizing DC and second harmonic signal from the harvester for backscattering communication. The DC power was utilized to power an RF amplifier IC and it enabled a sensing and a data transmission range of more than $75\,\mathrm{m}$.

Second, a hybrid RF/solar energy harvester module for $2.45\,\mathrm{GHz}$ with an integrated MCU, DCDC boost converter, and transceiver was developed for wireless indoor sensing. The DCDC converter was further improved and realized a power management circuit which has RF sensitivity of $-25\,\mathrm{dBm}$ and can be powered by a solar cell with minimum of $3\,\mathrm{lx}$ light irradiation that is as dark as night was realized. The HF oscillator signal for DC-DC boost conversion can be simultaneously utilized for backscattering modulation realizing a

continuous autonomous operation of backscattering tag. Also, a fully inkjet printed organic solar cell, which exhibits 0.2 to $0.25\,\mathrm{V}$ single cell open voltage under the room light condition, was developed.

Finally, a real-time active matching system for near-field power transfer was designed utilizing a genetic algorithm for wearable and in-vivo electronic devices. The active matching system can improve the power transfer efficiency by more than $70\,\%$ with the coil separation distance in the range of $60\,\%$ of coil diameter. The matching circuit design was optimized for a fast moving object by introducing a K-means clustering and the time to select the optimal matching circuit condition was reduced by 16 times from $64\,\mathrm{ms}$ in the previous design.

7.2 Contributions

The specific contributions of this dissertation are as follows:

1. Wearable flexible energy harvester for near-field RF EH
   (a) Characterization of EM field near a two-way talk radio and design of near-field RF energy harvesters.
      i. Characterization and estimation of RF input power from a near-field RF receiver utilizing a simulator software and numerical calculation utilizing S-parameters measurements.
      ii. Design, fabrication, and measurement of printed flexible near-field RF energy harvesters optimized for an MCU.
      iii. Assessment of the effect of a near-field RF energy harvester for communication through the measurements in anechoic chamber.
   (b) Analytic design of low-power real-time active matching circuit for near-field RF energy harvesters.

i. Low power active matching circuit design utilizing low-power variable capacitor ICs utilizing a original hybrid genetic algorithm and K-means clustering method.

(a) Design and demonstration of fully autonomous on-body sensor network utilizing a frequency doubler-based autonomous RF carrier emitter and backscatter sensor tags.

i. Design, fabrication, and characterization of a full-wave rectifier for $464\,\mathrm{MHz}$ to generate both DC and $928\,\mathrm{MHz}$ to interrogate on-body sensor tags. The DC power is used to power an RF amplifier to extend the range of operation. The generated $928\,\mathrm{MHz}$ signals are re-emitted from an on-body antenna which is isolated by utilizing AMC surface.

ii. Design, fabrication, and characterization of RF-harvester and switching transistor based backscatter sensor tag. A oscillator IC in the tag is powered by harvested DC power from the signal from $464\,\mathrm{MHz}$ UHF two-way talk radio and reflect the modulated $928\,\mathrm{MHz}$ signal emitted from a near-field harvester.

iii. Successful demonstration of bi-static backscatter radio communication to detect the signal from on-body sensor tags up to $75\,\mathrm{m}$ separation distance.

2. Hybrid RF/solar energy harvester for far-field RF EH.

(a) Development of a hybrid RF/solar harvester module with the capability of power management, sensing and communication.

i. Design and fabrication of a dual-port $2.45\,\mathrm{GHz}$ circularly polarized solar antenna for both communication and harvesting.

ii. Miniaturized rectifier for $2.45\,\mathrm{GHz}$ for DC combining with power from a solar cell.

iii. Module design with MSP430 MCU, CC2500 transmitter, and BQ25504 PMU for wireless sensing and charging.

(a) Development of an ultra-low power hybrid RF/PV energy harvester for high RF sensitivity.

i. System design and fabrication of a $59\,\mathrm{nW}$ DC-DC boost converter powered by ultra-low light below $3\,\mathrm{lx}$ for RF energy harvesting below $-20\,\mathrm{dBm}$ RF input power.

ii. Optimization of a $2.45\,\mathrm{GHz}$ energy harvester and charge tank capacitor for $-20\,\mathrm{dBm}$ RF input power through frequency domain simulation and numerical estimation.

iii. Design and fabrication of a fully printed organic solar cell with milti-layer printing of silver, P3HT:PCBM, PEI, and PIEDOT:PSS inks.

3. Active real-time matching circuit for near-field WPT.

(a) Development of a low-cost real-time active impedance matching system for in-vivo devices.

i. Design and characterization of open-helical type resonators for near-field WPT at $13.56\,\mathrm{MHz}$.

ii. Design of an active matching circuit with a combination of PIN diodes and lumped components through GA simulation.

iii. Development of a real-time active matching circuit controller system utilizing low-cost Arduino MCU.

iv. Development of a low-cost impedance matching performance estimation system utilizing directional-coupler and RF power detector IC.

v. Successful demonstration of a real-time active matching circuit operation based on brute-force iteration in less than $64\,\mathrm{ms}$.

(a) Development of an original active impedance matching circuit design method for WPT of moving objects utilizing K-means clustering.

   i. Development of a periodic S-parameters measurement system for characterization of the S-parameters of moving resonators utilizing LabView and VNA.

   ii. Design of an active matching circuit utilizing the measured S-parameters of resonators while moving and K-means clustering.

   iii. Design and characterization of a bias circuit for DC bias of the active matching circuit.

   iv. Performance comparison with a conventional passive matching circuit and reduced cell active matching circuit to prove the superiority of active matching circuit.

   v. Successful real-time active matching circuit operation time reduction more than 16 times from $64\,\mathrm{ms}$.

7.3 Future Work

This research has demonstrated the potential of RF energy harvesting and wireless power transfer technologies to replace the conventional power sources such as power supply cables and batteries. The extension of this work towards the realization of truly wireless society with low-cost IoT and WSN devices is as follows.

First of all, a conventional wireless sensor mote needs to reduce its power consumption drastically. Generally, this can be done by duty cycling the operation, but while the mote is in sleep mode, the power consumption is still relatively high and it prevents achieving an RF sensitivity below $1\,\mu\mathrm{W}$, which is the expected ambient RF power level in most locations. Also, with this low RF input power level, RF-DC conversion efficiency cannot be more than a single digit with conventional Schottky diodes. In the literature, a power management circuit with power consumption below $1\,\mathrm{nW}$ [38] and a rectifier with a tunnel diode which

achieved RF-DC conversion efficiency more than $10\,\%$ with input power below $1\,\mu\mathrm{W}$ [30] were reported. Similarly, relatively high required voltage level above $1\,\mathrm{V}$ prevents the direct utilization of RF harvester without DC-DC boost converter, which causes additional loss, in a system. In order to solve this issue, the further utilization of sub-threshold operation ICs, which enables the operation of ICs under $0.4\,\mathrm{V}$ [126], [127], needs to be considered.

Second, the further integration of system components such as antennas, diodes, transistors, and supercapacitors utilizing additive manufacturing technology needs to be studied. Nowadays, each major circuit component fabricated utilizing additive manufacturing technology is demonstrated. However, each reported result has different process flows which are not necessary compatible with each other. To realize a fully printed electronics, the integration of different processes will be a challenge.

Finally, with the emergence of new 5G communication utilizing milli-meter waves, the new types of RF energy harvesting needs to be considered. This includes RF energy harvesting from 5G communication carrier signals, but also the direct use of RF signals. For example, commonly used UHF band signals can be used as a modulation signal for milli-meter wave carrier signals.

The ideal of WPT has been around for more than 100 years since the idea was first announced by Tesla. His dream has not been truly realized yet, but with hope, the advances made in this work can be a suggestion for a large audience to inspire and encourage to make further progress this field of research, which make his dream comes true in near future.

7.4 Author's Publications

7.4.1 Journals

1. J. Bito, J. G. Hester, and M. M. Tentzeris, "Ambient RF Energy Harvesting From a Two-Way Talk Radio for Flexible Wearable Wireless Sensor Devices Utilizing Inkjet Printing Technologies," *IEEE Trans. Microw. Theory Techn.*, vol. 63, pp. 4533–4543, Dec 2015

2. J. Bito, S. Jeong, and M. M. Tentzeris, "A Real-time Electrically Controlled Active Matching Circuit Utilizing Genetic Algorithms for Wireless Power Transfer to Biomedical Implants," *IEEE Trans. Microw. Theory Techn.*, vol. 64, pp. 365–374, Feb 2016

3. J. Bito, R. Bahr, J. G. Hester, S. A. Nauroze, A. Georgiadis, and M. M. Tentzeris, "A Novel Solar and Electromagnetic Energy Harvesting System With a 3-D Printed Package for Energy Efficient Internet-of-Things Wireless Sensors," *IEEE Trans. Microw. Theory Techn.*, vol. 65, pp. 1831–1842, May 2017

4. J. Bito, S. Jeong, and M. M. Tentzeris, "A Novel Heuristic Passive and Active Matching Circuit Design Method for Wireless Power Transfer to Moving Objects," *IEEE Trans. Microw. Theory Techn.*, vol. 65, pp. 1094–1102, Apr. 2017

5. S. Kim, R. Vyas, J. Bito, K. Niotaki, A. Collado, A. Georgiadis, and M. Tentzeris, "Ambient RF Energy-Harvesting Technologies for Self-Sustainable Standalone Wireless Sensor Platforms," *Proc. IEEE*, vol. 102, pp. 1649–1666, Nov. 2014

6. J. G. Hester, S. Kim, J. Bito, T. Le, J. Kimionis, D. Revier, C. Saintsing, S. Wenjing, B. Tehrani, A. Traille, B. S. Cook, and M. M. Tentzeris, "Additively Manufactured Nanotechnology and Origami-Enabled Flexible Microwave Electronics," *Proc. IEEE*, vol. 103, pp. 583–606, Apr. 2015

7. S. A. Nauroze, J. G. Hester, B. K. Tehrani, W. Su, J. Bito, R. Bahr, J. Kimionis, and M. M. Tentzeris, "Additively Manufactured RF Components and Modules: Toward Empowering the Birth of Cost-Efficient Dense and Ubiquitous IoT Implementations," *Proc. IEEE*, pp. 1–21, 2017

8. V. Palazzi, J. Hester, J. Bito, F. Alimenti, C. Kalialakis, P. Mezzanotte, L. Roselli, A. Collado, A. Georgiadis, and M. M. Tentzeris, "A Novel Ultra-Lightweight Multi-Band Rectenna on Paper for RF Energy Harvesting in the Next Generation LTE Bands," *IEEE Trans. Microw. Theory Techn.*, vol. PP, no. 99, pp. 1–14, 2017

9. T.-H. Lin, J. Bito, J. G. Hester, J. Kimionis, R. A. Bahr, and M. M. Tentzeris, "On-body Long-range Wireless Backscattering Sensing System Using Inkjet-/3D-Printed Flexible Ambient RF Energy Harvesters Capable of Simultaneous DC and Harmonics Generation," *IEEE Trans. Microw. Theory Techn.*, Under review

7.4.2 Conferences

1. J. Bito, B. Tehrani, B. Cook, and M. Tentzeris, "Fully inkjet-printed multilayer microstrip patch antenna for ku-band applications," in *2014 IEEE Antennas and Propag. Society Int. Symp.*, IEEE, Jul. 2014

2. J. Bito, S. Kim, M. Tentzeris, and S. Nikolaou, "Ambient energy harvesting from 2-way talk-radio signals for for "smart meter and display applications," in *2014 IEEE Antennas and Propag. Society Int. Symp.*, IEEE, Jul. 2014

3. J. Bito, B. Tehrani, B. Cook, and M. Tentzeris, "Fully inkjet-printed multilayer microstrip patch antenna for Ku-band applications," in *2014 IEEE Antennas and Propag. Society Int. Symp.*, (Memphis, TN, USA), pp. 854–855, Jul. 2014

4. J. Bito, B. S. Cook, and M. M. Tentzeris, "A multi-coil wireless power transfer system utilizing dynamic matching for in-vivo and biomedical applications," in *2014 Asia-Pacific Microw. Conf.*, (Memphis, TN, USA), pp. 680–682, Nov. 2014

5. J. Bito and M. Tentzeris, "A Novel Flexible Wearable Magnetic Energy Harvester utilizing Inkjet Masking Techniques," in *2015 IEEE Antennas and Propag. Society Int. Symp.*, (Vancouver, Canada), Jul. 2015

6. J. Bito, S. Jeong, and M. M. Tentzeris, "A real-time electrically controlled active matching circuit utilizing genetic algorithms for biomedical WPT applications," in *2015 IEEE Wireless Power Transfer Conf.*, (Boulder, CO, USA), pp. 1–4, May 2015

7. J. Bito, J. G. Hester, and M. M. Tentzeris, "Ambient Energy Harvesting from a Two-way Talk Radio for Flexible Wearable Devices utilizing Inkjet Printing Masking," in *2015 IEEE MTT-S Int. Microwave Symp. Dig.*, (Phoenix, AZ, USA), pp. 1–4, May 2015

8. J. Bito, M. M. Tentzeris, and A. Georgiadis, "A hybrid heuristic design technique for real-time matching optimization for wearable near-field ambient RF energy harvesters," (San Francisco, CA, USA), Institute of Electrical and Electronics Engineers (IEEE), May 2016

9. J. Bito and M. M. Tentzeris, "Bias Circuit Design for a Real-time Electrically Controlled Active Matching Circuit utilizing p-i-n Diode Switches for Wireless Power Transfer," in *2016 IEEE Antennas and Propag. Society Int. Symp.*, (Fajardo, Puerto Rico), Jun-Jul. 2016

10. J. Bito, S. Jeong, and M. M. Tentzeris, "Heuristic passive and active matching circuit design method for wireless power transfer for moving objects," in *2016 IEEE Wireless Power Transfer Conf.*, (Aveiro, Portugal), pp. 1–4, May 2016

11. J. Bito, V. Palazzi, J. Hester, R. Bahr, F. Alimenti, P. Mezzanotte, L. Roselli, and M. M. Tentzeris, "Millimeter-wave ink-jet printed RF energy harvester for next generation flexible electronics," in *2017 IEEE Wireless Power Transfer Conf.*, (Taipei, Taiwan), IEEE, May 2017

12. J. Bito, J. G. Hester, and M. M. Tentzeris, "A fully autonomous ultra-low power hybrid RF/photovoltaic energy harvesting system with -25 dBm sensitivity," in *2017 IEEE Wireless Power Transfer Conf.*, (Taipei, Taiwan), IEEE, May 2017

13. J. Bito, R. Bahr, J. G. Hester, S. A. Nauroze, A. Georgiadis, and M. M. Tentzeris, "A Novel Solar and Electromagnetic Energy Harvesting System With a 3-D Printed Package for Energy Efficient Internet-of-Things Wireless Sensors," *IEEE Trans. Microw. Theory Techn.*, vol. PP, pp. 1–12, 2017

14. J. Bito, R. Bahr, J. Hester, J. Kimionis, A. Nauroze, W. Su, B. Tehrani, and M. M. Tentzeris, "Inkjet-/3d-/4d-printed autonomous wearable RF modules for biomonitoring, positioning and sensing applications," in *SPIE Defense+ Security*, pp. 101940–101940, International Society for Optics and Photonics, 2017

15. R. J. Vyas, J. Bito, S. Kim, and M. M. Tentzeris, "Harvesting wireless signals from two-way talk-radios to power smart meters and displays," in *2014 IEEE MTT-S Int. Microwave Symp. Dig.*, IEEE, Jun. 2014

16. B. K. Tehrani, J. Bito, B. S. Cook, and M. M. Tentzeris, "Fully inkjet-printed multilayer microstrip and T-resonator structures for the RF characterization of printable materials and interconnects," in *2014 IEEE MTT-S Int. Microwave Symp. Dig.*, (Tampa, FL, USA), pp. 1–4, Jun. 2014

17. J. H. Kim, J. Bito, and M. M. Tentzeris, "Design optimization of an energy harvesting RF-DC conversion circuit operating at 2.45GHz," in *2015 IEEE Antennas and Propag. Society Int. Symp.*, IEEE, Jul. 2015

18. S. Kim, J. Bito, S. Jeong, A. Georgiadis, and M. M. Tentzeris, "A flexible hybrid printed RF energy harvester utilizing catalyst-based copper printing technologies for far-field RF energy harvesting applications," in *2015 IEEE MTT-S Int. Microwave Symp. Dig.*, (Phoenix, AZ, USA), pp. 1–4, May 2015

19. A. Usman, J. Bito, and M. M. Tentzeris, "Flexible & planar implantable resonant coils for wireless power transfer using inkjet masking technique," in *2016 IEEE Topical Conference on Biomedical Wireless Technologies, Networks, and Sensing Systems (BioWireleSS)*, IEEE, Jan. 2016

20. S. A. Nauroze, J. Kimionis, J. Bito, W. Su, J. G. Hester, K. Nate, B. Tehrani, and M. M. Tentzeris, "Additive manufacturing technologies for near-and far-field energy harvesting applications," in *2016 IEEE Radio and Wireless Symposium (RWS)*, IEEE, Jan. 2016

21. S. Jeong, J. Bito, and M. M. Tentzeris, "Design of a novel wireless power system using machine learning techniques for drone applications," in *2017 IEEE Wireless Power Transfer Conf.*, (Taipei, Taiwan), IEEE, May 2017

22. X. He, J. Bito, and M. M. Tentzeris, "A drone-based wireless power transfer anc communications platform," in *2017 IEEE Wireless Power Transfer Conf.*, (Taipei, Taiwan), IEEE, May 2017

23. T.-H. Lin, J. Bito, J. G. Hester, J. Kimionis, R. A. Bahr, and M. M. Tentzeris, "Ambient Energy Harvesting from Two-Way Talk Radio for On-body Autonomous Wireless Sensing Network Using Inkjet and 3D Printing," (Honolulu, HI, USA), Institute of Electrical and Electronics Engineers (IEEE), May 2017

24. J. Iwata, J. Bito, and M. M. Tentzeris, "A wideband and high gain antenna on multilayer insulation blanket for rf energy harvesting," in *2017 IEEE Antennas and Propag. Society Int. Symp.*, (San Diego, CA, USA), Jun. 2017

25. T.-H. Lin, J. Bito, and M. M. Tentzeris, "Wearable inkjet printing energy harvester," in *2017 IEEE Antennas and Propag. Society Int. Symp.*, (San Diego, CA, USA), Jun. 2017

7.4.3 Book Chapters

1. B. K. Tehrani, J. Bito, J. G. Hester, W. Su, R. A. Bahr, B. S. Cook, and M. M. Tentzeris, *Advanced Antenna Fabrication Processes (MEMS/LTCC/LCP/Printing)*. Springer Singapore, 2015

7.4.4 Patents

1. J. Bito and M. M. Tentzeris, "Ambient energy harvesting from two-way talk radios for simultaneous DC supply and frequency doubling for on-body wireless sensing/communication network with a printed wearable flexible RF energy harvester," 01 2017 (Provisional Patent Filing)

2. J. Bito and M. M. Tentzeris, "Active and passive matching circuit system design utilizing a genetic algorithm and K-means clustering from measured S-parameters for wireless power transfer and near-field RF energy harvesting applications," 01 2017 (Provisional Patent Filing)

3. J. Bito and M. M. Tentzeris, "A Fully Autonomous Printed Ultra-low Power Hybrid RF/Photovoltaic Energy Harvesting System," 05 2017 (Provisional Patent Filing)

4. J. Bito and M. M. Tentzeris, "Simultaneous backscattering modulation and DC-DC boost conversion for energy autonomous sensing and communication," 07 2017 (Provisional Patent Filing)

REFERENCES

[1] J. Gubbi, R. Buyya, S. Marusic, and M. Palaniswami, "Internet of things (iot): A vision, architectural elements, and future directions," *Future Generation Computer Systems*, vol. 29, no. 7, 16451660, 2013.

[2] E. Kampianakis, J. Kimionis, K. Tountas, C. Konstantopoulos, E. Koutroulis, and A. Bletsas, "Wireless Environmental Sensor Networking With Analog Scatter Radio and Timer Principles," *IEEE Sensors J.*, vol. 14, no. 10, pp. 3365–3376, 2014.

[3] J. Kimionis, A. Bletsas, and J. N. Sahalos, "Increased range bistatic scatter radio," *IEEE Trans. Commun.*, vol. 62, no. 3, pp. 1091–1104, 2014.

[4] J. G. Hester and M. M. Tentzeris, "Inkjet-printed van-atta reflectarray sensors: A new paradigm for long-range chipless low cost ubiquitous smart skin sensors of the internet of things," *2016 IEEE MTT-S Int. Microwave Symp. Dig.*, 2016.

[5] S. Kim, R. Vyas, J. Bito, K. Niotaki, A. Collado, A. Georgiadis, and M. Tentzeris, "Ambient RF Energy-Harvesting Technologies for Self-Sustainable Standalone Wireless Sensor Platforms," *Proc. IEEE*, vol. 102, no. 11, pp. 1649–1666, 2014.

[6] S. Priya and D. J. Inman, *Energy harvesting technologies*. Springer, 2009, vol. 21.

[7] J. A. Paradiso and T. Starner, "Energy scavenging for mobile and wireless electronics," *IEEE Pervasive Comput.*, vol. 4, no. 1, pp. 18–27, 2005.

[8] R. J. Vyas, B. B. Cook, Y. Kawahara, and M. M. Tentzeris, "E-WEHP: A Batteryless Embedded Sensor-Platform Wirelessly Powered From Ambient Digital-TV Signals," *IEEE Trans. Microw. Theory Techn.*, vol. 61, no. 6, pp. 2491–2505, 2013.

[9] M. Pinuela, P. D. Mitcheson, and S. Lucyszyn, "Ambient RF Energy Harvesting in Urban and Semi-Urban Environments," *IEEE Trans. Microw. Theory Techn.*, vol. 61, no. 7, pp. 2715–2726, 2013.

[10] J. G. Hester, S. Kim, J. Bito, T. Le, J. Kimionis, D. Revier, C. Saintsing, S. Wenjing, B. Tehrani, A. Traille, B. S. Cook, and M. M. Tentzeris, "Additively Manufactured Nanotechnology and Origami-Enabled Flexible Microwave Electronics," *Proc. IEEE*, vol. 103, no. 4, pp. 583–606, 2015.

[11] B. Tehrani, B. Cook, J. Cooper, and M. Tentzeris, "Inkjet printing of a wideband, high gain mm-Wave Vivaldi antenna on a flexible organic substrate," in *2014 IEEE Antennas and Propag. Society Int. Symp.*, Memphis, TN, USA, 2014.

[12] J. Bito, B. Tehrani, B. Cook, and M. Tentzeris, "Fully inkjet-printed multilayer microstrip patch antenna for Ku-band applications," in *2014 IEEE Antennas and Propag. Society Int. Symp.*, Memphis, TN, USA, 2014, pp. 854–855.

[13] B. S. Cook, J. R. Cooper, and M. M. Tentzeris, "Multi-Layer RF Capacitors on Flexible Substrates Utilizing Inkjet Printed Dielectric Polymers," *IEEE Microw. Wireless Compon. Lett.*, vol. 23, no. 7, pp. 353–355, 2013.

[14] B. S. Cook, C. Mariotti, J. R. Cooper, D. Revier, B. K. Tehrani, L. Aluigi, L. Roselli, and M. M. Tentzeris, "Inkjet-printed, vertically-integrated, high-performance inductors and transformers on flexible LCP substrate," in *2014 IEEE MTT-S Int. Microwave Symp. Dig.*, Tampa, FL, USA, 2014, pp. 1–4.

[15] N. Sani, M. Robertsson, P. Cooper, X. Wang, M. Svensson, P. Andersson Ersman, P. Norberg, M. Nilsson, D. Nilsson, X. Liu, H. Hesselbom, L. Akesso, M. Fahlman, X. Crispin, I. Engquist, M. Berggren, and G. Gustafsson, "All-printed diode operating at 1.6 GHz," *Proc. of the Nat. Academy of Sciences*, vol. 111, no. 33, pp. 11 943–11 948, 2014.

[16] A. Kurs, A. Karalis, R. Moffatt, J. D. Joannopoulos, P. Fisher, and M. Soljai, "Wireless Power Transfer via Strongly Coupled Magnetic Resonances," *Science*, vol. 317, no. 5834, pp. 83–86, 2007.

[17] T. Imura, H. Okabe, and Y. Hori, "Basic experimental study on helical antennas of wireless power transfer for Electric Vehicles by using magnetic resonant couplings," in *2009 IEEE Vehicle Power and Propulsion Conf.*, Dearborn, MI, USA, 2009, pp. 936–940.

[18] D. Van Wageningen and T. Staring, "The qi wireless power standard," in *Power Electronics and Motion Control Conference (EPE/PEMC), 2010 14th International*, IEEE, 2010, S15–25.

[19] M. Philipose, J. R. Smith, B. Jiang, A. Mamishev, S. Roy, and K. Sundara-Rajan, "Battery-free wireless identification and sensing," *IEEE Pervasive Comput.*, vol. 4, no. 1, pp. 37–45, 2005.

[20] J. O. McSpadden and J. C. Mankins, "Space solar power programs and microwave wireless power transmission technology," *IEEE Microw. Mag.*, vol. 3, no. 4, pp. 46–57, 2002.

[21] S. Vatel, *MHI Demonstrates Wireless Power Transmission*, Skyworks Solutions, Inc., 2015.

[22] V. Liu, A. Parks, V. Talla, S. Gollakota, D. Wetherall, and J. R. Smith, "Ambient backscatter: Wireless communication out of thin air," *ACM SIGCOMM COMPUTER COMMUNICATION REVIEW*, vol. 43, no. 4, pp. 39–50, 2013.

[23] N. Tesla, "The transmission of electrical energy without wires," *Electrical World and Engineer*, vol. 1, 1904.

[24] T.-W. Yoo and K. Chang, "Theoretical and experimental development of 10 and 35 GHz rectennas," *IEEE Trans. Microw. Theory Techn.*, vol. 40, no. 6, pp. 1259–1266, 1992.

[25] S. Hemour and K. Wu, "Radio-Frequency Rectifier for Electromagnetic Energy Harvesting: Development Path and Future Outlook," *Proc. IEEE*, vol. 102, no. 11, pp. 1667–1691, 2014.

[26] C. R. Valenta and G. D. Durgin, "Harvesting Wireless Power: Survey of Energy-Harvester Conversion Efficiency in Far-Field, Wireless Power Transfer Systems," *IEEE Microw. Mag.*, vol. 15, no. 4, pp. 108–120, 2014.

[27] X. Lu, P. Wang, D. Niyato, D. I. Kim, and Z. Han, "Wireless Networks with RF Energy Harvesting: A Contemporary Survey," *IEEE Commun. Surveys Tuts.*, vol. 17, no. 2, pp. 757–789, 2015.

[28] J. McSpadden, L. Fan, and K. Chang, "Design and experiments of a high-conversion-efficiency 5.8-GHz rectenna," *IEEE Trans. Microw. Theory Techn.*, vol. 46, no. 12, 20532060, 1998.

[29] Y.-H. Suh and K. Chang, "A high-efficiency dual-frequency rectenna for 2.45- and 5.8-GHz wireless power transmission," *IEEE Trans. Microw. Theory Techn.*, vol. 50, no. 7, 17841789, 2002.

[30] C. H. P. Lorenz, S. Hemour, W. Li, Y. Xie, J. Gauthier, P. Fay, and K. Wu, "Overcoming the efficiency limitation of low microwave power harvesting with backward tunnel diodes," in *2015 IEEE MTT-S Int. Microwave Symp. Dig.*, Phoenix, AZ, USA, 2015, pp. 1–4.

[31] S. Imai, S. Tamaru, K. Fujimori, M. Sanagi, and S. Nogi, "Efficiency and harmonics generation in microwave to DC conversion circuits of half-wave and full-wave rectifier types," *2011 IEEE MTT-S Int. Microwave Symp. Dig.*, 2011.

[32] B. L. Pham and A.-V. Pham, "Triple bands antenna and high efficiency rectifier design for RF energy harvesting at 900, 1900 and 2400 MHz," in *2013 IEEE MTT-S Int. Microwave Symp. Dig.*, IEEE, 2013, pp. 1–3.

[33] J. Kimionis, A. Collado, M. M. Tentzeris, and A. Georgiadis, "Octave and decade printed uwb rectifiers based on nonuniform transmission lines for energy harvesting," *IEEE Trans. Microw. Theory Techn.*, 2017.

[34] H. Sun, Y. xin Guo, M. He, and Z. Zhong, "Design of a High-Efficiency 2.45-GHz Rectenna for Low-input-Power Energy Harvesting," *IEEE Antennas Wireless Propag. Lett.*, vol. 11, pp. 929–932, 2012.

[35] H. Sun, Y.-x. Guo, M. He, and Z. Zhong, "A Dual-Band Rectenna Using Broadband Yagi Antenna Array for Ambient RF Power Harvesting," *IEEE Antennas Wireless Propag. Lett.*, vol. 12, pp. 918–921, 2013.

[36] C. R. Valenta and G. D. Durgin, "Rectenna performance under power-optimized waveform excitation," in *2013 IEEE Int.Conf. on RFID*, Orlando, FL, USA, 2013.

[37] B. R. Marshall, M. M. Morys, and G. D. Durgin, "Parametric analysis and design guidelines of RF-to-DC dickson charge pumps for RFID energy harvesting," San Diego, CA, USA: Institute of Electrical & Electronics Engineers (IEEE), 2015.

[38] S. Bandyopadhyay, P. P. Mercier, A. C. Lysaght, K. M. Stankovic, and A. P. Chandrakasan, "A 1.1 nW energy-harvesting system with 544 pW quiescent power for next-generation implants," *IEEE J. of Solid-State Circuits*, vol. 49, no. 12, 28122824, 2014.

[39] T. Paing, J. Shin, R. Zane, and Z. Popovic, "Resistor Emulation Approach to Low-Power RF Energy Harvesting," *IEEE Trans. Power Electron.*, vol. 23, no. 3, pp. 1494–1501, 2008.

[40] E. J. Carlson, K. Strunz, and B. P. Otis, "A 20 mV Input Boost Converter with Efficient Digital Control for Thermoelectric Energy Harvesting," *IEEE J. Solid-State Circuits*, vol. 45, no. 4, pp. 741–750, 2010.

[41] S.-E. Adami, V. Marian, N. Degrenne, C. Vollaire, B. Allard, and F. Costa, "Self-powered ultra-low power DC-DC converter for RF energy harvesting," in *2012 IEEE FTFC*, Paris, France, 2012.

[42] K. Gudan, S. Shao, J. J. Hull, J. Ensworth, and M. S. Reynolds, "Ultra-low power 2.4GHz RF energy harvesting and storage system with -25dBm sensitivity," in *2015 IEEE Int.Conf. on RFID*, San Diego, CA, USA, 2015.

[43] K. Gudan, S. Shao, J. J. Hull, A. Hoang, J. Ensworth, and M. S. Reynolds, "Ultra-low power autonomous 2.4GHz RF energy harvesting and storage system," in *2015 IEEE Int. Conf. on RFID-TA*, Tokyo, Japan, 2015.

[44] E. Koutroulis, K. Kalaitzakis, and N. Voulgaris, "Development of a microcontroller-based, photovoltaic maximum power point tracking control system," *IEEE Trans. Power Electron.*, vol. 16, no. 1, 4654, 2001.

[45] Y. Huang, N. Shinohara, and T. Mitani, "A Constant Efficiency of Rectifying Circuit in an Extremely Wide Load Range," *IEEE Trans. Microw. Theory Techn.*, vol. 62, no. 4, pp. 986–993, 2014.

[46] S. Kim, J. Bito, S. Jeong, A. Georgiadis, and M. M. Tentzeris, "A flexible hybrid printed RF energy harvester utilizing catalyst-based copper printing technologies for far-field RF energy harvesting applications," in *2015 IEEE MTT-S Int. Microwave Symp. Dig.*, Phoenix, AZ, USA, 2015, pp. 1–4.

[47] L Yang, A. Rida, R. Vyas, and M. M. Tentzeris, "RFID Tag and RF structures on a Paper Substrate Using Inkjet-Printing Technology," *IEEE Trans. Microw. Theory Techn.*, vol. 55, no. 12, pp. 2894–2901, 2007.

[48] S. Jo, M. Kim, M. Kim, and Y. Kim, "Flexible thermoelectric generator for human body heat energy harvesting," *Electron. Let.*, vol. 48, no. 16, pp. 1013–1015, 2012.

[49] M. Stamos, N. Nicoleau, R. Torah, J. Tudor, N. R. Harris, A. Niewiadomski, and S. P. Beeby, "Screen printed piezoelectric generator for helicopter health and usage monitoring systems," 2008.

[50] Y.-B. Jeon, R Sood, J.-H. Jeong, and S.-G. Kim, "Mems power generator with transverse mode thin film pzt," *Sensors and Actuators A: Physical*, vol. 122, no. 1, pp. 16–22, 2005.

[51] R. R. Søndergaard, M. Hösel, and F. C. Krebs, "Roll-to-Roll fabrication of large area functional organic materials," *J. of Polymer Science Part B: Polymer Physics*, vol. 51, no. 1, pp. 16–34, 2013.

[52] P. Chen, H. Chen, and C. Qiu Jingand Zhou, "Inkjet printing of single-walled carbon nanotube/ruo2 nanowire supercapacitors on cloth fabrics and flexible substrates," *Nano Research*, vol. 3, no. 8, pp. 594–603, 2010.

[53] J. D. MacKenzie and C. Ho, "Perspectives on Energy Storage for Flexible Electronic Systems," *Proc. IEEE*, vol. 103, no. 4, pp. 535–553, 2015.

[54] J. G. Hester, Y. Fang, and M. M. Tentzeris, "Inkjet-printed, flexible, high performance, carbon nanomaterial based sensors for ammonia and DMMP gas detection," in *Proc. 45th European Microwave Conf.*, Paris, France, 2015.

[55] S. Zoltan, *Pulsed droplet ejecting system*, 1972.

[56] G. H. McKinley and M. Renardy, "Wolfgang von ohnesorge," *Physics of Fluids*, vol. 23, no. 12, p. 127 101, 2011.

[57] B. Derby, "Inkjet printing of functional and structural materials: Fluid property requirements, feature stability, and resolution," *Annual Review of Materials Research*, vol. 40, no. 1, 395–414, 2010.

[58] J. Li, F. Ye, S. Vaziri, M. Muhammed, M. C. Lemme, and M. Östling, "Efficient inkjet printing of graphene," *Advanced materials*, vol. 25, no. 29, pp. 3985–3992, 2013.

[59] J.-U. Park, M. Hardy, S. J. Kang, K. Barton, K. Adair, D. k. Mukhopadhyay, C. Y. Lee, M. S. Strano, A. G. Alleyne, J. G. Georgiadis, and et al., "High-resolution electrohydrodynamic jet printing," *Nature Materials*, vol. 6, no. 10, pp. 782–789, 2007.

[60] B. K. Tehrani, C. Mariotti, B. S. Cook, L. Roselli, and M. M. Tentzeris, "Development, characterization, and processing of thin and thick inkjet-printed dielectric films," *Organic Electronics*, vol. 29, pp. 135–141, 2016.

[61] B. K. Tehrani, J. Bito, B. S. Cook, and M. M. Tentzeris, "Fully inkjet-printed multilayer microstrip and T-resonator structures for the RF characterization of printable materials and interconnects," in *2014 IEEE MTT-S Int. Microwave Symp. Dig.*, Tampa, FL, USA, 2014, pp. 1–4.

[62] S. Crump, *Apparatus and method for creating three-dimensional objects*, US Patent 5,121,329, 1992.

[63] P. I. Deffenbaugh, R. C. Rumpf, and K. H. Church, "Broadband microwave frequency characterization of 3-D printed materials," *IEEE Trans. Compon. Packag. Technol.*, vol. 3, no. 12, pp. 2147–2155, 2013.

[64] S. Zhang, C. C. Njoku, W. G. Whittow, and J. C. Vardaxoglou, "Novel 3D printed synthetic dielectric substrates," *Microwave and Optical Technology Letters*, vol. 57, no. 10, pp. 2344–2346, 2015.

[65] S.-H. Chang, H. Kuan, H.-W. Wu, R.-Y. Yang, and M.-H. Weng, "Determination of microwave dielectric constant by two microstrip line method combined with em simulation," *Microwave and Optical Technology Letters*, vol. 48, no. 11, pp. 2199–2201, 2006.

[66] D. M. Pozar, *Microwave Engineering*, 4th ed. Hoboken, NJ, USA: John Wiley & Sons, Inc., 2011.

[67] K.-P. Latti, M. Kettunen, J.-P. Strom, and P. Silventoinen, "A review of microstrip t-resonator method in determining the dielectric properties of printed circuit board materials," *IEEE Trans. Instrum. Meas.*, vol. 56, no. 5, pp. 1845–1850, 2007.

[68] M. A. Green, *Solar cells: Operating principles, technology, and system applications*. Englewood Cliffs, NJ, USA: Prentice-Hall, Inc., 1982.

[69] S. Roundy, P. K. Wright, and J. Rabaey, "A study of low level vibrations as a power source for wireless sensor nodes," *Compt. Commun.*, vol. 26, no. 11, pp. 1131–1144, 2003.

[70] H. Kim, J. Kim, and J Kim, "A review of piezoelectric energy harvesting based on vibration," *Int. J. of Precision Eng. and Manufacturing*, vol. 12, no. 6, pp. 1129–1141, 2011.

[71] J. Bito, J. G. Hester, and M. M. Tentzeris, "Ambient RF Energy Harvesting From a Two-Way Talk Radio for Flexible Wearable Wireless Sensor Devices Utilizing Inkjet Printing Technologies," *IEEE Trans. Microw. Theory Techn.*, vol. 63, no. 12, pp. 4533–4543, 2015.

[72] K. Hwang, Y. Jung, Y. Heo, F. H. Scholes, S. E. Watkins, J. Subbiah, D. J. Jones, D. Kim, and D. Vak, "Toward Large Scale Roll-to-Roll Production of Fully Printed Perovskite Solar Cells," *Advanced Materials*, vol. 27, no. 7, pp. 1241–1247, 2015.

[73] T. M. Eggenhuisen, Y. Galagan, A. F.K. V. Biezemans, T. M.W. L. Slaats, W. Voorthuijzen, S Kommeren, S Shanmugam, J. Teunissen, A Hadipour, W. J. H. Verhees, S. C. Veenstra, M. J. J. Coenen, J. Gilot, R. Andriessen, and W. A. Groen, "High efficiency, fully inkjet printed organic solar cells with freedom of design," *J. of Materials Chemistry A*, vol. 3, no. 14, pp. 7255–7262, 2015.

[74] B. E. Kahn, "Patterning Processes for Flexible Electronics," *Proc. IEEE*, vol. 103, no. 4, pp. 497–517, 2015.

[75] T. N. D. Tibbits, P. Beutel, M. Grave, C. Karcher, E. Oliva, G. Siefer, A. Wekkeli, M. Schachtner, F. Dimroth, A. W. Bett, R. Krause, M. Piccin, N. Blanc, M. Munoz-Rico, C. Arena, E. Guiot, C. Charles-Alfred, C. Drazek, F. Janin, L. Farrugia, B. Hoarau, J. Wasselin, A. Tauzin, T. Signamarcheix, T. Hannappel, K. Schwarzburg, and A. Dobrich, "New efficiency frontiers with wafer-bonded multi-junction solar cells," in *Proc. of the 29th European Photovoltaic Solar Energy Conf. and Exhibiton*, 2014, pp. 1–4.

[76] M. Danesh and J. R. Long, "Photovoltaic Antennas for Autonomous Wireless Systems," *IEEE Trans. Circuits Syst. II*, vol. 58, no. 12, pp. 807–811, 2011.

[77] A. Collado and A. Georgiadis, "Conformal Hybrid Solar and Electromagnetic (EM) Energy Harvesting Rectenna," *IEEE Trans. Circuits Syst. I*, vol. 60, no. 8, pp. 2225–2234, 2013.

[78] G. Orecchini, L. Yang, M. M. Tentzeris, and L. Roselli, "Wearable battery-free active paper-printed RFID tag with human-energy scavenger," in *2011 IEEE MTT-S Int. Microwave Symp. Dig.*, 2011, pp. 1–1.

[79] P. Sharma and T. S. Bhatti, "A review on electrochemical double-layer capacitors," *Energy Conversion and Management*, vol. 51, no. 12, pp. 2901–2912, 2010.

[80] J. Bito, J. G. Hester, and M. M. Tentzeris, "Ambient Energy Harvesting from a Two-way Talk Radio for Flexible Wearable Devices utilizing Inkjet Printing Masking," in *2015 IEEE MTT-S Int. Microwave Symp. Dig.*, Phoenix, AZ, USA, 2015, pp. 1–4.

[81] J. Bito and M. Tentzeris, "A Novel Flexible Wearable Magnetic Energy Harvester utilizing Inkjet Masking Techniques," in *2015 IEEE Antennas and Propag. Society Int. Symp.*, Vancouver, Canada, 2015.

[82] M. Morales and Z. Shivers, *Appl. Note SLAA378D Wireless Sensor Monitor Using the eZ430-RF2500*, Texas Instruments, Inc., 2011.

[83] K. Niotaki, A. Georgiadis, and A. Collado, "Dual-band rectifier based on resistance compression networks," in *2014 IEEE MTT-S Int. Microwave Symp. Dig.*, Tampa, FL, USA, 2014, pp. 1–3.

[84] Y. Han, O. Leitermann, D. A. Jackson, J. M. Rivas, and D. J. Perreault, "Resistance Compression Networks for Radio-Frequency Power Conversion," *IEEE Trans. Power Electron.*, vol. 22, no. 1, pp. 41–53, 2007.

[85] Q. Gu, J. R. De Luis, A. S. Morris, and J. Hilbert, "An Analytical Algorithm for Pi-Network Impedance Tuners," *IEEE Trans. Circuits Syst. I*, vol. 58, no. 12, pp. 2894–2905, 2011.

[86] J. Bito, S. Jeong, and M. M. Tentzeris, "A real-time electrically controlled active matching circuit utilizing genetic algorithms for biomedical WPT applications," in *2015 IEEE Wireless Power Transfer Conf.*, Boulder, CO, USA, 2015, pp. 1–4.

[87] D. Arthur and S. Vassilvitskii, "K-means++: The Advantages of Careful Seeding," in *Proc. of the 18th Annu. ACM-SIAM Symp. on Discrete Algorithms*, New Orleans, LA, 2007, pp. 1027–1035.

[88] A. Feresidis, G. Goussetis, S. Wang, and J. Vardaxoglou, "Artificial magnetic conductor surfaces and their application to low-profile high-gain planar antennas," *IEEE TRANS. ANTENNAS PROPAG.*, vol. 53, no. 1, pp. 209–215, 2005.

[89] R. Bahr, T. Le, M. M. Tentzeris, S. Moscato, M. Pasian, M. Bozzi, and L. Perregrini, "RF characterization of 3D printed flexible materials-NinjaFlex Filaments," in *Proc. 45th European Microwave Conf.*, IEEE, 2015, pp. 742–745.

[90] J. Kimionis and M. M. Tentzeris, "Pulse Shaping: The Missing Piece of Backscatter Radio and RFID," *IEEE Trans. Microw. Theory Techn.*, vol. 64, no. 12, pp. 4774–4788, 2016.

[91] E Bekyarova, M Davis, T Burch, M. Itkis, B Zhao, S Sunshine, and R. Haddon, "Chemically functionalized single-walled carbon nanotubes as ammonia sensors," *The J. of Phys. Chem. B*, vol. 108, no. 51, pp. 19 717–19 720, 2004.

[92] T.-H. Lin, J. Bito, J. G. Hester, J. Kimionis, R. A. Bahr, and M. M. Tentzeris, "On-body Long-range Wireless Backscattering Sensing System Using Inkjet-/3D-Printed Flexible Ambient RF Energy Harvesters Capable of Simultaneous DC and Harmonics Generation," *IEEE Trans. Microw. Theory Techn.*, Under review.

[93] Y. Zhou, T. M. Khan, J. W. Shim, A. Dindar, C. Fuentes-Hernandez, and B. Kippelen, "All-plastic solar cells with a high photovoltaic dynamic range," *J. of Materials Chemistry A*, vol. 2, no. 10, p. 3492, 2014.

[94] J. Tong, S. Xiong, Y. Zhou, L. Mao, X. Min, Z. Li, F. Jiang, W. Meng, F. Qin, T. Liu, and et al., "Flexible all-solution-processed all-plastic multijunction solar cells for powering electronic devices," *Mater. Horiz.*, vol. 3, no. 5, pp. 452–459, 2016.

[95] Texas Instruments, "Bq25504-Ultra Low Power Boost Converter with Battery Management for Energy Harvester Applications," 2012.

[96] ——, "MSP430F22x4: MIXED SIGNAL MICROCONTROLLER," 2012.

[97] ——, "CC2500: Low-Cost Low-Power 2.4 GHz RF Transceiver," 2010.

[98] S. Shi, K. Hirasawa, and Z. N. Chen, "Circularly polarized rectangularly bent slot antennas backed by a rectangular cavity," *IEEE Trans. Antennas Propag.*, vol. 49, no. 11, pp. 1517–1524, 2001.

[99] R. Li, B. Pan, A. N. Traille, J. Papapolymerou, J. Laskar, and M. M. Tentzeris, "Development of a Cavity-Backed Broadband Circularly Polarized Slot/Strip Loop Antenna With a Simple Feeding Structure," *IEEE Trans. Antennas Propag.*, vol. 56, no. 2, pp. 312–318, 2008.

[100] T Nakatsuka, "Polylactic acid-coated cable," *Fujikura Tech. Rev*, vol. 3946, no. 7, 2011.

[101] J. Bito, R. Bahr, J. G. Hester, S. A. Nauroze, A. Georgiadis, and M. M. Tentzeris, "A Novel Solar and Electromagnetic Energy Harvesting System With a 3-D Printed Package for Energy Efficient Internet-of-Things Wireless Sensors," *IEEE Trans. Microw. Theory Techn.*, vol. PP, pp. 1–12, 2017.

[102] J. G. Hester and M. M. Tentzeris, "A mm-wave ultra-long-range energy-autonomous printed rfid-enabled van-atta wireless sensor: At the crossroads of 5g and iot," *2017 IEEE MTT-S Int. Microwave Symp. Dig.*, 2017.

[103] C. W. Tang, "Two-layer organic photovoltaic cell," *Applied Physics Letters*, vol. 48, no. 2, pp. 183–185, 1986.

[104] M. Hiramoto, H. Fujiwara, and M. Yokoyama, "Three-layered organic solar cell with a photoactive interlayer of codeposited pigments," *Applied Physics Letters*, vol. 58, no. 10, pp. 1062–1064, 1991.

[105] B. Kadem, A. Hassan, and W. Cranton, "Efficient P3HT:PCBM bulk heterojunction organic solar cells; effect of post deposition thermal treatment," *Journal of Materials Science: Materials in Electronics*, vol. 27, no. 7, pp. 7038–7048, 2016.

[106] C. N. Hoth, S. A. Choulis, P. Schilinsky, and C. J. Brabec, "High photovoltaic performance of inkjet printed polymer:fullerene blends," *Advanced Materials*, vol. 19, no. 22, pp. 3973–3978, 2007.

[107] Y. Zhou, C. Fuentes-Hernandez, J. Shim, J. Meyer, A. J. Giordano, H. Li, P. Winget, T. Papadopoulos, H. Cheun, J. Kim, and et al., "A universal method to produce low-work function electrodes for organic electronics," *Science*, vol. 336, no. 6079, pp. 327–332, 2012.

[108] G. Azzellino, A. Grimoldi, M. Binda, M. Caironi, D. Natali, and M. Sampietro, "Fully inkjet-printed organic photodetectors with high quantum yield," *Advanced Materials*, vol. 25, no. 47, pp. 6829–6833, 2013.

[109] J. Shin, S. Shin, Y. Kim, S. Ahn, S. Lee, G. Jung, S. Jeon, and D. Cho, "Design and Implementation of Shaped Magnetic-Resonance-Based Wireless Power Transfer System for Roadway-Powered Moving Electric Vehicles," *IEEE Trans. Ind. Electron.*, vol. 61, no. 3, pp. 1179–1192, 2014.

[110] T. Imura, H. Okabe, T. Uchida, and Y. Hori, "Study on open and short end helical antennas with capacitor in series of wireless power transfer using magnetic resonant couplings," in *35th Annual Conf. on IEEE Ind. Electron. Soc.*, Porto, Portugal, 2009, pp. 3848–3853.

[111] T. Imura and Y. Hori, "Maximizing Air Gap and Efficiency of Magnetic Resonant Coupling for Wireless Power Transfer Using Equivalent Circuit and Neumann Formula," *IEEE Trans. Ind. Electron.*, vol. 58, no. 10, pp. 4746–4752, 2011.

[112] T. C Beh, M. Kato, T. Imura, S. Oh, and Y. Hori, "Automated Impedance Matching System for Robust Wireless Power Transfer via Magnetic Resonance Coupling," *IEEE Trans. Ind. Electron.*, vol. 60, no. 9, pp. 3689–3698, 2013.

[113] H. M. Nemati, C. Fager, U. Gustavsson, R. Jos, and H. Zirath, "Design of Varactor-Based Tunable Matching Networks for Dynamic Load Modulation of High Power Amplifiers," *IEEE Trans. Microw. Theory Tech.*, vol. 57, no. 5, pp. 1110–1118, 2009.

[114] C. Sanchez-Perez, J. de Mingo, P. L. Carro, and P. Garcia-Ducar, "Design and Applications of a 300- 800 MHz Tunable Matching Network," *IEEE Trans. Emerg. Sel. Topics Circuits Syst.*, vol. 3, no. 4, pp. 531–540, 2013.

[115] J. M. Johnson and V. Rahmat-Samii, "Genetic algorithms in engineering electromagnetics," *IEEE Antennas Propag. Mag.*, vol. 39, no. 4, pp. 7–21, 1997.

[116] C. Sanchez-Perez, J. de Mingo, P. Garcia-Ducar, P. L. Carro, and A. Valdovinos, "Figures of merit and performance measurements for RF and microwave tunable matching networks," in *2011 European Microw. Integr. Circuits Conf.*, Manchester, United Kingdom, 2011, pp. 402–405.

[117] F. Casini, R. V. Gatti, V. Perrone, and R. Sorrentino, "A new approach to the analysis and synthesis of lossy reconfigurable matching networks," in *Proc. 39th European Microwave Conf.*, Rome, Italy, 2009, pp. 1235–1238.

[118] *Appl. Note Design with PIN diodes*, Skyworks Solutions, Inc., 2012.

[119] *DATA SHEET SMP1340 Series: Fast Switching Speed, Low Capacitance, Plastic Packaged PIN Diodes*, Skyworks Solutions, Inc., 2012.

[120] A. K. RamRakhyani, S. Mirabbasi, and M. Chiao, "Design and optimization of resonance-based efficient wireless power delivery systems for biomedical implants," *IEEE Trans. Biomed. Circuits Syst.*, vol. 5, no. 1, pp. 48–63, 2011.

[121] J. Bito, S. Jeong, and M. M. Tentzeris, "A Real-time Electrically Controlled Active Matching Circuit Utilizing Genetic Algorithms for Wireless Power Transfer to Biomedical Implants," *IEEE Trans. Microw. Theory Techn.*, vol. 64, no. 2, pp. 365–374, 2016.

[122] S. Lloyd, "Least squares quantization in PCM," *IEEE Trans. Inf. Theory*, vol. 28, no. 2, pp. 129–137, 1982.

[123] J. Bito and M. M. Tentzeris, "Bias Circuit Design for a Real-time Electrically Controlled Active Matching Circuit utilizing p-i-n Diode Switches for Wireless Power Transfer," in *2016 IEEE Antennas and Propag. Society Int. Symp.*, Fajardo, Puerto Rico, 2016.

[124] J. Bito, M. M. Tentzeris, and A. Georgiadis, "A hybrid heuristic design technique for real-time matching optimization for wearable near-field ambient RF energy harvesters," *2016 IEEE MTT-S Int. Microwave Symp. Dig.*, 2016.

[125] J. Bito, S. Jeong, and M. M. Tentzeris, "Heuristic passive and active matching circuit design method for wireless power transfer for moving objects," in *2016 IEEE Wireless Power Transfer Conf.*, Aveiro, Portugal, 2016, pp. 1–4.

[126] A. Wang, B. H. Calhoun, and A. P. Chandrakasan, *Sub-threshold design for ultra low-power systems*. Springer, 2006, vol. 95.

[127] A. Bryant, J. Brown, P. Cottrell, M. Ketchen, J. Ellis-Monaghan, and E. Nowak, "Low-power CMOS at Vdd=4kT/q," *Device Research Conf.*, 2001.

VITA

The author was born and raised in Toyooka, Japan. He received the B.S. in electrical and electronic engineering from Okayama University, Okayama, Japan in 2013. From 2010 to 2011, he joined the international programs in engineering (IPENG), and studied at University of Illinois Urbana-Champaign, Champaign, IL, USA. He received the M.S. and the Ph.D. in electrical and computer engineering from the Georgia Institute of Technology in 2016 and 2017, respectively. He is a recipient of the Japan Student Services Organization (JASSO) long term scholarship from 2013 to 2016.

In 2013, he joined the Agile Technologies for High-performance Electromagnetic Novel Applications (ATHENA) research group as a research assistant under the direction of Prof. Manos M. Tentzeris where he helped developing the energy autonomous flexible, wearable, and printed wireless sensing systems. During his time at Georgia Tech, he also experienced the internship at Texas Instruments (TI) in Dallas as a packaging engineer in 2016. After graduation, he accepted a research engineer position at TI.